

*Investigation of Vesicle Pool Dynamics at Activity
Modulated Inner Hair Cell Ribbon Synapses*

Doctorate of Philosophy (Ph.D.) Dissertation

For the award of the degree

Dr. rer. nat.

GGNB-Sensory and Motor Neuroscience Program

Division of Mathematics and Natural Sciences

Georg-August-Universität Göttingen

Submitted by

Rituparna Chakrabarti

From

Kolkata, India

Göttingen, Germany

2016

Examination Committee Members

Member of the Core Thesis Committee

1. Prof. Dr. Carolin Wichmann, Institute for Auditory Neuroscience and InnerEarLab, University Medical Center, Göttingen (1st Reviewer, Supervisor)
2. Prof. Dr. Thomas Dresbach, Center for Anatomy and Embryology, University Medical Center, Göttingen (2nd Reviewer)
3. Dr. Camin Dean, Trans-synaptic Signaling Group, European Neuroscience Institute, Göttingen

Member of the Extended Thesis Committee

1. Prof. Dr. Silvio. O. Rizzoli, Department of Neuro- and Sensory Physiology, University Medical Center, Göttingen
2. Prof. Dr. Jochen Staiger, Department of Neuroanatomy, University Medical Center, Göttingen
3. Dr. Manuela Schmidt, Somatosensory Signaling Group, Max-Planck Institute for Experimental Medicine, Göttingen

Date of submission: 11th December, 2016

Date of the oral examination: 26th January, 2017

Declaration

I hereby declare that this dissertation is written independently with no other sources and aids than cited

Rituparna Chakrabarti

11th December, 2016

Göttingen, Germany

Table of Contents

Table of Contents	v
List of Abbreviations	xi
Abstract	1
1. Introduction.....	3
1.1 Overview of cochlear organization and mechanics.....	3
1.2 Sensory transduction at the organ of Corti.....	4
1.3 The inner hair cells (IHCs)	5
1.4 The ribbon synapses	6
1.5 Proposed release mechanisms at ribbon type synapses.....	7
1.6 Unique molecular identity of IHCs	11
1.6.1 Scaffolding proteins at IHC ribbon synapses	11
1.6.2 Proteins mediating exocytosis at IHCs.....	12
1.7 Dynamic vesicle pools at IHC ribbon synapses	15
1.8 Filamentous organization at conventional and ribbon synapses	17
1.8.1 Filament organization and function away from the AZ membrane	18
1.8.2 Filament organization and function close to the AZ membrane.....	18
1.9 Aims of this study.....	19
1.9.1 Major objectives of this thesis.....	19
2. Materials and methods.....	23
2.1 Animals	23
2.1.1 Mouse lines and treatment conditions	23
2.2 Dissection of the apical turn of the organ of Corti	24
2.3 Sample preparation for transmission electron microscopy (TEM)	25

2.3.1 Conventional embedding.....	25
2.3.2 High-pressure freezing (HPF)	26
2.3.3 Optical stimulation in combination with HPF (Opto-HPF)	27
2.3.4 Freeze substitution (FS)	33
2.3.5 Trimming, ultrathin-sectioning and section staining.....	34
2.4 Transmission electron microscopy (TEM)	35
2.4.1 TEM for 2-D analysis and screening of sample quality.....	35
2.4.2 Single tilt axis electron-tomography for 3-D visualization and analysis.....	35
2.5 Image processing and quantification parameters	36
2.5.1 Quantification parameters for 2-D analysis of random sections.....	36
2.5.2 Tomogram generation performed with IMOD from the raw tilt series	38
2.5.3 Model rendering and quantification parameters for the 3-D tomogram analysis	38
2.6 Data analysis and statistical tests.....	43
2.7 Experimental workflow.....	44
2.8 Materials.....	44
2.8.1 Product details.....	44
2.8.2 Equipment.....	45
2.8.3 Solution details	46
3. Results.....	47
3.1 Otoferlin is critical for the reformation of properly sized and fusion-competent synaptic vesicles	49
3.1.1 Unaltered ultrastructural organization and ribbon synapse numbers at <i>Otof</i> ^{d515T/1515T} IHCs	49

3.1.2 <i>Otof</i> ^{d515T/515T} IHCs showed SV accumulation proximal to the AZ membrane, but an unaltered number of ribbon-associated SVs	50
3.1.3 Large vesicles (> 45 nm) accumulated in the MP and the RA pool upon mild-stimulation at the elevated temperature in <i>Otof</i> ^{d515T/515T}	51
3.1.4 The refinement of the vesicle pool analysis using electron tomography confirmed an increase in large vesicles in <i>Otof</i> ^{d515T/515T}	55
3.1.5 Summary	60
3.2 Tethering is crucial for replenishment of SVs at IHC ribbon synapses: Investigating the role of otoferlin in tethering and exocytosis	61
3.2.1 Unaltered morphology of wild-type and <i>Otof</i> ^{Pga/Pga} ribbon synapses upon inhibition/stimulation	61
3.2.2 Normal sized SVs were observed in the RA and MP pool of <i>Otof</i> ^{Pga/Pga} IHCs	62
3.2.3 More RA SVs were present in <i>Otof</i> ^{Pga/Pga} under inhibition	65
3.2.4 Pleomorphic vesicles cluster were present in <i>Otof</i> ^{Pga/Pga} IHCs	67
3.2.5 Investigation and filament classification of the RA pool at IHC ribbon synapses	69
3.2.6 Comparative analysis of RA filaments at wild-type and <i>Otof</i> ^{Pga/Pga} ribbon synapses	72
3.2.7 Refinement of the fractions for single and multiple-filaments	77
3.2.8 Unaltered filament length in RA pool upon stimulation	84
3.2.9 Investigation and tether classification of the MP pool at IHC ribbon synapses...	85
3.2.10 Upon stimulation SVs with single membrane-attached tethers increased in wild-type but modestly decreased in <i>Otof</i> ^{Pga/Pga} IHCs	87
3.2.11 The fraction of multiple-tethered SVs was increased at the <i>Otof</i> ^{Pga/Pga} AZ membrane	89
3.2.12 The fraction of docked vesicles was increased at <i>Otof</i> ^{Pga/Pga} AZs	91

3.2.13 Shorter tethers are found at the MP pool of <i>Otof</i> ^{Pga/Pga} ribbon synapses upon stimulation	93
3.2.14 Summary	95
3.3 Analysis of other proteins involved in tethering: RIM2α is a potential candidate ..	98
3.3.1 Unaltered ribbon synapse morphology was observed in <i>RIM2α KO</i>	98
3.3.2 Reduced number of SVs with filaments in the proximal part of the ribbon although, filament length in <i>RIM2α KO</i> IHCs was unaltered	99
3.3.3 Disruption of RIM2α reduces the fraction of MP tethered SVs	102
3.3.4 Summary	105
3.4 Implementation of HPF in combination with optogenetic stimulation	107
3.4.1 Cellular physiology showed IHCs can be evoked optogenetically	107
3.4.2 Verification of ChR-2 expression in hair cells	108
3.4.3 Ultrastructural preservation in <i>Ai32VC</i> transgenic mice after Opto-HPF/FS showed good structural preservation	108
3.4.4 LED stimulation in the HPM-100.....	109
3.4.5 Analysis of RA pool in <i>Ai32VC</i> mice after optical stimulation	110
3.4.6 Analysis of MP SV pool in <i>Ai32VC</i> mice after optical stimulation	114
3.4.7 SV diameter for RA SVs was larger than for MP SVs after 10 ms stimulus	119
3.4.8 Summary	120
4. Discussion	121
4.1 New role of otoferlin in vesicle reformation.....	121
4.1.1 Sustained component of exocytosis at IHC ribbon synapse requires otoferlin .	122
4.1.2 Large vesicles appear at 39 °C at <i>Otof</i> ^{I515T/I515T} IHC ribbon synapses	122
4.1.3 EM study argues against homotypic fusion of vesicles	123
4.1.4 Vesicle reformation is affected in <i>Otof</i> ^{I515T/I515T}	124

4.1.5 Conclusion.....	125
4.2 Stimulation alters the vesicle tethering at IHC ribbon synapses	127
4.2.1 Ribbon morphology was unaltered in the <i>Otof</i> ^{Pga/Pga} mutant.....	127
4.2.2 <i>Otof</i> ^{Pga/Pga} mutation does not alter the size of vesicles	128
4.2.3 In the <i>Otof</i> ^{Pga/Pga} mutants clusters of synaptic and pleomorphic vesicles are observed	128
4.2.4 Distinct vesicle pools determine different stages of release at IHC ribbon synapses.....	130
4.2.5 The <i>Otof</i> ^{Pga/Pga} mutation hinders multiple-filament formation at the distal part of the ribbon which is present in wild-type upon stimulation	131
4.2.6 Single membrane-attached tethers recruit vesicles to the membrane at both wild-type and <i>Otof</i> ^{Pga/Pga} IHC ribbon synapses	133
4.2.7 Further steps after recruitment of vesicles at the AZ membrane.....	134
4.2.8 Conclusion.....	136
4.3 Rab-3 interacting molecules (RIM) 2α promotes vesicle tethering to the AZ	139
4.3.1 Unaltered gross morphology of IHCs in <i>RIM2α KO</i>	139
4.3.2 Disruption of RIM2 α hinders vesicle tethering to the proximal ribbon part and AZ membrane	139
4.3.3 Conclusion.....	141
4.4 First glimpse at the early exocytosis in IHC ribbon synapses.....	143
4.4.1 Exocytosis in IHCs can be evoked by optogenetic stimulation.....	144
4.4.2 Considering the time points of the optical stimulation.....	145
4.4.3 Filament connectivity was unaltered in the RA pool.....	146
4.4.4 Synaptic vesicles at the ribbon redistribute to the membrane upon optical stimulation.....	146

4.4.5 Recruitment of vesicles mediated by tethers at the MP pool.....	147
4.4.6 Multiple-tethered and docked vesicles increase after 10 ms optical stimulation	148
4.2.7 Conclusion.....	149
Bibliography.....	153
Acknowledgments.....	167
Appendix information.....	169
Appendix I: Work flow for the results section 3.1.....	169
Appendix II: Work flow for the results section 3.2 and 3.3.....	170
Appendix III: Work flow for the results section 3.4.....	171
Curriculum vitae.....	XV

List of Abbreviations

(P)-	Postnatal Day
2-D	Two Dimension
3-D	Three Dimension
4-AP	4-Aminopyridine
ABR	Auditory Brain stem Response
AMPA	α -amino-3-hydroxy-5-methyl-4-isoxazolepropionic acid
AP-2 μ	Adaptor Protein-2 μ
ATP	Adenosin Tri Phosphate
AZ	Active Zone
<i>C. elegans</i>	<i>Caenorhabditis elegans</i>
Ca ²⁺	Calcium Ion
CaCl ₂	Calcium Chloride
CAPS	Ca ²⁺ -dependent Activator Protein for Secretion
CAST	(Cytomatrix of Active Zone)-Associated Structural Protein
CAZ	Cytomatrix of Active Zone
ChR-2	Channelrhodopsin-2
CO ₂	Carbon Dioxide
CsCl	Cesium Chloride
CtBP2	C-terminal Binding Protein
EDP	Electron Dense Projection
EGTA	Ethylene Glycol Tetra Acetic Acid
ELKS	Glutamate (E), Leucin (L), Lysine (K) and Serine (S) rich Protein
EM	Electron Microscope/y
EPSC	Excitatory Postsynaptic Current
FER	Ferlin
FS	Freeze Substitution
GA	Glutaraldehyde
GFP	Green Fluorescent Protein
GluR2/3	Glutamate receptor 2 and 3
GUI	Graphical User Interface
HEPES-HBSS	HEPES-Hanks' Balanced Salt Solution
HPF	High-Pressure Freezing
HPM	High-Pressure Machine
IHC	Inner Hair Cell

K ⁺	Potassium Ion
KCl	Potassium Chloride
KO	Knockout
KOH	Potassium Hydroxide
LED	Light-Emitting Diode
MET	Mechanoelectrical Transduction
MgCl ₂ -6H ₂ O	Magnesium Chloride Hexahydrate
MgSO ₄	Magnesium Sulfate
MP	Membrane-Proximal
mRNA	Messenger RNA (Ribonucleic Acid)
Munc13	Mammalian Homologue of Unc-13
Myo6	Myosin VI
Na ₃ C ₆ H ₅ O ₇ -2H ₂ O	Sodium Citrate Dihydrate
NaCl	Sodium Chloride
NF200	Neurofilament 200 kDa
NI	National Instrument
NMJ	Neuromuscular Junction
NPMC	Non-Parametric Multiple Comparison
OHC	Outer Hair Cell
Opto-HPF	Optical stimulation in combination with High-Pressure Freezing
OsO ₄	Osmium Tetroxide
Otof	Otoferlin
Pb(NO ₃) ₂	Lead(II) Nitrate
PCR	Polymerase Chain Reaction
PD (<u>in figures and tables</u>)	Presynaptic Density
PFA	Paraformaldehyde
PSD	Postsynaptic Density
R (<u>in figures and tables</u>)	Synaptic Ribbon
RA	Ribbon-Associated
RIM	Rab-3 Interacting Molecule
RIM-BP	RIM Binding Protein
ROI	Region of Interest
RRP	Readily Releasable Pool
RT	Room Temperature
RT-PCR	Real Time PCR
SEM	Standard Error of Mean
SNAP-25	Synaptosome-Associated Protein-25

SNARE	Soluble NSF Attachment Proteins Receptor
STED	Stimulated Emission Depletion
SV	Synaptic Vesicle
Syt	Synaptotagmin
TEA-Cl	Tetraethylammonium Chloride
TEM	Transmission Electron Microscope/y
TRC40	Transmembrane Recognition Complex
vAcht	Vesicular Acetylcholine Transporter
vGlut1	Vesicular Glutamate Transporter Type 1
vGlut3	Vesicular Glutamate Transporter Type 3
Wrb	Tryptophan(W)-Rich Basic Protein
YFP	Yellow Fluorescent Protein

Abstract

The inner hair cell ribbon synapses are the relay stations of the auditory pathway, attuned to transmit acoustic information at rates of up to hundreds of Hz. Such indefatigable signal transmission demands ultrafast vesicle replenishment mechanisms, which ensure a constant resupply of vesicles to the active zone. At these high-throughput synapses, the synaptic ribbon provides a molecular scaffold to orchestrate the spatial localization of synaptic vesicles. However, the molecular mechanism(s) coordinating vesicular release remains elusive. This thesis aims to correlate functional deficits of inner hair cell synaptic transmission with ultrastructural characteristics. Using advanced electron microscopy, snapshots of vesicle pools were captured under different stimulation paradigms, including short light pulses as well as mild and strong K⁺ stimulation to visualize early vesicular release and sustained exocytosis respectively. The images are then compiled into a montage to understand the vesicle dynamics in inner hair cells morphologically. Moreover, to decipher the molecular players maintaining vesicle pools at the active zone, different point and/or deletion mouse mutants of otoferlin – a key regulator for the last stages of exocytosis in inner hair cells – and the presynaptic scaffold Rab-3 interacting molecule (RIM) 2 α were investigated ultrastructurally.

Firstly, using hearing impaired mice carrying a temperature-sensitive mutation in the C₂C domain of otoferlin (*Otof*^{*f515T/1515T*}), I could show that otoferlin is involved in vesicle reformation. Here, coinciding with a vesicle replenishment deficit obtained by inner hair cell capacitance measurements, the ultrastructural phenotype was dominated by enlarged vesicle diameters.

Secondly, I focused on inter-structural connectivity by proteinaceous filaments. Here, two types of connections were characterized: (i) inter-connectors, which are formed between vesicles or (ii) tethers, linking vesicles to other synaptic structures such as the ribbon and/or the presynaptic membrane. A closer analysis of these structures showed a higher complexity of connections at the distal end of the ribbon upon stimulation. However, closer to the active zone the multiple-tethered and docked vesicles were rare. Using a replenishment-impaired otoferlin *pachanga* mutant (*Otof*^{*pga/pg α*}) allowed me to study the role of these filaments in vesicle replenishment. *Otof*^{*pga/pg α*} mice exhibit reduced filament connectivity, with compactly packed vesicles around the ribbon and accumulation of multiple-tethered and docked vesicles at the membrane. This suggested a role of otoferlin downstream of docking, such as vesicular fusion or subsequent release site clearance. Impairment of either one of these processes may result in the accumulation of release-

ready vesicles at the membrane, which in turn creates a roadblock for the vesicles at the ribbon. Finally, to find other potential vesicle tethering candidates at inner hair cells, RIM2 α was investigated. RIM2 α deficient inner hair cells revealed a reduced fraction of tethered vesicles at the membrane and proximal part of the ribbon (closer to the active zone), supporting the role of RIM2 α in vesicle tethering.

In the end, to obtain ultrafast immobilization, immediately after stimulation of vesicular release, an inner hair cell-specific channelrhodopsin-2 knock-in mouse model was used. Here, short light pulses prior to high-pressure freezing showed a fast refilling of the membrane-proximal vesicle pool, while ribbon-associated vesicles were reduced under these conditions. Therefore, optogenetic stimulation proved to be a useful tool to understand the structure-function relationship of inner hair cells. However, this experimental paradigm still requires further optimization to capture early exocytosis events, for example, vesicle fusion events.

1. Introduction

The auditory system allows animals to apprehend sound waves of different temporal characteristics and spatial localization. Physiologically, these sound waves are received regarding their frequency, amplitude, phase and waveform. Perception of the frequency and amplitude correspond to pitch and loudness, while the waveform determines the timbre and texture of the sound. Altogether, these define the ability of a species to distinguish between a wide range of sound helping them to navigate, evade and locate sources that are critical to their existence. The sensory-neuronal hearing in mammals relies on the cochlea in the inner ear (Fig. 1.1B). It is capable of transducing complex sound waves into electrical signals for further relay via auditory nerves to the higher orders in the auditory pathways of the central nervous system (Dallos, 1996). This requires an astonishing fidelity of sound-evoked neuronal transmission. The precise mechanism(s) by which the auditory system attains this is not completely understood so far.

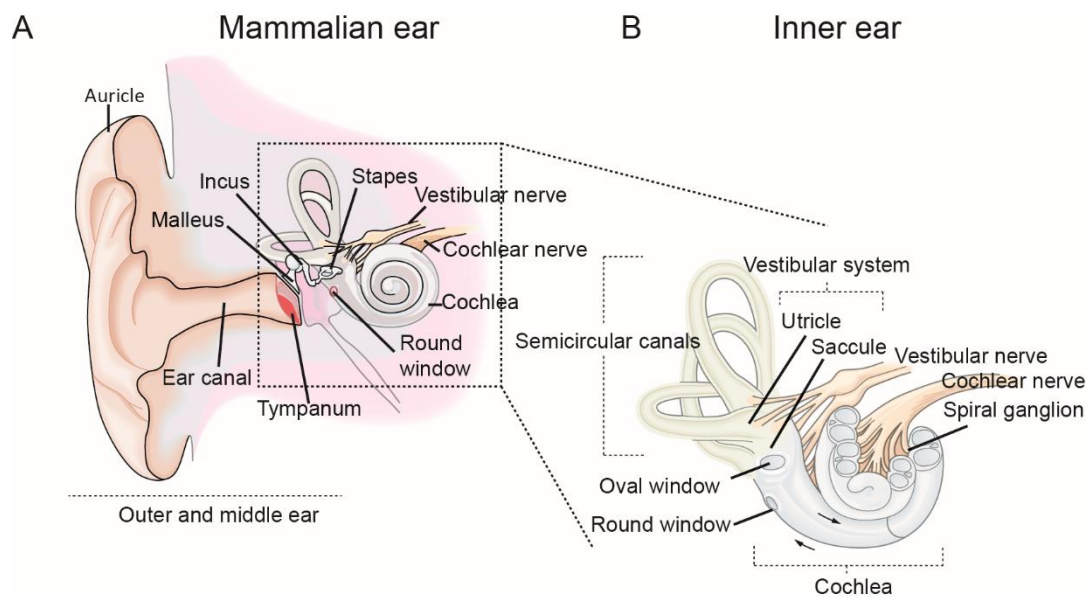


Figure 1.1: Anatomy of human ear highlighting the structures of the inner ear

(A) The outer ear focuses the acoustic signals into the ear canal. These sound waves migrate through the ear canal vibrating the tympanum. The three ossicles; malleus, incus and stapes in the middle ear, further relay the sound to the inner ear. **(B)** The inner ear consists of the semicircular canals that help to keep balance and the cochlea where the sound encoding takes place. Figure modified from Kandel, 2012.

1.1 Overview of cochlear organization and mechanics

The cochlea is a bony snail-like structure sheathed in the otic capsule of the temporal bone. The capability of the cochlea as a transducer for a wide range of sound intensities and frequencies relies on its intrinsic mechanical and biological features. The core of the cochlea consists of a bony stalk entwined with three fluid-filled compartments namely the

scala vestibuli, scala media and scala tympani (Fig. 1.2A). The scala vestibuli is at the top, separated from the scala media by the thin and flexible membrane of Reissner. Further, the scala media is separated from the scala tympani with a rigid partition that includes a flexible section of basilar membrane. The scala vestibuli and the scala tympani are perilymph filled (containing $\sim 5 \text{ mM K}^+$). The sensory organ of hearing, the organ of Corti (Fig. 1.2B), is localized in the endolymph-filled (containing $\sim 160 \text{ mM K}^+$) scala media. The difference in salt concentration plays a critical role in the transduction of sound at cochlea (Dallos, 1996). Sound vibrations are handed over from the middle ear to the scala vestibuli via the stapes, through the flexible oval window. This gives rise to a pressure wave that is further transmitted to the scala tympani and at the end released outward through the round window. This system of the pressure difference between the upper (scala vestibuli) and lower (scala tympani) fluid-filled compartments drives a vertical movement of the basilar membrane on top of which the organ of Corti is situated (Elliott and Shera, 2012; Raphael and Altschuler, 2003). The basilar membrane thickness varies from the base to apex (which is thinner, broader and less stiff) creating a tonotopy in the cochlea and this way determines the displacement of the membrane to different sound frequencies. The base of the basilar membrane is tuned for high-frequency sounds, whereas the apex of the basilar membrane is suited for low frequencies.

1.2 Sensory transduction at the organ of Corti

The organ of Corti (Fig. 1.2B) consists of different epithelial cells, $\sim 11 \text{ mm}$ long in mice and $\sim 34 \text{ mm}$ long in humans (Ashmore, 2008). It harbors $\sim 3,500$ hair cells of two types. The outer hair cells (OHCs) are arranged in rows of three and a single row of inner hair cells (IHCs). Each hair cell type carries out distinct function in the transduction process (Hudspeth, 2014; Kandel, 2012). The OHCs are cylindrical ($15 - 70 \mu\text{m}$ long) and are innervated by only 5 % of the afferent fibers (type II). They act as sound amplifiers on sound evoked movements of the tectorial membrane. This is achieved by negative stiffening of hair bundles (Russell et al., 1992) and further conformational changes of the cell (stretching or shrinking) carried out by prestin in the basolateral membrane (Liberman et al., 2002; Zheng et al., 2000). For in-depth review refer to (Ashmore, 2008; Dallos and Fakler, 2002). These hair cells are flanked by different supporting cells, e.g., Deiter's cells, inner and outer pillar cells and phalangeal cells. In addition to serving as the structural backbone, these cells maintain homeostasis at the organ of Corti. In this thesis, I will focus on IHCs that carry out the "true" sensory-neuronal hearing in mammals.

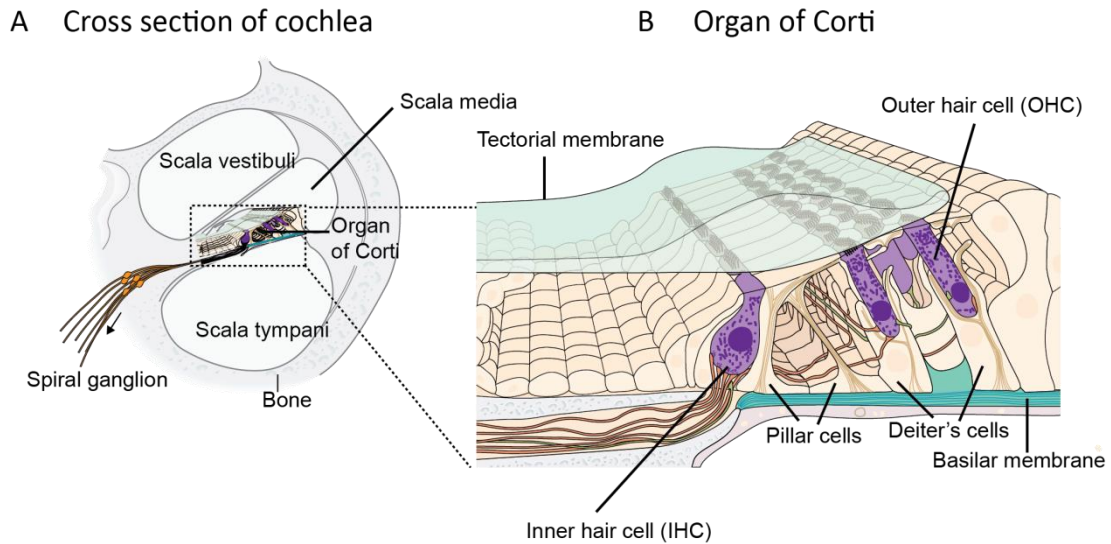


Figure 1.2: Cross-section of cochlea showing the organ of Corti

(A) The cochlea is partitioned into three compartments: the scala vestibuli, scala media, and scala tympani. (B) The organ of Corti sits on the basilar membrane and is bathed with by the endolymph of the scala media. The cross-section of the organ of Corti shows three rows of OHCs which amplifies the mechanical energy of sound by contracting and expanding. Separated by the tunnel of Corti (a fluid-filled space) is a single row of IHCs flanked by the pillar cells. Sound-evoked movements of the tectorial membrane result in displacement of their stereocilia, ultimately leading to secretion of neurotransmitter onto the boutons of afferent neurons contacting the IHCs at their basolateral surface. Figure modified from Kandel, 2012.

1.3 The inner hair cells (IHCs)

The IHCs are sensory neuro-epithelial cells that convert the mechanical sound vibrations to electrical pulses. IHCs are specialized to carry out dual functions based on their unique structure. The apical side of the IHCs receives the auditory stimulus, while the basolateral side carries out the neurotransmission (Fig. 1.3A). Similar to OHCs, the apical parts of IHCs are decorated with several rows of stereocilia, arranged in a staircase fashion. The number of stereocilia associated with a single IHC depends on the species and the localization of IHCs along the turn of the cochlea (20 - 50 stereocilia exists at the apical turn and it increases at the basal part of the cochlea). The tip links connect the stereocilia to adjacent cilia (Pickles et al., 1984). These filamentous tip links are composed of cadherin 23 and protocadherin 15 (Müller, 2008) and are coupled with mechano-electrical transduction (MET) channels. The vertical movement of the basilar membrane (described above) deflects the hair bundles of the OHCs, resulting in fluid displacement which moves the hair bundles of IHCs in turn. As a consequence the MET channels open and allow the influx of K^+ ions from the endolymph into the IHCs (Corey and Hudspeth, 1979). The resulting depolarization of IHCs activates opening of voltage-gated Ca^{2+} channels, signaling exocytosis of glutamate filled vesicles at the basolateral plasma membrane (Fig. 1.3B, C). At

a mature murine IHC the basolateral region consists of approximately 10 - 20 active zones (AZs) each characterized with a synaptic ribbon (Fig. 1.3C) and $\text{Ca}_v1.3$ Ca^{2+} channels juxtaposed to postsynaptic glutamatergic AMPA (α -amino-3-hydroxy-5-methyl-4-isoxazolepropionic acid) receptors (Wong et al., 2014).

Coming sections will describe the IHC ribbon synapses with parallels to other ribbon type synapses and conventional chemical synapses to bring forth the peculiarities of IHC ribbon synapses in terms of proteins, functionality and vesicle pools.

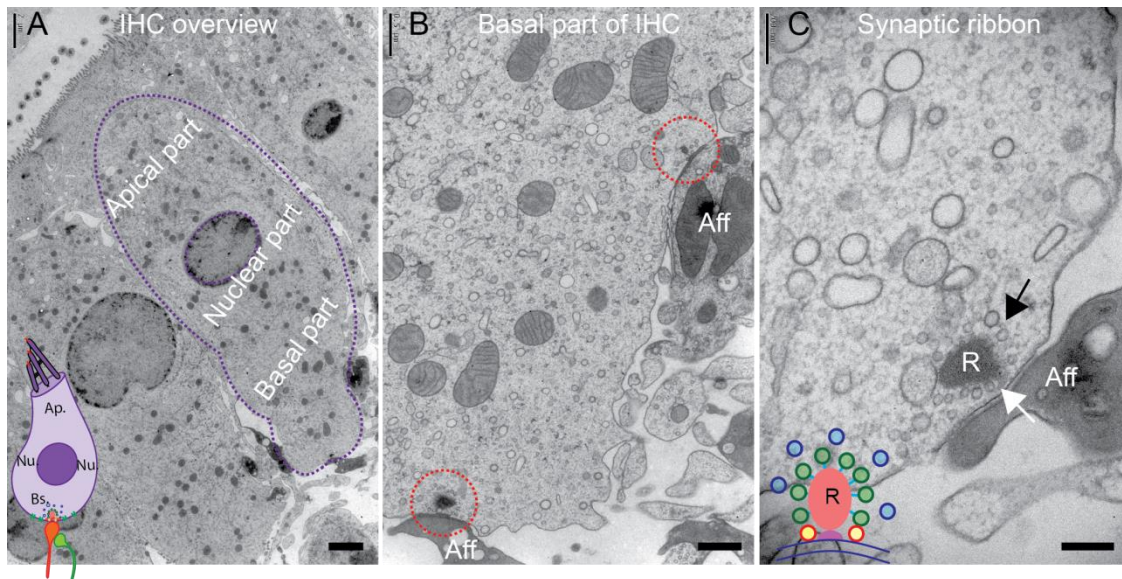


Figure 1.3: Electron micrographs of mice IHCs and synaptic ribbons

(A) Overview of some IHCs in a row at 800x magnification; scale bar, 2 μm . The inset represents a schematic drawing of an IHC for orientation. Each IHC can be divided into an apical (Ap), a nuclear (Nu) and a basal (Bs) part. (B) In the basal part of the IHCs, synaptic ribbons (encircled in red) are found opposite to an afferent nerve fiber (Aff). Magnification, 4,000x; scale bar, 0.5 μm . (C) The neurotransmission takes place at the synaptic ribbon (R), which is anchored to the AZ membrane (white arrow) and tethers SVs (black arrow) on its surface. Magnification, 12,000x; scale bar, 200 nm. The inset shows a schematic drawing for a ribbon synapse.

1.4 The ribbon synapses

The ribbon type synapses are not only found in the vertebrate auditory and vestibular hair cells but also features at other sensory cells; photoreceptors, retinal bipolar cells and pinealocytes (Eatock and Songer, 2011; Fuchs et al., 2003; Lenzi and von Gersdorff, 2001; Spiwox-Becker et al., 2008; Sterling and Matthews, 2005; Wichmann and Moser, 2015). Such synapses are named after the hallmark electron dense projection (EDP) called synaptic ribbon, anchored to the AZ membrane and extend several nanometers into the cytoplasm (for cochlear hair cells Smith and Sjöstrand, 1961; for retinal photoreceptors

Usukura and Yamada, 1987). Nonetheless, synaptic ribbons vary in size and shape depending on the cell type and species. For instance, the synaptic ribbons are round at frog saccular hair cell (Lenzi et al., 1999, 2002) and at the zebrafish lateral line hair cells (Nicolson, 2015). Whereas at the vertebrate cochlear hair cells, these are the ellipsoid shape (for cats, Liberman et al., 1990; for guinea pigs, Saito, 1990; Smith and Sjöstrand, 1961; for mice, Wichmann and Moser, 2015; Wong et al., 2014). Such variability probably reflects the structural adaptations of a synapse, catering to the specific functional need (von Gersdorff, 2001; Matthews and Fuchs, 2010; Moser et al., 2006). Furthermore, the shape, size and number of synaptic ribbons at IHCs undergo developmental refinements (Sobkowicz et al., 1982; Wong et al., 2014). An average mouse IHC ribbon synapse is ~ 400 nm in height and ~ 200 nm in width, to which synaptic vesicles (SVs) are tethered, maintaining proximity to the AZ membrane for neurotransmission (Moser et al., 2006; Sobkowicz et al., 1982).

Moreover, ribbon synapses share certain resemblances with other chemical synapses as well with respect to the molecular architecture. At the presynaptic terminal of chemical synapses, three major compartments (molecularly) can be defined: (i) an elaborate network of proteins at the cytomatrix of AZ (CAZ) (Südhof, 2012), (ii) proteins constituting the EDP that cluster SVs (Wichmann and Moser, 2015; Zhai and Bellen, 2004), and (iii) proteins associated with SVs (Südhof, 2013; Wichmann and Moser, 2015; Zhai and Bellen, 2004). However, despite sharing these common features with the conventional chemical synapses, ribbon type synapses differ to a great extent in terms of molecular composition and functionality (Matthews and Fuchs, 2010; Moser et al., 2006; Nouvian et al., 2006; Sterling and Matthews, 2005; Wichmann and Moser, 2015). The ribbon synapses facilitate highly synchronous mode of exocytosis with an ultrafast vesicle turnover rate at cochlear IHCs (Moser and Beutner, 2000; Pangrsic et al., 2010). This drives the postsynaptic spiral ganglion neurons to spike at hundreds of Hz (Geisler, 1998) to encode the acoustic information. However, the release mechanism(s) and molecular players maintaining the vesicle pools at IHC ribbons have only started to be unraveled.

1.5 Proposed release mechanisms at ribbon type synapses

The release mechanisms at the AZ, as well as the role of the synaptic ribbon at ribbon type synapses in general but in particular at IHC, are still enigmatic. Several roles have been assigned to synaptic ribbons and some of the putative hypotheses are described here.

First, an intact ribbon and its proper anchorage has been proposed to promote the readily releasable pool (RRP) of vesicles via clustering of Ca^{2+} channels at the vesicular release sites (Fig. 1.4A, Dick et al., 2003; Frank et al., 2010; Khimich et al., 2005; Maxeiner et al., 2016;

Sheets et al., 2011). Disruption of synaptic ribbon anchorage (Dick et al., 2003; Jing et al., 2013; Khimich et al., 2005) and/or occurrence of ribbon less AZs (Frank et al., 2010; Maxeiner et al., 2016) result in a reduction in the fast component of exocytosis (Frank et al., 2010; Maxeiner et al., 2016). Furthermore, at IHC ribbon synapses specifically, disruption of bassoon (major component of the presynaptic density 'the anchor') (Frank et al., 2010; Jing et al., 2013; Khimich et al., 2005) or ribeye (major component of synaptic ribbons) (Schmitz et al., 2000a) impairs clustering of Ca^{2+} channels (Frank et al., 2010; Sheets et al., 2011) and reduces the number of docked SVs at the AZ (Frank et al., 2010).

What makes ribbon synapse unique is not just their capability to cluster SVs at the release site for fast encoding of the incoming signal, it further coordinates the sustained neurotransmitter release over an extended period (Matthews and Fuchs, 2010; Moser et al., 2006). This brings us to the second model, the conveyor belt or crowd surfing model of SV release (Fig. 1.4B). Initially based on the ultrastructural observations at the retinal ribbon synapses (photoreceptors, Bunt, 1971; Gray and Pease, 1971), this model hypothesizes that the synaptic ribbon provides the surface for SVs to move along its length to the release site at the AZ membrane, which happens either in an ATP dependent (active transport, in association with motor proteins, von Gersdorff et al., 1996; Muresan et al., 1999) or an ATP independent manner (Graydon et al., 2014). This model has been proposed for frog saccular hair cell ribbon synapses as well (Lenzi and von Gersdorff, 2001). Moreover, at IHC ribbon synapses Ca^{2+} plays a role in the mobility of SVs because the sustained component of exocytosis can be blocked with Ca^{2+} buffer ethylene glycol tetraacetic acid (EGTA), but the RRP fusion remains unaffected (Moser and Beutner, 2000; Spassova et al., 2004). Therefore this model supports the hypothesis that ribbons assist in SV replenishment during the sustained release.

Additionally, recordings from primary afferent boutons of spiral ganglion neurons revealed the manner of vesicle release as well. It was shown that the amplitude and shape of excitatory postsynaptic currents (EPSC) are highly variable. This can be explained by a combination of multiple SVs released synchronously and asynchronously (Glowatzki and Fuchs, 2002). Furthermore, capacitance measurements of IHCs suggest that a coordinated exocytosis occurs at the ribbon synapse (Neef et al., 2007). Based on this, several possible mechanisms of multi-vesicular (or multi-quantal) fusion have been proposed (Matthews and Fuchs, 2010; Neef et al., 2007; Parsons and Sterling, 2003). These can be the synchronous release of two or more individual SVs at the same time (Fig. 1.4C, Fuchs et al., 2003) or the formation of large vesicles due to homotypic fusion around the synaptic ribbon and at the plasma membrane (Fig. 1.4D, Edmonds, 2004; Sterling and Matthews, 2005), before SV fusion. Alternatively, the variety of EPSC can also be explained by uni-

quantal release events, where a single SV is capable of releasing either through a full collapse or through a dynamic fusion pore that flickers. 2-color STED showed that AMPA receptors are tightly clustered in a ring-like fashion opposing the AZ. This provides a geometrical advantage where many AMPA receptors detect glutamate release from one SV and elicit large EPSCs (Fig. 1.4E, Chapochnikov et al., 2014).

In the end, modeling of Ca^{2+} influx showed that the large synaptic ribbon of frog saccular hair cells (~ 400 nm in diameter) and the associated dense CAZ do not allow free Ca^{2+} diffusion in the interior of the cytoplasm. As a consequence, synaptic ribbons were proposed to act as a diffusion barrier for SV release by a local increment of steady-state Ca^{2+} concentration (Graydon et al., 2011).

So far these proposed models are highly debatable and have their merits and demerits. The recent advancement in deciphering the molecular identity at these specialized synapses contributed significantly in understanding the release mechanism(s) (discussed in the next section). Moreover, incorporation of fast cryo-immobilization with high-pressure freezing (HPF) allowed close to the native-state structural preservation of IHCs (Chapochnikov et al., 2014; Jung et al., 2015a; Vogl et al., 2015). Furthermore, the temporal coupling between the stimulus and freezing can be achieved by combining optogenetic stimulation with HPF, as has been done for different conventional synapses (Opto-HPF, Kittelmann et al., 2013; Watanabe et al., 2013a, 2013b). This will help to capture highly dynamic release events and this way bridge the gap between morphology and biophysical properties at ribbon type synapses.

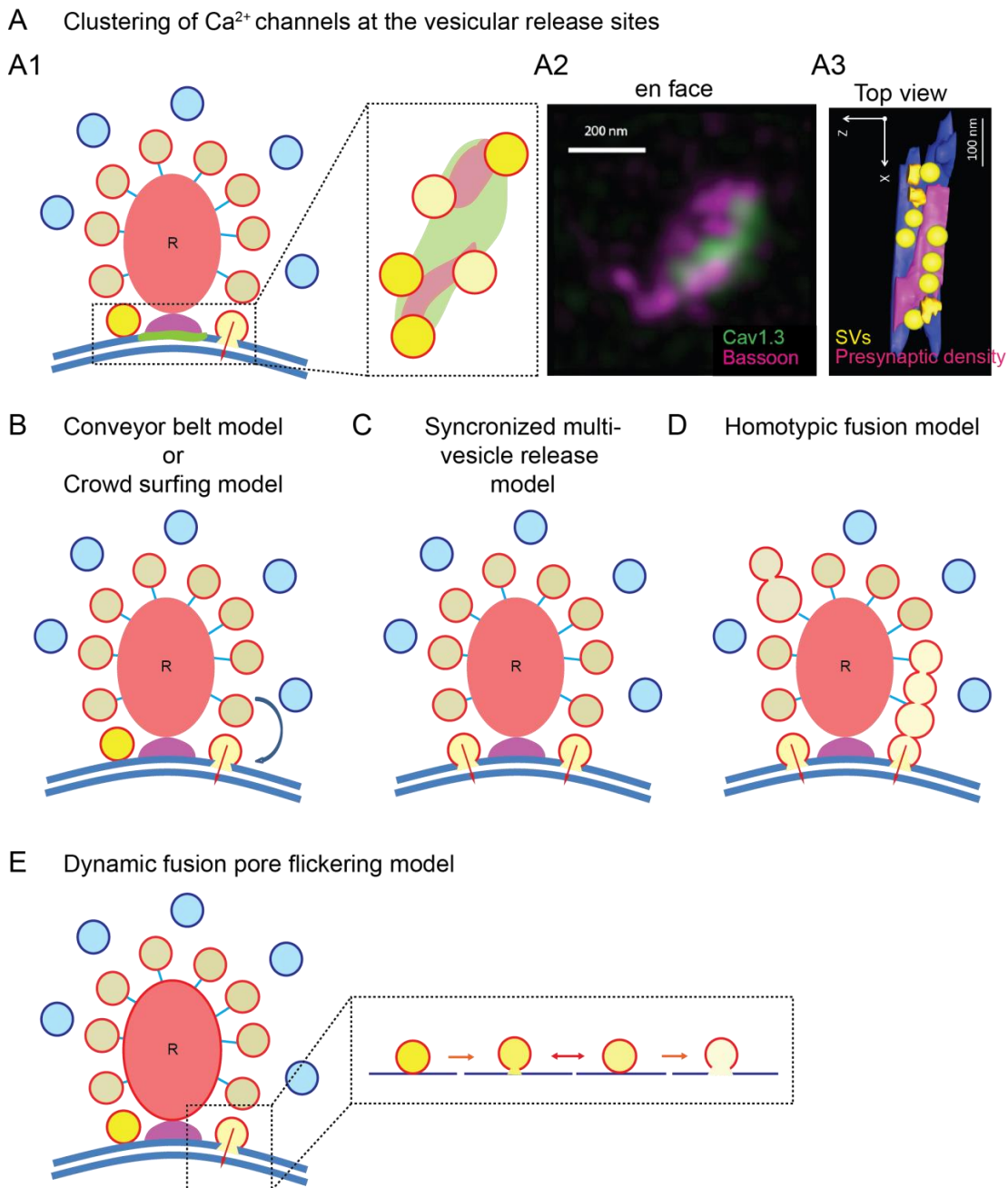


Figure 1.4: Proposed vesicle release models at ribbon synapses

(A-E) Simplified schematics is depicting probable release mechanisms at ribbon type synapses. Original references inspiring this schematic are mentioned in the text, section 1.5. **(A1)** Role of the ribbon in promoting a large RRP of vesicles via clustering of Ca²⁺ channels at vesicular release sites. **(A2)** 2-color STED microscopy image at IHC ribbon synapse (en-face). The presynaptic density protein bassoon (magenta) and the voltage-gated Ca²⁺ channels controlling vesicle release (green; Ca_v1.3) are aligned juxtaposed at each synapse. Scale bar, 200 nm. The image is taken from (Rutherford, 2015). **(A3)** Top view of an electron tomographic 3-D reconstruction: SVs (yellow) are arranged in parallel to the presynaptic density close to the membrane (blue). Scale bar, 100 nm. **(B)** The conveyor belt or crowd surfing model for SV release hypothesize that the SVs move along its length to the release site at the AZ membrane in an ATP dependent or an ATP

independent manner. **(C)** The scenario of synchronized vesicular fusion, where two or more SVs are released at the same time. **(D)** Homotypic fusion of vesicles, resulting in large vesicles and tubular structures before fusion. **(E)** Uni-quantal release scenario, occurring with subsequent fusion pore opening and closing.

1.6 Unique molecular identity of IHCs

1.6.1 Scaffolding proteins at IHC ribbon synapses

Study of several mutants of AZ proteins helped in deciphering the function of ribbon synapses to a significant extent. The unique scaffolding component of the synaptic ribbon is the protein ribeye (Magupalli et al., 2008; Schmitz et al., 2000a). It consists of two domains, ribbon specific A domain helps in the structural organization of the ribbon and a B domain homologous to C-terminal binding protein (CtBP2), which is a transcription repressor in most tissues (Schmitz et al., 2000a). Recently, ribeye deletion showed ribbon-less retinal photoreceptor synapses (Maxeiner et al., 2016) which accounted for the severe reduction in the fast and sustained component of exocytosis, confirming its vitality at the ribbon synapses (Maxeiner et al., 2016). Additionally, $Ca_v1.3a$ clusters were absent at the AZ of *ribeye a/b knockdown* in the neuromast hair cells in zebrafish (Sheets et al., 2011). However, the cochlear IHC specific *ribeye knockout (KO)* still awaits investigation. Apart from this, the scaffolding protein bassoon forms the presynaptic density at the base of the synaptic ribbon (Dick et al., 2003; Frank et al., 2010; Jing et al., 2013; Khimich et al., 2005). Disruption of bassoon at IHC ribbon synapses resulted in floating ribbons, impaired clustering of Ca^{2+} channels and a reduced number of membrane-proximal vesicles. Further, the Ca^{2+} currents and the fast component of exocytosis at IHCs was reduced (Frank et al., 2010; Jing et al., 2013; Khimich et al., 2005).

Another large scaffolding protein is piccolo, which is homologous to the bassoon. Piccolo seems to also be present at the synaptic ribbon (Dick et al., 2001; Khimich et al., 2005) but only the short isoform of piccolo called piccolino is expressed (Regus-Leidig et al., 2013). Upon *piccolino knockdown*, photoreceptor ribbon synapses were altered in shape (Regus-Leidig et al., 2014). Implications of piccolino at the IHC cell ribbon synapses still need to be identified. Additionally, ERC [CAST (CAZ associated structural protein)/ELKS (named after the most frequent amino acid first letter glutamate (E), leucine (L), lysine (K), and serine (S))] proteins in addition to bassoon and piccolo are believed to organize SV release at conventional synapses (Hida and Ohtsuka, 2010; Ohara-Imaizumi et al., 2005). At photoreceptor ribbon synapses ERC has been identified (tom Dieck et al., 2012). However, IHC specific deletion of ERC awaits future investigations. In short, the primary scaffolding proteins of the ribbon type synapses help in maintaining the structural and functional integrity of these synapses.

1.6.2 Proteins mediating exocytosis at IHCs

Apart from the scaffolding roles described above individual proteins of CAZ coordinate SV release and the organization of Ca^{2+} channels at the release sites, for efficient Ca^{2+} triggered exocytosis (Südhof, 2012, 2013). At conventional synapses, fusion of SVs at the AZ membrane is mediated by the soluble NSF attachment proteins receptor (SNAREs) complex. This comprises of the vesicular proteins synaptobrevin 1 and 2 and the presynaptic membrane proteins, the synaptosome-associated protein (SNAP)-25 and syntaxin. Additionally, synapsin, synaptophysin and complexin participate in exocytosis (Südhof, 2012, 2013). IHC ribbon synapses appear unique in this aspect, compared to conventional synapses. The vesicular proteins synapsin and synaptophysin (Safieddine and Wenthold, 1999) and SNARE regulatory protein complexin are absent in IHCs (Strenzke et al., 2009). The *complexin 1* KO did not show any exocytosis defect in IHCs (Strenzke et al., 2009). However, expression of neuronal SNARE proteins showed controversial results. Earlier studies showed expression of SNAREs mRNA and protein at IHCs quite similar to conventional synapses (Safieddine and Wenthold, 1999; Uthaiah and Hudspeth, 2010), but Nouvian et al., 2011 argued against the presence of neuronal SNAREs because at IHCs exocytosis (both fast and slow components) remained insensitive to botulinum toxin serotype E (specific to SNAP-25) and serotype C and D (specific to syntaxin 1-3 and synaptobrevin 1-3). Additionally, since *synaptobrevin 1/2 double-KOs* and *SNAP-25 KOs* are lethal at birth (Borisovska et al., 2005; Washbourne et al., 2002), organotypic organs of Corti cultures were investigated which did not show any exocytosis deficit. However, real-time nested PCR detected mRNA of all the neuronal SNAREs in IHCs. Therefore, SNARE mRNA seems to be present but no AZ localization could be identified at IHC ribbon synapses (Nouvian et al., 2011). Similarly, conventional priming factors like the mammalian homologous of Unc-13 (Munc13) and the Ca^{2+} -dependent activator protein for secretion (CAPS) seems not required for exocytosis at IHC ribbon synapses (Vogl et al., 2015). However, a presynaptic scaffolding molecule; Rab-3 interacting proteins (RIMs) which mediate vesicle priming by direct interaction with Munc13 (Deng et al., 2011) at conventional synapses, were shown to be present in the photoreceptor ribbon synapses (both RIM1 and RIM2) (tom Dieck et al., 2005) and recently at IHC ribbon synapses (specifically RIM2 α , RIM2 β and RIM3 γ), are expressed at IHCs (Jung et al., 2015a). One objective of the thesis is to understand the role of RIM2 α in SV tethering at AZ membrane and synaptic ribbon. The details of RIM protein will be described in section 1.6.2.2.

Additionally, synaptotagmin (Syt) 1 and 2 (multiple C_2 -domain proteins) are considered as the calcium sensors for SV fusion in the central nervous system and they interact with SNAREs (Rizo et al., 2006). The multiple C_2 -domains of Syt mediate Ca^{2+} dependent exocytosis (Rizo and Südhof, 1998). At mature IHCs neither Syt 1 nor Syt 2 are expressed

(Beurg et al., 2010; Reisinger et al., 2011; Safieddine and Wenthold, 1999). However, Syt 4 (Safieddine and Wenthold, 1999) and otoferlin (Otof) were identified in IHCs (Roux et al., 2006) and the latter has been suggested as a possible Ca^{2+} sensor (Johnson and Chapman, 2010; Roux et al., 2006). In the pursuit of functional equivalence of Otof and Syt 1, viral-mediated gene transfer was incorporated. Syt 1 was overexpressed in IHC *Otof KO* and Otof was expressed in *Syt 1 KO* chromaffin cells. Neither of which could restore the Ca^{2+} triggered exocytosis in the respective systems (Reisinger et al., 2011). Otoferlin's precise function at IHCs is not completely deciphered and I aim to further highlight the role of otoferlin at IHC ribbon synapses in this thesis.

1.6.2.1 Otoferlin

Otoferlin belongs to the ferlin protein family, which is highly conserved in the eukaryotic systems (Lek et al., 2012). Ferlin proteins are characterized by tandem C_2 domains and a C-terminal transmembrane domain. Otoferlin consists of six C_2 domains ($\text{C}_2\text{A} - \text{C}_2\text{F}$) (Pangršič et al., 2012). It shares 28 % structural homology with *C. elegans* FER-1 (Achanzar and Ward, 1997) and 38 % with human Dysferlin (Yasunaga et al., 2000).

The pathogenic mutation study of the ferlin family proteins indicated their role in cellular trafficking (Bernatchez et al., 2009), membrane repair (Covian-Nares et al., 2010) and Ca^{2+} dependent fusion (Dulon et al., 2009). A point mutation in exon 18 of the human otoferlin gene causes an autosomal recessive form of non-syndromic deafness (DFNB9) (Yasunaga et al., 1999). So far ~ 60 pathogenic missense mutations have been identified in the C_2 domains of human otoferlin gene, of which 10 are between the C_2C to C_2F domains (Pangršič et al., 2012; Rodríguez-Ballesteros et al., 2008). These mutations cause auditory synaptopathy (Rodríguez-Ballesteros et al., 2003, 2008; Varga et al., 2003), few of which have been associated with temperature-sensitive hearing loss in patients (Marlin et al., 2010; Varga et al., 2006; Wang et al., 2010). Despite impaired hearing, the otoacoustic emission is mostly intact suggesting that otoferlin not be involved in OHC transduction.

In post-hearing onset mice models, immunofluorescence against otoferlin strictly confined to IHCs (Roux et al., 2006). Additionally, immunogold electron microscopy (EM) and immunohistochemistry/with confocal microscopy revealed the localization of otoferlin at SVs associated with the ribbon (Roux et al., 2006) and at the membrane (Jung et al., 2015b; Roux et al., 2006; Strenzke et al., 2016; Vogl et al., 2015). Over the years the functionality of otoferlin in hair cell neurotransmission has been brought forward Using different mice and zebrafish models (Chatterjee et al., 2015; Pangrsic et al., 2010; Pangršič et al., 2012; Roux et al., 2006; Strenzke et al., 2016; Vogl et al., 2015). Initially, otoferlin was shown to be essential in the last steps of exocytosis, because its absence nearly abolished vesicle

fusion in *Otof* *KOs*, despite the presence of docked SVs at the ultrastructural level (Roux et al., 2006). Subsequent research highlighted these last steps, where otoferlin has been implicated in SV tethering and priming (Pangrsic et al., 2010; Vogl et al., 2015) in addition to AZ clearance (Jung et al., 2015b; Pangrsic et al., 2010).

In this thesis, two otoferlin mutant mouse lines have been studied extensively. The first one is a *knockin* mouse line, carrying the Ile515Thr (I515T) point mutation in the C₂C domain of the mouse otoferlin gene (*Otof*^{d515T/I515T}) (published recently in Strenzke et al., 2016). I515T was identified in one of the otoferlin alleles in siblings suffering from profound hearing impairment with temperature rise to ≥ 38.1 °C (Varga et al., 2006). At normal body temperatures, patients had mild low-frequency hearing loss and difficulties in speech comprehension in a quiet and noisy environment with no auditory brainstem response (ABR). The *Otof*^{d515T/I515T} mouse mutant stipulate the human hearing impairment phenotype but with less pronounced heat sensitivity (Strenzke et al., 2016). The second mouse line used in this thesis are the deaf otoferlin *pachanga* mouse mice (*Otof*^{Pga/Pga}), with a point mutation caused by a substitution of an aspartate to a glycine in the C₂F domain of the mouse otoferlin gene (Schwander et al., 2007). This line serves as a mouse model for the human deafness DFNB9 (Rodríguez-Ballesteros et al., 2003; Varga et al., 2003), exhibiting no ABRs and severe SV replenishment deficits (Pangrsic et al., 2010). The study of *Otof*^{d515T/I515T} and *Otof*^{Pga/Pga} mutants allowed investigation of the partial loss of otoferlin compare to complete loss of otoferlin in *Otof* *KOs*. Both *Otof*^{d515T/I515T} and *Otof*^{Pga/Pga} displayed perturbed membrane localization of otoferlin. The absolute membrane-bound otoferlin in *Otof*^{Pga/Pga} mutant was severely reduced compared to wild-type and only 3 % was retained (Pangrsic et al., 2010), compared to 34 % in *Otof*^{d515T/I515T} (Strenzke et al., 2016). The hearing phenotype comparison of *Otof* *KO*, *Otof*^{Pga/Pga} and *Otof*^{d515T/I515T} indicates that sound encoding scales with the amount of membrane-bound otoferlin at IHCs (Pangrsic et al., 2010; Roux et al., 2006; Strenzke et al., 2016; Vogl et al., 2015). In this study, the functionality of otoferlin protein in maintaining vesicle pool dynamics was tested to answer the open question associated with otoferlin functionality, which has not been identified so far in the case of complete loss of otoferlin (Roux et al., 2006; Vogl et al., 2015).

1.6.2.2 Rab-3 interacting molecule (RIM)

The RIM family proteins are multi-domain proteins first identified as an interacting partner of SV protein Rab-3. These proteins are evolutionary conserved; only one RIM gene is found in invertebrates. However, in vertebrates, four RIM genes (RIM 1-4) are found, coding seven proteins in the family (two α-RIMs, two β-RIMs and three γ-RIMs). RIM1α and 2α, consist of full complements of RIM domains (N-terminal zinc finger, a PDZ and two C₂

domains). RIM1 β and 2 β comprise of all the domains of α -RIMs, except N-terminal Rab-3-binding part in the zinc finger in case of RIM1 β and whole zinc finger domain in RIM2 β . RIM2 γ , 3 γ and 4 γ consist of a short N-terminal flanking sequence before the C-terminal C₂ domains (Mittelstaedt et al., 2010; Wang and Südhof, 2003). RIM1 and RIM2 interact with Ca²⁺ channels, by directly interacting with auxiliary β (Ca_v β) subunits (Gebhart et al., 2010; Kiyonaka et al., 2007) and pore-forming Ca_v α subunits (Coppola et al., 2001; Kaeser, 2011). Additionally, indirect interactions with Ca²⁺ channels exists via RIM-binding proteins (RIM-BP) (Acuna et al., 2015; Hibino et al., 2002). Moreover, RIMs are proposed as a linker in between SVs and Ca²⁺ channels at the conventional synapses (Kaeser, 2011; Stanley, 1993). RIMs interact with most of the other CAZ proteins; in cultured hippocampal neurons RIM1 was shown to directly activate Munc13 and promotes vesicle priming (Deng et al., 2011), vesicle docking in the calyx of Held (RIM2; Han et al., 2011) and vesicle tethering to the AZ in mice cerebrocortical synaptosomes (RIM1; Fernández-Busnadiego et al., 2013).

Recently it was shown that not all RIM isoforms are expressed in mature IHCs. Mainly RIM2 α are expressed, but also RIM2 β and RIM3 γ are detected by immunohistochemistry and confocal microscopy at the AZ. However RIM1 and RIM4 are not expressed (Jung et al., 2015a). The *RIM1/2 double-KOs* (lacking both RIM2 α and 2 β) and the *RIM2 α KOs* shows a mild hearing synaptopathy, with elevated ABR thresholds. In line with the immunohistochemistry data, *RIM1 α KOs* showed normal ABR threshold and waveforms verifying that RIM1 is absent in IHCs. Additionally, the sound amplification by OHC is intact in all the RIM mutants in this study (Jung et al., 2015a). Moreover, the IHC synaptopathy is intensified due to the reduced number of Ca²⁺ channels at the AZ membrane with a substantial decrease in Ca²⁺-currents. Further, both the fast component of exocytosis upon 20 ms depolarization and the sustained exocytosis upon \geq 20 ms depolarization are significantly reduced in the *RIM21/2 double-KOs* and the *RIM2 α KOs*. However, the Ca²⁺-influx and exocytosis coupling are unaffected in the RIM2 α deficient mice it indicates that RIM2 is involved in vesicle release (Jung et al., 2015a). In this thesis, *RIM2 α KO* mice are investigated at ultrastructure to strengthen the role of RIM2 in tethering vesicles to the AZ (partly published in Jung et al., 2015a) and at the synaptic ribbon.

1.7 Dynamic vesicle pools at IHC ribbon synapses

Classically three pools of SVs have been defined for nerve terminals. According to this model localization of SVs determines the release kinetics of the vesicles. The readily releasable pool (RRP) consists of only 1 - 2 % of all the SVs in the nerve terminal, which are docked and primed at the AZ membrane and released immediately upon stimulation. On depletion of the RRP, the recycling pool of SVs (10 - 20 % of all the SVs) comes into play. Upon moderate stimulation, these behindhand vesicles from the recycling pool are

recruited at the AZ membrane. Intense stimulation possesses the capability to deplete these vesicles and hires the SVs from the reserve pool (80 - 90 % of all the SVs) (Rizzoli and Betz, 2005). However, substantial intermixing (spatial, not functional) of SV pools occurs especially between the recycling and reserve pools (Denker and Rizzoli, 2010; Rizzoli and Betz, 2005). Refinement of the model led to the conclusion that on arrival of the stimulus, a fraction of SVs from the recycling pool gets docked and primed for fusion and eventually the recycling pool gets depleted. Similar to the previous model, only upon strong stimulation, recruitment of the reserve pool of SVs occurs. Furthermore, the mobility of the recycling and reserve pool of SVs dramatically varies in between different nerve terminal (Fig.1.5A, Denker and Rizzoli, 2010; Rizzoli and Betz, 2005).

At IHCs two functional vesicle pools are widely accepted based on the capacitance measurements, the initial exponential phase upon 10 - 20 ms depolarization of IHCs represents the RRP (Moser and Beutner, 2000; Rutherford and Roberts, 2006), while the linear phase upon > 20 ms depolarization of IHCs represents the sustained release (Moser and Beutner, 2000). A complete understanding of IHC ribbon synapse function requires observation of these synapses with increased spatial resolution. For this transmission electron microscopy (TEM) is the central method of choice to study the vesicle pools. This allows estimation of the vesicle pool size and its morphometry at a single synapse and single vesicle level. The plastic embedded specimens can be sectioned ultrathin (20 - 30 nm) and are therefore much more accurate compared to light microscopy regarding resolution. Incorporation of electron tomography further enhances the Z-resolution significantly (Virtual sections of a tomogram typically 0.5 – 1.5 nm thick, Chen et al., 2008).

Ultrastructural studies of frog saccular hair cells based on rather slow glutaraldehyde fixations proposed that the small population of vesicles in membrane proximity represent the rapid phase of exocytosis (the “ultrafast pool”) (Lenzi and von Gersdorff, 2001; Lenzi et al., 1999). Whereas, the vesicles located just behind (tethered to the synaptic ribbon) are the ones which represent the “rapidly releasable pool” (Lenzi et al., 1999). This pool is capable of sustaining the tonic release (von Gersdorff, 2001) by allowing hair cells to get adapted upon continuously graded depolarization over a long period at the hair cells (Lenzi et al., 2002) and therefore can encode steady-state sound information (Glowatzki and Fuchs, 2002). However, the study of the vesicle pool dynamics by incorporating HPF is at its early stage. Therefore, clear demarcation of vesicle pools is still missing.

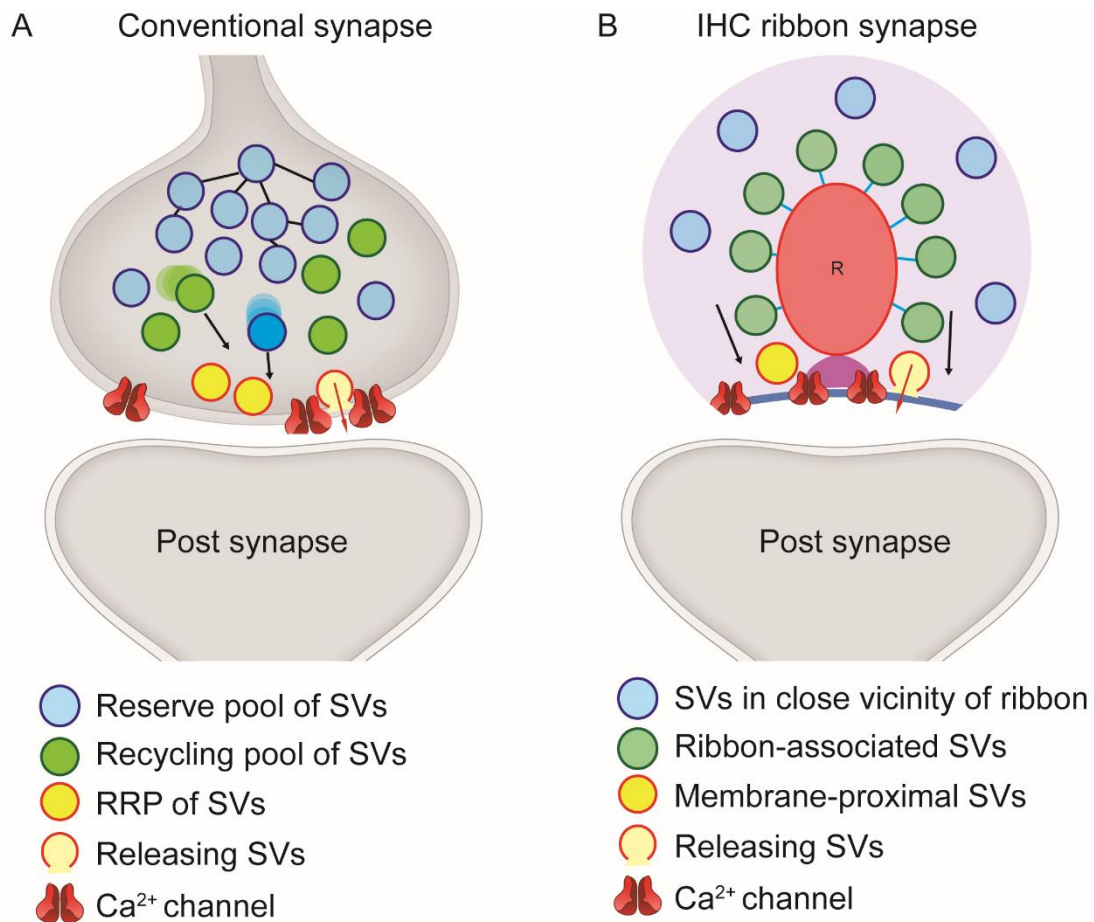


Figure 1.5: Vesicle pools of conventional synapse v/s IHC ribbon synapse

(A) The classical three vesicle pool model at conventional synapses is taking into account the spatial intermixing of vesicles. The RRP consists of the vesicles docked at the AZ before being primed and release. Only a few vesicles from the recycling pool are 'lucky' which make its way to the AZ membrane to be docked upon arrival of the stimulus and are released first. Upon continuous stimulation at high-frequency causes the recycling pool depletion and recruitment of reserve pool vesicles. Model simplified from (Denker and Rizzoli, 2010). **(B)** The over-simplified two vesicle pool model based on the ultrastructural studies of frog saccular hair cells. The small population of membrane-proximal SVs represents the "ultrafast pool" (Lenzi and von Gersdorff, 2001; Lenzi et al., 1999). The ribbon-associated vesicles located just behind sustains the tonic release (von Gersdorff, 2001) represents the "rapidly releasable pool" (Lenzi et al., 1999). However, a clear demarcation of vesicle pools is still missing at IHCs.

1.8 Filamentous organization at conventional and ribbon synapses

Proteins are increasingly being identified at IHCs. Striking peculiarities of the ribbon synapses make it important to investigate how these proteins are structurally organized at the AZ. The cytomatrix of presynaptic terminals at conventional synapses are abundant with electron dense proteinaceous structures (filaments) (Hirokawa et al., 1989; Landis et al., 1988). Similar filaments are also seen at IHC ribbon synapses (Frank et al., 2010; Jung et

al., 2015a; Sobkowicz et al., 1982; Vogl et al., 2015). However, the precise organization and composition of these filaments are unknown at IHC ribbon synapses. With the advancement of EM sample preparation and visualization methods (HPF or cryo in combination with tomography), the structural significance of these filaments came to light for both conventional and ribbon synapses. The structure of such filaments has been associated with three major functions which are described below.

1.8.1 Filament organization and function away from the AZ membrane

At conventional synapses, the filaments organize the vesicle pool by inter-connecting adjacent SVs (inter-connectors). These were for the first time described in the vertebrate synapses after quick freeze-etching (Hirokawa et al., 1989; Landis et al., 1988). However, these studies were limited by the tissue depth (20 - 30 nm). In the recent years HPF followed by cryo-EM (Fernández-Busnadiego et al., 2010)/freeze substitution (FS) (Cole et al., 2016; Helmprobst et al., 2015; Siksou et al., 2007; Stigloher et al., 2011) or by plunge freezing (Fernández-Busnadiego et al., 2010, 2013) reproduced these observations. Variable length of inter-connectors is observed in 3-D electron tomograms depending on the species and the synapse preparation (on average 25 - 30 nm long) (Fernández-Busnadiego et al., 2010; Siksou et al., 2007; Stigloher et al., 2011). Moreover, the density of the inter-connectors increases in the distal region of the presynaptic terminal away from the AZ membrane allowing tight clustering of SVs at resting conditions (Cole et al., 2016; Landis et al., 1988). So far synapsin has been associated with these inter-connectors (Hirokawa et al., 1989; Takei et al., 1995). However, synapsin independent subset of inter-connectors is present at the presynapse as in *synapsin triple-KO* mice the inter-connectors were not completely abolished (Siksou et al., 2007). The meshwork of inter-connectors is proposed to limit the diffusion of SVs and maintain the vesicular pool at the presynaptic terminal (Fernández-Busnadiego et al., 2010; Hirokawa et al., 1989). This hypothesis is based on increased vesicle mobility (Betz and Henkel, 1994; Fernández-Busnadiego et al., 2010) and release (Fernández-Busnadiego et al., 2010), upon KCl stimulation (Nicholls and Sihra, 1986) or treatment with phosphatase inhibitor okadaic acid (capable of altering the phosphorylation of synapsin, Jovanovic et al., 2001) in synaptosomal preparations (Fernández-Busnadiego et al., 2010). In case of IHCs, synapsins are absent (Safieddine and Wenthold, 1999) and the inter-connectors are not studied until now. Additionally, synaptic ribbon showed filaments radiating from the core synaptic ribbon (Sobkowicz et al., 1982) but the morphology and organization are uninvestigated so far.

1.8.2 Filament organization and function close to the AZ membrane

A generic term for the filaments closer to the AZ membrane is tether at conventional synapses. In the previous studies of conventional synapses, single tethers emanating from

the membrane was observed (variable length 5 - 120 nm, on average 40 nm) to connect a SV to the AZ membrane (Cole et al., 2016; Fernández-Busnadiego et al., 2010, 2013; Helmprobst et al., 2015; Landis et al., 1988; Siksou et al., 2007, 2009; Stigloher et al., 2011). These tethers are proposed as a path for the SVs to move towards the AZ membrane (Cole et al., 2016; Siksou et al., 2007), however, the molecules guiding the SVs are not identified yet (Siksou et al., 2011). Additionally, these single tethers have been proposed as a prerequisite for release (Fernández-Busnadiego et al., 2010, 2013; Stigloher et al., 2011; Verhage and Sørensen, 2008) followed by multiple-tethers for a tight spatial coupling to the AZ membrane (Fernández-Busnadiego et al., 2010, 2013) prior docking (Imig et al., 2014; Siksou et al., 2007). Putative tethering proteins at the conventional synapses are the SNARE complex proteins (Fernández-Busnadiego et al., 2010). Additionally RIM1 α and Munc13 seems to participate in these process as well (Fernández-Busnadiego et al., 2013), although the proteins constituting these tethers remain to be identified. Additionally, IHC exocytosis seems to operate without many of the neuronal priming factors (described above). Currently, RIM2 α and otoferlin have been investigated for tethering at the IHC AZ membrane (Jung et al., 2015a; Vogl et al., 2015). In *Otof* *KOs* the fraction of SVs with short tethers (< 10 nm) were reduced by two-thirds (Vogl et al., 2015). However, in the *KOs* the tethers are not completely abolished. This indicates that other proteins might be involved in tethering at IHC ribbon synapses.

1.9 Aims of this study

The aim of this study was to gain deeper insight into the vesicle pools governing different functional release states at IHC ribbon synapses. In order to do so, a systematic ultrastructural analysis was performed for two morphologically distinct pools of vesicles: (i) the membrane-proximal (MP) and (ii) the ribbon-associated (RA) vesicle pool.

1.9.1 Major objectives of this thesis

Four major objectives in this thesis were the following:

1. *To evaluate the effect of the I515T missense mutation in the C₂C domain of otoferlin on vesicle release*

The I515T mutation was identified in human patients suffering from hearing loss with onset of fever or rise in body temperature due to physical activities (Varga et al., 2006). The intention was to induce an increased temperature condition in a mouse model carrying the same mutation (*Otof*^{I515T/I515T}) and gain new insight into the role of otoferlin in synaptic neurotransmission at IHC ribbon synapses. Therefore, I compared the vesicle pools at physiological (36 °C) and elevated temperatures (39 °C) in wild-type littermate control (*Otof*^{+/+}) and *Otof*^{I515T/I515T} ribbon synapses using electron

tomography (Strenzke et al., 2016). Additionally, severe hearing impairments in other otoferlin mouse mutants studied till date, either went along with a severe reduction in otoferlin level (in *Otof*^{Pga/Pga}, 70 % reduction, Pangrsic et al., 2010) or the protein was completely abolished (in *Otof* KOs, Roux et al., 2006). These studies implicated otoferlin in the last steps of exocytosis (Roux et al., 2006) and replenishment (Pangrsic et al., 2010). However, other potential roles of otoferlin at different stages of neurotransmission might be masked due to such severe impairments. By studying a mutant mouse line with an intermediate hearing defect, I intend to bring forth other unidentified roles of otoferlin in maintaining the dynamic vesicle pools at IHC ribbon synapses (Strenzke et al., 2016).

2. *To examine the organization and morphology of proteinaceous filaments (tethers and inter-connectors) at wild-type IHC ribbon synapses*

The organization and morphology of filaments connecting SVs with each other and with components of the presynaptic AZ are still unknown for IHC ribbon synapses. However, at conventional synapses disturbances in filament morphology were associated with SV release and replenishment (Fernández-Busnadiego et al., 2010, 2013; Siksou et al., 2007; Stigloher et al., 2011). Therefore, I further wanted to investigate whether these filaments are involved in the regulation of vesicle release, replenishment or resupply at IHC ribbon synapses. In order to achieve this, ribbon synapse morphological vesicle pools were studied in an activity dependent manner, to correlate the structure and organization of these filaments to their functions. Exocytosis was either triggered by depolarizations using high K⁺ solution (Chapochnikov et al., 2014; Jung et al., 2015b; Pangrsic et al., 2010; Vogl et al., 2015) or inhibited by preventing Ca²⁺ influx (Chapochnikov et al., 2014; Pangrsic et al., 2010; Strenzke et al., 2016) for 15 min coupled with fast immobilization of samples by HPF.

3. *To investigate the role of the synaptic proteins RIM2α and otoferlin in coordinating the filament organization at the synaptic ribbon and AZ membrane*

It was shown that release at IHCs operates without the neuronal SNARE complex, Munc13/CAPS, and RIM1α proteins (Jung et al., 2015a; Nouvian et al., 2011; Vogl et al., 2015). This raises the question, which proteins are involved in SV replenishment/docking/priming at IHCs. First, I investigated the role of filaments in vesicle replenishment. The vesicle morphology and vesicular filament distribution at the ribbon and the AZ membrane were analyzed in replenishment-impaired otoferlin mutant mice (*Otof*^{Pga/Pga}) (replenishment deficiency previously published in Pangrsic et al., 2010), upon stimulation in comparison to wild-type. Next, I wanted to investigate if

the SV tethering is different from conventional synapses in the absence of neuronal docking and priming factors at IHCs. Therefore, the IHC specific *RIM2α* KOs' MP (Jung et al., 2015a) and RA pools were investigated.

4. *Bridging the gap between IHC physiology and morphology by combining optogenetic stimulation with HPF (Opto-HPF)*

The stimulation paradigm above (long, high K^+ extracellular solution stimulation) cannot be applied with temporal precision and therefore I might not be able to capture fast and early exocytosis events at IHC ribbon synapses. For example, the determination of the RRP size immediately after stimulation is not possible due to the lack of temporal coupling between stimulus and freezing. To overcome this, I planned to incorporate Opto-HPF (Kittelmann et al., 2013; Watanabe et al., 2013a, 2013b) for the first time at the IHC ribbon synapses. This would allow a very short and tissue-specific stimulus (in this thesis 10 ms) to be applied immediately before freezing allowing observation of the dynamic exocytosis events at IHC ribbon synapses

2. Materials and methods

2.1 Animals

In this thesis, post-hearing onset mice (postnatal day (P14 - 19)) were used. All experiments were conducted in compliance with national animal care guidelines and were approved by the University of Göttingen Board for animal welfare and the animal welfare office of the state of Lower Saxony. The mouse lines, conditions and references to the original publications used in this study are listed below.

2.1.1 Mouse lines and treatment conditions

2.1.1.1 Ile515Thr (I515T) otoferlin mutant ($Otof^{d515T/I515T}$) and wild-type littermate control ($Otof^{+/+}$) mice

This mouse line is published in Strenzke et al., 2016 and was used for the result section 3.1 of this thesis.

- i. $Otof^{+/+}$ at 36 °C inhibitory condition – 2 animals;
- ii. $Otof^{+/+}$ at 39 °C inhibitory condition - 2 animals;
- iii. $Otof^{+/+}$ at 36 °C mild-stimulatory condition - 2 animals;
- iv. $Otof^{+/+}$ at 39 °C mild-stimulatory condition - 2 animals;
- v. $Otof^{d515T/I515T}$ at 36 °C inhibitory condition - 2 animals;
- vi. $Otof^{d515T/I515T}$ at 39 °C inhibitory condition - 2 animals;
- vii. $Otof^{d515T/I515T}$ at 36 °C mild-stimulatory condition - 2 animals;
- viii. $Otof^{d515T/I515T}$ at 39 °C mild-stimulatory condition - 2 animals.

2.1.1.2 C57/BL6 mice (wild-type)

Mouse line is available at Jackson's laboratory. These mice were used as controls for the result section 3.2 of this thesis.

- i. Wild-type inhibitory condition - 3 animals;
- ii. Wild-type strong-stimulatory condition - 3 animals.

2.1.1.3 Otoferlin *pachanga* mutant ($Otof^{Pga/Pga}$) mice

This mouse line published in Schwander et al., 2007 and were used for the result section 3.2 of this thesis. Since it was a homozygous breeding, C57/BL6 mice (wild-type) were used as controls (see above method section 2.1.1.2).

- i. $Otof^{Pga/Pga}$ inhibitory condition - 2 animals;
- ii. $Otof^{Pga/Pga}$ strong-stimulatory condition - 2 animals.

2.1.1.4 *RIM2 α* knock-out (*RIM2 α KO*) and wild-type littermate control (*RIM2 α Con*) mice

The mouse line was published in (Jung et al., 2015a; Schoch et al., 2006) and were used for the result section 3.3 of this thesis.

- i. *RIM2 α KO* - 1 animal;
- ii. Wild-type littermate control (*RIM2 α Con*) - 1 animal.

2.1.1.5 *Ai32-vGLUT3-Cre* line (*Ai32VC*)

These mice were used for the result section 3.4 of this thesis. Mice were generated by Cre-dependent expression of channelrhodopsin-2 (ChR-2) reported previously (Madisen et al., 2012). The line with the *Ai32* construct tagged with an EYFP (a variant of ChR-2 with H134R point mutation) (Nagel et al., 2003, 2005) was cross bred with *vGlut3-cre* mice (Jung et al., 2015a) for hair cell (both IHC and OHC) specific expression of the *Ai32* construct. For the experiments, heterozygous *Ai32VC* mice were used.

- i. *Ai32VC*-10 ms optical stimulation – 1 animal;
- ii. *Ai32VC* (without-light control) – 1 animal;
- iii. Wild-type (*C57/BL6*) (without-light control) – 1 animal.

2.2 Dissection of the apical turn of the organ of Corti

Mice were decapitated after anesthetizing them with CO₂. The skull was cut sagittally into halves and transferred into a Petri dish containing ice-cold HEPES-Hanks' balanced salt solution (HEPES-HBSS) (see section 2.8.3) (Fig. 2.1A). The brain was scooped out of the skull, thus exposing the cavity for flocculus (Fig. 2.1B). The bony labyrinth of the cochlea and the vestibular system (inner ear) was twisted out gently from the skull floor with 5 mm forceps (Fig. 2.1C). A small window was created at the apex of the cochlea using a blunt forceps. This opening served as the entry point for removing the bony wall of the cochlea. After removing the bones, the organ of Corti was unwrapped from the modiolus delicately (Fig. 2.1D, E). Using a pair of 55 mm forceps, a cut was made at the end of the apical turn (1st turn) (Fig. 2.1F) and the tissue was transferred for the next steps using a micro-spatula.

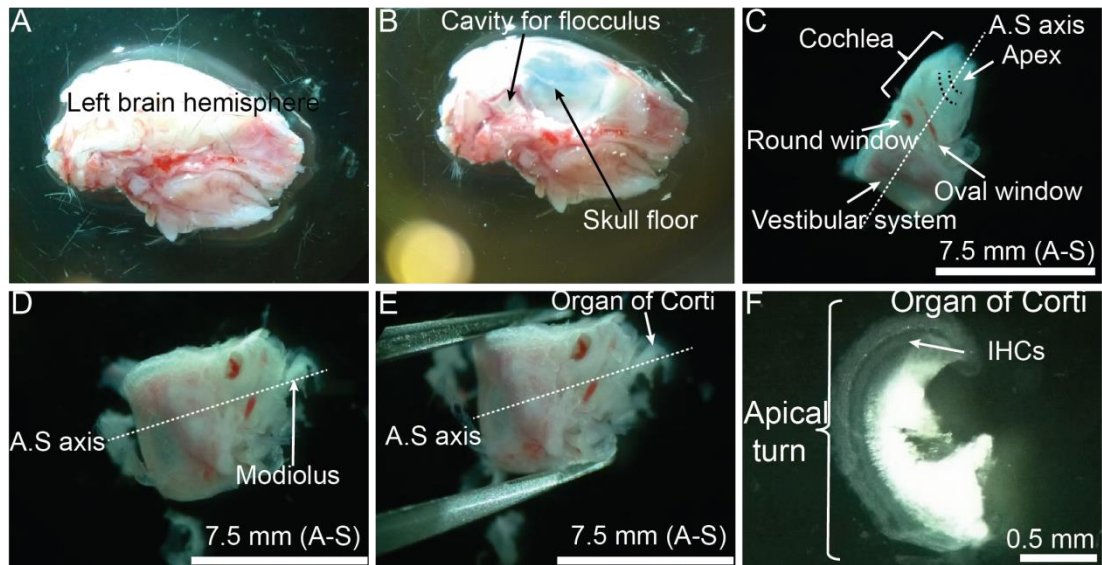


Figure 2.1: Dissection for extracting mice organ of Corti apical turn

(A) The exposed left brain hemisphere after sagittal cut of the skull. (B) The brain hemisphere is removed and the cavity for flocculus is exposed. (C) Closer view of the inner ear after surrounding bones are removed. (D-E) A small opening is made at the cochlear apex, and the bony wall of the cochlea is removed further, exposing the organ of Corti. (F) Dissected apical turn of the organ of Corti.

2.3 Sample preparation for transmission electron microscopy (TEM)

2.3.1 Conventional embedding

This methodology was employed to study the vesicle pool dynamics of the temperature-sensitive *Otof*^{H515T/I515T} mutant compared to the wild-type littermate control (*Otof*^{+/+}) (for result section 3.1, mouse line described above in 2.1.1, see Appendix I for a simplified workflow). The organs of Corti were explanted as described in section 2.2 and incubated for 1 min 45 s in pre-warmed (at 36 °C or 39 °C), mild-stimulatory (Neef et al., 2014; Strenzke et al., 2016) or inhibitory solution (Chapochnikov et al., 2014; Pangrsic et al., 2010; Strenzke et al., 2016), solution details in section 2.8.3). Thereafter, samples are processed for conventional embedding for electron microscopy (EM) (Jung et al., 2015b; Strenzke et al., 2016; Vogl et al., 2016; Wong et al., 2014). The tissue was first fixed in Fixative 1 for 1 h on ice (see 2.8.3). Subsequently, the tissue was transferred into Fixative 2 and incubated overnight at 4 °C (see 2.8.3). On the second day, samples were washed in 0.1 M sodium cacodylate buffer and post-fixed on ice for 1 h with 1 % osmium tetroxide in 0.1 M sodium cacodylate buffer. This was followed by two washing steps of 10 min each in sodium 0.1 M cacodylate buffer and three short washing steps in distilled water (each wash for 10 min). Further, *en bloc* staining was performed with 1 % uranyl acetate in distilled

water for 1 h on ice. After a brief wash with distilled water, a dehydration series was performed on ice with increasing ethanol concentrations (Table 2.1) (see later section 2.8.3 for solution details).

Duration (min)	Condition	Concentration of ethanol (v/v)
5	On ice, in a glass snap vial	30 %
5	On ice, in a glass snap vial	50 %
10	On ice, in a glass snap vial	70 %
10	On ice, in a glass snap vial	95 %
10	On ice, in a glass snap vial	95 %
12	On ice, in a glass snap vial	100 % (anhydrous ethanol)
12	On ice, in a glass snap vial	100 % (anhydrous ethanol)
12	On ice, in a glass snap vial	100 % (anhydrous ethanol)

Table 2.1: Increasing concentration of ethanol for dehydration series

After that, samples were infiltrated in Epon resin as described in Table 2.2.

Duration (h)	Condition	Concentration (v/v)
0.5	Room temperature (RT), in a glass snap vial, on a rotating wheel	100 % ethanol and Epon resin (1:1)
1.5	RT, in a glass snap vial, on a rotating wheel	100 % ethanol and Epon resin (1:1)
Overnight	RT, in a glass snap vial, on a rotating wheel	100 % Epon
3–5	RT, in a glass snap vial, on a rotating wheel	100 % Epon

Table 2.2: Epon-ethanol infiltration series

Finally, samples were embedded in fresh 100 % Epon and polymerized at 70 °C for 48 h.

2.3.2 High-pressure freezing (HPF)

This methodology was employed for the tether analysis in wild-types, *Otof*^{Pga/Pga}, *RIM2α* *KOs* and *RIM2α* *Con* (for the result sections 3.2 and 3.3, mouse line described above in section 2.1.1.2, 3, and 4, also see Appendix II for a simplified workflow). The apical turns of the organs of Corti were dissected and placed in either inhibitory solution (Pangrsic et al., 2010; Strenzke et al., 2016) or strong-stimulatory solution (Chapochnikov et al., 2014; Jung et al., 2015b; Vogl et al., 2015) for 15 min at RT (employed for result section 3.2). For the experiments in result section 3.3, the apical turn of organs of Corti was placed in HEPES-HBSS (Jung et al., 2015a) at RT (solution details in section 2.8.3). High-pressure freezing (HPF) was performed by previous publications (Chapochnikov et al., 2014; Jung et al., 2015a; Vogl et al., 2015, sample assembly before loading are shown in Fig. 2.2). The organ of Corti was placed onto type A specimen planchette (Leica Microsystems) of 3 mm Ø and 0.2 mm depth, filled with either strong-stimulatory/inhibitory solution (for result section 3.2) or HEPES-HBSS (for result section 3.3). The flat side of the type B aluminum planchette

(Leica Microsystems), of 3 mm \varnothing and 0.1 mm depth, had been dipped in 1-hexadecen (Sigma-Aldrich) before placing onto the sample firmly to facilitate removing of air bubbles. Samples were frozen immediately using the HPM-100 (Leica Microsystems) and rapidly transferred into liquid nitrogen for storage. The details of the product, equipment and solutions can be found in section 2.8.

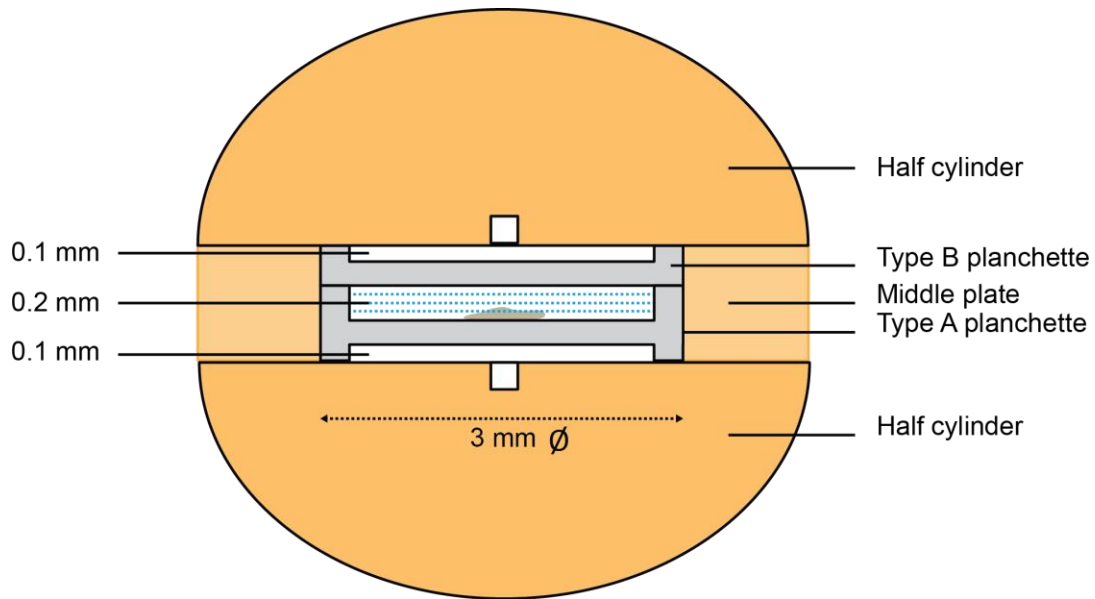


Figure 2.2: Sample loading for HPF

The sample is sandwiched between a type A and a type B planchette, the depth of the type A planchette was filled with the required solution without air bubbles. For detailed assembly refer to the text in section 2.3.2.

2.3.3 Optical stimulation in combination with HPF (Opto-HPF)

Optical stimulation in combination with HPF (Opto-HPF) methodology, was employed in order to achieve a spatial and temporal resolution of IHC vesicle pool dynamics in the *Ai32VC* mouse line, littermate wild-type and *C57/BL6* control mice (for the result section 3.4, mouse line described above in section 2.1.1.5, also see Appendix III for the workflow). HPF coupled with optical stimulation as a methodology to study vesicle pool dynamics was introduced previously in Kittelmann et al., 2013 and Watanabe et al., 2013a, 2013b. Here similar experimental approach was incorporated using HPM-100 (Leica Microsystems). Further customization and modifications incorporated for our system are described in detail in the coming sections (2.3.3.1, 2 and 3).

2.3.3.1 Setup for stimulation and freezing relay

An external blue LED stimulation relay setup was installed outside the Leica HPM-100 by Gerhard Hoch (AG Moser, Institute for Auditory Neuroscience, UMG, Göttingen). This setup had three compartmental roles: (i) external control of the light intensity and duration (account for *stimulus*). (ii) Precise control of the time point at which the freezing process initiates by crosstalk with the optical trigger box (account for *HPM START* and *HPM* delays from the start). (iii) Command relay to the *accelerometer* to initiate the mechanical sensing process from *HPM START* till the end of the freezing process. Details of how these three processes are cumulatively affecting the stimulation paradigm are explained in the next section 2.3.3.2.

To have an external control of the intensity and duration of the light stimulation used for Opto-HPF (Fig. 2.3) a *LLS 3*-LED (Light-emitting diode), blue light (473 nm) source (Schott and Moritex) was used for stimulation. *LLS-3* allowed the distinction between manual (by intensity control knob) and automated intensity control (through *RSS-232* input). A National Instrument (NI) card *PCI 6221* (37 pins) was used for computational time and amplitude relay to the light source. A flexible optical fiber (Leica Microsystems) transmitted the blue light from the source to the sample inside the high-pressure chamber. Product details are mentioned in section 2.8.1.

Next, the *START remote port* of the optical trigger box was connected to the HPM-100 via *J3* cable. This allowed *START* and *PAUSE* of the freezing process externally (can be manual/automatic). Light pulse duration could be defined manually or automatically to have different duration of stimulation for the specimen. Currently, for the experiments (described in results section 3.4), 10 ms optical pulse stimulation was used.

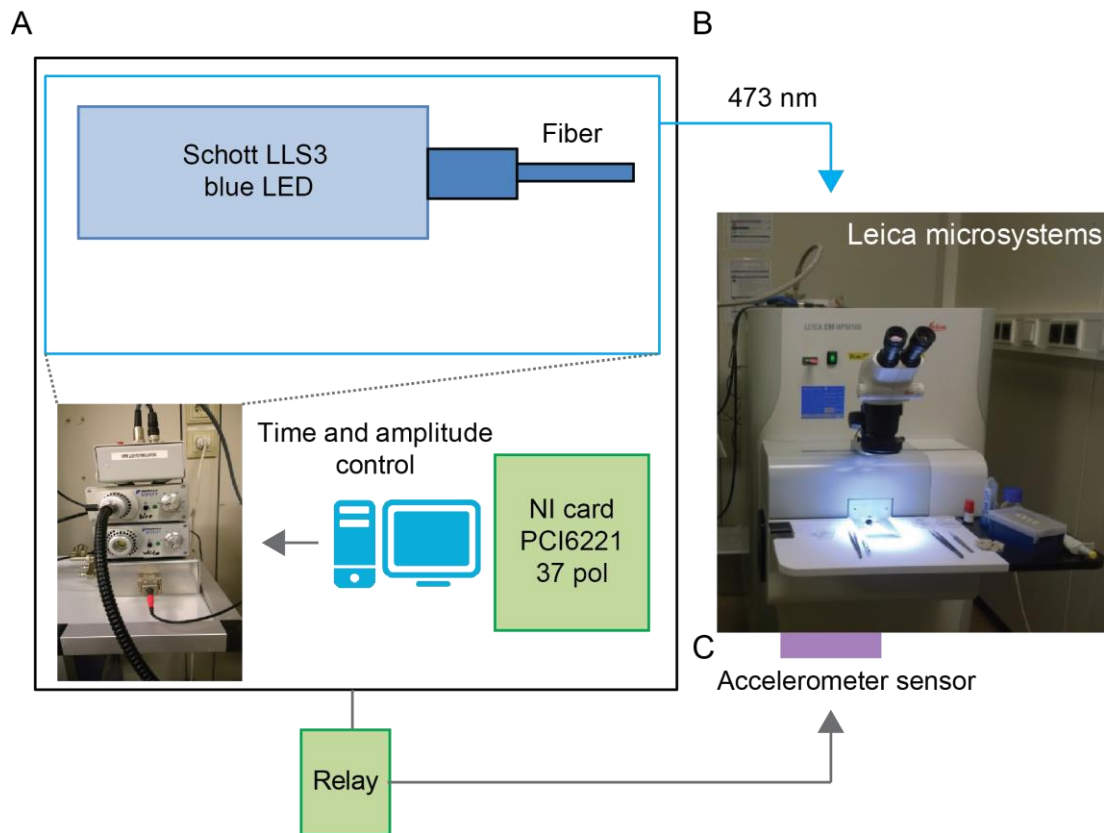


Figure 2.3: Setup for stimulation and freezing relay

(A) Simplistic flow diagram depicting the compartments of the external stimulation setup used for: control of the light intensity and duration, precise control of the time point at which the freezing process initiates and command relay to (C) the *accelerometer* to initiate the mechanical sensing process of the HPM 100. (B) Leica Microsystems HPM-100.

2.3.3.2 Determination of stimulation paradigms and temporal coupling of stimulus and freezing

HPM-100 (Leica Microsystems) allows immediate initiation of the freezing after loading of the sample on the cartridge mount and pressing the *process* button of the HPM-100. Details regarding the instrument can be found here: <https://www.leica-microsystems.com>. The HPM-100 is integrated with the light stimulation device, but the company configuration did not allow the precise control of the freezing onset immediately after the stimulation was over. Therefore, Gerhard Hoch set up an external control for the *stimulus* relay and the freezing process initiation (described in previous section 2.3.3.1). In order to know the interval between *stimulus* and freezing, several time delays ($T_{HPM \text{ delay from } START}$) were determined. From the HPM-100 a freezing curve was obtained for every experiment that correlated the temperature and pressure during freezing, but not on an absolute time

scale. Therefore, an external *accelerometer* was placed at the base of the HPM-100 to monitor the movements inside the HPM during the freezing process. This way, the absolute time scale (ms) was determined based on the initial pressure build-up (critical pressure of 1700 bar) required for freezing and the duration when the pressure was applied on the sample during freezing, finalized by a rapid pressure drop.

Once, the HPM was ready for freezing, externally the freezing process was paused by pressing the *PAUSE remote* of the trigger box (Leica Microsystems). After that samples were mounted (mounting of the sample will be described in the next section 2.3.3.3) and loaded on to the cartridge mount of HPM-100, subsequently were shot into the machine. Due to the initial *PAUSE*, the samples were held for some time until the HPM-100 received the *START* command to initiate freezing. This was considered as time point 0 (*HPM START*). In our machine, it takes 400 ms from the *HPM start* for liquid N₂ entry into the freezing chamber ($T_{N_2 \text{ entry}}$) (data provided by Leica Microsystems). Further, the *accelerometer* provided the time delay encountered due to the mechanics inside the HPM-100 ($T_{\text{mechanics}}$): (i) the valves opening ($T_{\text{valve opening}}$), (ii) the initial pressure build up inside the chamber ($T_{\text{initial pressure}}$) and (iii) the pressure drop after the freezing was over ($T_{\text{pressure drop}}$). These time points were set to the absolute time axis by correlating the end of the freezing (marked by the pressure drop, data obtained from HPM-100, not absolute scale) with the duration from pressure onset till drop took by the *accelerometer*, assuming the last strong signal to correlate to the onset of pressure drop (Paul Wurzinger, Leica Microsystems, personal communication). The $T_{\text{mechanics}}$ delay for our machine was estimated to be 85 ms, on averaging six test measurements (the data provided initially by Leica Microsystems was ~ 72 ms). Also, we accounted the time delay for the specimen to reach 0 °C ($T_{\text{specimen at 0}}$). The exact temperature at the specimen could not be monitored (Watanabe et al., 2013b), as the *thermal sensor* output obtained from HPM-100 only provide the information of the temperature at the freezing chamber (sensor is placed before the specimen sandwich). However, in our instrument, the freezing chamber reaches 0 °C, ~ 8 ms after it was flooded with liquid N₂ ($T_{\text{chamber at 0}}$) (this was obtained from HPM-100, for each shot by summation of *rise time* and *shift p/T*), quite similar to what has been reported earlier (Watanabe et al., 2013b). Further, delays were caused due to the time required for the sapphire disc to cool down ($T_{\text{sp. at 0}}$) (0.01 ms, as estimated in Watanabe et al., 2013b) and for the sample center to reach 0 °C ($T_{\text{sample center at 0}}$) (1.1 ms, as estimated in Watanabe et al., 2013b). Therefore, the specimen should reach 0 °C ($T_{\text{specimen at 0}} = T_{\text{chamber at 0}} + T_{\text{sp. at 0}} + T_{\text{sample center at 0}}$) in less than 9.11 ms in our machine. Likely, these are overestimations with the assumption that there was no cooling of the sample in first 8 ms after the chamber was filled with liquid N₂,

as stated previously (Watanabe et al., 2013b). However, we estimated for 494.11 ms delay from the *HPM START* which was calculated as follows:

$T_{HPM \text{ delay from } START}$

$$= T_{N2 \text{ entry}} + (T_{mechanics}) + (T_{specimen \text{ at } 0})$$

$$= T_{N2 \text{ entry}} + (T_{Valve \text{ opening}} + T_{initial \text{ pressure buildup}} + T_{pressure \text{ drop}}) + (T_{chamber \text{ at } 0} + T_{sp. \text{ at } 0} + T_{sample \text{ center at } 0})$$

$$= 400 + 85 + 8 + 0.01 + 1.1 = 494.11.$$

The stimulus onset was back-calculated based on the $T_{HPM \text{ delay from } START}$ retroactive to the freezing. For the very first attempt described in this thesis, 10 ms stimulation paradigm was applied as described in Fig. 2.4. Using the *Matlab* graphical user interface (GUI) (developed by Gerhard Hoch), we initiated a 10 ms light pulse with 469 ms delay from the HPM start expecting that at 479th ms sample was frozen (based on the initial data obtained from Leica for $T_{mechanics} = 72$ ms). However, that seems not to be the case. With this paradigm, we appeared to miss the very early and ultrafast events (getting over within 1-5 ms of the stimulation) at IHC ribbon synapses since the 10 ms pulse was over 15 ms before the sample was frozen. Currently, further calibrations are ongoing to account for the fluctuations due to $T_{mechanics}$ and the exact time coupling. In the end, using the *Matlab* GUI, we were able to control stimulation parameters like intensity, light pulse time, HPM delays and modes.

The amount of light for the sample inside the HPM-100 was measured using an external chamber setup that was built by Kai Bodensiek (AG Moser, Institute for Auditory Neuroscience, UMG, Göttingen). This setup mimicked the mechanical and optical arrangement inside the HPM-100, based on the technical drawing kindly provided by Leica Microsystems (not described in this thesis). Currently, for the first experiments (results section 3.4) the total intensity was measured to be 34.6 mW with a mean intensity of 1.2 mW/mm² and a peak of 6 mW/mm².

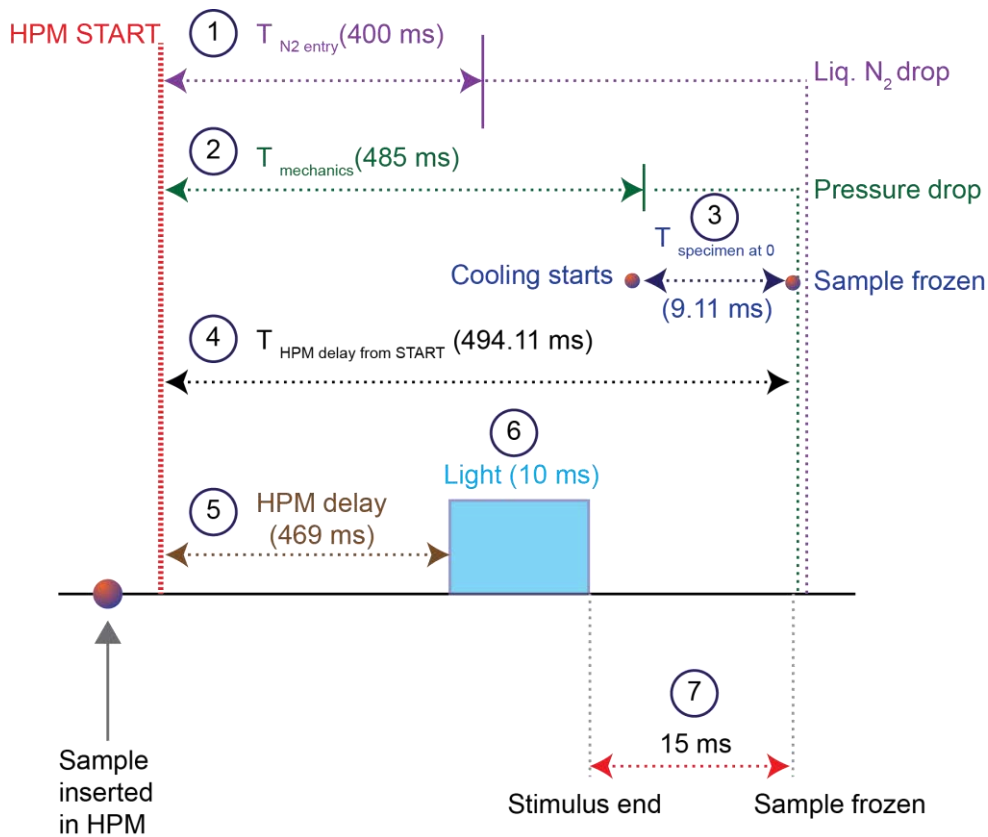


Figure 2.4: 10 ms stimulation paradigm used

Simplified flow diagram depicting the delays considered for 10 ms stimulation, in brief. 1. $T_{N_2 \text{ entry}}$, 400 ms from the *HPM start*. 2. $T_{\text{mechanics}}$, 485 ms (initial data provided by Leica 472 ms). 3. $T_{\text{specimen at 0}}$, 9.11 ms (based on Watanabe et al., 2013b). Summation of 1, 2 and 3 account for $T_{\text{HPM delay from the START}}$, 494.11 ms. Stimulus is calculated ex-post-facto from the time when the sample is frozen. For the 1st experiment, a 10 ms light pulse is initiated with 469 ms delay from the HPM START (5. HPM delay) expecting that at 479th ms sample freeze (based on the initial data obtained from Leica for $T_{\text{mechanics}} = 72$ ms). However, fluctuations of the pressure build-up and the pressure application are encountered. Thus for this experiment, ~ 15 ms delay is detected. For a detailed description refer to the text in section 2.3.3.2.

2.3.3.3 Sample mounting for Opto-HPF

The assembly of the sample loading for Opto-HPF was further modified from section 2.3.2 allowing the samples to be exposed to light for the stimulation inside the HPM-100. Due to the insertion mechanism of the sample, it had to be mounted upside down (Fig. 2.5). To do so, the apical turn of the organ of Corti was explanted in HEPES-HBSS as described in section 2.2 at RT. The sapphire disc of 6 mm \varnothing and 0.12 mm thickness (Leica Microsystems) was placed into a sample holder middle plate with a rim of 0.2 mm (Leica Microsystems). Thereafter, 1st 6 mm \varnothing and 0.2 mm thick spacer ring (Leica Microsystems) was placed,

forming a cavity. The organ of Corti was then placed into this cavity that was filled with extracellular solution (solution details in section 2.8.3). The 0.2 mm side of the 6 mm \varnothing type A aluminum planchette (Leica Microsystems) was placed onto the sample firmly. Next, 2nd spacer ring (same dimensions as 1st one) was placed over the planchette, making a 1.02 mm sample enclosure. Finally, the samples were sandwiched between two transparent cartridges (Leica Microsystems). For these experiments, 1-hexadecene was not used (described previously in section 2.3.2), only the glucose of the extracellular solution served as a cryo-protectant. The sample sandwich was then flipped 180° during the insertion process allowing the sample to face towards the light source inside HPM-100. Further, the samples were stimulated and frozen as described in section 2.3.3.2. The frozen organs of Corti were immediately transferred into liquid nitrogen for storage.

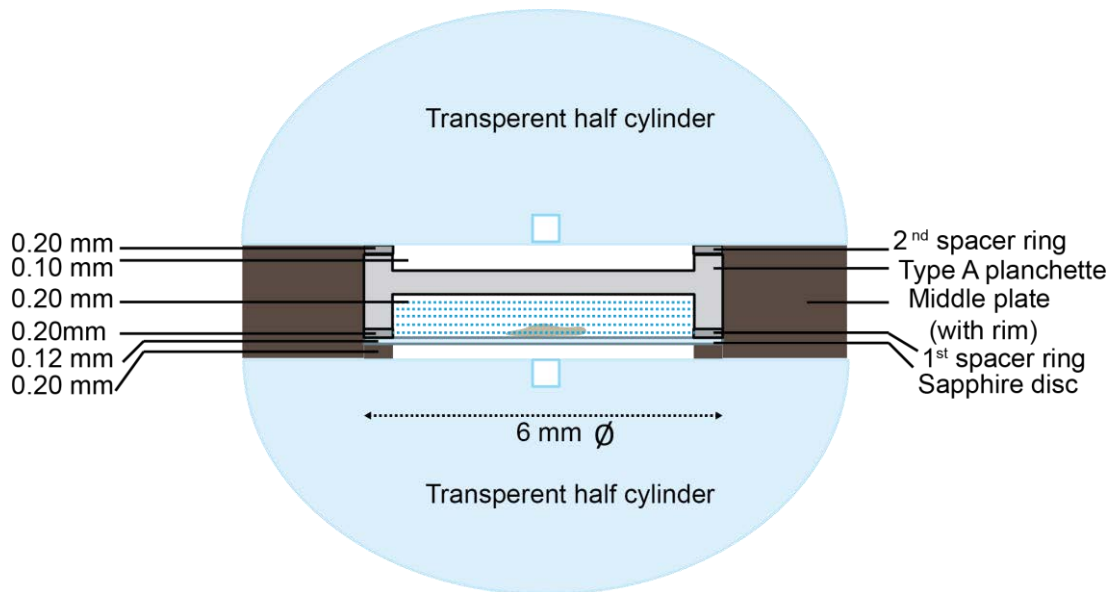


Figure 2.5: Upside down mounting of the sample for Opto-HPF

The sample is sandwiched between type A planchette and sapphire disc, the depth of the cavity filled with the required solution without air bubbles. For detailed assembly refer to the text in section 2.3.3.3.

2.3.4 Freeze substitution (FS)

Freeze substitution (FS) was performed in an EM AFS2 (Leica Microsystems) according to published work (Chapochnikov et al., 2014; Jung et al., 2015a; Siksou et al., 2007; Vogl et al., 2015). Briefly, the samples were incubated for four days in 0.1 % tannic acid in acetone at -90 °C. Three washing steps with acetone (1 h each) were performed at -90 °C. Then 2 % osmium tetroxide in acetone was applied to the sample and incubated at -90 °C for 7h. The

temperature was raised to -20 °C (5 °C/h increment) for 14 h in the same solution. Further, the samples were then incubated at -20 °C for 17 h, in the same solution. The temperature was further raised from -20 °C to 4 °C over the period of 2.4 h (10°C/h increment). When the temperature reached 4 °C, samples were washed in acetone three times (1 h each) and brought to RT. Finally, samples were infiltrated in Epon resin as described below in Table 2.3.

Duration (h)	Conditions	Concentration (v/v)
2-3	RT, in a glass snap vial, on a rotating wheel	100 % acetone and Epon resin (1:1)
1	RT, in a glass snap vial, on a rotating wheel	100 % acetone and Epon resin (1:1)
Overnight	RT, in a glass snap vial, on a rotating wheel	100 % Epon
3-5	RT, in a glass snap vial, on a rotating wheel	100 % Epon

Table 2.3: Epon-acetone infiltration series

On the next day, samples were embedded in fresh 100 % Epon and polymerized at 70 °C for 48 h.

2.3.5 Trimming, ultrathin-sectioning and section staining

2.3.5.1 Trimming of EPON blocks with embedded samples

After sample polymerization (described in section 2.3.1 and 2.3.4) the blocks were trimmed first with a fine file (DiAtome) to get closer to the region of interest (ROI). In this case till the tunnel of Corti located abneural from the single row of inner hair cells (IHCs), served as a reference point (refer to Fig. 2.1 F to see the localization of IHCs in a whole mount preparation of apical turn of the organ of Corti). Thereafter, the excess of polymerized resin was removed with a razor blade to get a small trapeze-shaped block face.

2.3.5.2 Formvar coating of copper grids

Prior to the sectioning (described in next section 2.3.5.3) of the trimmed EPON blocks, grids were coated with 1 % formvar in water-free chloroform (solution detail in section 2.8.3). A glass graduated cylinder (50 ml) equipped with a tap at the bottom was filled with formvar solution. A clean glass object slide was placed into the cylinder. The tap was opened quickly, to have optimal drag force so that a thin layer of formvar was coated onto the slide (silver to light gold color, ~ 80-90 nm thick). After that it was allowed to dry in a dust free area. After that with a razor blade, the edges of the slides were scratched on both sides loosening the formvar film. Slowly the slide was immersed into a beaker filled with distilled water so that the loosened formvar film floats onto the water surface. Subsequently, grids were placed on the formvar film with the shiny (smooth) side facing up. Using forceps, a

little pressure was carefully applied on every grid to ensure proper attachment of formvar with the coarse side of the grid grids. The completely packed formvar film was picked up with a piece of parafilm (for the slot grids) or with the paper covering the parafilm (for the mesh grids) and placed onto a Petri dish for drying. Air bubbles were released by making small holes on the film periphery and grid-free areas. 3.05 mm \emptyset , copper slot grids (Plano) were used to place the ultrathin sections. Additionally, 3.05 mm \emptyset , copper 100 mesh grids (Plano) were used for picking up semithin sections for electron-tomography.

2.3.5.3 Sectioning of embedded samples and post-staining

70 nm ultrathin sections were obtained using an Ultracut E ultramicrotome (Leica Microsystems) with a 35° diamond knife (DiAtome) for 2-D TEM image acquisition (described in section 2.4.1). For EM-tomography, semithin 250 nm sections were obtained (described in section 2.4.2). Next, post-staining was performed with 4 % uranyl acetate in water or uranyl acetate replacement solution (EMS) for 40 min and briefly (< 1 min) with Reynold's lead citrate in a closed staining compartment in the presence of NaOH to exclude atmospheric CO₂ to avoid lead precipitates. After that, grids were washed two times on water droplets with previously boiled distilled water. The details of the product, equipment and solutions can be found in section 2.8.

2.4 Transmission electron microscopy (TEM)

2.4.1 TEM for 2-D analysis and screening of sample quality

A JEM 1011 (JEOL) TEM was used to acquire images of random sections at 80 kV. Electron micrographs were obtained at a 12,000x magnification to specifically image ribbon synapses (Conventional embedding, Fig. 2.6C and HPF/FS, Fig. 2.6E) and a 5,000x and 2,500x for the overview of IHCs (Conventional embedding, Fig. 2.6A and HPF/FS, Fig. 2.6B). Equipment details are given in section 2.8.2.

2.4.2 Single tilt axis electron-tomography for 3-D visualization and analysis

Electron-tomography was performed as described in Jung et al., 2015a; Strenzke et al., 2016 and Vogl et al., 2015. 10 nm gold particles (British Bio Cell) were applied to both sides of the 250 nm stained mesh grids 5-10 min before image acquisition. Single axis tilt series were acquired at 200 kV with a JEM 2100 (JEOL) TEM, mostly from -60° to +60° with an 1° increment at a 12,000x magnification, using the Serial-EM software package (Mastronarde, 2005). In some cases, tilt series were acquired only from -25 and/or +58° because a grid bar was coming into the visual field at higher angles. Such tomograms were included in the analysis only when the tomogram quality was sufficient. Tomograms were generated using the IMOD package etomo (Kremer et al., 1996, also see <http://bio3d.colorado.edu/>, as described in section 2.5.3, Jung et al., 2015a; Strenzke et al., 2016).

2.5 Image processing and quantification parameters

2.5.1 Quantification parameters for 2-D analysis of random sections

Random sections were analyzed manually with the program ImageJ (version 1.47v, National Institute of Health, USA). For the result section 3.1, two morphological vesicle pools at ribbon synapses were analyzed, (i) membrane-proximal (MP) vesicles (in the first row with ≤ 25 nm vesicle membrane-to-AZ membrane and 80 nm along either side of the presynaptic density) and (ii) ribbon-associated (RA) vesicles that were defined as all vesicles in the first row in ≤ 80 nm distance around the ribbon (excluding MP vesicles; Fig. 2.6D). The number of SVs in each pool was counted using the ImageJ *Cell counter*. For the calculation of vesicle diameters, the average of the longest and the shortest axis was measured (Strenzke et al., 2016). Further, the length (L_{axis}) and width (W_{axis}) of the ribbon excluding the presynaptic density were quantified (Fig. 2.6D). Surface area/ribbon was computed using the formula:

$$\text{Surface area} = \pi L_{axis} W_{axis} / 2.$$

For the result sections 3.2, 3.3 and 3.4, random ultrathin section images were obtained at a 12,000x magnification for visual inspection of the sample quality (Fig. 2.6B, E) after HPF/FS (described in sections 2.3.2, 2.3.3.3 and 2.3.4). The systematic 2-D analysis was not performed for these samples; instead, a subsequent 3-D analysis was conducted (described in the next section 2.5.3 for all the three projects).

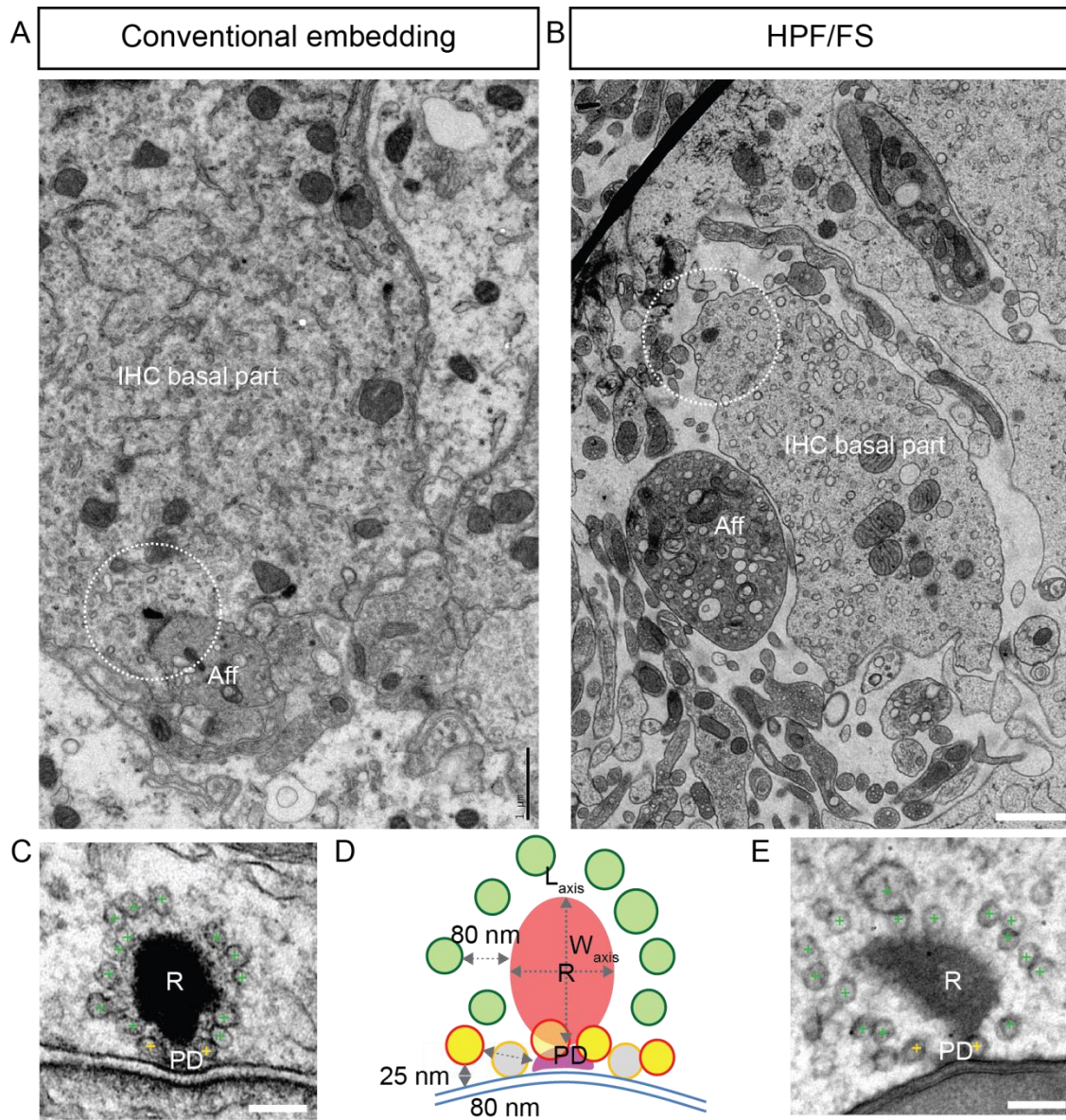


Figure 2.6: Quantification parameters for 2-D analysis of random sections

(A-B) Electron micrographs are focusing on the basal part of IHCs, fixed by conventional aldehyde (A) and HPF/FS (B) for EM. The ribbon synapses are located juxtaposed to the postsynaptic afferent nerve fibers (Aff) (encircled with white dotted line). Scale bar, 1 μm ; magnification, 800x. Both fixation methods provided a good structural preservation of IHCs. Images A and B are kindly provided by Carolin Wichmann. (C, E) Electron micrograph showing ribbon synapses after aldehyde fixation (C) and HPF/FS (E). Both sample preparation techniques obtained well-preserved ribbon synapses. The synaptic ribbons (R) are anchored properly by presynaptic densities (PD), to the continuous AZ membrane. In both methods, a halo of SVs is observed around the ribbon (green cross, RA SVs; yellow cross, MP SVs). Scale bar, 100 nm; magnification, 12,000x.

(D) Illustration depicting the criteria for random section analysis (not drawn to scale). RA SVs (green) are defined as those SVs that are in the first row ≤ 80 nm distant from the ribbon (R); MP SVs (yellow) are defined as those SVs that are in the first row, ≤ 25 nm membrane-to-membrane distance from the AZ membrane (blue) and ≤ 80 nm from the presynaptic density on both sides. Used in Strenzke et al., 2016.

2.5.2 Tomogram generation performed with IMOD from the raw tilt series

All tomograms were generated from their respective raw tilt series (*.mrc file extension) using the Serial-EM software package (Mastronarde, 2005). For the Windows version, the Unix-like environment (Cygwin) was installed. For in-depth introduction and tutorial to IMOD refer to the webpage of the Boulder laboratory for 3-D EM (<http://bio3d.colorado.edu/>). Briefly here, the *.mrc file extensions were renamed to *.st for recognition by eTomo (GUI of the IMOD) as a single stack. Further, pre-processing steps were followed to identify camera artifact, like random x-rays which cause extremely dark or bright pixels. These were replaced with neighboring average values by the program *Ccderaser*. Thereafter, the image stack was coarsely aligned by using the programs *Tiltcorr*, *Xftoxg* and *Newstack*. Following this computationally a fiducial model was generated based on the position of 10 nm gold particles that were applied as described in section 2.4.2. Then, these were traced through all projection images by running the program *Beadtrack*. For the fine alignment step and reduction of residual error mean, the program *Tiltalign* was executed to resolve the tilt displacements between each projection view (or tilt view). Further, a sample tomogram with a thickness of 1000 virtual sections was created (covering a larger thickness than the original section). Then, three small sample tomograms were reconstructed; near the top, middle and bottom of the tilt images for the minimal volume calculation of the final tomogram. This defines the x, y-axis angles and the z-position of the section with boundary line demarcations at the end of biological sample tomograms. For the final alignment, program *Tomopitch* was employed, a full-aligned stack was linearly interpolated. During reconstruction, the projections were binned three times, resulting in a final isotropic voxel size of 1.188 nm at a magnification of 12,000x. Finally, the actual tomogram was created using back projection algorithm of the program *Tilt*. The tomogram volume was trimmed for the region of interest in the x, y and z-planes of the virtual sections of the tomogram in a post-processing procedure.

2.5.3 Model rendering and quantification parameters for the 3-D tomogram analysis

Tomograms were segmented semi-automatically using 3dmod. For in-depth introduction and tutorial to 3dmod refer to the webpage of the Boulder laboratory for 3-D electron microscopy (<http://bio3d.colorado.edu/>) (Kremer et al., 1996).

2.5.3.1 Model generation for synaptic ribbons, pre-synaptic densities and AZ membranes

For the result sections, 3.1 to 3.4 synaptic ribbons and the presynaptic density were assigned as *closed* objects and were manually segmented for the first 10, middle 20 and last 10 virtual sections and then interpolated across the Z-stack using the *interpolator* tool of 3dmod. Interpolation was corrected manually in each virtual section thereafter. AZ membranes were manually segmented in each virtual section of the tomogram because of their irregularities (Jung et al., 2015a; Strenzke et al., 2016). In the result sections, 3.1 and 3.3 a surface area measurement was not performed in the tomograms (3-D). Instead, analysis of the ribbon size in random ultrathin section (described above in section 2.5.1, for result section 3.1) or in a virtual section of tomograms at the maximum projection of the synaptic ribbon (similar to random ultrathin sections described above in section 2.5.1, for result section 3.3) was performed. For the result sections, 3.2 and 3.4 a surface area and volume model for the ribbon was generated by meshing the contours (Helmprobst et al., 2015, used this for presynaptic densities at the NMJ of zebrafish). Result outputs were obtained in $\text{nm}^2/\text{tomogram}$ and $\text{nm}^3/\text{tomogram}$ for surface area and volume respectively.

2.5.3.2 Model for vesicles (synaptic vesicles, flattened vesicles, pleomorphic vesicles and bulk endocytic compartments)

i. Definition of the RA and the MP pool in tomograms

This definition was used for all the tomograms analyzed for the results in section 3.1 to 3.4. RA SVs were defined as the first row of vesicles with a maximal distance of 80 nm from the ribbon surface to the vesicle membrane in each tomogram (Jung et al., 2015a; Strenzke et al., 2016) (Fig. 2.7A2, B2). MP SVs were defined as the vesicles localized in the first row, with a maximum 50 nm membrane-to-membrane distance vertically to the AZ-membrane and with a maximum lateral distance (vesicle outer edge) of 100 nm to the presynaptic density (Jung et al., 2015a; Strenzke et al., 2016) (Fig. 2.7A3, B3).

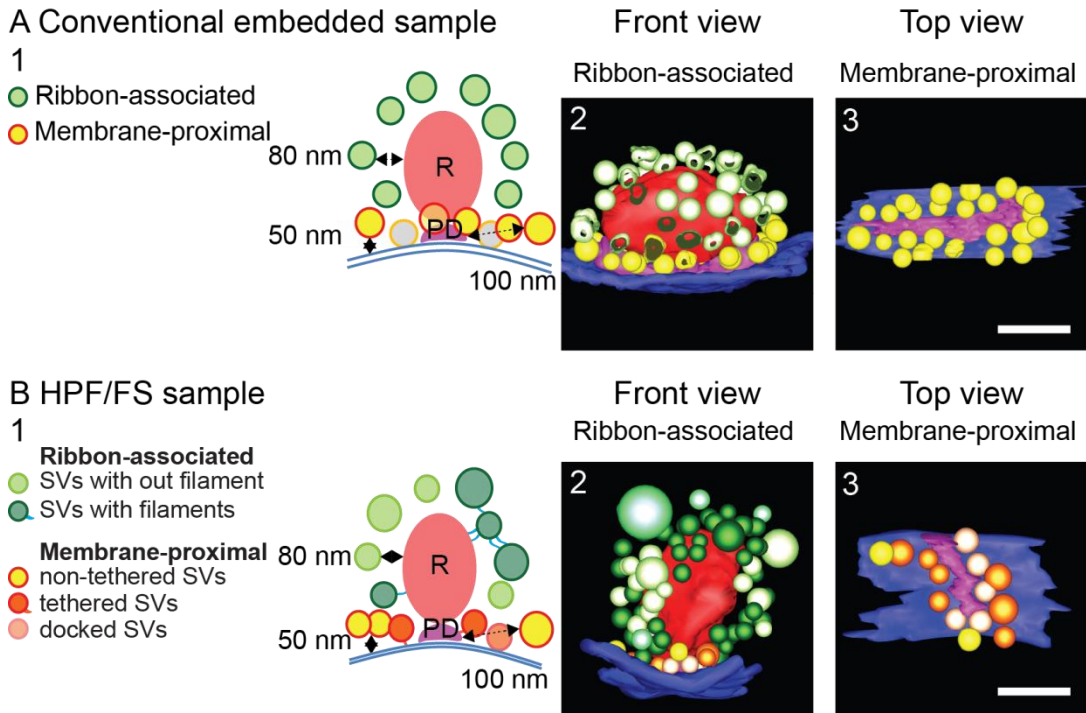


Figure 2.7: Definition of the RA and the MP pool for tomogram analyses

(A) Used for conventional aldehyde-fixed samples, modified from Strenzke et al., 2016 and **(B)** used for HPF/FS samples.

(A1) The illustration is depicting the analysis parameters of the tomograms (not drawn to scale). RA SVs (green) are defined as vesicles in the first row ≤ 80 nm distant from the ribbon (R); MP SVs (yellow) as vesicles in the first row ≤ 50 nm membrane-to-membrane distance from the AZ membrane (blue) and ≤ 100 nm from the presynaptic density (PD). Analysis parameter is used in Strenzke et al., 2016.

(A2) 3-D reconstruction of the RA vesicles pool (front view). RA SVs in light green, the AZ membrane in blue, the presynaptic density in pink and ribbons in red. Scale bar, 100 nm.

(A3) 3-D reconstruction of the MP vesicles pool (top view). For better visualization, ribbons are not shown; MP SVs in yellow, other synaptic components are color coded similar to A2. Scale bars, 100 nm. (A2-A3 published in Strenzke et al., 2016)

(B1) The illustration is summarizing the tomogram analysis (not drawn to scale). Vesicles are assigned to the following pools: RA SVs in the first row, ≤ 80 nm from the ribbon surface (R, with filaments in dark green and without filaments in light green) and MP SVs (with tethers in orange, without tethers in yellow and docked in light orange), in the first row ≤ 50 nm membrane-to-membrane distance from the AZ membrane (blue) and ≤ 100 nm from the presynaptic density (PD, pink). Analysis parameter is used in Jung et al., 2015a

(B2) 3-D reconstruction of the RA vesicles pool (front view). RA SVs; without filaments in light green, with filaments in dark green other synaptic components are color coded similar to A2. Scale bars, 100 nm.

(B3) 3-D reconstruction of the MP vesicles pool (top view). For better visualization, ribbons are not shown; MP SVs (non-tethered in yellow, tethered in orange and docked in light orange) other synaptic components are color coded similar to A2. Scale bars, 100 nm.

ii. Annotation of round vesicles

Next, all round vesicles (RA, MP and pleomorphic vesicles, for the result sections 3.1 to 3.4) were annotated using a spherical *scattered* object at its maximum projection in the tomogram marking the outer leaflet of the vesicles. The diameter of the sphere was adjusted for each vesicle. For the result section 3.1, the diameter was measured manually using the *measuring* drawing tool in 3dmod (Strenzke et al., 2016). For the result section 3.2 the vesicles radius (r) were determined automatically (Helmprobst et al., 2015), using the program *imodinfo option -p*, of IMOD software package (Kremer et al., 1996). Then the diameter (D) was computed with $D = 2r$. The automated and manual diameter measurements were comparable. Therefore, in the result section 3.4 I continued with the automated diameter measurements. All outputs were obtained in nm/tomogram.

iii. Annotation of flattened vesicles and bulk-endocytic compartments

All flattened vesicles in the MP and RA pool (for the result section 3.1) were assigned as closed objects and segmented using the *sculpt* drawing tool. The longest axis through the structure was considered as their size (Strenzke et al., 2016). Similarly, for bulk endocytic compartments (large vesicular or tubular structures) and large irregular vesicular structures (for result section 3.2) close to ribbons were annotated as stated above. Again, the longest axis was considered as their size. All outputs were obtained in nm/tomogram.

iv. Counting of vesicles

For counting round SVs (for the result sections 3.1 to 3.4), flattened vesicles (for the result section 3.1) and pleomorphic vesicles (for result section 3.2) the tomogram stack (*.rec) was converted into TIFF images (*.tif) using the program *mrc2tif* for further ImageJ analysis. The images were opened as a *sequence* and considered as *hyper-stack* in ImageJ. For better visualization, the contrast was selected at 0.4 % saturated pixel and adapted across all virtual sections. Using the plugin *cell counter* in ImageJ the round and flattened vesicles were labeled and counted. All counts obtained from ImageJ were tallied with the output information obtained from IMOD using the program *imofinfo option -F*, that prints the full report of the objects in the model (for detailed description of the program *imodinfo* please refer to <http://bio3d.colorado.edu/imod/doc/man/imodinfo.html>) (Kremer et al., 1996). Since a large number of pleomorphic vesicles were present in a single cluster (for result section 3.2) it was cumbersome to be counted manually, they were counted in IMOD automatically using the program *imodinfo option -p*, that prints the information of the point objects (Kremer et al., 1996). Outputs were obtained in count/tomogram. Furthermore, capturing a full ribbon in every tomogram was difficult (Jung et al., 2015a;

Strenzke et al., 2016). Therefore the fraction of a particular morphological class of vesicles was calculated per tomogram (*number of a particular morphological class of vesicle in a pool/total pool size*). For the result section 3.1, the fraction of flattened vesicles/ tomogram was calculated in the MP and RA pool (Strenzke et al., 2016).

2.5.3.3 Performance of filaments analysis

In this thesis, a detailed filament (tethers and inter-connectors) analysis was carried out for the RA and the MP pool (for result section 3.2 to 3.4). Only those electron-dense filaments were considered that connected at least one SV to a defined anchorage point, i.e., the synaptic ribbon, the presynaptic density, the AZ membrane and/or the neighboring SV. Remaining filamentous structures in the cytoplasm were ignored. After achieving the desired contrast and brightness, vesicles were counted in the MP and RA pool (described above in section 2.5.3.2 point iv). Further, for the RA and the MP pool different classes of SVs with filaments were identified and the respective fractions were calculated (as described in section 2.5.3.2 point iv, in detail will be explained in result sections 3.2, 3.3 and 3.2.4 in due course).

Next, the filament length was analyzed in the RA and the MP pools (Fig. 2.8A, B). The tomogram stack was converted to TIFF images for ImageJ analysis (as described above in section 2.5.3.2 point iv). Using the *multi-point selection* tool of ImageJ the filament starting (X_1, Y_1, Z_1) and ending (X_2, Y_2, Z_2) coordinates were defined as ROIs in the stack and length was calculated according to the formula (Jung et al., 2015a; Vogl et al., 2015):

$$\text{Filament length} = \sqrt{(X_2 - X_1)^2 + (Y_2 - Y_1)^2 + (Z_2 - Z_1)^2}.$$

All output measurements were obtained in nm/tomogram.

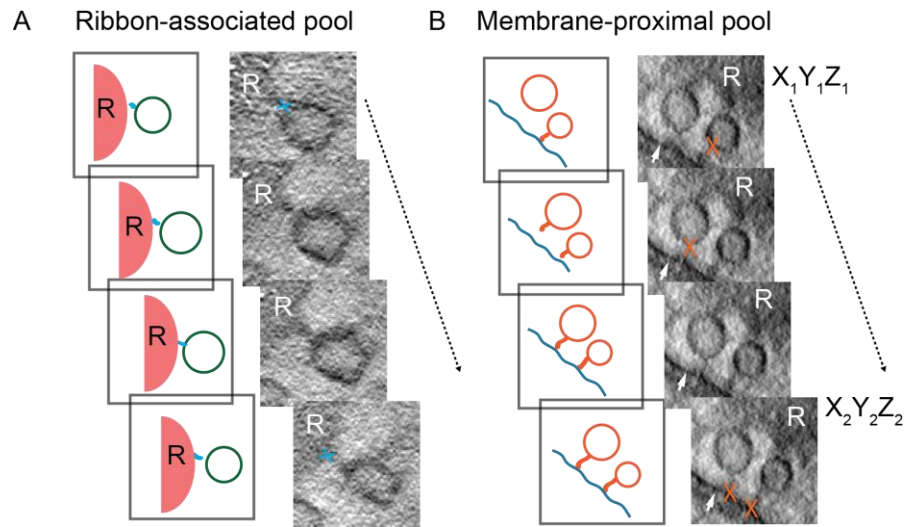


Figure 2.8: Filament length analysis for RA and MP SVs

(A-B) Shown are four exemplary consecutive virtual tomographic sections depicting a (A) RA SV tethered to the ribbon (R) and (B) two MP SVs tethered to the membrane (white arrowhead) respectively. The left panel of each depicts a simplified illustration of the same. The tethers are tracked from coordinates (RA SV; blue cross and MP SVs; orange crosses), X_1, Y_1, Z_1 to X_2, Y_2, Z_2 for the length measurements. Scale bar, 100 nm; magnification, 12,000x.

2.5.3.4 Docked SV analysis

To identify morphologically docked vesicles a 0-2 nm distance from the AZ to the vesicle membrane was considered (Imig et al., 2014), with a limited isotropic voxel value of 1.188 nm at a 12,000x magnification (for result sections 3.2 and 3.4). They were annotated as described in section 2.5.3.2 point ii and counted as described in section 2.5.3.2 iv. To analyze the localization of these vesicles at the AZ membrane, the distance of docked vesicles from the presynaptic density was measured/tomogram.

2.6 Data analysis and statistical tests

Data are presented as mean \pm SEM unless otherwise specified. The statistical tests and graphs are plotted using IGOR software 6.37. Normality was assessed with the *Jarque-Bera test*. The *F test* was used to assess equality of variance in normally distributed data sets. The unpaired, *two-tailed Wilcoxon-Rank-Sum test* (also known as *Mann-Whitney U-test*) was used to compare data of non-parametric distribution or when variances of experimental groups were unequal. In case of parametric and equal-variance data, *Student's unpaired two-tailed t-test* was used to compare two samples. To detect differences in multiple comparisons p-values were computed by *one way ANOVA* followed by *Tukey's test* for parametric data or *Kruskal-Wallis test* followed by non-parametric multiple comparisons test for non-parametric data. In case a group can be divided into sub-

groups (example: fraction of large vesicles in RA pool, fraction of docked SVs, fraction of SVs with multiple-tethers in the MP pool and SVs with short tethers (≤ 15 nm), Fisher's exact Chi-Square-test was performed using Graph Pad Prism as described previously (Fernández-Busnadiego et al., 2013; Vogl et al., 2015). The used statistical test and the sample size are mentioned in the respective figure legends and tables in Chapter 3.

2.7 Experimental workflow

Please refer to appendix section of this thesis to have an overview of the experimental workflow incorporated in this thesis for the results section 3.1 (Appendix I), 3.2 and 3.3 (Appendix II) and 3.4 (Appendix III).

2.8 Materials

2.8.1 Product details

Product	Company	Cat. No.
1-Hexadecane	Sigma Aldrich	52276.5ml
4-(2-hydroxyethyl)-1-piperazineethanesulfonic acid (HEPES)	Sigma Aldrich	H3375
4-Aminopyridine (4-AP)	Sigma Aldrich	275875
Acetone, glass distilled	Carl Roth	5025.5
Anhydrous beads (0.3 nm, Typ 564, Perlfom, Molecular sieve)	Carl Roth	8487.2
Calcium chloride (CaCl ₂)	Sigma Aldrich	793639
Cesium chloride (CsCl)	Sigma Aldrich	746487
Chloroform	Merck & Co.	1.024.451.000
Copper 100 mesh grids	Plano	G2410C
Copper slot grid 3.05 mm	Plano	G2500C
Embedding moulds	Plano	G3533
EPON pre-mix kit	Plano	R1140
Ethanol	Sigma Aldrich	32205
Ethylene glycol-bis(β -aminoethyl ether)-N,N,N',N'-tetraacetic acid (EGTA)	Sigma Aldrich	E3889
Glass slides	VWR	630-1986
Glutaraldehyde (GA)	Sigma-Aldrich	G7651
Grid boxes	Plano	B801003080
Lead(II)nitrate (Pb(NO ₃) ₂)	Carl Roth	HN32.1
Magnesium chloride hexahydrate (MgCl ₂ -6H ₂ O)	Sigma Aldrich	M2670
Magnesium sulfate (MgSO ₄)	Sigma Aldrich	746452
Osmium tetroxide (OsO ₄)solid	Sigma Aldrich	201030.250g.D
Osmium tetroxide liquid	Sigma Aldrich	75632.5ml
Paraformaldehyde (PFA)	Carl Roth	0335.1

Potassium chloride (KCl)	Sigma Aldrich	746436
Potassium hydroxide (KOH)	Merck & Co.	105033
Protein A 10 nm gold	Plano	EM.GC10/4
Sample holder half cylinder cartridge	Leica Microsystems	16770135
Sample holder middle plate	Leica Microsystems	16770136
Sample holder half cylinder cartridge (transparent)	Leica Microsystems	16770179
Sample holder middle plate with rim, 6 mm Ø	Leica Microsystems	16770160
Sapphire disc 6 mm Ø	Leica Microsystems	16770158
Sodium cacodylate trihydrate	Sigma Aldrich	CO250.10g
Sodium chloride (NaCl)	Sigma Aldrich	746398
Sodium citrate dihydrate (Na ₃ C ₆ H ₅ O ₇ ·2H ₂ O)	Merck & Co.	567446
Spacer ring 6 mm Ø and 200 µm thick	Leica Microsystems	16770180
Specimen carriers Type A, 3 mm Ø	Leica Microsystems	16770152
Specimen carriers Type A, 6 mm Ø	Leica Microsystems	16770181
Specimen carriers Type B, 3 mm Ø	Leica Microsystems	16770153
Specimen carriers Type B, 6 mm Ø	Leica Microsystems	16770182
Tannic Acid	Sigma-Aldrich	403040
Tetraethylammonium chloride (TEA-Cl)	Sigma-Aldrich	T2265
Uranyl acetate replacement	EMS	22405
Vinylec E (Formvar®) Resin	TED Pella, inc.	19222

Table 2.4: Products used for the experiments

2.8.2 Equipment

Product	Company
EM AFS2	Leica Microsystems
EM HPM100	Leica Microsystems
JEM-1011	JEOL
JEM-2100	JEOL
LLS3-LED blue light source (A20955)	Schott and Moritex
NI PCI-6221 (37 Pins) card	National instrumentation
Orius SC1000 CCD camera	GATAN
Trigger box	Leica Microsystems
Ultra 35° diamond knife	DiAtome
Ultracut E	Leica Microsystems

Table 2.5: Equipment used for the experiments

2.8.3 Solution details

Solution	Concentrations, using and storing conditions
Anhydrous ethanol	Anhydrous beads are filled up to the level mark of 200 ml, volume further filled till 1000 ml, stored air tight under hood undisturbed.
Extracellular solution for optical stimulation (in mM)	NaCl 107, HEPES 10, KCl 2.8, MgCl ₂ -6H ₂ O 1, CaCl ₂ 2, CsCl 1, 4-AP 5, TEA-Cl 35, glucose 2 mg/ml. pH was adjusted to 7.2 with NaOH. Osmolarity: 300 mOsmol
Fixative 1	4 % (w/v) PFA and 0.5 % (v/v) GA in phosphate buffer. Used on ice under the hood
Fixative 2	2 % glutaraldehyde in 0.1M cacodylate buffer. Used on ice under the hood
Formvar solution	1 % (w/v) in water-free chloroform, light protected, used under the hood
HEPES-Hanks' balanced salt solution (in mM)	NaCl 141.7, HEPES 10, KCl 5.36, MgCl ₂ -6H ₂ O 1, MgSO ₄ -7H ₂ O 0.5, glucose 2 mg/ml, L-glutamine 0.5 mg/ml. pH was adjusted to 7.2 with NaOH. Osmolarity: 290 mOsmol
Inhibitory solution (in mM)	NaCl 130, HEPES 10, KCl 5, MgCl ₂ -6H ₂ O 3, EGTA 5, glucose 2 mg/ml. pH was adjusted to 7.2 with NaOH. Osmolarity: 290 mOsmol
Mild-stimulatory solution (in mM)	NaCl 108, HEPES 10, KCl 40, MgCl ₂ -6H ₂ O 1, CaCl ₂ 1.3, glucose 2 mg/ml. pH was adjusted to 7.2 with NaOH. Osmolarity: 290 mOsmol
OsO ₄	2 % in acetone (w/v) (for freeze substitution) and 1 % (v/v) in cacodylate (for conventional embedding). Prepared freshly on the day of the experiment under the hood.
Reynold's lead citrate	1.33 g Pb(NO ₃) ₂ and 1.76 g Na ₃ C ₆ H ₅ O ₇ -2H ₂ O in 92 ml water, dissolvable only upon heating, with constant stirring, in the end, 8 ml 1 M NaOH was added. Thereafter, filtered and stored air tight at 4° C. Used under the hood and centrifuged 10 min before every use.
Sodium cacodylate buffer	0.1 M in H ₂ O, pH 7.2-7.4. Storage at 4° C till use. Used under the hood.
Strong-stimulatory solution (in mM)	NaCl 95, HEPES 10, KCl 50, MgCl ₂ -6H ₂ O 1, CaCl ₂ 5, glucose 2 mg/ml. pH was adjusted to 7.2 with NaOH. Osmolarity: 290 mOsmol
Uranyl acetate	4 % in H ₂ O. Storage in sealed eppendorf cups under the hood.
Water-free chloroform	CaCl ₂ powder filled up to the level mark of 100 ml, volume further filled till 600 ml (mark) with Chloroform, mixed once well, further stored airtight under the hood undisturbed.

Table 2.6: Solutions used for the experiments

3. Results

Active zones (AZ) at cochlear inner hair cells (IHCs) are characterized by the presence of electron dense projections called synaptic ribbons surrounded by a halo of synaptic vesicles (SVs) located in the presynaptic compartment of the IHCs (Smith and Sjöstrand, 1961). The ribbons are anchored by presynaptic densities to the AZ membranes juxtaposed to the postsynaptic densities (PSD) of the afferent nerve fiber. Currently, the mode of SV release and the associated molecular machinery at IHC ribbon synapses is not well understood. This thesis addressed these question by looking at the vesicle pool dynamics on the ultrastructural level at IHC ribbon synapses under different activity states and in wild-type compared to mutants for the IHC specific protein otoferlin (*Otof*) and the presynaptic protein Rab-3 interacting molecule 2 α (RIM2 α). This chapter is subdivided into four sections. In the first part (section 3.1), I highlight a new role of *Otof* in SV reformation by studying a temperature-sensitive *Otof* mutant (*Otof*^{515T/515T}) (this part of the thesis is published in Strenzke et al., 2016). In the second part (section 3.2), I revisited the ultrastructure of the otoferlin mutant *pachanga* (*Otof*^{Pga/Pga}) that revealed a replenishment deficit (Pangrsic et al., 2010) using high-pressure freezing and freeze substitution (HPF/FS). A comparative study of wild-type and *Otof*^{Pga/Pga} mutant mice allowed proposing a release sequence of SVs at IHC ribbon synapses. Additionally, the results bring forth the involvement of proteinaceous tethers crucial for SV replenishment at the ribbon and AZ membrane. Subsequently, I highlight the role of otoferlin in release site clearance during the sustained phase of exocytosis. In the third part (section 3.3), I investigated SV tethering at the AZ membrane to further identify proteins crucial for tether formation at ribbon synapses by studying the *RIM2 α knockout (KO)* (this part of the thesis is partially published in Jung et al., 2015a). Finally, in section 3.4 I bridged the gap between IHC physiology and morphology by combining optogenetics with HPF (Opto-HPF). This allowed me to achieve a temporal and spatial resolution to capture early dynamic exocytosis events at the IHC ribbon synapses. This methodology was described previously for *C. elegans* neuromuscular junction (NMJ) (Kittelmann et al., 2013; Watanabe et al., 2013a) and hippocampal neuronal cultures (Watanabe et al., 2013b). The key findings of each project are elaborated in this chapter.

Published online: October 11, 2016

Article



Hair cell synaptic dysfunction, auditory fatigue and thermal sensitivity in otoferlin Ile515Thr mutants

Nicola Strenzke^{1,2,*†}, Rituparna Chakrabarti^{2,3,4,†}, Hanan Al-Moyed^{4,5,†}, Alexandra Müller^{2,4,5}, Gerhard Hoch⁶, Tina Pangrsic^{2,7}, Gulnara Yamanbaeva^{1,2,4}, Christof Lenz^{8,9}, Kuan-Ting Pan⁸, Elisabeth Auge¹, Ruth Geiss-Friedlander¹⁰, Henning Urlaub^{2,8,9}, Nils Brose^{2,11}, Carolin Wichmann^{2,3,**} & Ellen Reisinger^{2,5,11,***}

PMID: 27729456 and DOI:10.15252/emj.201694564

The first part of this thesis (3.1) is a collaborative study with the groups of Carolin Wichmann, Nicola Strenzke, Ellen Reisinger, Nils Brose, Henning Urlaub, Ruth Geiss-Friedlander and Tina Pangršič Vilfan. Recently, published in the EMBO journal, 2016.

Author's contribution:

NS, I (RC) and HA-M contributed equally to work. In this thesis, I will present the transmission electron microscopy and electron tomography data solely acquired and analyzed by me. Any other data used here, from the co-authors will be cited as Strenzke et al., 2016 and the name of the author will be mentioned in due course.

3.1 Otoferlin is critical for the reformation of properly sized and fusion-competent synaptic vesicles

3.1.1 Unaltered ultrastructural organization and ribbon synapse numbers at *Otof*^{d515T/I515T} IHCs

The introduction of the I515T mutation in the mice *OTOF* gene reduced otoferlin levels by 65 % in IHCs (Strenzke et al., 2016). It was important to verify if this reduction in protein levels translates into a structural deficit at the level of individual ribbon synapses. Therefore, random ultrathin (70 nm) sections were analyzed after conventional embedding for electron microscopy (EM). This method yielded a good ultrastructural preservation of IHCs (Fig. 3.1A). At 12,000x magnification, good resolution for the vesicle pool analysis was obtained and intact synaptic ribbons anchored to the membrane and the classical halo of clear SVs around the ribbon for both *Otof*^{f+/+} and *Otof*^{d515T/I515T} samples (P14) were observed (Fig. 3.1B). Further, to check if the mutation resulted in gross changes of the ribbon structure, the surface area/ribbon in random ultrathin sections was calculated excluding the presynaptic density (as described in section 2.5.1). The surface area/ribbon was proportionate for both genotypes (Fig. 3.1C, *Otof*^{f+/+} = $(18 \pm 12) \times 10^3 \text{ nm}^2$, n = 114 ribbon synapses and *Otof*^{d515T/I515T} = $(17 \pm 8) \times 10^3 \text{ nm}^2$, n = 143 ribbon synapses). The statistical tests and the number of ribbons analyzed are mentioned in the legend of Fig. 3.1. Further, Hanan Al-Moyed (AG Reisinger, InnerEarLab, University Medical Center, Göttingen) showed well defined juxtaposed localization of CtBP2 (synaptic ribbon marker) and GluR2/3 (postsynaptic glutamate receptor) using immunohistochemistry and confocal microscopy on P14-P16 organs of Corti. Moreover, she found that the number of synapses/IHC remained comparable between *Otof*^{f+/+} and *Otof*^{d515T/I515T} (*Otof*^{f+/+} = 14.1 ± 0.4 , n = 35 IHCs and *Otof*^{d515T/I515T} = 14.9 ± 0.2 , n = 63 IHCs) (Strenzke et al., 2016). In conclusion, the I515T mutation in otoferlin does not alter the gross morphology of IHC ribbon synapses, in spite of reduced otoferlin levels at the IHCs (Strenzke et al., 2016).

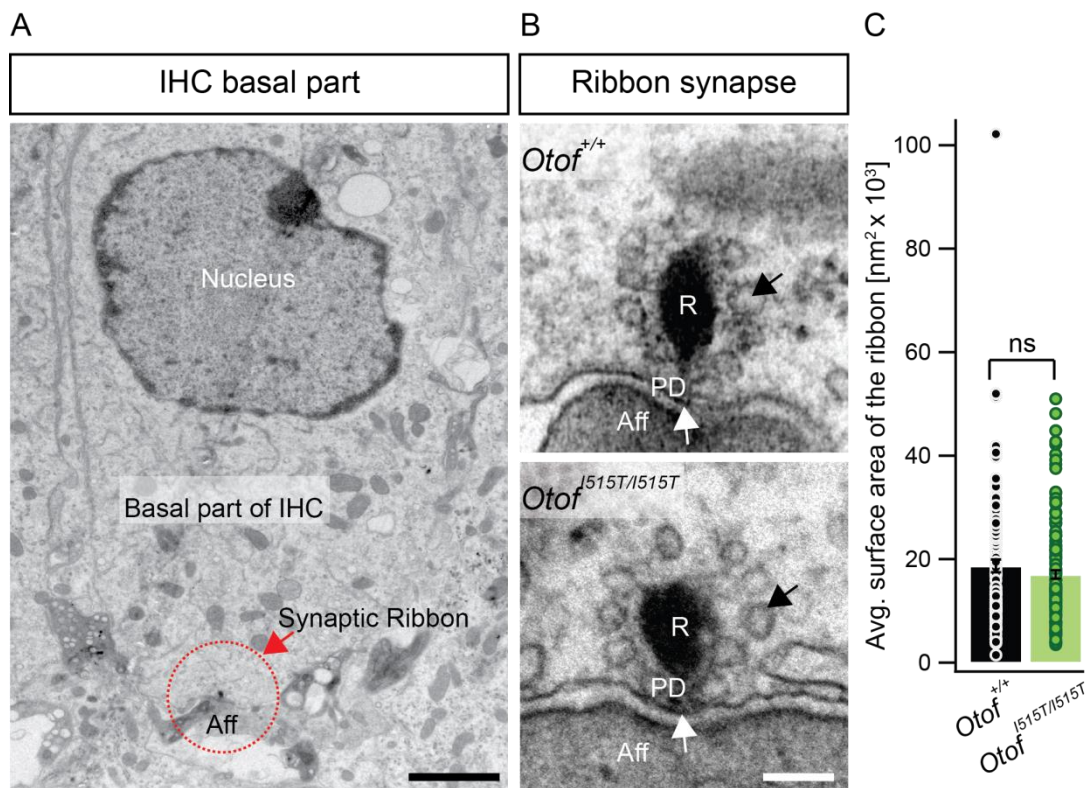


Figure 3.1: Morphology of *Otof*^{+/+} and *Otof*^{I515T/I515T} IHCs and ribbon synapses

(A) EM samples prepared using the conventional embedding protocol exhibit a good structural preservation of IHCs. A representative overview of an IHC in an *Otof*^{+/+} organ of Corti. Synaptic ribbons are located at the basal part of IHCs opposite to postsynaptic afferent nerve fibers (Aff). A typical ribbon synapse is encircled with a red dotted line. Scale bar, 1 μm , magnification, 1500x.

(B) Electron micrographs of synaptic ribbons (R) in *Otof*^{+/+} (upper panel) and *Otof*^{I515T/I515T} (lower panel) IHCs, anchored properly to the AZ membrane (white arrow) by the presynaptic density (PD). In both genotypes, a halo of SVs (black arrow) is observed around the ribbon. Scale bar, 100 nm; magnification, 12,000x.

(C) The average surface area ($\text{nm}^2 \times 10^3$)/synaptic ribbon is unaltered between *Otof*^{+/+} and *Otof*^{I515T/I515T}. Data are represented as mean \pm SEM. P-value is calculated with the Wilcoxon-Rank-Sum test. *Otof*^{+/+}, n = 114 ribbons; *Otof*^{I515T/I515T}, n = 143 ribbons, ns p > 0.05.

3.1.2 *Otof*^{I515T/I515T} IHCs showed SV accumulation proximal to the AZ membrane, but an unaltered number of ribbon-associated SVs

Otof^{I515T/I515T} mice had a moderate hearing impairment with enhanced adaptation rate of afferent nerve fibers to repetitive sound stimulus (Strenzke et al., 2016). Further, it was demonstrated that in mutant IHCs during prolonged stimulation the sustained component of exocytosis (50 ms or longer) was strongly reduced (Strenzke et al., 2016), most likely due to an impaired replenishment of the RRP for the next round of release (Pangrsic et al., 2010). Moreover, pre-embedding immunogold EM and immunofluorescence microscopy unanimously showed the localization of otoferlin at the plasma membrane of *Otof*^{+/+} (Strenzke et al., 2016; Vogl et al., 2015) and *Otof*^{I515T/I515T} mutant IHCs (Strenzke et al.,

2016). Also, otoferlin immunogold labeled cellular compartments partially showed clathrin coated structures indicating an endosomal origin. These structures were significantly bigger in *Otof*^{d515T/I515T} than *Otof*^{+/+} and exceeded (Strenzke et al., 2016) the average size of a SV (Neef et al., 2014). An increased size of otoferlin-labeled endosomal structures might point towards impaired vesicle turn over. Therefore, I wanted to investigate the effect of the I515T mutation on SV turnover on the level of individual ribbon synapses. Further, I was interested in the effect of a temperature shift on *Otof*^{d515T/I515T} mutant compared to wild-type ribbon synapses (Strenzke et al., 2016). Therefore, I analyzed the synaptic ultrastructure and SV pool dynamics at activity altered IHC ribbon synapses in P14-P15 mouse model at different temperatures.

Systematically, ribbon synapses were analyzed following inhibition (5 mM K⁺ and 0 mM Ca²⁺ and 5 mM EGTA) (Chapochnikov et al., 2014; Pangrsic et al., 2010; Strenzke et al., 2016) or mild-stimulation (40 mM K⁺ and 1.3 mM Ca²⁺) (Neef et al., 2014; Strenzke et al., 2016) for 1 min 45 sec at 36 and 39 °C in ultrathin sections (solution details in materials and methods section 2.8.3, also see experimental work flow in Appendix I for simplicity). SVs in direct contact with the AZ membrane were considered as morphologically docked in ultrathin sections (Pangrsic et al., 2010). However, conventional aldehyde fixation for EM could cause an aggregation of proteins making it difficult to differentiate real morphologically docked and not-docked vesicles. Therefore, the term membrane-proximal (MP) was used in this study (see section 2.5.1 for the criteria of MP vesicles). I observed in *Otof*^{d515T/I515T} ribbon synapses at both temperatures (36 and 39 °C) that the average number of MP SVs/ribbon increased only upon stimulation, while it remained unchanged in *Otof*^{+/+} (Table 3.1B, Strenzke et al., 2016). In the ribbon-associated (RA) pool the average number of RA SVs/ribbon was unchanged under both temperatures and both activity states (Table 3.1A, Strenzke et al., 2016).

3.1.3 Large vesicles (> 45 nm) accumulated in the MP and the RA pool upon mild-stimulation at the elevated temperature in *Otof*^{d515T/I515T}

Next, I determined the size of the SVs for the MP and the RA pool in both activity states at 36 and 39 °C, in random ultrathin sections. In both, *Otof*^{+/+} and *Otof*^{d515T/I515T} mutant IHCs, the majority of vesicles had a size of 35 - 45 nm (Fig. 3.2D, E, Strenzke et al., 2016), as described previously (Neef et al., 2007, 2014). At physiological temperature (36 °C) the *Otof*^{d515T/I515T} mutation did not change the SV size in the RA and the MP pool (Table 2.1A, B, Strenzke et al., 2016). Moreover, I did not encounter large vesicles (> 45 nm) in either the MP or the RA pool (Fig. 3.2D, E and Table 3.1C, D, Strenzke et al., 2016). Although, frequently large vesicles were found in a radius of 350 nm around the ribbon (excluding the

RA vesicles), but no significant difference in counts or diameters could be observed between *Otof*^{+/+} and *Otof*^{d515T/1515T} at 36 °C (data not shown).

At elevated temperature (39 °C), in addition to normal sized vesicles of 35 - 45 nm, larger vesicles (> 45 nm) became frequent in the RA and the MP pool of *Otof*^{+/+} and *Otof*^{d515T/1515T} mutants (Fig. 3.2D,E). Upon stimulation I found that the number of large SVs in the MP pool significantly increased in *Otof*^{d515T/1515T} compared to *Otof*^{+/+} IHCs, but was less frequent in the inhibitory condition in the mutant (Fig. 3.2F and Table 3.1D, Strenzke et al., 2016). On the contrary, RA vesicles were on average larger under inhibitory than stimulatory conditions for *Otof*^{+/+} and *Otof*^{d515T/1515T} ribbon synapses, whereby *Otof*^{d515T/1515T} had more large vesicles compared to *Otof*^{+/+} upon stimulation (Fig. 3.2G and Table 3.1C, Strenzke et al., 2016). The statistical tests and the number of vesicles and ribbons analyzed are mentioned in the legend of Fig. 3.3 and Table 3.1.

In conclusion the analysis of random ultrathin sections revealed an increased number of large sized vesicles in *Otof*^{d515T/1515T} in the RA and the MP pool mainly at the elevated temperature. Additionally, immunogold EM showed otoferlin localize to large endosomal structures (Strenzke et al., 2016). The size of these structures significantly increased in *Otof*^{d515T/1515T} mutants (Strenzke et al., 2016). Taken together, vesicle enlargement could indicate improper membrane recycling during mild-stimulation, in turn, translates to impaired sustained exocytosis at the mutant IHCs (Strenzke et al., 2016). Therefore, to understand the localization, shape and size of these large vesicles in 3-D, electron tomography was incorporated next (section 3.1.4).

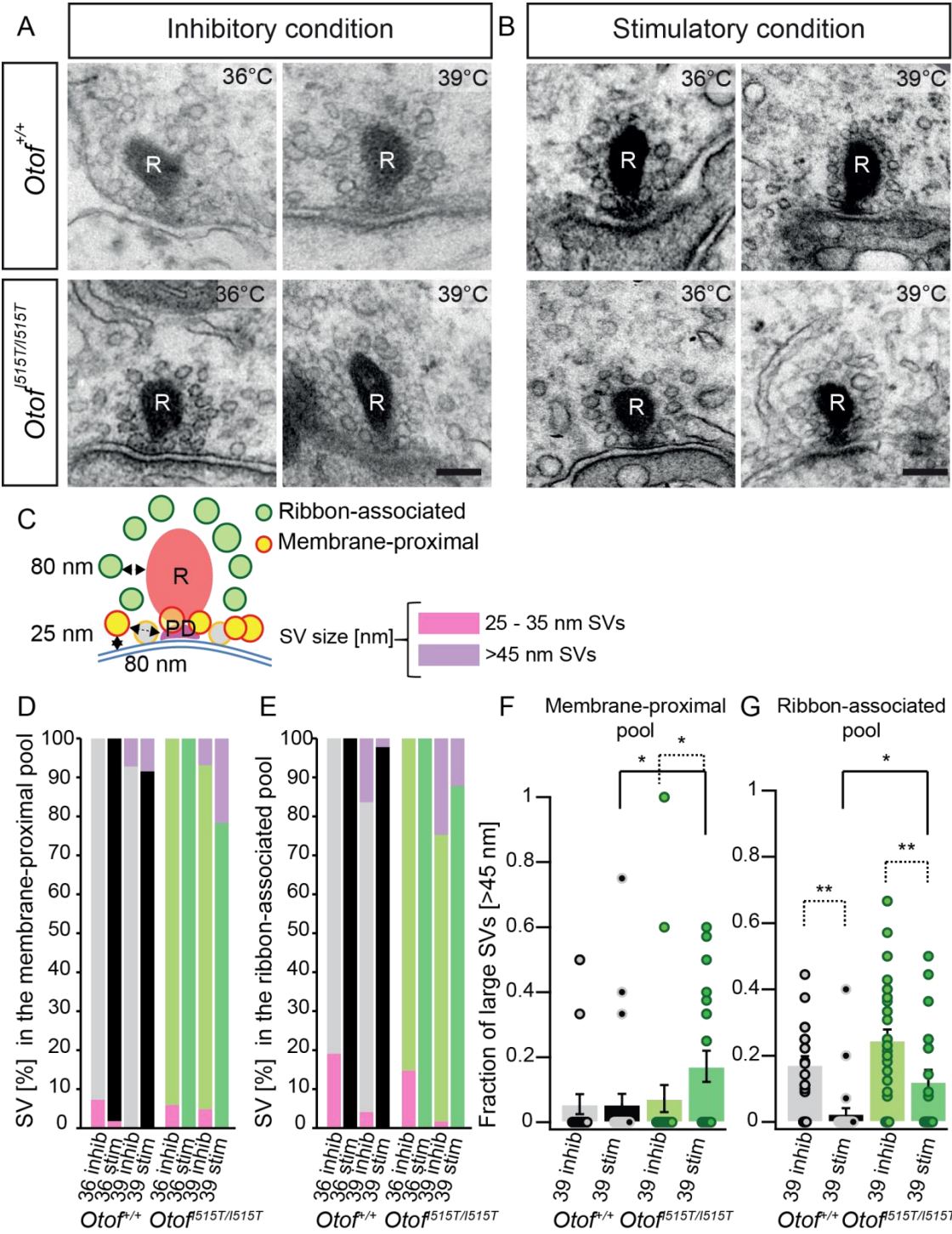




Figure 3.2: The I515T mutation alters the size of SVs

(A-B) Representative electron micrographs of IHC ribbon synapses in *Otof*^{I515T/I515T} and *Otof*^{+/+} IHCs (conventional embedding) after incubation in 40 mM K⁺ (stimulation) or 0 Ca²⁺ (inhibition) for 1 min 45 sec at 36 and 39 °C. Each solution was pre-warmed for 10 min at the according temperature. Scale bars, 100 nm; magnification, 12,000x.

(C) Illustration depicting the criteria for random section analysis (not drawn to scale). The RA and MP SVs are defined and quantified as shown in Fig. 2.7 panel A and are color-coded to the inset legend.

(D-E) Data are represented as % of SVs. The size distribution of MP **(D)** and RA **(E)** vesicles for inhibitory and stimulatory conditions at 36 and 39 °C in random ultrathin sections. The majority of SVs is normal sized (35 - 45 nm diameter).

(F-G) Larger vesicles (> 45 nm) appear only at 39 °C in *Otof*^{+/+} and especially in *Otof*^{I515T/I515T} IHCs. Data are represented as mean ± SEM, (F; Kruskal-Wallis test followed by non-parametric multiple comparison (NPMC) test and G; one way ANOVA followed by Tukey's test). **p < 0.01; *p < 0.05, data from 2 mice and 21-36 ribbon synapses are analyzed for each genotype and condition. Figure modified from Strenzke et al., 2016.

Parameter	Condition	<i>Otof</i> ^{+/+}	n	<i>Otof</i> ^{I515T/I515T}	n	p-values
A Number of SVs in the RA pool	36 °C Inhibition	8.6 ± 0.5	36	9.3 ± 0.7	21	0.9 §
	36 °C Stimulation	8.8 ± 0.7	25	9.9 ± 0.5	34	0.8 §
	39 °C Inhibition	8.9 ± 0.6	24	9.6 ± 0.5	36	0.8 §
	39 °C Stimulation	8.4 ± 0.6	27	8.6 ± 0.5	21	1.0 §
B Number of SV in the MP pool	36 °C Inhibition	2.3 ± 0.1		2.4 ± 0.2		p > 0.05 #
	36 °C Stimulation	2.2 ± 0.2		3.5 ± 0.3		p < 0.01 #
	39 °C Inhibition	2.3 ± 0.1		2.8 ± 0.1		p > 0.05 #
	39 °C Stimulation	2.6 ± 0.2		4 ± 0.3		p < 0.05 #
C Number of large (> 45 nm) vesicles in the RA pool	36 °C Inhibition	0		0		
	36 °C Stimulation	0		0		
	39 °C Inhibition	1.5 ± 0.2		2.4 ± 0.3		3.28E-05 §
	39 °C Stimulation	0.2 ± 0.1		1.04 ± 0.3		0.018 §
D Number of large (> 45 nm) vesicles in the MP pool	36 °C Inhibition	0		0		
	36 °C Stimulation	0		0		
	39 °C Inhibition	0.2 ± 0.1		0.2 ± 0.1		p > 0.05 #
	39 °C Stimulation	0.2 ± 0.1		0.9 ± 0.3		p < 0.05 #

Table 3.1 Random section EM analysis of *Otof*^{I515T/I515T} and *Otof*^{+/+}

Data are presented as mean ± SEM. P-values are calculated by one way ANOVA followed by Tukey's test (§) or Kruskal-Wallis test followed by NPMC (#) test reflecting differences between *Otof*^{I515T/I515T} and *Otof*^{+/+} under different treatment conditions. Data from 2 mice and 21-36 ribbon synapses for each genotype and condition were analyzed. Table modified from Strenzke et al., 2016.

3.1.4 The refinement of the vesicle pool analysis using electron tomography confirmed an increase in large vesicles in *Otof*^{d515T/1515T}

To further explore the localization of the observed large sized vesicles electron tomography (method section 2.4.2) was performed on the samples. *Otof*^{f+/+} and *Otof*^{d515T/1515T} mice (P14-P15) were compared after stimulation at 36 and 39 °C (Fig. 3.3A-D). This permitted me to analyze the spatial distribution, size and shape of vesicles in all 3-dimensions. In contrast to the results obtained from random sections, the average SV count/tomogram remained comparable in all genotypes and conditions (36/39 °C RA pool: Fig. 3.4D, Table 3.2B, E and 36/39 °C MP pool: Fig. 3.4L, Table 3.2H, K, Strenzke et al., 2016). However, the average SV diameter was significantly increased for *Otof*^{d515T/1515T} ribbon synapses in both vesicle pools at 36 and 39 °C (36/39 °C RA pool: Fig. 3.4C, Table 3.2A, D and 36/39 °C MP pool: Fig. 3.4K, Table 3.2G, J, Strenzke et al., 2016).

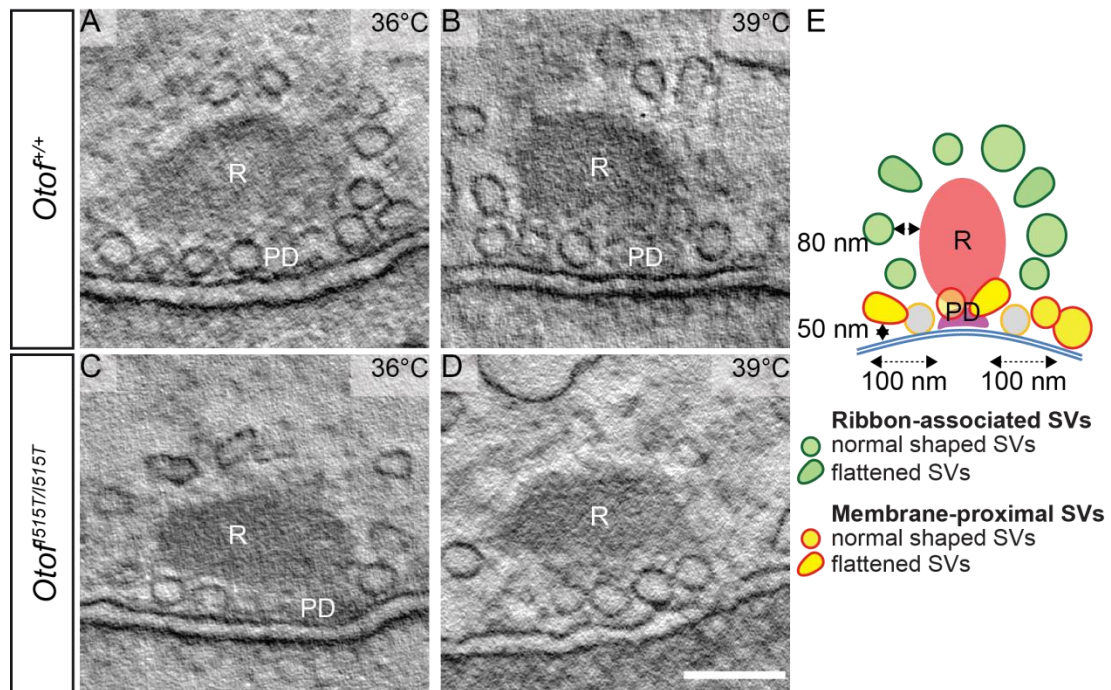
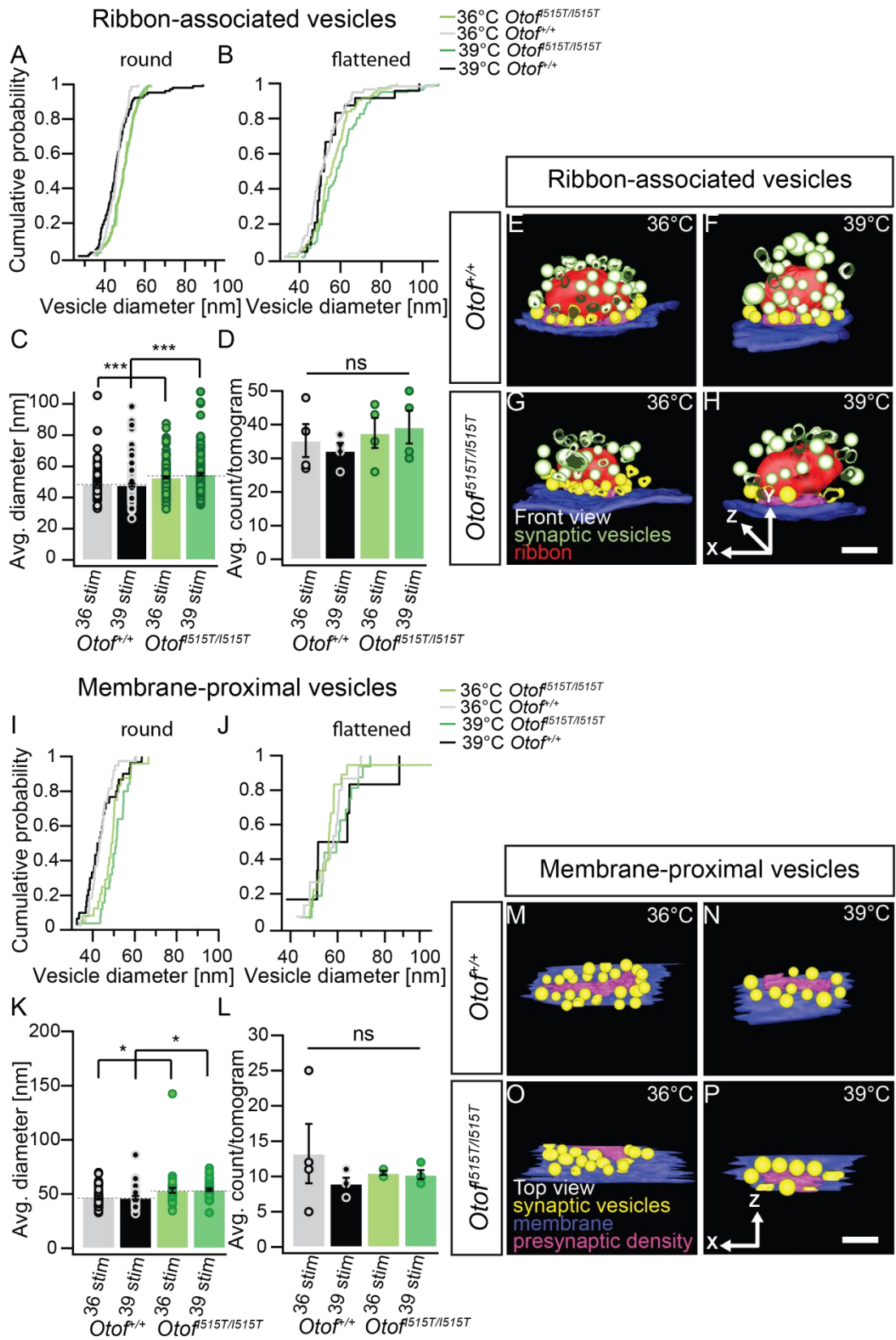


Figure 3.3: Tomographic virtual sections reconfirmed large vesicles in *Otof*^{d515T/1515T} IHCs

(A-D) Exemplary virtual sections from EM tomograms for the stimulatory condition at 36 and 39 °C of *Otof*^{f+/+} (A, B) and *Otof*^{d515T/1515T} (C, D) mice. Scale bar, 100 nm; magnification, 12,000x.

(E) The illustration is depicting the analysis parameters for the tomograms (not drawn to scale). The RA and MP SVs are defined as described in Fig. 2.7 panel A. Color-coded according to the inset legend. Figure modified from Strenzke et al., 2016.

Furthermore, I observed that quite some SVs were not properly shaped and often appeared flattened in particular during mild-stimulation in the mutant. Therefore, these flattened vesicles in the RA and the MP pool were analyzed separately. These vesicles were observed in all four conditions around the ribbon and close to the AZ membrane (RA pool at 36 °C: Table 3.2C and 39 °C: Table 3.2F; MP pool at 36 °C: Table 3.2I and 39 °C: Table 3.2L, Strenzke et al., 2016). The quantification of the flattened vesicles, by measuring the longest axis revealed that also the size remained unaltered irrespective of the temperature/genotype or vesicle pool (Fig. 3.4B, 36 and 39°C RA pool: Table 3.2A, D; Fig. 3.4J, 36 and 39°C MP pool: Table 3.2G, J, Strenzke et al., 2016). The statistical tests and the number of vesicles and ribbons analyzed are mentioned in the legend of Fig. 3.4 and Table 3.2.



←

Figure 3.4: The RA and the MP pool in *Otof*^{Δ515T/Δ515T} have large vesicles, but unaltered vesicle counts at 36 and 39 °C in the stimulatory condition

(A-H) Tomogram analysis of RA SVs.

(A-B) The cumulative probability distribution of the diameters of round vesicles **(A)** and the longest axis of flattened vesicles **(B)** in the RA pool. Round vesicles in samples fixed at 36 and 39°C are larger at *Otof*^{Δ515T/Δ515T} IHC ribbon synapses, but the longest axes of flattened vesicles are comparable for both genotypes. Data from 2 mice (round SVs, n = 75-105; flattened vesicles, n = 24-81) are presented for each genotype and condition.

(C) The average diameter of the RA vesicles is larger in *Otof*^{Δ515T/Δ515T} at both temperatures. Data from 2 mice and n = 129-157 SVs are shown for each genotype and condition.

(D) The average count of RA vesicles/tomogram is unaltered between the genotypes/temperatures. Data from 2 mice and 4 tomograms are analyzed for each genotype and condition.

In C and D, data are represented as mean ± SEM, p-values are calculated with the Kruskal-Wallis test followed by NPMC; *** p < 0.001 and ns p > 0.05.

(E-H) 3-D reconstruction of the RA pool of SVs (front view) of *Otof*^{+/+} **(E, F)** and *Otof*^{Δ515T/Δ515T} **(G, H)** ribbon synapses. The RA SVs are shown in light green, the AZ membrane in blue, the presynaptic density in pink and ribbons in red (also see Fig.2.7 panel A). Scale bar, 100 nm.

(I-P) Tomogram analysis of MP SVs.

(I-J) The cumulative probability distribution of the diameters of round vesicles **(I)** and the longest axis of flattened vesicles **(J)** in the MP pool. Round vesicles in samples fixed at both temperatures are significantly larger in *Otof*^{Δ515T/Δ515T} IHC synapses, but the longest axes of flattened vesicles are comparable for both genotypes. Data from 2 mice (round SVs, n = 24-38; flattened vesicles, n = 6-18) are presented for each genotype and condition.

(K) The average diameter of the MP vesicles is larger in *Otof*^{Δ515T/Δ515T} at both temperatures. Data from 2 mice and n = 36-53 SVs are shown for each genotype and condition.

(L) The average count of RA vesicles/tomogram is unaltered between all genotypes/temperature. Data from 2 mice and 4 tomograms are analyzed for each genotype and condition.

In C, p-values are calculated with one way ANOVA followed by Tukey's test and in D, with the Kruskal-Wallis test followed by NPMC; * p < 0.05 and ns p > 0.05. C-D, data are represented as mean ± SEM.

(M-P) 3-D reconstruction of the MP vesicle pool (top view, with synaptic ribbon not displayed for better visualization) of *Otof*^{+/+} **(M, N)** and *Otof*^{Δ515T/Δ515T} **(O, P)** ribbon synapses. The MP SVs in yellow, other synaptic components are color-coded similar to panel E-H (also see Fig. 2.7 panel A). Scale bars, 100 nm. Figure modified from Strenzke et al., 2016.

		Parameters		<i>Otof</i> ^{+/+}	<i>Otof</i> ^{J515T/J515T}	p-values	
Vesicles in ribbon-associated pool	36°C Stimulation	A	Vesicle diameter [nm]	Normally shaped	45.6 ± 0.5 n _{Vesicles} = 81	49.4 ± 0.7 n _{Vesicles} = 75	0.003 §
				Flattened	52.7 ± 1.4 n _{Vesicles} = 60	56.4 ± 1.8 n _{Vesicles} = 75	p > 0.05 #
				Total pool	48.6 ± 0.7	53.0 ± 0.7	p < 0.001 #
		B	Vesicle count per ribbon synapse, n _{Synapses} = 4	Normally shaped	20.3 ± 1.1	18.8 ± 1.9	p > 0.05 #
				Flattened	15.0 ± 3.7	18.8 ± 3.1	p > 0.05 #
				Total pool	35.3 ± 4.9	37.5 ± 5.5	p > 0.05 #
	C	Fraction of flattened vesicles	0.4 ± 0.04	0.49 ± 0.03	p > 0.05 #		
	39°C Stimulation	D	Vesicle diameter [nm]	Normally shaped	46.4 ± 0.9 n _{Vesicles} = 105	49.2 ± 0.7 n _{Vesicles} = 76	0.03 §
				Flattened	55.0 ± 2.7 n _{Vesicles} = 24	60.3 ± 1.4 n _{Vesicles} = 81	p > 0.05 #
				Total pool	48.0 ± 0.9	55.0 ± 0.9	p < 0.001 #
		E	Vesicle count per ribbon synapse, n _{Synapses} = 4	Normally shaped	26.3 ± 3.6	19.0 ± 3.1	p > 0.05 #
				Flattened	6.0 ± 2.7	20.5 ± 2.6	p > 0.05 #
Total pool				32.3 ± 2.3	39.5 ± 4.8	p > 0.05 #	
F	Fraction of flattened vesicles	0.2 ± 0.10	0.5 ± 0.10	p > 0.05 #			

Vesicles in membrane-proximal pool	36° C Stimulation	G	Vesicle diameter [nm]	Normally shaped	44.6 ± 0.9 n _{Vesicles} = 38	48.6 ± 1.4 n _{Vesicles} = 24	0.02 §
				Flattened	56.5 ± 2.04 n _{Vesicles} = 15	60.0 ± 5.0 n _{Vesicles} = 18	0.9 §
				Total pool	47.3 ± 1.2	53.5 ± 2.4	p < 0.01 §
		H	Vesicle count per ribbon synapse, n _{Synapse} = 4	Normally shaped	10.0 ± 3.6	6.0 ± 0.7	p > 0.05 #
				Flattened	3.8 ± 0.4	4.5 ± 0.3	p > 0.05 #
				Total pool	13.3 ± 4.2	10.5 ± 0.3	p > 0.05 #
	I	Fraction of flattened vesicles	0.3 ± 0.10	0.4 ± 0.10	p > 0.05 #		
	39° C Stimulation	J	Vesicle diameter[nm]	Normally shaped	44.0 ± 1.4 n _{Vesicles} = 30	50.7 ± 1.2 n _{Vesicles} = 25	0.001 §
				Flattened	59.4 ± 6.7 n _{Vesicles} = 6	59.1 ± 2.1 n _{Vesicles} = 16	0.9 §
				Total pool	46.6 ± 1.8	54 ± 1.3	0.02 §
		K	Vesicle count per ribbon synapse, n _{Synapse} = 4	Normally shaped	7.5 ± 1.3	6.3 ± 0.63	p > 0.05 #
				Flattened	1.5 ± 0.9	4 ± 0.4	p < 0.01 #
Total pool				9.0 ± 0.8	10.3 ± 0.63	p > 0.05 #	
L	Fraction of flattened vesicles	0.2 ± 0.10	0.4 ± 0.0	p > 0.05 #			

← Table 3.2: Electron tomogram analysis after stimulation at 36 °C and 39 °C

Data are presented as mean \pm SEM. P-values are calculated by one way ANOVA followed by Tukey's test (§) or Kruskal-Wallis test followed by NPMC (#) test reflecting differences between *Otof*^{d515T/1515T} and *Otof*^{+/+} under different treatment conditions. Table modified from Strenzke et al., 2016.

3.1.5 Summary

In section 3.1 IHC ribbon synapses were in detail investigated at the ultrastructural level to resolve the components required to maintain a tonic transmission upon stimulation. The tomogram analysis revealed that the MP and RA pool size remained comparable between *Otof*^{+/+} and *Otof*^{d515T/1515T}. However, the average vesicle diameter was significantly enlarged in the mutants at 36 and 39 °C. Additionally, immunogold EM indicated otoferlin labeling on enlarged endosomal compartments (Strenzke et al., 2016), which were on average larger in diameter than SVs (Neef et al., 2014; Strenzke et al., 2016). These compartments were significantly bigger in *Otof*^{d515T/1515T} IHCs (Strenzke et al., 2016). Therefore, I propose that *Otof*^{d515T/1515T} mutant ribbon synapses suffer from SV reformation defect where due to reduced otoferlin protein levels (~ 65 % reduction from the *Otof*^{+/+}) proper sized vesicles cannot be formed to a normal extend from endocytic compartments.

3.2 Tethering is crucial for replenishment of SVs at IHC ribbon synapses: Investigating the role of otoferlin in tethering and exocytosis

In this part, I focused on examining SV tethering, possibly a crucial factor for maintaining exo-endocytosis SV cycle at IHC ribbon synapses. In order to do so, I opted for HPF/FS (as described in section 2.3.2 and 2.3.4) for a close to native state structural preservation with immobilization of samples within milliseconds (Hammarlund et al., 2007; Imig et al., 2014; Jung et al., 2015a; Moor, 1987; Rostaing et al., 2006; Siksou et al., 2007; Stigloher et al., 2011; Vogl et al., 2015). Explanted organs of Corti were frozen after either 15 min strong stimulation, which will be referred as stimulation in this section (50 mM K⁺ and 5 mM Ca²⁺) (described in Chapochnikov et al., 2014; Jung et al., 2015b; Pangrsic et al., 2010; Vogl et al., 2015) or 15 min inhibition (5 mM K⁺, 0 Ca²⁺ and 5 mM EGTA) (described in Chapochnikov et al., 2014; Pangrsic et al., 2010; Strenzke et al., 2016) (solution details are provided in materials and methods section 2.8.3, also see Appendix II for a simplified work flow for this part). Additionally, *Otof*^{Pga/Pga} mutants with SV replenishment impairment (Pangrsic et al., 2010) were used as a comparative model to bring out the role of SV tethering in replenishment and maintenance of vesicle pool dynamics during sustained phase of exocytosis.

3.2.1 Unaltered morphology of wild-type and *Otof*^{Pga/Pga} ribbon synapses upon inhibition/stimulation

After HPF and FS, I first checked for an artifact-free freezing quality for wild-type (P14-P16) and *Otof*^{Pga/Pga} (P14-P19) inhibitory and stimulatory conditions. Initially, I inspected the basal part of the IHCs in 70 nm ultrathin sections (Fig. 3.5B-E) as a first quality control and thereafter the ribbon synapses in greater detail in tomograms (Fig. 3.6A-D). All samples used for analysis showed an excellent ultrastructural preservation and were comparable to previously described studies in IHCs with same methodology (Chapochnikov et al., 2014; Jung et al., 2015a; Vogl et al., 2015). Only those samples were considered for analysis, which showed well-preserved AZ membranes, intact presynaptic densities anchoring the synaptic ribbons, and visible tethers between SVs and ribbons and/or AZ membranes (Fig. 3.6A-D).

As a first step, I measured the surface area of synaptic ribbons in tomograms to understand if the mutation causes alteration of the ribbon size, but no difference was observed between wild-type and *Otof*^{Pga/Pga} under both conditions (Fig. 3.6E and Table 3.3A). This reconfirmed that the gross ribbon morphology was unaltered in *Otof*^{Pga/Pga} as described previously (Pangrsic et al., 2010). The statistical tests and the number of ribbons analyzed are shown in the legend of Fig. 3.6 and Table 3.3.

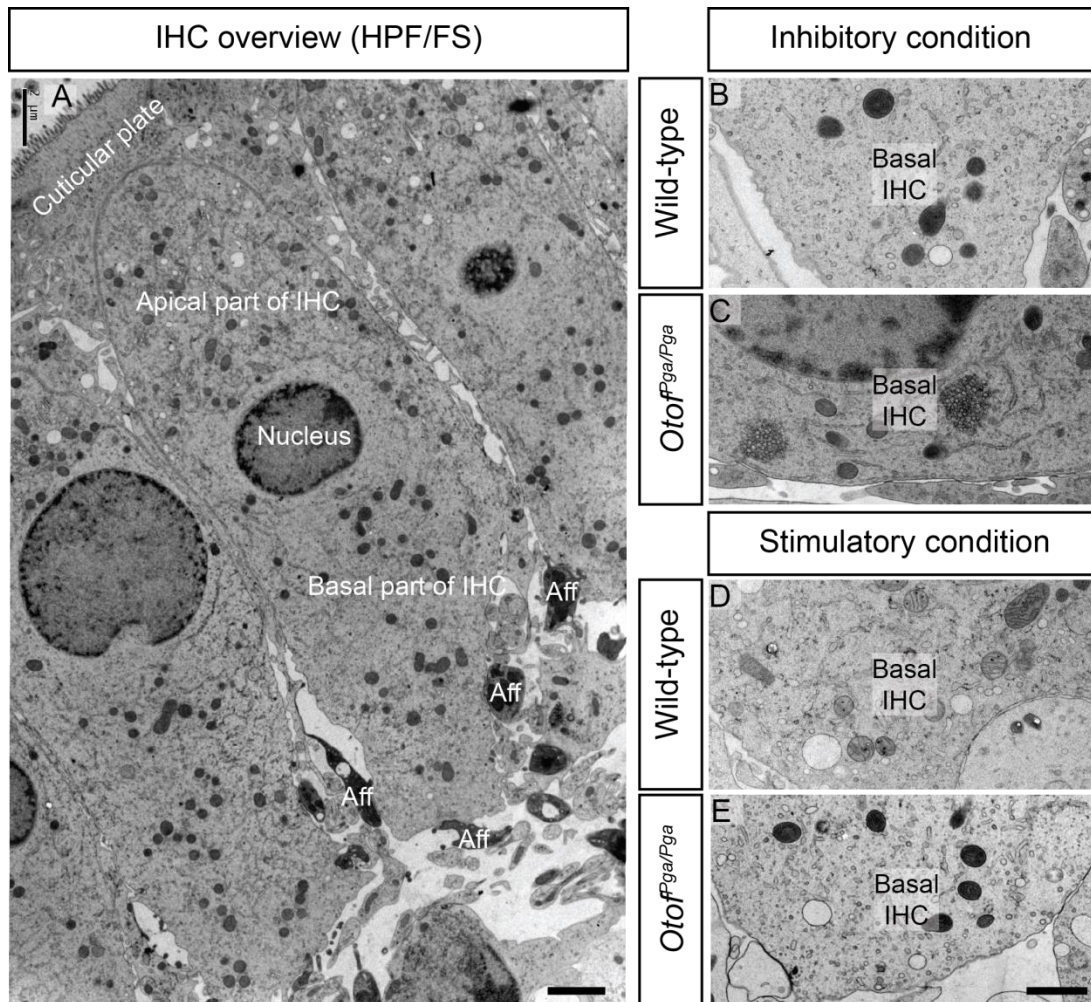


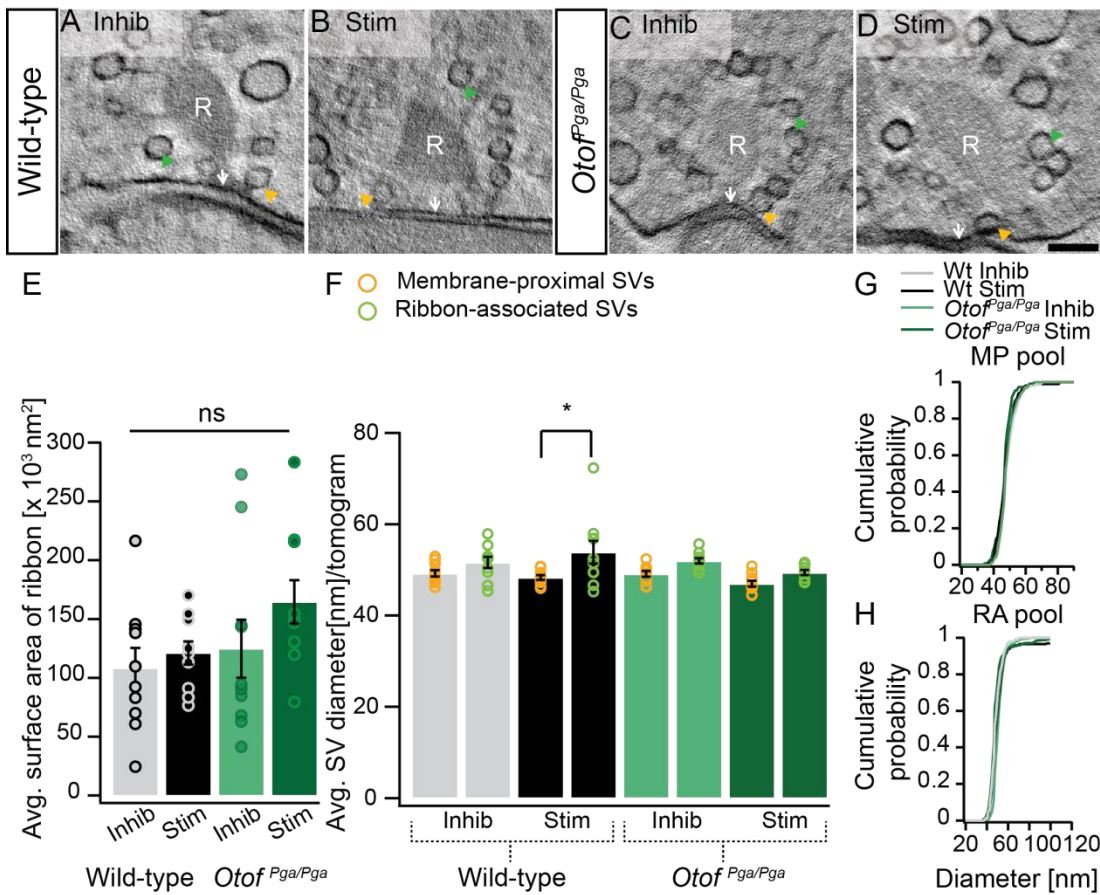
Figure 3.5: Comparable IHC and ribbon synapse morphology in wild-type and *Otof*^{Pga/Pga} mice
(A) EM samples prepared by HPF/FS exhibit a good structural preservation of the IHCs. Shown is a representative overview of three wild-type IHCs in a row. Scale bar, 2 μm; magnification, 800x.
(B-E) Electron micrographs of the IHC basal region after incubation at room temperature in either 50 mM K⁺ (stimulation) or 0 Ca²⁺ (inhibition) solution for 15 min. The inhibitory condition of wild-type **(B)** and *Otof*^{Pga/Pga} **(C)** IHCs; the stimulatory condition of wild-type **(D)** and *Otof*^{Pga/Pga} **(E)** IHCs. Scale bar, 1 μm; magnification, 2,500x. Images B-E are acquired by Susann Michanski (AG Wichmann, Institute for Auditory Neuroscience, Göttingen).

3.2.2 Normal sized SVs were observed in the RA and MP pool of *Otof*^{Pga/Pga} IHCs

Previously it has been shown that in *Otof*^{515T/515T} mice the vesicle diameter increased due to a proposed reformation defect (described in section 3.1, Strenzke et al., 2016). Therefore, to evaluate whether the increased activity at the IHCs affects the SVs diameter in *Otof*^{Pga/Pga} animals, the average vesicle diameter/tomogram was measured in wild-type and *Otof*^{Pga/Pga} in inhibitory and stimulatory conditions (Fig. 3.6F). As before, the vesicles of

two morphologically distinct vesicle pools were defined at the IHC ribbon synapses: (i) RA and (ii) MP vesicles (for definition of each pool refer to section 2.5.3.2 point i and Fig. 2.7 panel B) (Jung et al., 2015a; Strenzke et al., 2016). Generally, in IHCs a broad vesicle size distribution was observed, especially in the RA pool and 350 nm around the ribbon. I observed that with HPF/FS most of the SVs were in the range of 35 - 45 nm in both, wild-type and *Otof*^{Pga/Pga} inhibitory and stimulatory conditions (Fig. 3.6G-H), comparable to results obtained from conventional embeddings for EM (Strenzke et al., 2016). Further, as described previously for random sections (Chapochnikov et al., 2014), upon stimulation the average SV diameter/tomogram in wild-type IHCs was significantly bigger in the RA pool compared to MP vesicles, whereas under inhibitory conditions the average SV diameter/tomogram remained unaltered (Fig. 3.6F and Table 3.3B, C). The statistical tests and the number of ribbons analyzed are mentioned in the legend of Fig. 3.6 and Table 3.3.

In conclusion, the SVs once formed maintain a constant size (~ 40 nm) at both wild-type and *Otof*^{Pga/Pga} IHC ribbon synapses. However, in wild-type upon strong stimulation sometimes bulk endocytosis events were captured possibly forming large vesicles at the ribbon (Fig. 3.6I-J).



Bulk endocytosis at wild-type ribbon synapse

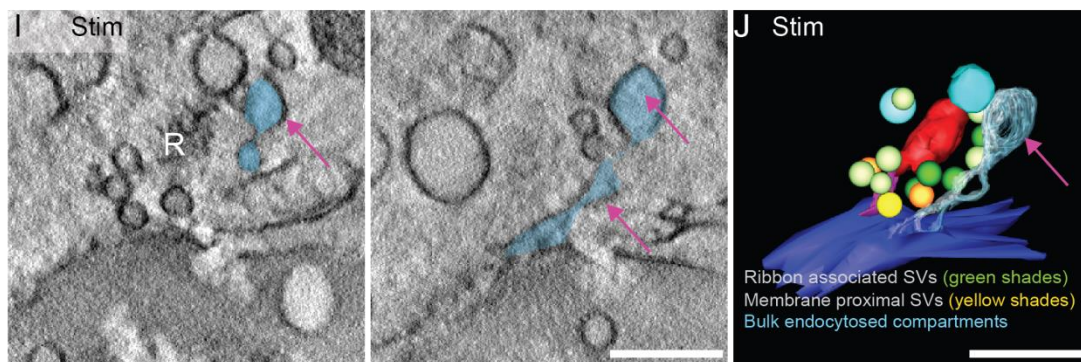


Figure 3.6: Synaptic ribbon size and SV diameter are comparable between wild-type and *Otof^{Pga/Pga}* ribbon synapses

(A-D) Representative tomographic virtual sections of wild-type (A-B) and *Otof^{Pga/Pga}* (C-D) ribbon synapses. Intact AZs (white arrows) and proper presynaptic densities with normal anchorage of the synaptic ribbons (R) are found in wild-type and mutants under both conditions. Ribbons are surrounded by a halo of SVs: the RA (green arrowheads) and the MP (yellow arrowheads) vesicles. Scale bar, 100 nm; magnification, 12,000x.

(E) The average surface area ($\text{nm}^2 \times 10^3$)/synaptic ribbon per tomogram is unaltered in the wild-type and the *Otof^{Pga/Pga}* for both conditions.

(F) The average SV diameter is unaltered for RA (green circles) and MP SVs (yellow circles) in most of the conditions. Only after stimulation in wild-type, the RA vesicles are significantly bigger compared to the MP vesicles. E-F Data are represented as mean \pm SEM. P-values are calculated with one way ANOVA followed by Tukey's test, n = 10 tomograms for each genotype and condition. * p < 0.05 and ns p > 0.05.

(G-H) Cumulative probability distributions of SVs are overlapping for all investigated genotypes and conditions. (G) The MP SVs, inhibitory: wild-type = 102; *Otof*^{Pga/Pga} = 123, stimulatory: wild-type = 99; *Otof*^{Pga/Pga} = 111. (H) The RA SVs, Inhibitory: wild-type = 270; *Otof*^{Pga/Pga} = 538, stimulatory wild-type = 262; *Otof*^{Pga/Pga} = 420.

(I) Representative tomographic virtual sections of a wild-type ribbon synapse upon stimulation, depicting a bulk-endocytic compartment (sky blue, pink arrow) close to the ribbon (R). Scale bar, 100 nm; magnification, 12,000x.

(J) 3-D reconstruction (front view) from the same tomogram with: ribbon (red), presynaptic density (pink), AZ membrane (blue), RA SVs (light and dark green), MP SVs (yellow and orange) and endocytic compartments (light blue, pink arrow). Scale bar, 100 nm. Images I-J, are kindly provided by Carolin Wichmann.

	Parameter	Condition	Wild-type	<i>Otof</i> ^{Pga/Pga}	p-values
A	Ribbon surface area [10 ³ nm ²]	Inhibitory	108 \pm 17	125 \pm 25	0.9 §
		Stimulatory	121 \pm 90	165 \pm 19	0.3 §
B	SV diameter in RA pool [nm]	Inhibitory	51.6 \pm 1.2	52.0 \pm 0.6	0.9 §
		Stimulatory	53.9 \pm 2.5	49.4 \pm 0.6	1.0 §
C	SV diameter in MP pool [nm]	Inhibitory	49.3 \pm 0.7	49.1 \pm 0.6	1.0 §
		Stimulatory	48.3 \pm 0.5	47.0 \pm 0.6	1.0 §

Table 3.3: Ribbon surface area and vesicle diameter at wild-type and *Otof*^{Pga/Pga} IHC ribbon synapses

Data are presented as mean \pm SEM. P-values are calculated by one way ANOVA followed by Tukey's test (§) for a parametric multiple comparison reflecting differences between the wild-type and the *Otof*^{Pga/Pga} under different conditions. Data are acquired from three wild-type mice each for inhibitory and stimulatory conditions and two *Otof*^{Pga/Pga} mice each for inhibitory and stimulatory conditions. Ten tomograms are analyzed for each genotype and condition.

3.2.3 More RA SVs were present in *Otof*^{Pga/Pga} under inhibition

In order to elaborate the role of the synaptic ribbon in vesicle resupply for the next round of release, vesicle numbers were analyzed in the RA pool. A previous study on Adaptor protein (AP)-2 μ mutants demonstrated that due to the lack of this endocytic protein, the distal ribbon part became partially depleted of SVs, indicating its role in initial vesicle resupply (Jung et al., 2015b) and speculatively, the existence of two functionally distinct zones at the ribbon (Chapochnikov et al., 2014; Jung et al., 2015b). Therefore, ribbons here were divided into a proximal (closer to AZ membrane, excluding MP pool) and a distal (away from the AZ membrane) part. The average vesicle count/tomogram in the first row around the ribbon (\leq 80 nm distance from the SV membrane to ribbon surface) was

comparable between inhibitory and stimulatory conditions of wild-type (Fig. 3.7B, D, H, I) and between inhibitory and stimulatory conditions of *Otof^{Pga/Pga}* ribbon synapses (Fig. 3.7C, E, H, I) (for values refer to Table 3.5A). Interestingly, under inhibition of *Otof^{Pga/Pga}* ribbon synapses significantly more vesicles resided in the distal (Fig. 3.7H) and the proximal (Fig. 3.7I) ribbon parts compared to wild-type inhibitory condition (Fig. 3.7F, G). Moreover, I also observed that the SVs around the ribbon were more densely packed without fusing with one another in *Otof^{Pga/Pga}* IHCs irrespective of the activity state (Fig. 3.7C, E).

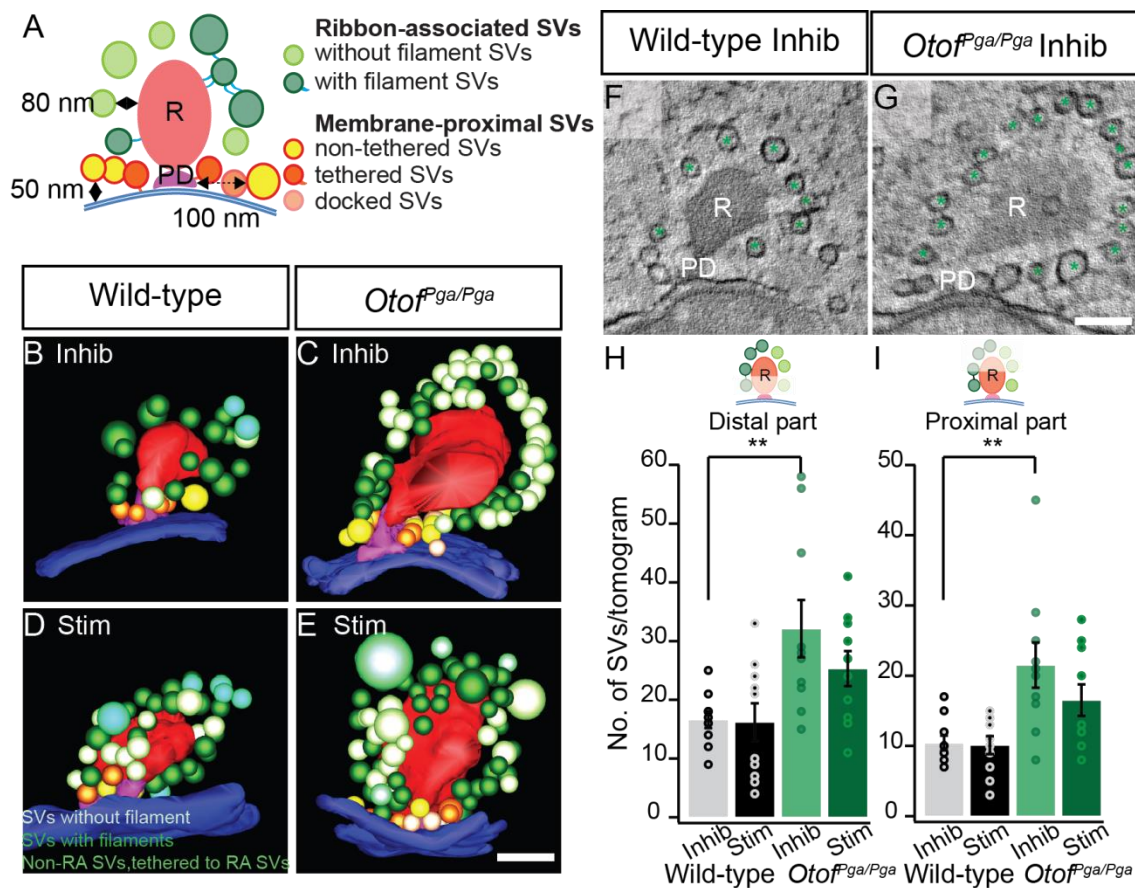


Figure 3.7: The number of RA SVs increased at the distal and the proximal ribbon part at the *Otof^{Pga/Pga}* inhibitory condition

(A) The illustration is summarizing the tomogram analysis, not drawn to scale. Vesicles are assigned to the following pools: RA and MP SVs according to parameters described in Fig. 2.7 panel B. The vesicles in each pool are color-coded according to the inset legend.

(B-E) 3-D reconstructions from tomograms in wild-type (B, C) and *Otof^{Pga/Pga}* (D, E), for both conditions (inhibitory (B, C); stimulatory (D, E)). Color-coded is similar to the illustration (also see Fig.2.7 panel B). For clarity, filaments are not depicted. Scale bar, 100 nm.

(F-G) Representative virtual sections of wild-type and *Otof^{Pga/Pga}* under the inhibitory condition. Counted RA SVs are marked with green asterisks. Scale bar, 100 nm; magnification, 12,000x.

(H-I) The average number of SVs per tomogram remains comparable between stimulatory and inhibitory conditions of wild-type and *Otof*^{Pga/Pga} for the distal **(H)** and the proximal **(I)** part of the ribbon. Significantly more SVs are observed at inhibited *Otof*^{Pga/Pga} compared to inhibited wild-type ribbon synapses, at both parts of the ribbon. Data are represented in mean \pm SEM. P-values are calculated by one way ANOVA followed by Tukey's test, n = 10 tomograms for each genotype and condition,** p < 0.01.

3.2.4 Pleomorphic vesicles cluster were present in *Otof*^{Pga/Pga} IHCs

Strikingly, in all analyzed *Otof*^{Pga/Pga} IHCs, clear core pleomorphic vesicle clusters were observed in the cytoplasm (Fig. 3.8). In the inhibitory condition of *Otof*^{Pga/Pga}, these vesicle clusters were found adjacent to synaptic ribbons (24 ± 4.3 nm, the distance measured between the outer edge of the cluster to the ribbon surface). This phenomenon was observed in six out of 13 tomograms obtained from inhibited *Otof*^{Pga/Pga} IHCs. Three tomograms with these clusters qualified our quality control of intact membrane and properly anchored ribbons and were analyzed further. Each analyzed cluster contained hundreds of vesicles (210 – 332, average: 285 ± 38 vesicles), densely packed in the tomogram volume ($0.035 - 0.053 \mu\text{m}^3$, average of $0.0451 \pm 0.005 \mu\text{m}^3$). In inhibitory conditions, vesicles from a cluster often intermixed with the RA pool (Fig. 3.8G, H). An average of 55.2 ± 3.4 % of RA vesicles also belonged to a pleomorphic vesicle cluster at the affected ribbon synapse (n = 3 tomograms).

I resorted to vesicle size as a parameter to distinguish the pleomorphic vesicles from SVs as the nature of such vesicles is still unknown. A pleomorphic cluster comprised of vesicles of variable diameters. Moreover, the average diameter of vesicles in these clusters were significantly bigger than the RA SVs (*Otof*^{Pga/Pga} inhibitory condition: pleomorphic vesicle diameter in the cluster: 40.4 – 153.5 nm, average of 57.2 ± 0.4 nm, n = 3 tomogram, *Otof*^{Pga/Pga} RA SV diameter: 37.5 - 82.2 nm, average of 52.2 ± 0.6 nm, n = 10 tomograms). For a detailed analysis, one cluster was selected randomly from *Otof*^{Pga/Pga} stimulatory and inhibitory conditions. In stimulated IHCs of *Otof*^{Pga/Pga} such a cytoplasmic cluster consisted of larger vesicles than those found in *Otof*^{Pga/Pga} inhibitory conditions, adjacent to the synaptic ribbon (Fig. 3.8 K', *Otof*^{Pga/Pga} inhibitory = 58.0 ± 0.5 nm, n = 332 pleomorphic vesicles in a cluster from one tomogram and *Otof*^{Pga/Pga} stimulatory = 66.3 ± 1.4 nm, 161 pleomorphic vesicles in a cluster from one tomogram) (Fig. 3.8 K). Interestingly, I never encountered such vesicle clusters in wild-type IHCs, but similar structures were also observed in the cytosol of *Otof* KOs by Carolin Wichmann (Fig. 3.8J), though less frequent than in *Otof*^{Pga/Pga} IHCs. Previously, similar compartments were already reported using conventional embedding in mutants for the tryptophan-rich basic protein (Wrb), which is part of the targeting pathways of C-tail anchored protein (TRC40 pathway) (Vogl et al., 2016).

Therefore, here I conclude that these pleomorphic vesicles are bigger than the SVs of IHCs. However, the molecular nature of these vesicles is still unknown, but they did not structurally resemble bulk endocytic events observed in stimulated wild-type tomograms (Fig. 3.6I, J).

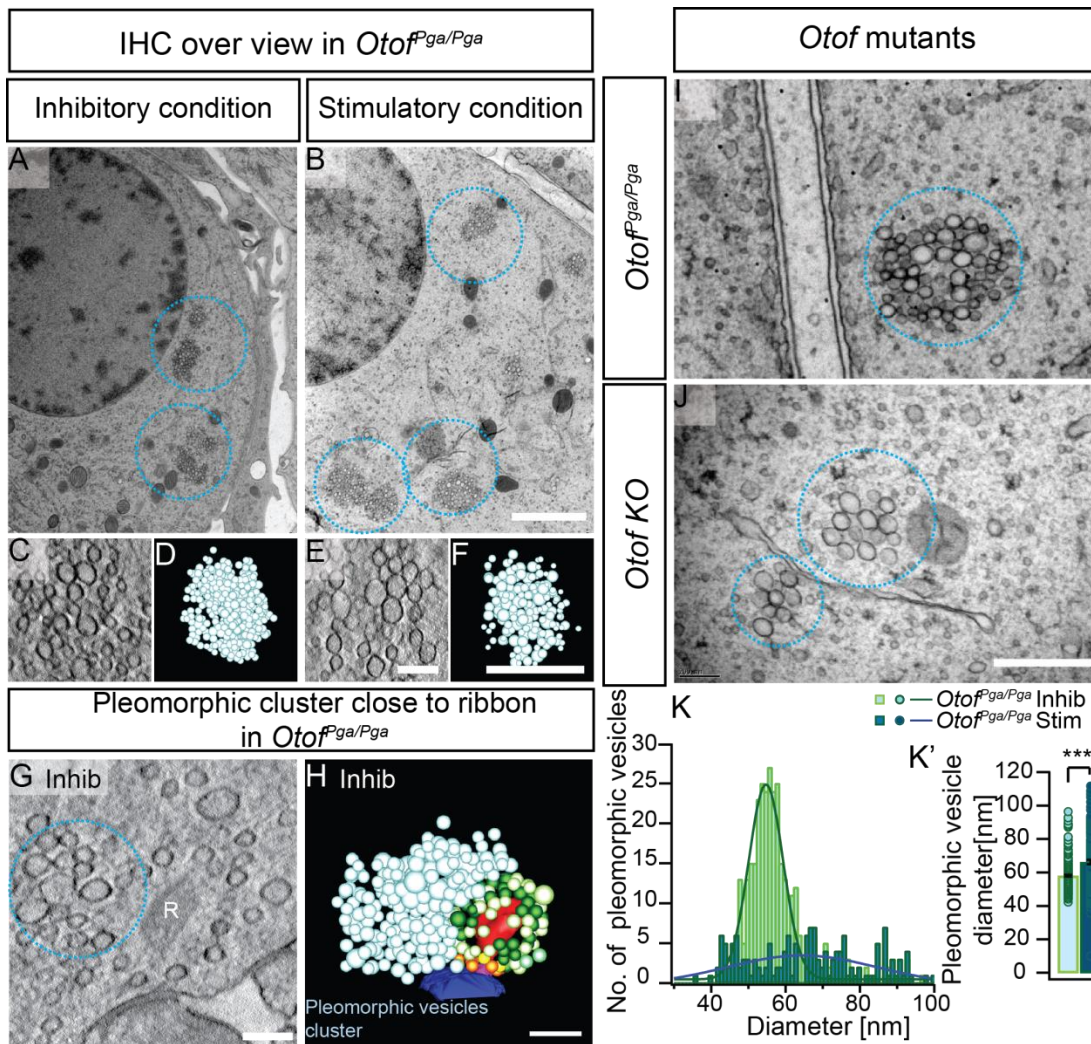


Figure 3.8: Pleomorphic vesicle clusters occur in *Otof*^{Pga/Pga} IHCs

(A-B) Representative electron micrographs with cytosolic pleomorphic vesicle clusters (encircled with blue dotted line) found in IHCs of *Otof*^{Pga/Pga} inhibitory (A) and stimulatory (B) conditions. Scale bar, 1 μ m; magnification, 2,500x.

(C, E) Example tomographic virtual sections: inhibitory (C) and stimulatory (E) condition. Scale bar, 100 nm; magnification, 12,000x.

(D, F) Corresponding 3-D reconstructions: inhibitory (D) and stimulatory (F) conditions, with cytosolic pleomorphic vesicles (light blue) in *Otof*^{Pga/Pga} IHCs. Scale bar, 200 nm.

(G) These cytosolic vesicle clusters (encircled with blue dotted line) are adjacent to synaptic ribbons (R) and overlap with RA SVs in *Otof*^{Pga/Pga} inhibitory samples. Scale bar, 100 nm; magnification, 12,000x.

(H) 3-D reconstruction of the same ribbon synapse showing a pleomorphic vesicle cluster (light blue). Other synaptic compartments are color-coded similar to Fig. 3.7. Scale bar, 100 nm.

(I-J) Electron micrographs are depicting cytosolic pleomorphic vesicle clusters in *Otof^{Pga/Pga}* and *Otof KO* IHCs. J, the image is kindly provided by Carolin Wichmann. Scale bar, 1 μ m; magnification, 5,000x.

(K) Representative vesicle size distribution within a pleomorphic vesicle cluster for an *Otof^{Pga/Pga}* inhibitory (closer to the ribbon) and a stimulatory pleomorphic vesicle cluster (away from the ribbon) (n = 1 tomogram for each condition). The data are fitted with a Gaussian fit (green for inhibitory and blue for stimulatory).

(K') The graph is representing the average diameter of pleomorphic vesicles within a cluster in *Otof^{Pga/Pga}* IHCs. The pleomorphic vesicles under stimulatory conditions are observed in the cytoplasm away from the ribbon. These pleomorphic vesicles are significantly bigger than the pleomorphic vesicles belonging to a typical cluster selected from an *Otof^{Pga/Pga}* inhibitory IHC (closer to the ribbon). Data are represented in mean \pm SEM. P-value is calculated by two-tailed Wilcoxon-rank-sum test, *Otof^{Pga/Pga}* inhibitory, n = 332 pleomorphic vesicles and *Otof^{Pga/Pga}* stimulatory, n = 161 pleomorphic vesicles, ** p < 0.01.

3.2.5 Investigation and filament classification of the RA pool at IHC ribbon synapses

Previously, it has been shown that an elaborate organization of proteinaceous tethers and inter-connectors exists associated with SVs in the presynaptic terminal of mice excitatory synapse between parallel fibers and Purkinje cells (Landis et al., 1988), rat hippocampal neurons (Siksou et al., 2007), cerebrocortical synaptosomes (Fernández-Busnadiego et al., 2010) and at the neuromuscular junction (NMJ) of *C. elegans* (Stigloher et al., 2011) and zebrafish (Helmprobst et al., 2015). The structure of such filaments has been associated with three major functions at the synapses (i) organization of SVs in the presynaptic terminal, (ii) transport of SVs to the AZ membrane and (iii) linking of SVs to the AZ, allowing spatial coupling to the AZ membrane prior docking (Cole et al., 2016; Fernández-Busnadiego et al., 2010, 2013; Helmprobst et al., 2015; Hirokawa et al., 1989; Landis et al., 1988; Siksou et al., 2007; Stigloher et al., 2011).

In this study, a “similar” filamentous organization of tethers and inter-connectors (together will be termed as filaments) was observed around the synaptic ribbon with high resolution (at 12,000x magnification, 1 isotropic voxel = 1.188 nm) on incorporating HPF and EM tomography. Additionally, in IHCs SVs tethered to the AZ membrane were reported previously (Frank et al., 2010; Jung et al., 2015a; Vogl et al., 2015). However, the filaments around IHC synaptic ribbons were not described in detail so far. Such filaments might represent a fundamental mechanism ensuring the reliable resupply of SVs for the high vesicle turnover at IHC ribbon synapses. Therefore, I systematically analyzed the morphometry of filaments in the RA vesicle pool in inhibitory and stimulatory conditions of wild-type and *Otof^{Pga/Pga}* ribbon synapses.

At wild-type ribbon synapses next to SVs without filaments (wild-type average = 25.5 %, wild-type inhibitory = 28 %, and wild-type stimulatory = 23 %, n = 10 tomogram for each

condition), two major categories of SVs with filaments were encountered. These can be classified strictly based on their localization as (i) ribbon-attached tethers and (ii) ribbon-associated inter-connectors (Fig. 3.9B, C, F and G). Moreover, eight subcategories were identified (Table 3.4 A-H). The complexity of these filaments increases further away from the AZ membrane in the distal part of the ribbon.

	Filament category	Number of filament	Connecting SVs	% in wild-type		
				Inhibitory	Stimulatory	Average
A	Ribbon-attached tethers	1	with ribbon (R)	21	10	15.5
B	Ribbon-associated inter-connectors	1	within SVs	20	15	17.5
C	Ribbon-attached tethers	≥ 2	with R	1	2	1.5
D	Ribbon-associated inter-connectors	≥ 2	within SVs	15	23	19.0
E	Single ribbon-attached tethers + single ribbon-associated inter-connectors	≥ 2	with R + within SVs	12	15	13.5
F	Single ribbon-attached tethers + multiple ribbon-associated inter-connectors	≥ 2	with R + within SVs	2	5	3.5
G	Multiple ribbon-attached tethers + single ribbon-associated inter-connectors	≥ 2	with R + within SVs	1	6	3.5
H	Multiple ribbon-attached tethers + multiple ribbon-associated inter-connectors	≥ 2	with R + within SVs	0	1	0.5

Table 3.4: Eight filament categories are found at wild-type IHC ribbon synapses

Similar filament categories were also observed at *Otof*^{Pga/Pga} ribbon synapses (Fig. 3.9 D, E, H and I), which will be described in comparison to wild-type in the following sections 3.2.6 and 3.2.7.

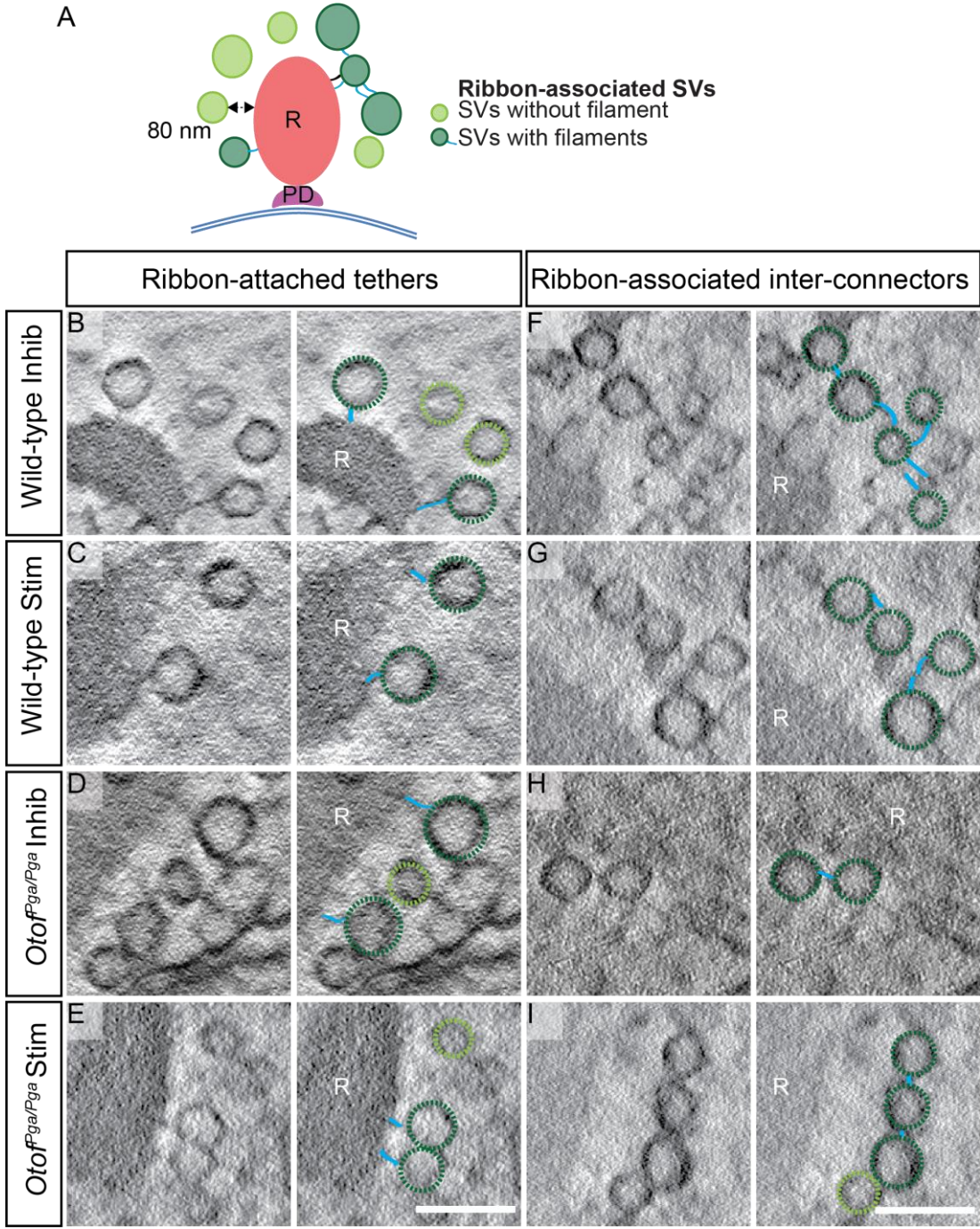


Figure 3.9: Filament organization found around the ribbon at wild-type and *Otof^{Pga/Pga}* ribbon synapses

(A) Illustration of the types of different categories of RA SVs with or without filaments. Color-coded according to Fig. 2.7 panel B.

(B-I) Tomographic virtual sections from wild-type and *Otof*^{Pga/Pga}. Wild-type: Inhibitory (B, F); Stimulatory (C, G); *Otof*^{Pga/Pga}: Inhibitory (D, H); stimulatory (E, I) conditions. Two filament sub-categories are observed around the ribbon, (B-E) ribbon-attached tethers and (F-I) ribbon-associated inter-connectors. These can be single or multiple per SV. Scale bar, 100 nm; magnification, 12,000x. For clarity SVs without (light green dotted circles) and with filaments (SVs: dark green dotted circles, filaments: blue lines) are highlighted.

3.2.6 Comparative analysis of RA filaments at wild-type and *Otof*^{Pga/Pga} ribbon synapses

In this section, I analyzed how the spatial organization and morphology of the different filaments change upon stimulation in wild-type. Further, how these changes translate into replenishment impairment in *Otof*^{Pga/Pga} ribbon synapses were compared.

3.2.6.1 Stimulation increased the number of filaments/SVs in wild-type and *Otof*^{Pga/Pga}

I observed that the number of filaments per SV increased significantly upon stimulation for both wild-type and *Otof*^{Pga/Pga} synapses (Table 3.5B, Fig. 3.10A). To understand whether also the number of vesicles with filaments increased, I pooled all vesicles with filaments from the observed categories of filaments in the RA pool described in Table 3.4. In a 250 nm semithin section used for tomography, not always the complete ribbon, but at least half of it was included (Frank et al., 2010; Jung et al., 2015a). To take this into account, I normalized the vesicle count by calculating the fraction of vesicles with filaments: The number of vesicles with filaments per tomogram was divided by the total number of vesicles in the respective pool per tomogram.

The fraction of SVs with filaments was unaltered between wild-type inhibitory and stimulatory conditions (Fig. 3.10B, Table 3.5C). However, upon stimulation, the fraction of SVs with filaments showed a strong trend towards reduction in *Otof*^{Pga/Pga} compared to wild-type ribbon synapses (Fig. 3.10B, C, D and Table 3.5C). The reduction of SVs with filaments was significantly aggravated in inhibited *Otof*^{Pga/Pga} synapses compared to inhibited wild-type and stimulated *Otof*^{Pga/Pga} ribbon synapses (Fig. 3.10B, Table 3.5C). The statistical tests and the number of ribbons analyzed are mentioned in the legend for Fig. 3.10 and Table 3.5.

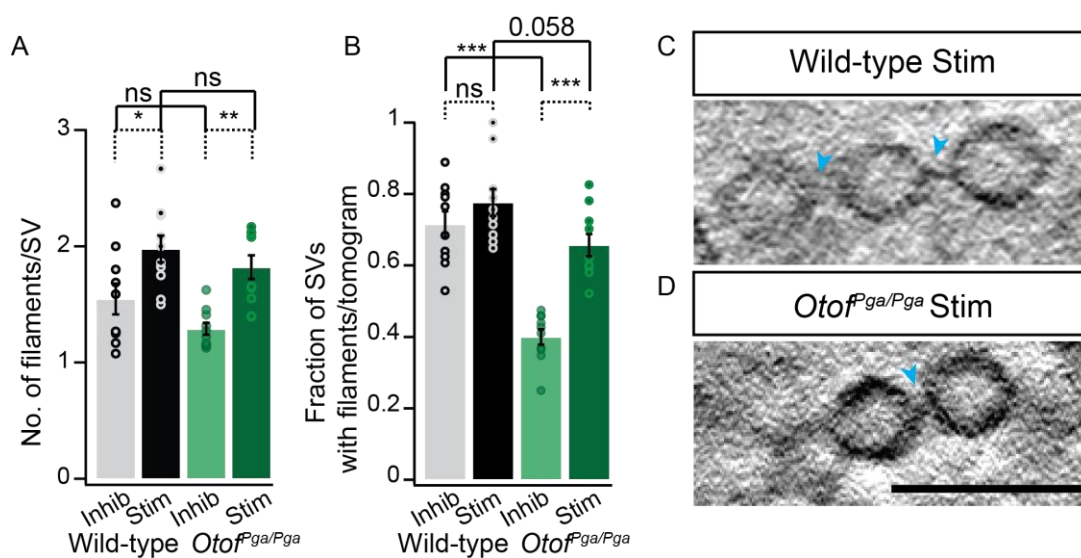


Figure 3.10: The filament number per vesicle increases upon stimulation at IHC ribbon synapses in the RA pool

(A) The number of filaments/SV increases upon stimulation at wild-type and *Otof^{Pga/Pga}* ribbon synapses.

(B) The fraction of SVs with filaments/tomogram is comparable between wild-type inhibitory and stimulatory conditions. Upon stimulation, *Otof^{Pga/Pga}* ribbons show a strong trend towards reduction in the fraction of SV with filament compared to the wild-type stimulatory condition. The reduction in the fraction of SVs with filaments is more pronounced in *Otof^{Pga/Pga}* under inhibition compared to wild-type inhibitory and *Otof^{Pga/Pga}* stimulatory conditions. A-B, data are represented in mean \pm SEM. P-values are calculated by one way ANOVA followed by Tukey's test, $n = 10$ tomograms for each genotype and condition. * $p < 0.05$, ** $p < 0.01$, *** $p < 0.001$, ns $p > 0.05$ and exact p-value is written in case of a trend.

(C-D) Representative virtual sections of stimulatory wild-type (C) and *Otof^{Pga/Pga}* (D) ribbon synapses. Filaments inter-connecting adjacent SVs are highlighted by blue arrowheads. Scale bar, 100 nm; magnification, 12,000x.

In conclusion, during prolonged stimulation the average number of filaments per SV increases at both, wild-type and *Otof^{Pga/Pga}* ribbon synapses. However, at mutant synapses, it seems that fewer SVs with filaments are present.

3.2.6.2 Upon stimulation the number of SVs with multiple-filaments was increased in wild-type but decreased in *Otof^{Pga/Pga}*

For conventional synapses, it was described that the degree of connectivity determined the dynamics and/or stability of the SV organization at the presynaptic terminal (Fernández-Busnadiego et al., 2010; Siksou et al., 2007). Possibly, this might be similar for IHC ribbon synapses in order to sustain exocytosis over a long period. Therefore, I analyzed SVs with single and multiple-filaments separately to account whether the complexity of tethering changes due to an effect of stimulation and/or mutation.

I observed that the fraction of SVs with single filaments was significantly reduced upon stimulation in wild-type compared to the respective inhibitory condition. However, the fraction of SVs with single filaments was comparable between wild-type and *Otof*^{Pga/Pga} stimulated synapses. In *Otof*^{Pga/Pga} inhibitory conditions, the fraction of SVs with single filaments was only slightly reduced (Fig. 3.11A, Table 3.5D). In contrast, the fraction of SVs with multiple-filaments increased significantly upon stimulation in wild-type and *Otof*^{Pga/Pga} compared to their inhibitory conditions. Hereby, at *Otof*^{Pga/Pga} inhibited ribbons, the reduction of SVs with multiple-filaments was more pronounced than at wild-type inhibited synapses (Fig. 3.11B, Table 3.5E). The statistical tests and the number of ribbons analyzed are mentioned in the legend of Fig. 3.11 and Table 3.5.

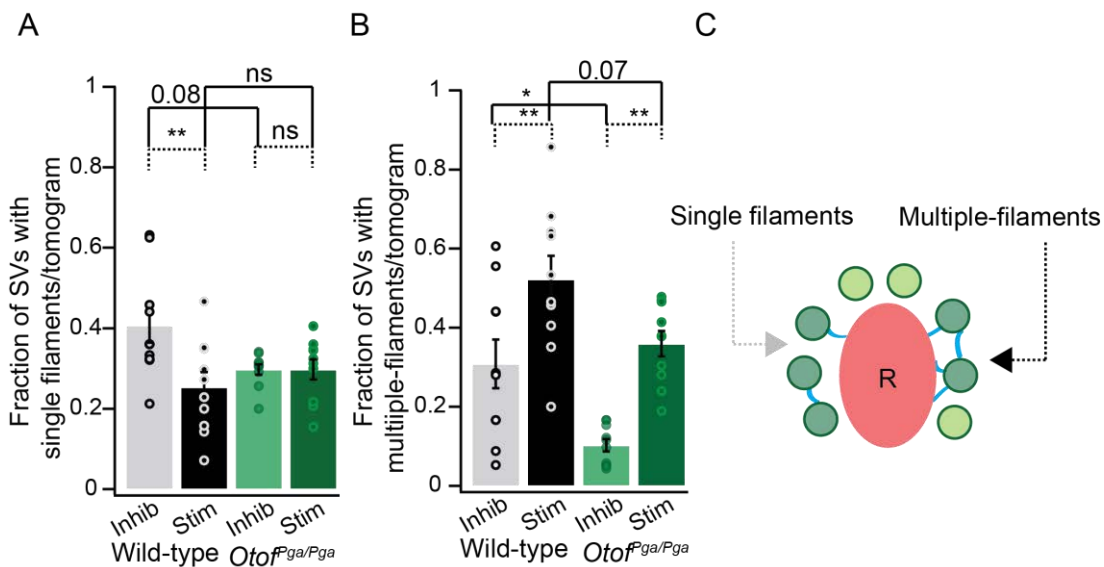


Figure 3.11: Filament complexity increases upon stimulation in the RA pool of IHC ribbon synapses

(A) The fraction of SVs with single filaments is significantly reduced in wild-type upon stimulation compared to wild-type inhibitory conditions but is comparable between wild-type and *Otof*^{Pga/Pga} stimulatory conditions. Wild-type and *Otof*^{Pga/Pga} inhibitory conditions are comparable as well.

(B) The fraction of SVs with multiple-filaments increases significantly upon stimulation in both wild-type and *Otof*^{Pga/Pga} upon stimulation, compared to their respective inhibitory control. Hereby, *Otof*^{Pga/Pga} under stimulatory condition does not reach the wild-type stimulatory level. In the *Otof*^{Pga/Pga} inhibitory condition, the fraction of SVs with multiple-filaments/tomogram is significantly reduced compared to inhibited wild-type.

A-B, data are represented in mean \pm SEM. P-values are calculated by one way ANOVA followed by Tukey's test, n = 10 tomograms for each genotype and condition. * p < 0.05, ** p < 0.01, ns p > 0.05 and exact p-value is written in case of a trend.

(C) Illustration depicting the single (gray arrow) and multiple- (black arrow) filaments in the RA pool, SVs with filaments are depicted in dark green and without filaments in light green. Not drawn to scale.

In short, increased filament connectivity was observed mainly at wild-type IHC ribbon synapses upon stimulation. The increased filament connectivity was modestly reduced in the *Otof*^{Pga/Pga} stimulatory condition. Two functional scenarios might be possible: firstly, this could represent a scaffold around the synaptic ribbon to keep SVs close to cope with the demanding task of sustained release. Secondly, filaments could provide a mechanism for SV transport along the ribbon to the AZ membrane, as it was proposed earlier for photoreceptor ribbon synapses (Bunt, 1971; Gray and Pease, 1971).

Parameter	Condition	Wild-type	<i>Otof</i> ^{Pga/Pga}	p-values
A No. of SVs	Inhibitory	26.40 ± 1.8	53.60 ± 7.6	0.003 §
	Stimulatory	26.30 ± 4.1	41.80 ± 5.0	0.2 §
B No. of filaments/SV	Inhibitory	1.54 ± 0.13	1.30 ± 0.05	0.3 §
	Stimulatory	2.00 ± 0.11	1.82 ± 0.10	0.7 §
C Fraction of SVs with filaments	Inhibitory	0.71 ± 0.04	0.40 ± 0.02	2.30E-07 §
	Stimulatory	0.80 ± 0.04	0.70 ± 0.03	0.058 §
D Fraction of SVs with single filaments	Inhibitory	0.40 ± 0.04	0.30 ± 0.01	0.080§
	Stimulatory	0.25 ± 0.04	0.30 ± 0.04	0.7 §
E Fraction of SVs with multiple-filaments	Inhibitory	0.30 ± 0.06	0.10 ± 0.01	0.017 §
	Stimulatory	0.52 ± 0.06	0.40 ± 0.03	0.070 §

Table 3.5: Fraction of SVs with or without filaments in the RA pool

Data are presented as mean ± SEM. P-values are calculated by one way ANOVA followed by Tukey's test (§) for a parametric multiple comparison reflecting differences between wild-type and *Otof*^{Pga/Pga} under different conditions. Data are acquired from three wild-type mice each for inhibitory as well as for stimulatory conditions and two *Otof*^{Pga/Pga} mice each for inhibitory and stimulatory conditions. Ten tomograms for each genotype and condition are analyzed.

3.2.6.3 Stimulation results in more SVs with multiple-filaments at the distal ribbon part in wild-type

To further narrow down the position of single and multiple-filaments, the distal and the proximal part of the ribbon were analyzed separately (Fig. 3.12) as done earlier for the RA SV counts. At the distal part of the ribbon (away from the AZ membrane), SVs with single filaments were significantly reduced at wild-type ribbons but were unaltered at *Otof*^{Pga/Pga} upon stimulation (Fig. 3.12A, Table 3.6A). In line with this observation, the fraction of SVs with multiple-filaments increased at wild-type and *Otof*^{Pga/Pga} synapses upon stimulation

compared to their respective inhibitory conditions (Fig. 3.12A, Table 3.6B). When comparing the mutant to wild-type, the fraction of SVs with multiple-filaments was significantly reduced at *Otof*^{Pga/Pga} ribbon synapses under both conditions (Fig. 3.12A, Table 3.6B).

In the proximal part of the ribbon (closer to the AZ membrane) no differences were observed, neither for the fraction of SVs with single filaments (Fig. 3.12B, Table 3.6D) nor the fraction of SVs with multiple-filaments (Fig. 3.12B, Table 3.6E). This suggests a role of the distal part of the ribbon in organizing SVs by increasing the number of filaments upon stimulation. Whether the increased connectivity is mediating vesicle resupply or even transport cannot be ruled out.

Finally, I examined the distribution of those SVs without filaments. The largest fraction of SVs without filaments was found under inhibited conditions in *Otof*^{Pga/Pga} at both ribbon parts (Fig. 3.12A-B, Table 3.6C, F). This complements my previous observation (section 3.2.3), where more RA SVs accumulate at *Otof*^{Pga/Pga} ribbons under inhibitory conditions. The statistical tests and the number of ribbons analyzed are mentioned in the legend of Fig. 3.12 and Table 3.6.

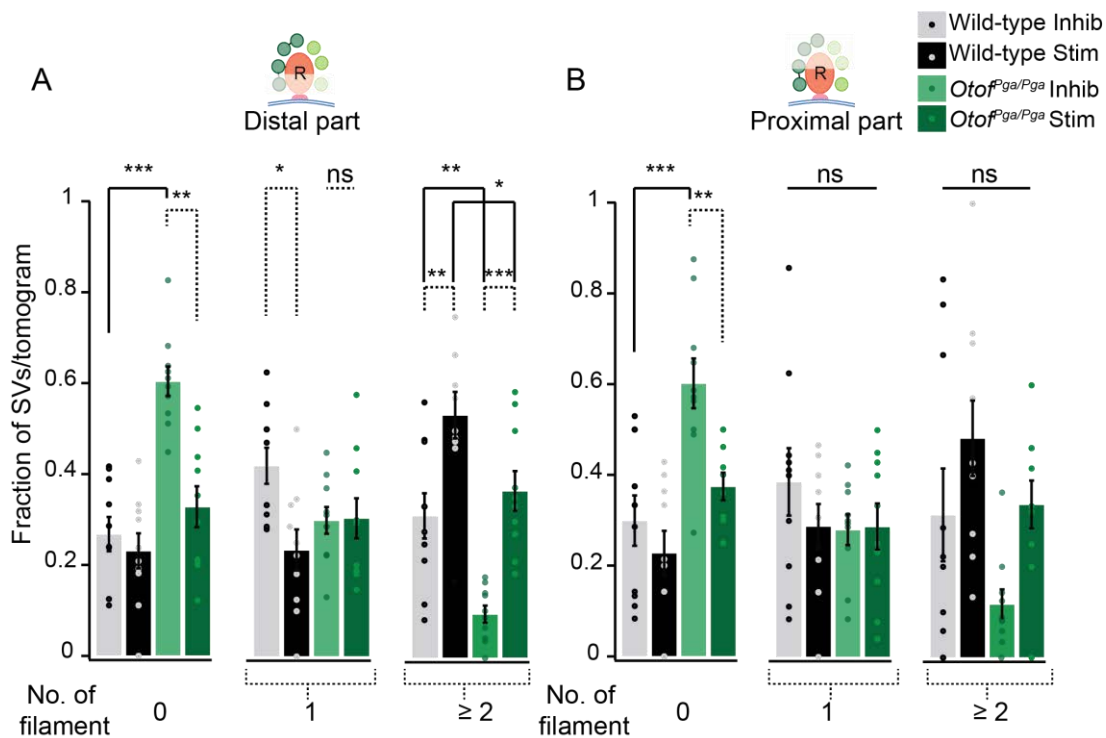


Figure 3.12: The fraction of SVs with multiple-filaments increased in the distal part of the ribbon at wild-type but was reduced at *Otof*^{Pga/Pga} ribbon synapses

(A-B) The graph is showing the fraction of SVs/tomogram in the distal (A) and the proximal (B) part of the ribbon. Filaments are classified as single and multiple-filaments. Data are represented as mean \pm SEM.

(A) The fraction of SVs with single filaments/tomogram is significantly reduced in the distal part upon stimulation at wild-type ribbon synapses but is unaltered for all conditions in the (B) proximal part. The fraction of SVs with multiple-filaments/tomogram is significantly increased upon stimulation in wild-type and *Otof^{Pga/Pga}* IHCs, but *Otof^{Pga/Pga}* does not reach the wild-type level. P-values are calculated by one way ANOVA followed by Tukey's test, n = 10 tomograms for each genotype and condition. * p < 0.05, ** p < 0.01, *** p < 0.001 and ns p > 0.05.

	Parameter	Condition	Wild-type	<i>Otof^{Pga/Pga}</i>	p-values
Distal part of the ribbon	A	Inhibitory	0.42 ± 0.04	0.30 ± 0.03	0.1 §
		Stimulatory	0.23 ± 0.05	0.30 ± 0.04	0.6 §
	B	Inhibitory	0.31 ± 0.05	0.10 ± 0.02	0.005 §
		Stimulatory	0.53 ± 0.05	0.40 ± 0.05	0.044 §
	C	Inhibitory	0.30 ± 0.04	0.60 ± 0.03	0.0004 §
		Stimulatory	0.23 ± 0.04	0.33 ± 0.05	0.1 §
Proximal part of the ribbon	D	Inhibitory	0.40 ± 0.07	0.30 ± 0.03	0.5 §
		Stimulatory	0.30 ± 0.05	0.30 ± 0.05	1 §
	E	Inhibitory	0.31 ± 0.10	0.12 ± 0.03	0.2 §
		Stimulatory	0.50 ± 0.08	0.34 ± 0.05	0.5 §
	F	Inhibitory	0.30 ± 0.05	0.60 ± 0.05	2.77E-06 §
		Stimulatory	0.23 ± 0.05	0.40 ± 0.03	0.3 §

Table 3.6: Fraction of SVs in the distal and proximal half of the ribbon

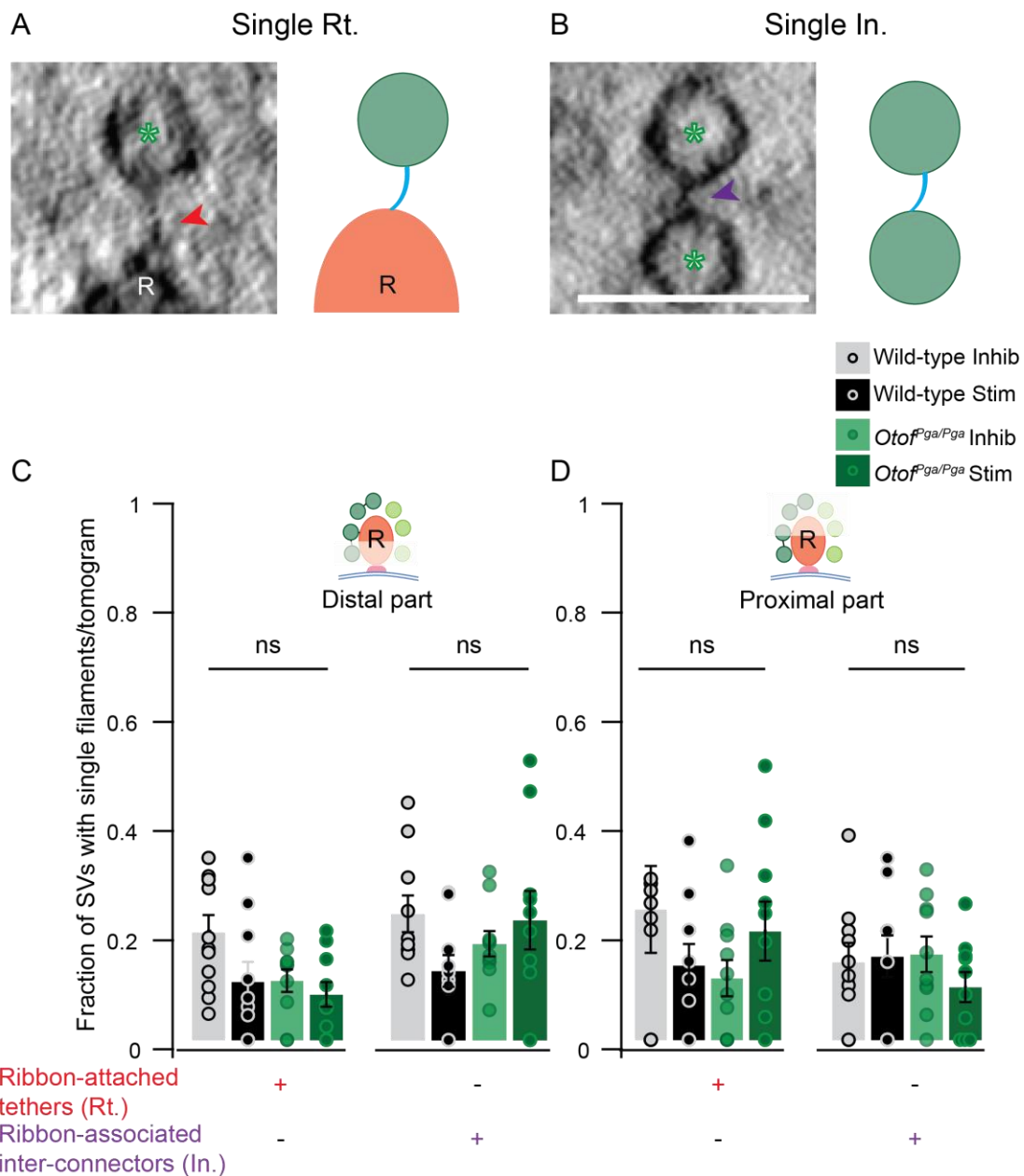
P-values are calculated by one way ANOVA followed by Tukey's test (§) for a parametric multiple comparison reflecting differences between wild-type and *Otof^{Pga/Pga}* under different conditions. Data are acquired from three wild-type mice each for inhibitory as well as for stimulatory conditions and two *Otof^{Pga/Pga}* mice each for inhibitory and stimulatory conditions. Ten tomograms for each genotype and condition were analyzed.

3.2.7 Refinement of the fractions for single and multiple-filaments

Finally, I wanted to understand which filament category (described in section 3.2.5, Table 3.4) was explicitly involved in increasing the filament connectivity during stimulation in wild-type and *Otof^{Pga/Pga}*. Therefore, the fraction of each filament category was analyzed separately (as described in the previous section 3.2.6) in both parts of the ribbon.

First, the fraction of SVs with single ribbon-attached tethers (directly tethered to the ribbon with a single filament, Fig. 3.13A) and the fraction of SVs with single ribbon-associated inter-connectors (interconnected with a single filament, Fig. 3.13B) were analyzed in the distal and the proximal ribbon part in wild-type and the mutant under

inhibition and stimulation. I observed that the fraction of SVs with single ribbon-attached tethers (distal ribbon part, Table 3.7A; proximal ribbon part, Table 3.7F) and single ribbon-associated inter-connectors (distal ribbon part, Table 3.7B; proximal ribbon part, Table 3.7G) were comparable in both genotypes regardless of the state of activity (Fig. 3.13C, D). The statistical tests and the number of ribbons analyzed are mentioned in the legend of Fig.3.13 and Table 3.7.



←

Figure 3.13: Single ribbon-attached tethers and ribbon-associated inter-connectors are unaffected by the activity state or mutation

(A-B) Example virtual sections from the wild-type inhibitory condition showing SVs with single filaments.

(A) SVs with single ribbon-attached tethers (Single Rt.). SVs under this category (with green asterisks) are tethered with one filament (red arrowhead) directly to the synaptic ribbon (R). Scale bar, 100 nm; magnification, 12,000x. Illustration in the right panel depicts the same category of filaments, not drawn to scale.

(B) SVs with a single ribbon-associated inter-connector (Single In.). SVs under this category (green asterisk) are interconnected to the next SV with a single filament (purple arrowhead). Scale bar, 100 nm; magnification, 12,000x. Illustration in the right panel depicts the same category of filaments. Not drawn to scale.

(C-D) The fraction of SVs with single ribbon-attached tethers (Single Rt., +) and the fraction of SV with single ribbon-associated inter-connectors (Single In., +) are unaltered for all genotypes and conditions at the distal **(C)** and the proximal **(D)** ribbon part. Data are represented in mean \pm SEM. P-values are calculated by one way ANOVA followed by Tukey's test, n = 10 tomograms for each genotype and condition; ns p > 0.05.

Next, I investigated the fraction of SVs with multiple ribbon-attached tethers (Fig. 3.14A) and the fraction of SVs with multiple ribbon-associated inter-connectors (Fig. 3.14B, C). These were analyzed in the same way as described above (in distal and proximal ribbon parts). In my tomograms, very rarely multiple ribbon-attached tethers were observed at IHC ribbon synapses and it remained unaltered irrespective of the state of activity of the IHCs or the genotype in both parts of the ribbon (Fig. 3.14E, F; distal ribbon part, Table 3.7C; proximal ribbon part, Table 3.7H). However, in IHCs quite often SVs were arranged around the ribbon with multiple ribbon-associated inter-connectors at both parts of the ribbon (Fig. 3.14B-D). In wild-type upon stimulation, no difference was encountered for the fraction of SVs with multiple ribbon-associated inter-connectors neither at the distal nor the proximal ribbon part (Fig. 3.14E, F; distal ribbon part, Table 3.7D; proximal ribbon part, Table 3.7I). *Otof*^{Pga/Pga} stimulated ribbon synapses maintained a similar fraction of SVs with multiple ribbon-associated inter-connectors at both parts (Fig. 3.14E, F). However, at *Otof*^{Pga/Pga} inhibited ribbon synapses a significant reduction for the fraction of SVs with multiple ribbon-associated inter-connectors was observed. This change was only detectable at the distal part upon comparing wild-type inhibitory and *Otof*^{Pga/Pga} stimulatory conditions (Fig. 3.14E and for distal ribbon part Table 3.7D). In contrast, at the proximal part, the fraction of SVs with multiple ribbon-associated inter-connectors was comparable irrespective of the state of activity of the IHCs or the genotype (Fig. 3.14F and for proximal ribbon part, Table 3.7I).

Furthermore, in the tomograms, I observed that a certain fraction of SVs had both types of filaments i.e. ribbon-attached tethers and ribbon-associated inter-connectors (Fig. 3.14D).

Four combinations were observed for single SVs under this category in terms of the number of the associated filaments. Therefore, for simplicity of the analysis whenever a SV had both filament types, it was scored under one superior category (named both Rt. and In.), irrespective of the number of ribbon-attached tethers or ribbon-associated inter-connectors. Upon stimulation in wild-type the fraction of SVs with both Rt. and In. increased significantly at the distal part of the ribbon compared to wild-type inhibitory conditions (Fig. 3.14E, Table 3.7E), but remained unchanged in the proximal part (Fig. 3.14F, Table 3.7J). In *Otof*^{Pga/Pga} stimulated IHCs, the fraction of SVs with both Rt. and In. was significantly reduced compared to wild-type stimulatory conditions at the distal part (Fig. 3.14E, Table 3.7E). However, in the proximal part of the ribbon no difference was observed (Fig. 3.14F, Table 3.7J). The statistical tests and the number of ribbons analyzed are mentioned in the legend for Fig. 3.14 and Table 3.7.

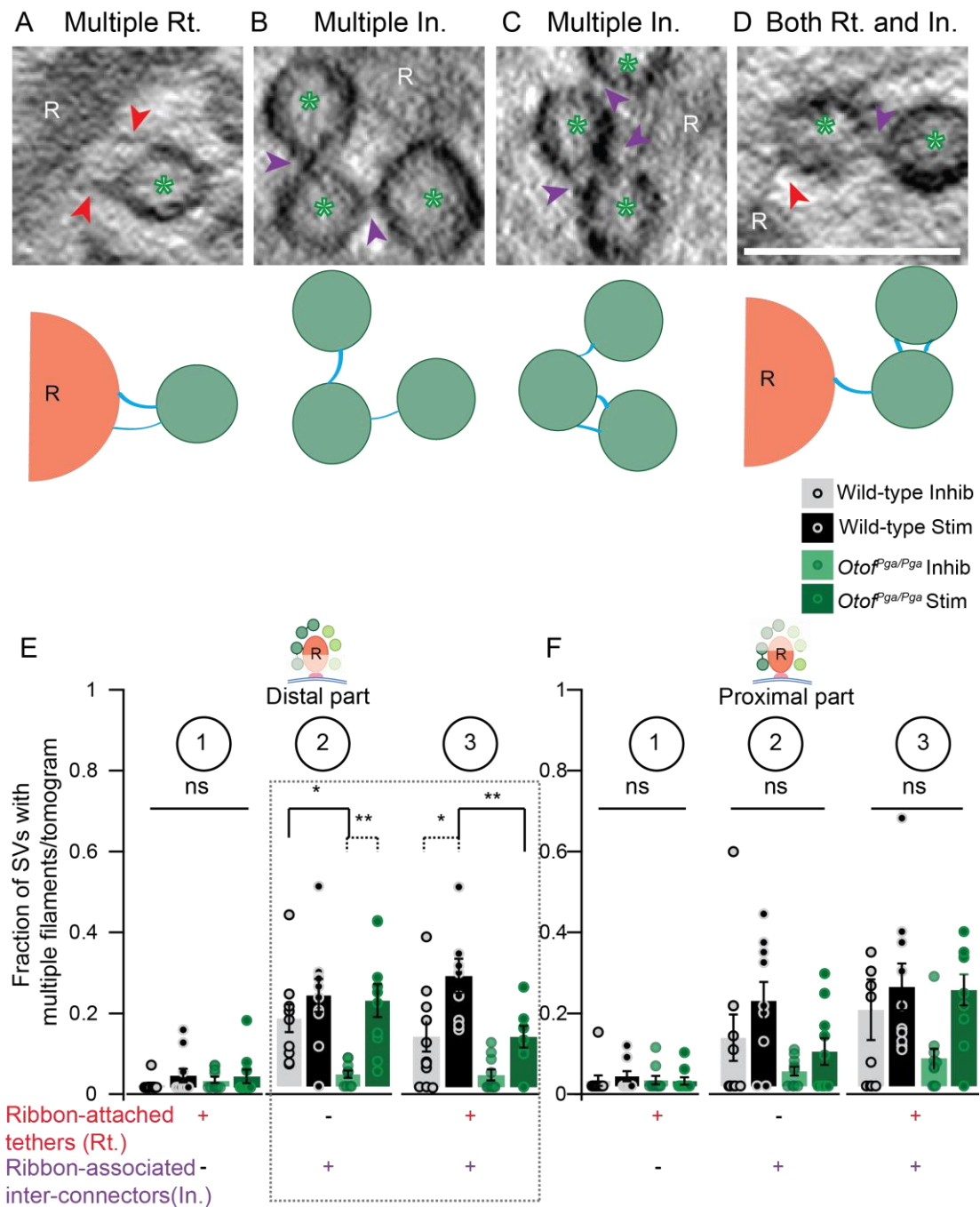


Figure 3.14: Upon stimulation SVs with both ribbon-attached tethers and -associated inter-connectors increase in wild-type but are reduced in *Otof^{Pga/Pga}*
(A-D) Example virtual sections from the wild-type inhibitory condition showing SVs with multiple-filaments.

(A) SVs with more than one ribbon (R)-attached tether (Multiple Rt.; green asterisk with tether highlighted by red arrowheads). Scale bar, 100 nm; magnification, 12,000x. According illustration is shown in the lower panel. Not drawn to scale.

(B-C) SVs with more than one ribbon (R)-associated inter-connector (Multiple In.; green asterisk with tether highlighted by purple arrowheads). Scale bar, 100 nm; magnification, 12,000x. According illustration is shown in the lower panel: dark green SVs and blue filaments. Not drawn to scale.

(D) SVs with both ribbon-attached tethers and ribbon-associated inter-connectors (Both Rt. and In; green asterisk with ribbon-attached tether highlighted by red arrow head and -associated inter-connected to an adjacent SV highlighted by purple arrow head). Scale bar, 100 nm; magnification, 12, 000x. The simplified illustration is shown in the lower panel.

(E1) In the distal part, the fraction of SVs with multiple ribbon-attached tethers (Multiple Rt., red plus) is unaltered for all the genotypes and conditions. **(E2)** The fraction of SVs with multiple ribbon-associated inter-connectors (Multiple In., +) is only reduced at *Otof*^{Pga/Pga} inhibitory compared to wild-type inhibitory as well as *Otof*^{Pga/Pga} stimulatory synapses. **(E3)** The fraction of SVs with both ribbon-attached tethers (+) and - associated inter-connectors (+) (Both Rt. and In. category) increases significantly in the wild-type stimulatory compared to the wild-type inhibitory condition. In stimulated *Otof*^{Pga/Pga} IHCs the fraction is significantly reduced compared to stimulated wild-type IHCs.

(F1) In the proximal part of the ribbon, no changes are observed for multiple Rt. (+), **(F2)** multiple In. (+) and **(F3)** for the both Rt. and In. (both + and +) for all the conditions and genotypes.

For E and F, data are represented as mean ± SEM. E1, F1 p-values are calculated by Kruskal-Wallis followed by NPMC test, n = 10 tomograms for each genotype and conditions. ns p > 0.05. For E2, E3, F2 and F3, p-values are calculated by one way ANOVA followed by Tukey's test, n = 10 tomograms for each genotype and condition; ns p > 0.05, * p < 0.05 and ** p < 0.01.

In conclusion, at wild-type ribbon synapses the number of multiple-filaments elevated at the distal part of the ribbon upon stimulation, hereby especially the category of vesicles that are tethered to the ribbon and also connect to another vesicle was affected. This arrangement was reduced in *Otof*^{Pga/Pga} stimulated ribbon synapses, probably reflecting a replenishment deficit.

	Parameter	Condition	Wild-type	<i>Otof</i> ^{Pga/Pga}	p-values
Distal part of the ribbon	A Fraction of SVs with single ribbon-attached tethers	Inhibitory	0.20 ± 0.02	0.10 ± 0.02	0.1 §
		Stimulatory	0.10 ± 0.04	0.08 ± 0.02	0.9 §
	B Fraction of SVs with single ribbon-associated inter-connectors	Inhibitory	0.23 ± 0.03	0.18 ± 0.02	0.7 §
		Stimulatory	0.13 ± 0.03	0.22 ± 0.05	0.3 §
	C Fraction of SVs with multiple ribbon-attached tethers	Inhibitory	0.01 ± 0.01	0.02 ± 0.01	p > 0.05 #
		Stimulatory	0.03 ± 0.02	0.03 ± 0.02	p > 0.05 #
	D Fraction of SVs with multiple ribbon-associated inter-connectors	Inhibitory	0.17 ± 0.03	0.03 ± 0.01	0.03 §
		Stimulatory	0.17 ± 0.03	0.21 ± 0.04	0.1 §
	E Fraction of SVs with both ribbon-attached tethers and ribbon-associated inter-connectors	Inhibitory	0.13 ± 0.04	0.03 ± 0.01	0.2 §
		Stimulatory	0.30 ± 0.04	0.13 ± 0.02	0.01 §

Proximal part of the ribbon	F Fraction of SVs with single ribbon-attached tethers	Inhibitory	0.24 ± 0.08	0.11 ± 0.03	0.8 §
		Stimulatory	0.14 ± 0.04	0.20 ± 0.05	0.4 §
	G Fraction of SVs with single ribbon-associated inter-connectors	Inhibitory	0.14 ± 0.04	0.20 ± 0.03	0.9 §
		Stimulatory	0.15 ± 0.04	0.10 ± 0.03	0.6 §
	H Fraction of SVs with multiple ribbon-attached tethers	Inhibitory	0.01 ± 0.01	0.01 ± 0.01	p > 0.05 #
		Stimulatory	0.02 ± 0.01	0.01 ± 0.01	p > 0.05 #
	I Fraction of SVs with multiple ribbon-associated inter-connectors	Inhibitory	0.12 ± 0.06	0.04 ± 0.01	0.5 §
		Stimulatory	0.21 ± 0.05	0.10 ± 0.03	0.1 §
	J Fraction of SVs with both ribbon-attached tethers and ribbon-associated inter-connectors	Inhibitory	0.19 ± 0.08	0.07 ± 0.03	0.4 §
		Stimulatory	0.25 ± 0.06	0.24 ± 0.04	0.1 §

← **Table 3.7: Fraction of SVs at the distal and the proximal part of IHC ribbon synapses**

Data are represented as mean ± SEM. P-values are calculated by one way ANOVA followed by Tukey’s test (§) for a parametric multiple comparison or by Kruskal-Wallis test followed by NPMC (#) reflecting differences between wild-type and *Otof^{Pga/Pga}* under different conditions. Data are acquired from three wild-type mice each for inhibitory and stimulatory conditions and two *Otof^{Pga/Pga}* mice each for inhibitory and stimulatory conditions. Ten tomograms for each genotype/condition were analyzed.

3.2.8 Unaltered filament length in RA pool upon stimulation

As described in the previous sections (3.2.5 to 3.2.7), I observed that the organization of SVs in the RA pool changed upon stimulation. So far, I concentrated on the occurrence of filaments. In this section, I investigate, whether the filament lengths are affected depending on the activity of the IHCs as well. The length was measured in 3-D in the tomographic stacks of virtual sections as it has been described previously (Jung et al., 2015a; Vogl et al., 2015) (also see section 2.5.3.3 and Fig. 2.8A). In the RA pool of wild-type and *Otof^{Pga/Pga}*, in inhibitory and stimulatory conditions, the length of a single filament was comparable to the lengths of individual filaments from the multiple-filament categories. Moreover, in wild-type and *Otof^{Pga/Pga}* irrespective of the condition, ribbon-attached tethers (combined single and multiple) were longer than the ribbon-associated inter-connectors (combined single and multiple). However, the average length of single ribbon-attached tethers and ribbon-associated inter-connectors was comparable between wild-type and *Otof^{Pga/Pga}*, in both conditions. The statistical tests and the number of ribbons analyzed are mentioned in Table 3.8.

	Filamen length [nm]	Condition	Wild-type	<i>Otof^{Pga/Pga}</i>	p-values
A	Total filament	Inhibitory	23.9 ± 1.4	20.1 ± 0.8	0.09 §
		Stimulatory	21.1 ± 1.2	20.1 ± 1.2	0.9 §
B	Total single filament	Inhibitory	22.3 ± 1.7	21.6 ± 1.4	0.9 §
		Stimulatory	20.0 ± 1.3	21.0 ± 1.4	0.9 §
C	Total multiple-filament	Inhibitory	23.6 ± 1.6	18.1 ± 1.0	0.09 §
		Stimulatory	21.5 ± 1.2	19.2 ± 1.09	0.9 §
D	Single ribbon-attached tether	Inhibitory	25.6 ± 1.8	26.9 ± 1.9	0.9 §
		Stimulatory	21.4 ± 1.7	25.3 ± 2.09	0.7 §
E	Single ribbon-associated inter-connector	Inhibitory	16.5 ± 1.6	13.6 ± 0.9	0.9 §
		Stimulatory	18.9 ± 1.6	15.8 ± 1.5	0.8 §

Table 3.8: Filament length in the RA pool

Data are represented as mean ± SEM. P-values are calculated by one way ANOVA followed by Tukey’s test (§) for a parametric multiple comparison reflecting differences between wild-type and *Otof^{Pga/Pga}* under different conditions. Data are acquired from three wild-type mice each for inhibitory and stimulatory conditions and two *Otof^{Pga/Pga}* mice each for inhibitory and stimulatory conditions. Ten tomograms for each genotype and condition are analyzed.

3.2.9 Investigation and tether classification of the MP pool at IHC ribbon synapses

Tethers are present in association with SVs at the AZ membrane of IHC ribbon synapses (Frank et al., 2010; Jung et al., 2015a; Vogl et al., 2015). Such tethers might be involved in recruitment of vesicles and/or assist in SV fusion (Gerber et al., 2008; Verhage and Sørensen, 2008), as previously described for NMJs (Helmprobst et al., 2015; Stigloher et al., 2011), hippocampal neurons (Siksou et al., 2007, 2009), in synaptosomal preparations (Fernández-Busnadiego et al., 2010, 2013), and at ribbon synapses of IHCs (Jung et al., 2015a; Vogl et al., 2015). However, a detailed morphological characterization for IHC ribbon synapse tethers at the membrane is still missing. In order to test if tethers at the AZ membrane are involved in SV recruitment prior release, as proposed earlier (Fernández-Busnadiego et al., 2013; Stigloher et al., 2011), the MP vesicles were studied after stimulation in wild-type and *Otof^{Pga/Pga}*. MP vesicles were defined as SVs ≤ 50 nm distance between SV-AZ membranes and 100 nm along the membrane at both sides of the presynaptic density. In this pool at wild-type ribbon synapses, mostly single tethers were found: (i) single membrane-attached (Table 3.9A, Fig. 3.15B, C) and single presynaptic density-attached tethers (Table 3.9B, Fig. 3.15F, G, B). Also, (ii) vesicles with multiple-tethers were observed (Table 3.9C, Fig. 3.17A, C, D) that will be described later in section 3.2.11. In contrast to the RA vesicle pool, inter-connectors between adjacent SVs were mainly absent in the MP pool. Further, not all SVs in the MP pool were tethered. Non-tethered (wild-type average = 39 %, wild-type inhibitory = 49% and wild-type stimulatory = 29%, n = 10 tomogram each) as well as morphologically docked vesicles were observed as well (wild-type average = 2%, wild-type inhibitory = 0 % and wild-type stimulatory = 4%, n = 10 tomogram each, Fig. 3.18B-D, will be described later in section 3.2.12). In general, similar tether categories were observed at *Otof^{Pga/Pga}* ribbon synapses (Fig. 3.15 D, E, H and I) and will be described in comparison to wild-type in the coming sections. These observations demonstrate a diversity of MP SVs at IHC ribbon synapses which was not described so far. Whether these morphological sub-pools represent different release competences at the IHC ribbon synapses needs to be determined.

Tether category	Number of tethers	SVs connecting to	% in wild-type		
			Inhibitory	Stimulatory	Average
A Single membrane-attached tethers	1	AZ membrane	34	62	48
B Single presynaptic density tethers	1	presynaptic density	16	5	10
C Multiple-tethers	≥ 2	AZ membrane or presynaptic density or both	2	0	1

Table 3.9: Classification of tethered SV in the MP pool

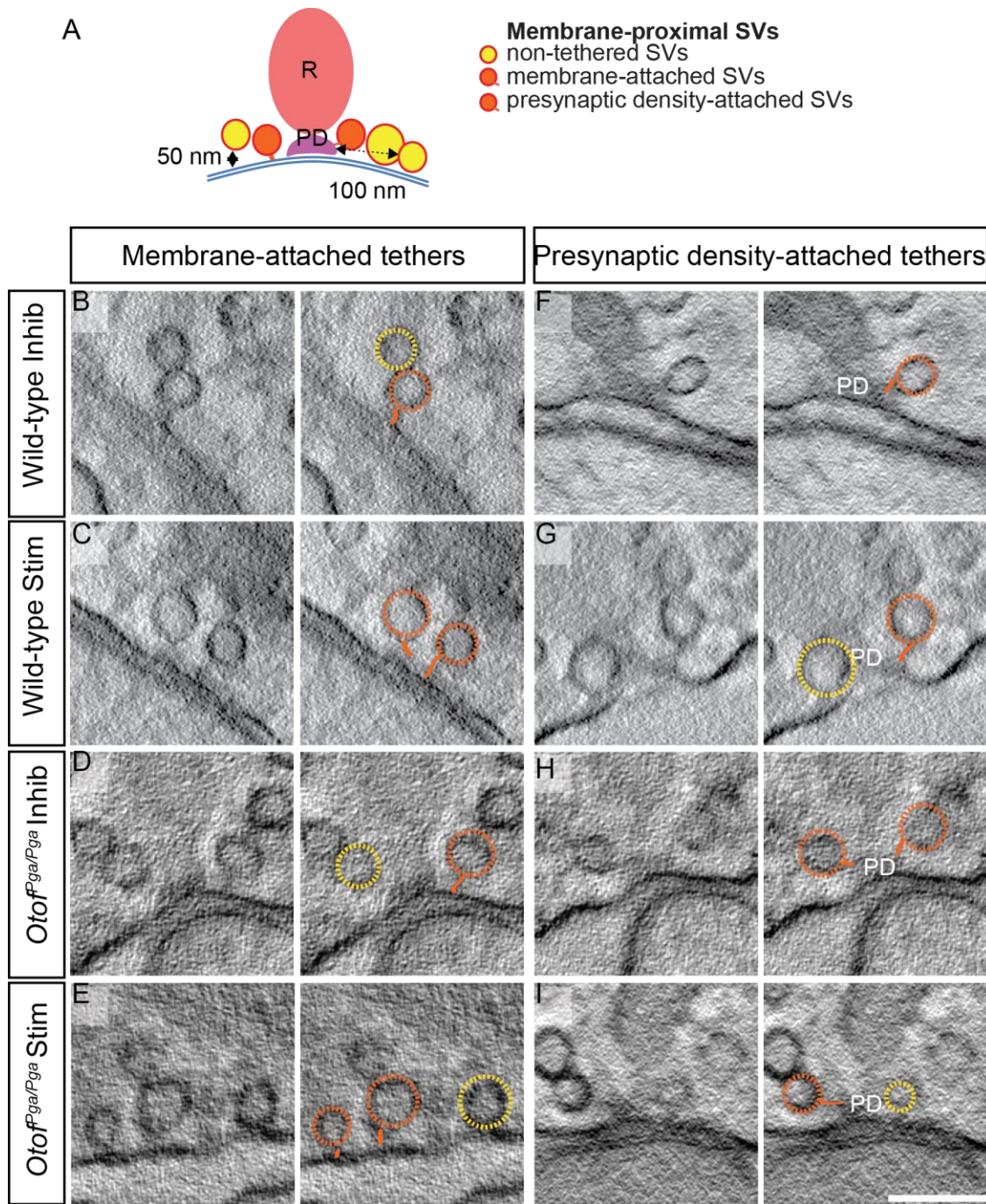


Figure 3.15: Tether categories in the MP pool of wild-type and *Otof^{Pga/Pga}* ribbon synapses
(A) A simplified illustration is depicting SV categories in the MP pool. These vesicles are quantified in accordance with Fig. 2.7 B. The SVs analyzed in the MP pool are mentioned in the inset legend.

(B-I) Representative tomographic virtual sections from wild-type: inhibitory **(B, F)**; stimulatory **(C, G)** and *Otof*^{Pga/Pga}: inhibitory **(D, H)**; stimulatory **(E, I)** conditions. Two major tether categories are observed in the MP pool: **(B-E)** membrane-attached and **(F-I)** presynaptic density-attached tethers. Scale bar, 100 nm; magnification, 12,000x. For clarity, SVs with tethers (orange dotted lines with orange tethers as lines) and without tethers (yellow dotted lines) are highlighted.

3.2.10 Upon stimulation SVs with single membrane-attached tethers increased in wild-type but modestly decreased in *Otof*^{Pga/Pga} IHCs

I calculated the total number of MP vesicles (tethered, non-tethered and docked together) per tomogram in wild-type and *Otof*^{Pga/Pga} in the respective inhibitory and stimulatory condition. I found the count to be comparable between wild-type and *Otof*^{Pga/Pga} for both activity states (Table 3.10A). This was in contrast to findings described in a previous publication where the number of MP SVs was decreased upon stimulation in both wild-type and *Otof*^{Pga/Pga} compared to their inhibitory conditions (Pangrsic et al., 2010). Next, the MP pool was subdivided, and the fractions of non-tethered, tethered and docked SVs were analyzed for each genotype and condition. In wild-type upon stimulation, the fraction of non-tethered vesicles showed a robust trend towards reduction compared to their inhibitory condition (Fig. 3.16A, C and G1, Table 3.10B). However, at *Otof*^{Pga/Pga} ribbon synapses upon stimulation, the fraction of non-tethered SVs was significantly reduced compared to their inhibitory condition (Fig. 3.16B, D, G1 and Table 3.10B).

Subsequently, the fraction of tethered SVs was calculated. As described in the previous section 3.2.9, SVs with single tethers in the MP pool can be either membrane- or presynaptic density-attached (Fig. 3.16E-F). Therefore, I determined the fraction of both sub-pools (Fig. 3.16G2,3 and Table 3.10E, F). In the MP pool, SVs were predominantly membrane-attached via a single tether for both conditions at wild-type as well as *Otof*^{Pga/Pga} ribbon synapses. Upon stimulation, the fraction of SVs with single membrane-attached tethers significantly increased in wild-type compared to the inhibitory condition. For stimulated *Otof*^{Pga/Pga} IHCs, no difference was observed for the single membrane-attached tethers compared to the *Otof*^{Pga/Pga} inhibitory condition, but a reduction (trend) was observed compared to stimulated wild-type (Fig. 3.16G and Table 3.10E). The fraction of SVs with single presynaptic density-attached tethers remained comparable in all conditions and genotypes (Fig. 3.16E and Table 3.10F). The statistical tests and the number of ribbons analyzed are mentioned in the legend of Fig.3.16 and Table 3.10.

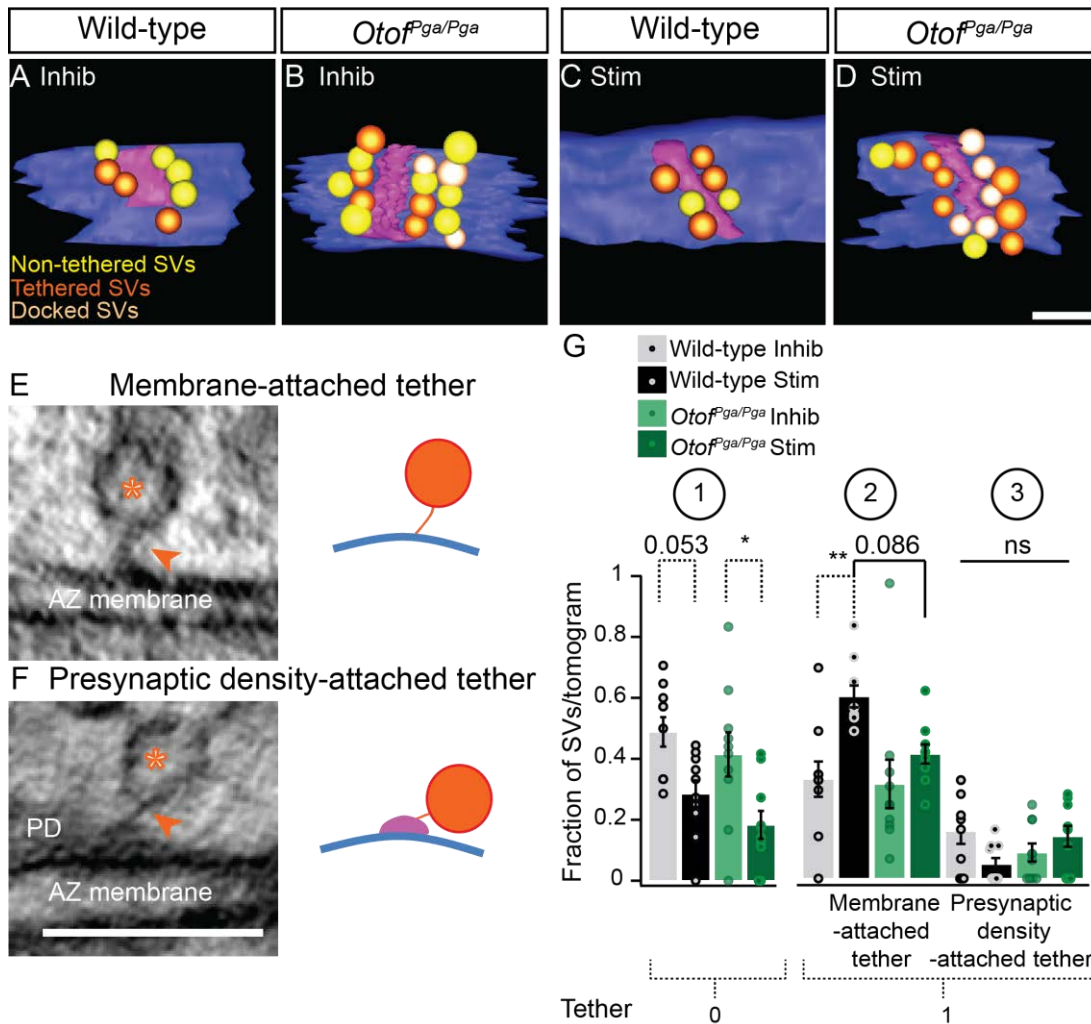


Figure 3.16: Upon stimulation SVs with single membrane-attached tethers increased in wild-type but are reduced slightly at *Otof^{Pga/Pga}* ribbon synapses

(A-D) 3-D reconstructions from tomograms representing the MP pool (top view), for better resolution the synaptic ribbon is not shown in the current tomograms. Color-coded similar to the inset legend in A and quantified according to Fig. 2.7 panel B. Scale bar, 100 nm. The total SV number is unaltered in both genotypes and conditions.

(E, F) Example tomographic virtual sections from the wild-type inhibitory condition: (E) SV (orange asterisk) with a single membrane-attached tether (orange arrowhead). (F) SV (orange asterisk) with a single presynaptic density-attached tether (orange arrowhead). Scale bar, 100 nm; magnification, 12,000x. According illustrations are shown in the right panel; SV (orange), tether (orange line) and AZ membrane (blue). Not drawn to scale.

(G) The graph is representing the fraction of SVs/tomogram: (G1) the fraction of SVs without tethers is reduced in wild-type and *Otof^{Pga/Pga}* stimulatory conditions. (G2) The fraction of SVs with single membrane-attached tethers increase upon stimulation in wild-type but reduced slightly in *Otof^{Pga/Pga}*. (G3) The fraction of SVs with single presynaptic density-attached tethers is comparable in all conditions and genotypes. Data are represented in mean \pm SEM. P-values are calculated by one way ANOVA followed by Tukey's test, $n = 10$ tomograms for each genotype and condition; * $p < 0.05$, ** $p < 0.01$, ns $p > 0.5$.

Parameter	Condition	Wild-type	<i>Otof</i> ^{Pga/Pga}	p-values
A No. of SVs	Inhibitory	10.2 ± 1.6	12.3 ± 1.8	0.7 §
	Stimulatory	9.9 ± 1.1	11.1 ± 0.9	0.9 §
B Fraction of non-tethered SVs	Inhibitory	0.50 ± 0.05	0.41 ± 0.07	0.8 §
	Stimulatory	0.30 ± 0.04	0.02 ± 0.05	0.5 §
C No. of tethers/SV	Inhibitory	1.10 ± 0.07	1.30 ± 0.09	0.060 §
	Stimulatory	1.00 ± 0.00	1.20 ± 0.05	0.2 §
D Fraction of tethered SVs	Inhibitory	0.51 ± 0.05	0.52 ± 0.07	1.0 §
	Stimulatory	0.70 ± 0.04	0.70 ± 0.05	1.0 §
E Fraction of membrane-attached SVs (single tether)	Inhibitory	0.34 ± 0.06	0.32 ± 0.08	1.0 §
	Stimulatory	0.62 ± 0.04	0.42 ± 0.03	0.086 §
F Fraction of presynaptic density-attached SVs (single tether)	Inhibitory	0.20 ± 0.04	0.09 ± 0.03	0.4 §
	Stimulatory	0.05 ± 0.02	0.14 ± 0.04	0.2 §

Table 3.10: Fraction of SVs in the MP pool

Data are represented as mean ± SEM. P values are calculated by one way ANOVA followed by Tukey's test (§) for a parametric multiple comparison reflecting differences between wild-type and *Otof*^{Pga/Pga} under different conditions. Data were acquired from three wild-type mice and two *Otof*^{Pga/Pga} mice each for inhibitory and stimulatory conditions. Ten tomograms for each genotype and condition were analyzed.

3.2.11 The fraction of multiple-tethered SVs was increased at the *Otof*^{Pga/Pga} AZ membrane

In the previous section (3.2.10), I described those SVs which either did not have a tether or were only associated via a single tether in the AZ. Next, I started with the analysis of the fraction of SVs with multiple-tethers in the MP pool of wild-type and *Otof*^{Pga/Pga} ribbon synapses. Rarely, multiple-tethers were captured at wild-type ribbon synapses (wild-type inhibitory = 2/102 SVs; wild-type stimulatory = 0/99 SVs; Fig. 3.17A, B and E). Strikingly, at the *Otof*^{Pga/Pga} ribbon synapses, multiple-tethered SVs were frequent in both conditions (*Otof*^{Pga/Pga} inhibitory = 16/123 SVs; *Otof*^{Pga/Pga} stimulation = 11/111 SVs; Fig. 3.17C, D and E).

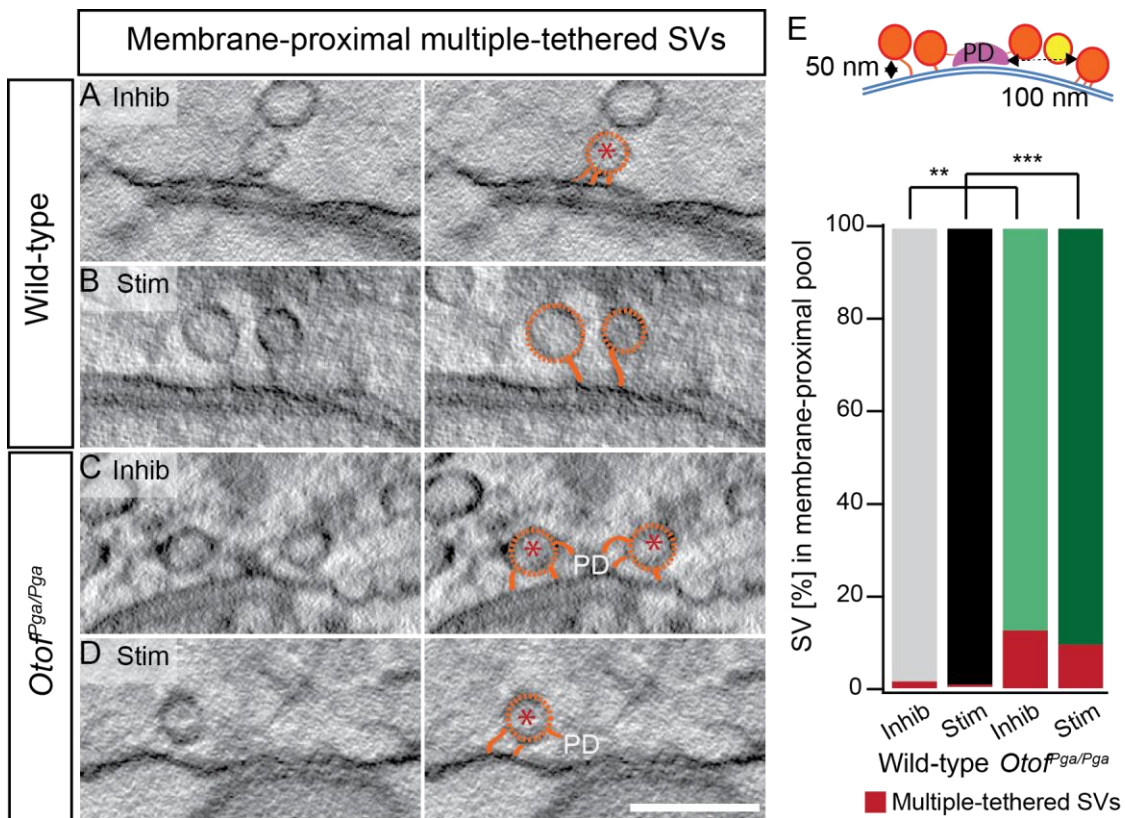


Figure 3.17: Multiple-tethered SVs are increased at *Otof^{Pga/Pga}* ribbon synapses

(A-D) Representative tomographic virtual sections from wild-type: inhibitory (A) and stimulatory (B) as well as *Otof^{Pga/Pga}*: inhibitory (C) and stimulatory (D) conditions. Tethered SVs (A-D) are highlighted in orange with orange tether(s), multiple-tethered SVs (A, C, D) are marked with a red asterisk. Scale bar, 100 nm; magnification, 12,000x.

(E) The graph is representing the percentage of multiple-tethered SVs in the MP pool. Very few multiple-tethered SVs are visible in wild-type under inhibitory conditions (A, E), but none upon stimulation (B, E). A significant increase in multiple-tethered SVs is observed for *Otof^{Pga/Pga}* inhibitory, (C, E) and stimulatory (D, E) conditions. Data are represented in %. P-values are calculated by Fisher's exact chi-square test. Wild-type inhibitory, n = 102 SVs, wild-type stimulatory, n = 99, *Otof^{Pga/Pga}* inhibitory, n = 123 and *Otof^{Pga/Pga}* stimulatory, n = 111 (10 tomograms each); ** p < 0.01 and *** p < 0.001.

Why do multiple tethers accumulate in the mutant? Either multiple tethers close to the AZ membrane are in general a rare event in wild-type or their lifetime is too short to be captured in wild-type upon stimulation, but become visible in the mutants due to its impairment in sustained exocytosis. If the latter would be true, possibly, other release states also accumulate at *Otof^{Pga/Pga}* AZs. To further corroborate this, I analyzed the occurrence of docked vesicles.

3.2.12 The fraction of docked vesicles was increased at *Otof*^{Pga/Pga} AZs

For the analysis of docked vesicles, morphologically docked vesicles were defined according to a former study (0-2 nm from the AZ membrane, Imig et al., 2014, also described in section 2.5.3.4). In wild-type only upon strong stimulation, docked vesicles were observed. In agreement with the hypotheses stated in section 3.2.11, the number of docked SVs was strikingly increased at *Otof*^{Pga/Pga} AZs. In particular upon stimulation docked vesicles accumulate at *Otof*^{Pga/Pga} AZ membranes (wild-type inhibitory = 0/102 SVs, wild-type stimulatory = 4/99 SVs, *Otof*^{Pga/Pga} inhibitory = 8/123 SVs; *Otof*^{Pga/Pga} stimulation = 18/111 SVs; Fig. 3.18 B-D and E). A general feature at IHC ribbon synapses is the fact that MP SVs were mainly aligned closed to the presynaptic density for both wild-type and *Otof*^{Pga/Pga} (Fig. 3.18B-D, also see the 3-D reconstructions in Fig.3.16B,D), similar to previous descriptions via serial 3-D reconstructions and/or tomograms for wild-type ribbon synapses (Frank et al., 2010; Vogl et al., 2015; Wong et al., 2014). This arrangement likely keeps docked SVs in proximity to Ca²⁺ channels (Frank et al., 2010; Wong et al., 2014). Therefore, I first concentrated on docked vesicles that were in a distance of ≤ 100 nm from the presynaptic density (MP pool). Upon closer inspection, some docked SVs were also found further away from the presynaptic density along the membrane (≤ 500 nm, peripheral docked SVs). To understand, where exactly most docked vesicles localize, I measured the distance of each docked SV from the presynaptic density in the MP pool and the peripheral pool (Fig. 3.18G). Interestingly, upon stimulation docked vesicles were found significantly closer to the presynaptic density at the *Otof*^{Pga/Pga} compared to wild-type stimulatory IHCs. In wild-type inhibitory condition docked vesicles were found distant from the presynaptic density, even more than in wild-type stimulatory conditions (wild-type inhibition = 191.4 ± 6.3 nm; wild-type stimulation = 185.6 ± 63 nm, *Otof*^{Pga/Pga} inhibition = 96.1 ± 28.9 nm; *Otof*^{Pga/Pga} stimulation = 46.6 ± 18.8 nm) (Fig. 3.18G). In conclusion, a striking accumulation of docked vesicles was observed in the mutant, those were found in particular close to the presynaptic density.

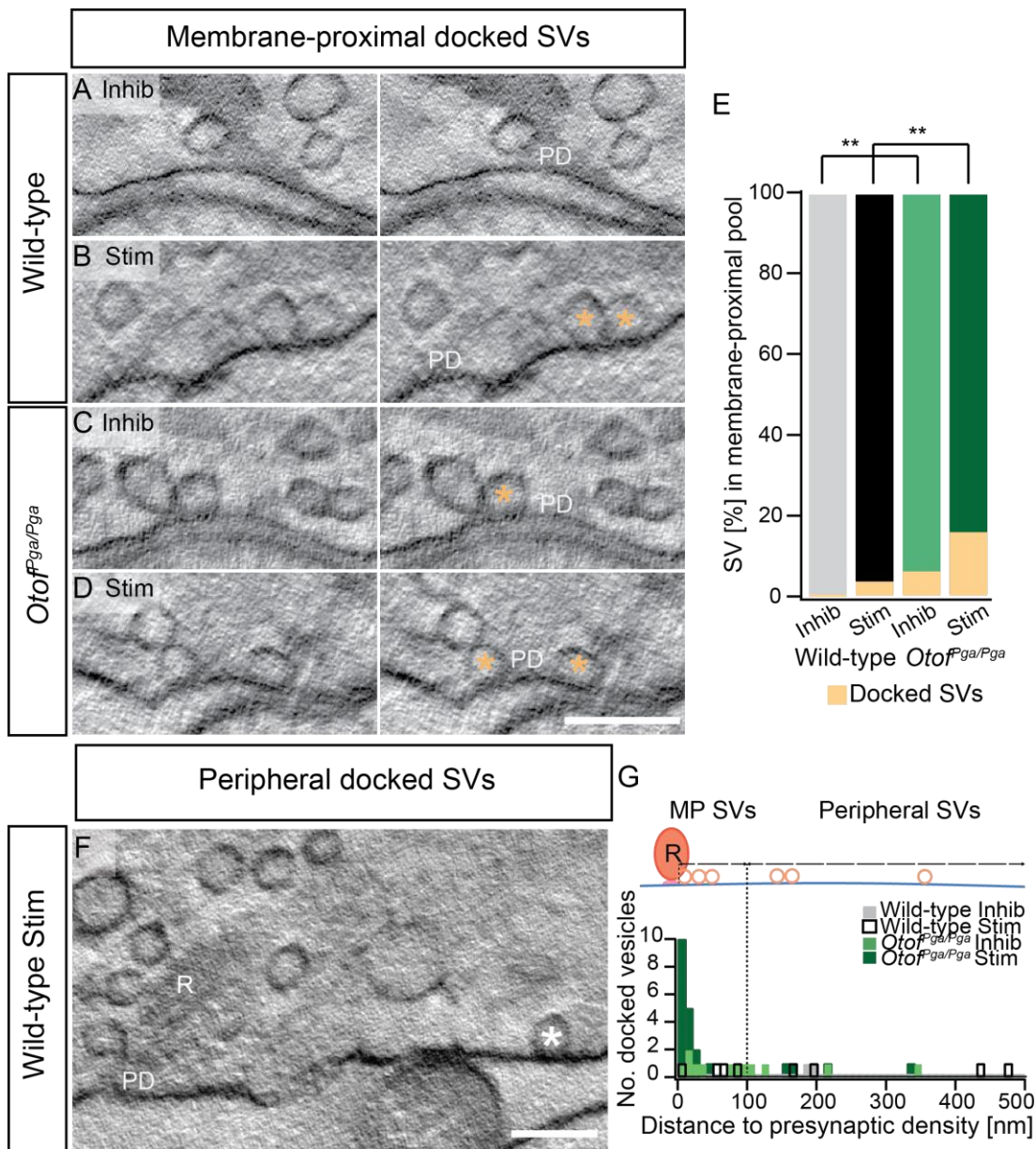


Figure 3.18: Docked SVs accumulate at *Otof^{Pga/Pga}* ribbon synapses

(A-D) Representative tomographic virtual sections from the wild-type inhibitory (A), stimulatory (B) and *Otof^{Pga/Pga}* inhibitory (C), stimulatory (D) conditions. MP, docked SV (B-D) are highlighted with light orange asterisks. Scale bar, 100 nm; magnification, 12,000x.

(E) The graph is representing the percentage of docked SVs in the MP pool. Rarely docked SVs are visible in wild-type under stimulatory conditions but not in the inhibitory condition. A significant increase of docked SVs is observed for the *Otof^{Pga/Pga}* inhibitory and the stimulatory conditions. Data are represented in %. P-values are calculated by Fisher's exact chi-square test. Wild-type inhibitory, n = 102 SVs, wild-type stimulatory, n = 99, *Otof^{Pga/Pga}* inhibitory, n = 123 and *Otof^{Pga/Pga}* stimulatory, n = 111 (10 tomograms each); ** p < 0.01.

(F) The virtual tomographic section from a stimulated wild-type ribbon synapse, showing an example of a peripherally docked SV (white asterisk) 475.5 nm away from the presynaptic density.

(G) Histogram distribution plot is showing the distance of docked SVs from the presynaptic density (0-100 nm: MP pool; 100-500 nm: peripheral SV pool).

3.2.13 Shorter tethers are found at the MP pool of *Otof*^{Pga/Pga} ribbon synapses upon stimulation

In rat cerebrocortical synaptosomes preparations the length of the tethers determines how closely the SVs are aligned to the AZ membrane (Fernández-Busnadiego et al., 2010). The authors showed that SVs were first linked to the AZ membrane via a single long tether and after that multiple short tethers are formed before docking (Fernández-Busnadiego et al., 2013). Therefore, I wanted to test if the tether length alters depending on the activity of the ribbon synapses and if the different filament categories differ in length. Tether lengths were measured as described in sections 3.2.8 and 2.5.3.3 (Fig 3.19C, Jung et al., 2015a; Vogl et al., 2015). I could not observe any difference in tether length in the MP pool of wild-type stimulatory compared to wild-type inhibitory conditions. Interestingly, at stimulated *Otof*^{Pga/Pga} ribbon synapses the tether length was significantly shorter compared to stimulated wild-type ribbon synapses (Fig. 3.19A, Table 3.11A). Further, tether length of single membrane- and presynaptic density-attached tethers were measured (Fig. 3.19B). Both categories of tethers were also shorter at stimulated *Otof*^{Pga/Pga} compared to stimulated wild-type ribbon synapses (Fig. 3.19B, Table 3.11D, E). However, the multiple-tether length remained comparable for both genotypes and conditions (Fig. 3.19B, Table 3.11C). Therefore, the reduced overall tether length in *Otof*^{Pga/Pga} was a result of shorter single membrane- and presynaptic density-attached tethers.

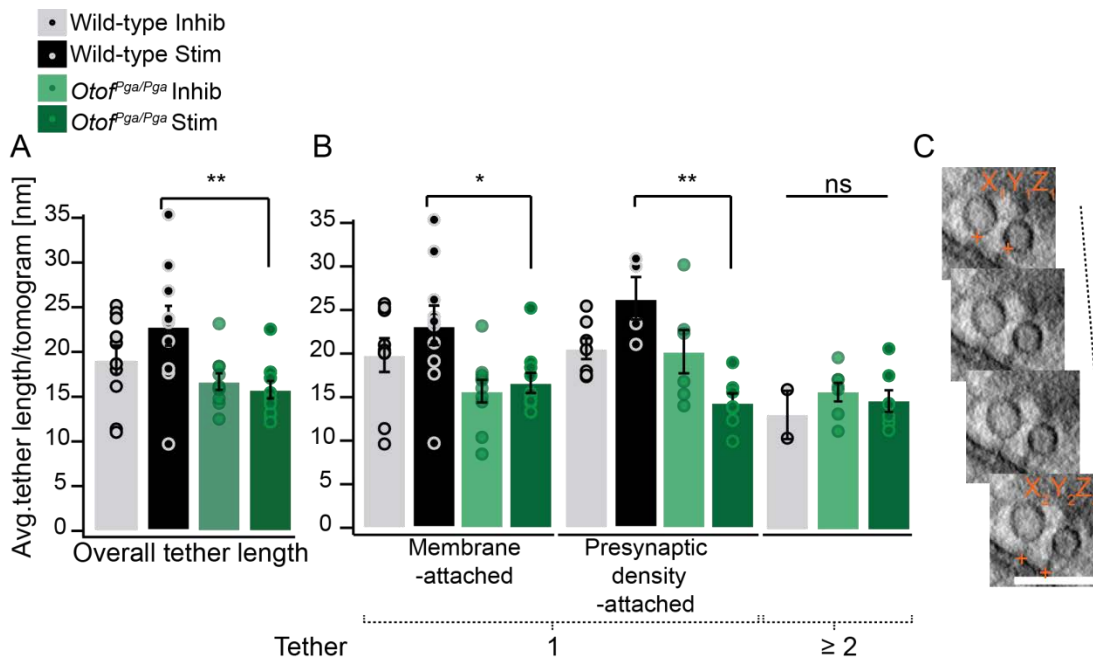


Figure 3.19: Shorter tethers are observed in the MP pool of *Otof*^{Pga/Pga} ribbon synapses

(A) Significantly shorter tethers are present at *Otof*^{Pga/Pga} compared to wild-type ribbon synapses upon stimulation.

(B) Single membrane-attached, as well as presynaptic density-attached tethers, are significantly shorter in *Otof*^{Pga/Pga} compared to wild-type upon stimulation, but the lengths of multiple-tethers are unaltered. Data are represented in mean \pm SEM. P-values are calculated by one way ANOVA followed by Tukey's test, $n = 10$ tomograms each genotype and condition; ns $p > 0.5$, * $p < 0.05$, ** $p < 0.01$.

(C) Shown are four exemplary consecutive virtual tomographic sections of the wild-type stimulatory condition depicting two membrane-tethered synaptic vesicles. The tethers are tracked from coordinates (orange cross), X_1, Y_1, Z_1 to X_2, Y_2, Z_2 for the length measurements. Scale bar, 100 nm; magnification, 12,000x.

	Tether length [nm]	Condition	Wild-type	<i>Otof</i> ^{Pga/Pga}	p-values
A	Total tether	Inhibitory	19.1 \pm 1.6	16.7 \pm 0.9	0.6 §
		Stimulatory	22.9 \pm 2.3	15.8 \pm 1.0	0.01 §
B	Total single tether	Inhibitory	19.9 \pm 1.6	17.0 \pm 0.8	0.7 §
		Stimulatory	22.9 \pm 2.1	16.3 \pm 1.2	0.02 §
C	Total multiple tether	Inhibitory	13.0 \pm 2.8	15.6 \pm 1.0	0.9§
		Stimulatory	NIL	14.5 \pm 1.2	--
D	Single membrane-attached tether	Inhibitory	19.8 \pm 1.9	15.7 \pm 1.3	0.3§
		Stimulatory	23.2 \pm 2.3	16.6 \pm 1.1	0.04§
E	Single presynaptic density-attached	Inhibitory	20.6 \pm 1.2	20.2 \pm 2.5	$p > 0.05$ #
		Stimulatory	26.3 \pm 2.4	14.4 \pm 1.0	$p < 0.01$ #

← **Table 3.11: Analyzed tether lengths in the MP pool**

Data are represented as mean \pm SEM. P-values are calculated by one way ANOVA followed by Tukey's test (*) or Kruskal-Wallis test followed by NPMC test (#) differences between wild-type and *Otof^{Pga/Pga}* under different conditions. Data are acquired from three wild-type mice each for inhibitory and stimulatory conditions and two *Otof^{Pga/Pga}* mice each for inhibitory and stimulatory conditions. Ten tomograms for each genotype and condition are analyzed.

3.2.14 Summary

In section 3.2, a detailed investigation of SV localization and tethering at IHC ribbon synapses was performed for wild-type and *Otof^{Pga/Pga}* mice (characterized previously in Pangrsic et al., 2010; Schwander et al., 2007). It has been proposed that SV replenishment of the RRP be disrupted in the *Otof^{Pga/Pga}* mice (Pangrsic et al., 2010), therefore served as an excellent model to study the sustained phase of exocytosis. Furthermore, HPF/FS provided a faithful correlation of synaptic ultrastructure and function of IHCs in wild-type and *Otof^{Pga/Pga}* mice. I observed the existence of sub-pools of SVs in the already defined morphological RA and MP pools (Chapochnikov et al., 2014; Lenzi and von Gersdorff, 2001; Lenzi et al., 1999; Pangrsic et al., 2010; Strenzke et al., 2016) based on the association of filaments and tethers. Namely in the RA pool: ribbon-attached tethers and ribbon-associated inter-connectors (these could be single and multiple); in the MP pool: membrane-attached tethers and presynaptic density attached tethers (mostly single, but also multiple are present). Therefore, it is tempting to speculate that these SVs represent different release states at IHC ribbon synapses. Tethering at the wild-type ribbon appears more complex upon stimulation, especially in the distal ribbon part. This complexity reduced significantly in the *Otof^{Pga/Pga}* mutants. Further, in *Otof^{Pga/Pga}* mice large pleomorphic vesicle clusters with variable sized vesicles were observed in the cytoplasm. These pleomorphic clusters were found in the proximity to synaptic ribbons during inhibition. The size of such vesicles was bigger than the SVs but was not similar to the bulk-endocytic vesicles.

At the MP pool of wild-type IHC ribbon synapses, most of the SVs were linked via single membrane-attached tethers upon stimulation, possibly representing an initial attachment to the AZ membrane, quite similar to conventional synapses (Fernández-Busnadiego et al., 2010; Stigloher et al., 2011). This step seems to be unaffected at the *Otof^{Pga/Pga}* mutants. Rarely, multiple-tethered and morphologically docked SVs were observed in wild-type. However, the presence of such SVs was notably increased at *Otof^{Pga/Pga}* synapses, specifically upon stimulation. Here, the docked SVs appeared to accumulate in proximity to the presynaptic density, where at the base Ca^{2+} channels are clustered at the membrane to ensure a tight Ca^{2+} influx-vesicle coupling (Frank et al., 2010; Jung et al., 2015a; Wong et

al., 2014). I propose that due to impaired sustained vesicle release, intermediate release steps like multiple-tether formation and docking of SVs were captured because of obstruction downstream of SV docking or fusion. As a further consequence, SVs were compactly packed in the RA pool of *Otof*^{Pga/Pga} synapses. In the end, I could not pin down the molecular nature of these tethers with the current experiments. However, otoferlin remains a vital candidate involved in the process of SV tethering (Vogl et al., 2015).

Rab3-interacting molecules 2 α and 2 β promote the abundance of Ca_v1.3 Ca²⁺ channels at hair cell active zones

Sangyong Jung^{a,b,1}, Tomoko Oshima Takago^{a,c,1}, Rituparna Chakrabarti^{c,d,e,2}, Aaron B. Wong (黃沛樂)^{a,c,e,2,3}, Zhizi Jing^{c,e,f}, Gulnara Yamanbaeva^{c,e,f}, Maria Magdalena Picher^{c,e,g}, Sonja M. Wojcik^h, Fabian Göttfert^{c,i}, Friederike Predoehl^g, Katrin Michel^{j,k}, Stefan W. Hell^{b,1}, Susanne Schoch^{j,k}, Nicola Strenzke^{e,f,4}, Carolin Wichmann^{d,e,4}, and Tobias Moser^{a,b,e,g,4}

PMID: 26034270, DOI: 10.1073/pnas.1417207112

The coming section (3.3) is a collaborative study with the groups of Carolin Wichmann, Tobias Moser, Nicola Strenzke, Susanne Schoch and Stefan W. Hell, published in the PNAS PLUS, 2015.

Author's contribution:

S.J. and T.O.T. are the first co-authors. I (R.C.) and A.B.W. are the second co-authors. In this thesis, I will present the electron tomography data solely acquired and analyzed by me. Any other data used here, from the co-authors will be cited as Jung et al., 2015a and the name of the author will be mentioned in due course.

3.3 Analysis of other proteins involved in tethering: RIM2 α is a potential candidate

In the previous section, I showed that in *Otof*^{Pga/Pga} tethering at the distal ribbon part was altered, while it is not clear whether otoferlin directly or indirectly influences tether formation. Since even in *Otof* *KOs* tethers were still present (Vogl et al., 2015), I was interested in elaborating further potential candidates for tether formation at the AZ membrane of IHC ribbon synapses. RIM is a key protein for neurotransmitter release (Wang and Südhof, 2003). It mediates priming of SVs by activating Munc13 for exocytosis (Deng et al., 2011). In post-hearing onset IHCs, RIM1 α is not present (Jung et al., 2015a), whereas, RIM2 α and RIM2 β were shown to be the major RIM isoforms at IHC ribbon synapses (Jung et al., 2015a). Previously, it has been shown using STED microscopy that Ca²⁺ channels cluster in strip-like pattern below the ribbon (P14) (Frank et al., 2010; Jung et al., 2015a; Rutherford, 2015). Furthermore, in *RIM2 α* *KO* IHCs, a reduced immunofluorescence for Ca²⁺ channels was detected (Jung et al., 2015a). Additionally, the depolarization-evoked capacitance (ΔC , a physiological readout for exocytosis) in response to 20 ms stimulation was reduced in *RIM2 α* *KO* mice, as well as the sustained release (Jung et al., 2015a). Although RIM2 α deficient mice had a very mild hearing impairment (Jung et al., 2015a), it served as an important mutant to study the correlation of tether formation to synaptic physiology deficit (specifically SV priming). Previously, RIM1 was shown to be involved in tethering vesicles at the synapses of mice cerebocortical synaptosomal preparations. Using cryo-EM tomography, it was demonstrated, that in *RIM1 α* *KO* synaptosomes the number of tethers per SV was significantly reduced, whereas the tether length was longer at the membrane (Fernández-Busnadiego et al., 2013). Further, RIM2 α is a candidate for linking SVs and Ca²⁺ channels in IHC ribbon synapses (Jung et al., 2015a), important for a nano-domain-like coupling of SVs with the Ca²⁺ channels (Frank et al., 2010; Jung et al., 2015a; Wong et al., 2014). I investigated SV tethering in *RIM2 α* *KO* in comparison with wild-type littermate controls (*RIM2 α* *Con*) at P14-15 IHC ribbon synapses using electron tomography (described in section 2.4.2) after HPF/FS (described in section 2.3.2/2.3.4). Of note, the *RIM2 α* *Cons* and *RIM2 α* *KOs* here are studied under resting conditions (frozen in HEPES-Hanks' balanced salt solution, see 2.8.3 for solution detail, as well refer to Appendix II to get an over view of the experimental work flow).

3.3.1 Unaltered ribbon synapse morphology was observed in *RIM2 α* *KO*

First, tomograms were analyzed to check if the synaptic morphology was altered in *RIM2 α* *KOs*. I observed that the ribbon synapse surface area/tomogram excluding the presynaptic density was comparable between *RIM2 α* *Cons* and *RIM2 α* *KOs* (Fig. 3.20C, *RIM2 α* *Con* = $(54 \pm 7.5) \times 10^3 \text{ nm}^2$, n = 10 tomograms; *RIM2 α* *KO* = $(54 \pm 7.5) \times 10^3 \text{ nm}^2$, n = 10 tomograms). Furthermore, in all tomograms of *RIM2 α* *KO* ribbon synapses, properly anchored ribbons were observed (Fig. 3.20A-B) (Jung et al., 2015a). SangYong Jung (AG Moser, Institute of

Auditory Neuroscience, Göttingen) employed immunohistochemistry followed by confocal microscopy for synapse counting in *RIM2α Con* and *RIM2α KO* IHCs (P14-21) using CtBP2 (a marker for synaptic ribbon) and GluR2/3 (a marker for postsynaptic glutamate receptor). The number of synapses/IHC was comparable in control and KO animals (Jung et al., 2015). Therefore, EM and light microscopy together showed that the gross morphology of ribbon synapse remained unaltered in the absence of RIM2α (Jung et al., 2015a).

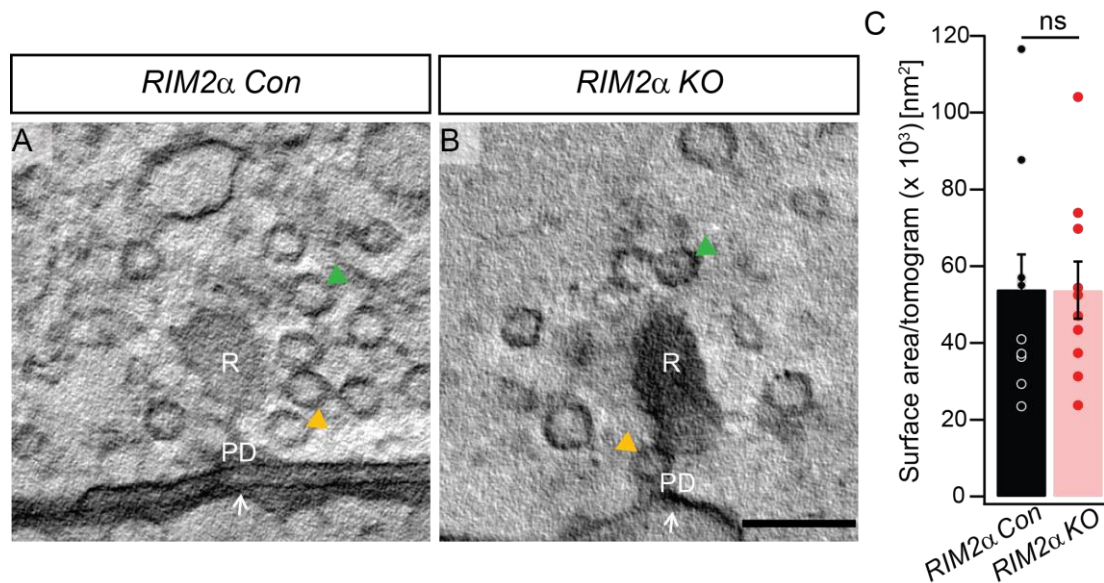


Figure 3.20: Gross morphology of *RIM2α Con* and *RIM2α KO* ribbon synapses remains comparable (A-B) Representative tomographic virtual sections of *RIM2α Con* (A) and *RIM2α KO* (B) ribbon synapses. Intact AZs (white arrows) and proper presynaptic densities with normal anchorage of synaptic ribbons (R) are found in *RIM2α Con* and *RIM2α KO* mice. Ribbons are surrounded by a halo of SVs: RA (green arrowheads) and MP (yellow arrowheads). Scale bar, 100 nm; magnification, 12,000x. (C) The graph is representing the average surface area (nm² × 10³)/synaptic ribbon tomogram. The surface area of the synaptic ribbon remains unaltered at the *RIM2α KO*s. Data are represented in mean ± SEM. P-values are calculated with Student's unpaired two-tailed t-test, n = 10 tomograms for each genotype.

3.3.2 Reduced number of SVs with filaments in the proximal part of the ribbon although, filament length in *RIM2α KO* IHCs was unaltered

Next, the RA SVs were analyzed in the tomograms. At all analyzed ribbon synapses, a spatially organized halo of SVs was observed around the ribbon for both genotypes (Fig. 3.20A-B). The SVs number/tomogram in the RA pool was unaltered at *RIM2α*-deficient synapses (*RIM2α Con* = 28.2 ± 3.5, n = 10 tomograms; *RIM2α KO* = 29.0 ± 3.9, n = 10 tomograms) (Jung et al., 2015a).

Further, to evaluate if the filamentous organization in RA pool of the KO's was altered, the fraction of SVs with filaments/tomogram was analyzed (as described earlier in section 3.2.6), revealing a trend towards a reduced fraction of SVs with filaments in *RIM2α KO*s compared to the *RIM2α Con* (Fig. 3.21D and Table 3.12A). Interestingly, only on dividing the ribbon into a distal and a proximal part (as described in section 3.2.6), I observed that the fraction of SVs with filaments/tomogram was significantly reduced in the *RIM2α KO* ribbon synapse in the proximal part of the ribbon (closer to the AZ membrane). In the distal part, no changes were observed (Fig. 3.21E and Table 3.12B, C).

In order to evaluate if a deficiency of *RIM2α* also alters the filament length in the RA pool, filament lengths were analyzed in 3-D (described in section 2.5.3.3 and 3.2.8). However, the average filament length/tomogram remained unaltered in the *RIM2α KO* ribbon synapses (Fig. 3.21F, *RIM2α Con* = 30.3 ± 1.4 nm, n = 10 tomograms; *RIM2α KO* = 27.8 ± 2.1 nm, n = 10 tomograms). The statistical tests and the number of ribbons analyzed are mentioned in the legend for Fig. 3.21 and Table 3.12.

In conclusion, *RIM2α* deficient IHCs maintain the same number of SVs around the ribbon. However, at the proximal part of the ribbon, the fraction of SVs with filaments was significantly reduced in *RIM2α KO* IHCs.

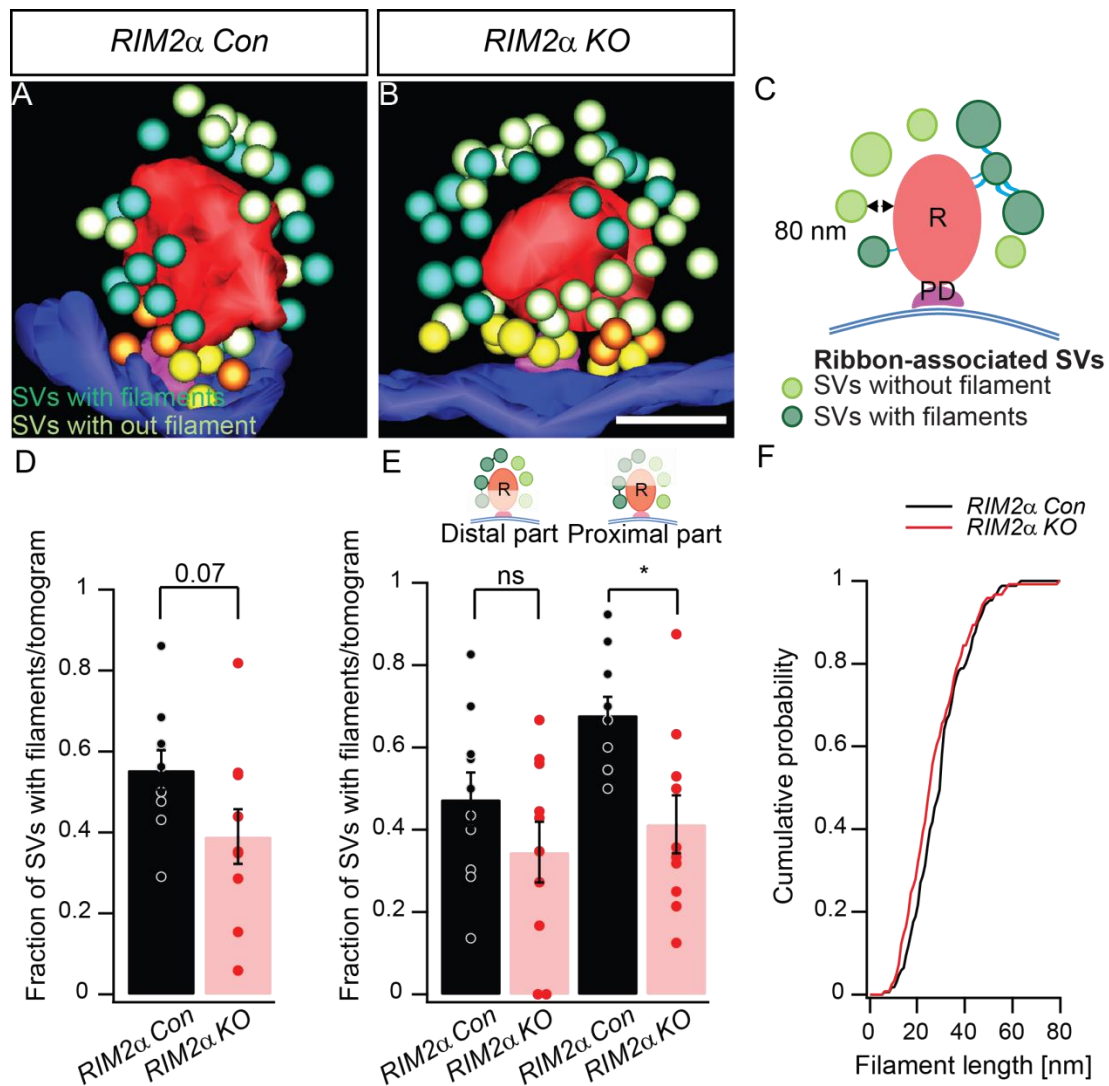


Figure 3.21: Fraction of SVs with filaments decreases in the proximal ribbon part of *RIM2α KO* ribbon synapses

(A-B) Depicted are 3-D reconstructions of the RA SVs (front view) in *RIM2α Con* (A) and *RIM2α KO* (B). RA SVs are classified as vesicles with filaments and without filament, color-codes are mentioned in the inset legend A. For clarity these filaments are not depicted. Other synaptic compartments are color-coded as Fig. 2.7 panel B. The panels A-B are published in Jung et al., 2015a

(C) Illustration summarizing the tomogram analysis, not drawn to scale. The RA SVs are defined and analyzed as for Fig. 2.7 panel B.

(D) The graph is representing the fraction of SVs with filaments/tomogram in the RA pool. The fraction of SVs with filaments shows a trend towards reduction in *RIM2α KO*s compared to *RIM2α Cons*. Data are represented as mean \pm SEM. P-values are calculated with Student's unpaired two-tailed t-test, $n = 10$ tomograms for each genotype. Exact p-value is written in case of a trend.

(E) The ribbon was divided into a distal and a proximal part. The fraction of SVs with filaments shows a significant reduction in *RIM2α KO*s compared to *RIM2α Cons* in the proximal part of the ribbon. Data are represented as mean \pm SEM. P-values are calculated by one way ANOVA followed by Tukey's test, $n = 10$ tomograms for each genotype; ** $p < 0.05$ and ns $p > 0.05$.

(F) The cumulative probability distribution of RA filament length. The filament length is unaltered in the RA pool of *RIM2 α KO*s. *RIM2 α Cons*, n = 170 SVs with filaments and *RIM2 α KO*s, n = 122 SVs with filaments. Panels A-B are published in Jung et al., 2015a.

3.3.3 Disruption of *RIM2 α* reduces the fraction of MP tethered SVs

2-color STED microscopy demonstrated that *RIM2 α* is localized in a strip-like fashion between the ribbon and Ca^{2+} channels in the AZ membrane (Jung et al., 2015a), similar localization as observed before for presynaptic density (enriched in bassoon), clustering Ca^{2+} channels (Frank et al., 2010; Rutherford, 2015; Wong et al., 2014). Similar to my former observations (described in section 3.2.9) the SVs in the MP pool were either non-tethered or had a single tether to the membrane or to the presynaptic density. In all analyzed tomograms I did not encounter multiple-tethered or docked SVs at the AZ membrane for both *RIM2 α Con* and *RIM2 α KO* (Fig. 3.22A-B). Here, resting conditions were used, the absence of multiple-tethered or docked vesicles strengthens the idea that these stages were seen in wild-type synapses upon continuous stimulation, but very rarely due to fast release and therefore might not be observed under resting condition (as described in section 3.2.11 and 3.2.12).

Similar to the RA SV pool (described above in section 3.3.2) the total number of MP SVs was unaltered in *RIM2 α KO* compared to *RIM2 α Con* (*RIM2 α Con* = 7.0 ± 0.7 , n = 10 tomograms; *RIM2 α KO* = 8.0 ± 1.01 , n = 10 tomograms) (Jung et al., 2015a). However, I observed that the fraction of tethered SVs/tomogram (membrane- and presynaptic density-attached tethers together) was significantly reduced in MP pool of *RIM2 α KO*s (Fig. 3.22D and Table 3.12D). To test whether a particular sub-pool of tethered SVs contributes standalone to this reduction of tethered vesicles at *RIM2 α KO* ribbon synapses, the membrane- and presynaptic density-attached tethers were analyzed separately (as described earlier in section 3.2.10). However, no statistical significance could be observed separately, because 60 % and 70 % of the analyzed tomograms from *RIM2 α KO*s did not have any membrane- and presynaptic density-attached tethers respectively in the MP pool accounting for low sample size for statistical analysis (Fig. 3.22E and Table 3.12).

Next, in order to evaluate if deficiency of *RIM2 α* increases the tether length similar to previous observation in *RIM1 α KO* mice in cerebrocortical synaptosomes (Fernández-Busnadiego et al., 2013), tether length/tomogram was analyzed in 3-D in the MP pool of *RIM2 α Cons* and *RIM2 α KO*s (as described in section 2.5.3.3 and 3.2.13). However, the tether length/tomogram remained unaltered for both membrane- and presynaptic density-attached tethers in *RIM2 α KO*s (Fig. 3.22F, *RIM2 α Con* = 23 ± 1.3 nm; *RIM2 α KO* = 23.9 ± 1.7

nm) (Jung et al., 2015a). The statistical tests and the number of ribbons analyzed are mentioned in the legend for Fig. 3.22 and Table 3.12.

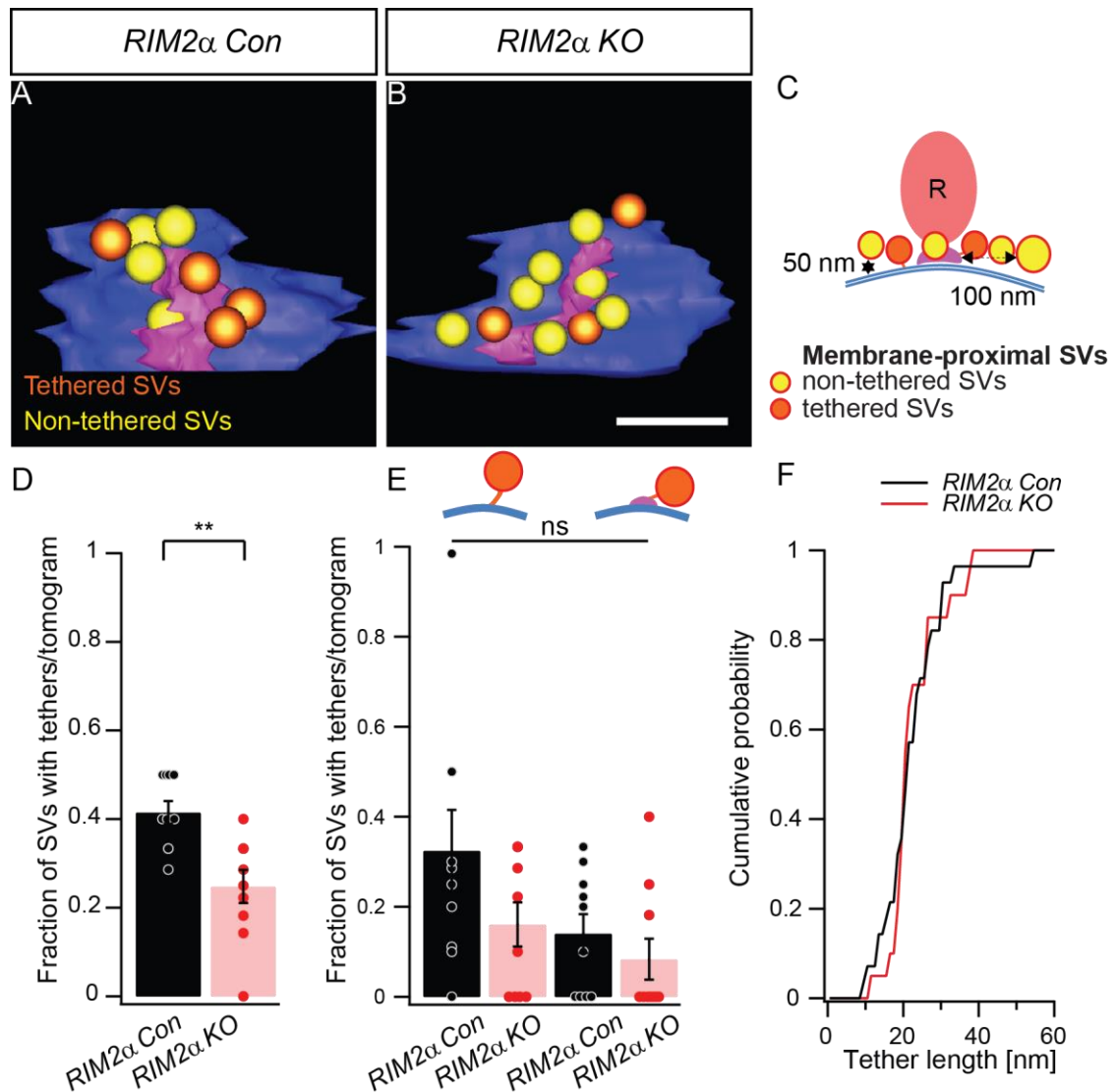


Figure 3.22: MP pool of *RIM2α* Con and *RIM2α* KO ribbon synapses

(A-B) Shown are 3-D reconstructions of the MP SVs (top view) in *RIM2α* Con **(A)** and *RIM2α* KO **(B)** mice. MP SVs are classified as tethered SVs (orange) and non-tethered SVs (yellow). For clarity, these tethers are not depicted. Other synaptic compartments are color-coded as described previously in Fig. 2.7 panel B. Scale bar, 100 nm.

(C) The depicted illustration is summarizing the tomogram analysis in accordance with Fig. 2.7 panel B, not drawn to scale.

(D) The graph is representing the fraction of tethered SVs/tomogram in the MP pool, which is significantly reduced in *RIM2α KO*s compared to *RIM2α Cons*. Data are represented in mean ± SEM. P-values are calculated with Student’s unpaired two-tailed t-test, n = 10 tomograms for each genotype; ** p < 0.01.

(E) The graph is depicting the individual fractions of SVs with membrane-attached tethers and of SVs with presynaptic density attached tethers, which are unaltered. Data are represented in mean ± SEM. P-values are calculated by one way ANOVA followed by Tukey’s test, n = 10 tomograms for each genotype; ns p > 0.05.

(D) The cumulative probability distribution of MP tether length. The tether length is unaltered in the MP pool of *RIM2α KO*s. *RIM2α Cons*, n = 28 tethered SVs and *RIM2α KO*s, n = 21 tethered SVs. Figure modified from (Jung et al., 2015a).

	Parameter	<i>RIM2α Con</i>	<i>RIM2α KO</i>	p-values	
Ribbon-associated pool	A	Fraction of SVs with filaments (whole ribbon)	0.60 ± 0.05	0.40 ± 0.07	0.07 §
	B	Fraction of SVs with filaments	0.50 ± 0.07	0.34 ± 0.07	0.5 §
	C	Fraction of SVs with filaments	0.70 ± 0.04	0.41 ± 0.07	0.03 §
Membrane-proximal pool	D	Fraction of tethered SVs	0.41 ± 0.03	0.25 ± 0.04	0.006 Δ
	E	Fraction of membrane-attached SVs	0.32 ± 0.01	0.20 ± 0.05	0.2 §
	F	Fraction of presynaptic density-attached SVs	0.14 ± 0.04	0.08 ± 0.05	0.9 §

Table 3.12: Fraction of SVs with filaments and tethers in the RA and the MP pool of *RIM2α Con* and *RIM2α KO* mice

Data are represented as mean ± SEM to show differences between *RIM2α Cons* and *RIM2α KO*s. In (A, B) p-values are calculated by Student’s unpaired two-tailed t-test (§). In (B, C) and (E, F) p-values are calculated one way ANOVA followed by Tukey’s test (§). In (D) p-value is calculated by two-tailed Wilcoxon-Rank-Sum test (data are acquired from one *C57/BL6* wild-type, one *RIM2α Con* and one *RIM2α KO* animal). Ten tomograms for each genotype were analyzed.

3.3.4 Summary

In section 3.3, I investigated tethering in the RA and the MP vesicle pool of *RIM2α Con* and *RIM2α KO* IHC ribbon synapses. In IHCs of *RIM2α KO*s, the fraction of SVs tethering to the AZ membrane (Jung et al., 2015a) and the proximal ribbon part (close to the AZ membrane) were significantly reduced. However, the length of the tethers (Jung et al., 2015a) and filaments remained unaltered. This implies, that RIM2α is either directly or indirectly involved in tethering of SVs to the AZ (Jung et al., 2015a), but possibly also to the proximal ribbon part.

3.4 Implementation of HPF in combination with optogenetic stimulation

It has been proposed that SVs situated close to the AZ membrane represent the “ultrafast release pool” and SVs further away around the ribbon are accessible for slower release (Lenzi et al., 1999). In the first three parts of this thesis further refinements to this standing hypothesis has been made, indicating that not all SVs in the MP pool at IHC ribbon synapses are morphologically similar. Therefore, they could represent different release states. Further, SVs tethered via multiple-tethers (Fernández-Busnadiego et al., 2010, 2013) and docked at the AZ membrane (Imig et al., 2014), the proposed steps before release at conventional synapses were rarely found at wild-type ribbon synapses (described in sections 3.2.11, 3.2.12 and 3.3.3) and if at all observed, mostly upon stimulation. In the sections 3.2 and 3.3, HPF allowed a quick immobilization of the samples with near-to-native state structural preservation (Helmprobst et al., 2015; Imig et al., 2014; Jung et al., 2015a; Moor, 1987; Rostaing et al., 2006; Siksou et al., 2007; Stigloher et al., 2011; Vogl et al., 2015), therefore allowed to capture dynamic processes involved in maintenance of SV pools during prolonged stimulation at the IHC ribbon synapses. However, the temporal resolution at which extremely fast exocytosis steps occur at the IHCs was still not achieved by using stimulation solutions. Earlier it has been shown that the neuronal activity can be optically evoked and has been described as a promising tool to investigate the transient events of exo/endocytosis ultrastructurally (Kittelmann et al., 2013; Watanabe et al., 2013a, 2013b). Therefore, in this part of the thesis, for the first time, I incorporated optogenetic stimulation in combination with HPF (Opto-HPF) (described in section 2.3.3) (Kittelmann et al., 2013; Watanabe et al., 2013a, 2013b) at IHC ribbon synapses. This allowed a precise and specific control of the stimulation duration, coupled with the freezing time onset to capture the structural correlates of early exocytosis events at IHC ribbon synapses. In this study, optical stimulation was achieved by the transgenic expression of a channelrhodopsin-2 variant (ChR-2-H134R) under the control of the vGlut3 promoter in order to control SV release. This ensured expression of ChR almost exclusively in IHCs (*Ai32VC* mice, P14-16).

3.4.1 Cellular physiology showed IHCs can be evoked optogenetically

First, the IHC physiology was tested. During the Master’s thesis, Lina María Jaime Tobón (AG Moser, Institute for Auditory Neuroscience, Göttingen) performed perforated patch-clamp experiments on IHCs in the presence of the K⁺ channel blocker tetraethyl ammonium-Cl (TEA-Cl) and 4-aminopyridine (4-AP). The photocurrents were measured in voltage clamp mode and to measure the induced depolarization she switched to current clamp mode. She found that 5 ms of optogenetic stimulation were enough to stimulate release at IHC ribbon synapses (Jaime Tobón, 2015). Illumination with 473 nm blue light resulted in a photo depolarization current that increased with increasing light intensities

(Jaime Tobón, 2015) (5 ms pulse: $\sim 4 \text{ mW/mm}^2$ photo depolarization to -73 mV and $\sim 1822 \text{ mW/mm}^2$ photo depolarization to 0 mV). At higher light intensities, a strong depolarization was elicited reaching up to 0 mV within ms, resulting in strong exocytosis exceeding the size of the RRP (Jaime Tobón, 2015). Therefore, ChR-2 rapidly depolarize IHCs within few ms in response to a short light pulse, thus was suitable for Opto-HPF experiments described in the next sections.

3.4.2 Verification of ChR-2 expression in hair cells

For electro-physiological experiments, an analysis of the expression of ChR-2 was not performed systematically by immunohistochemistry. This was required to confirm that the vGlut3 promoter efficiently controlled the expression of the ChR-2-construct that should be specifically targeted to the plasma membrane of the IHCs. Expression and localization of the ChR-2-construct could be confirmed using fluorescence imaging since the construct used here contained a ChR-2-YFP fusion protein. The fluorescence of YFP was clearly observed upon excitation with 490 nm light before patch-clamp recordings (Lina María Jaime Tobón) (Fig. 3.23B). Before starting the EM experiments, the plasma membrane expression of ChR-2 was reconfirmed by immunohistochemistry and confocal microscopy in P14-16 *Ai32VC* mouse line. Anti-GFP (labeling the YFP fused to the ChR-2) and anti-NF200 (to label the spiral ganglion neurons) was used to stain whole mount preparations of the apical turn of the organ of Corti. All the IHCs in *Ai32VC* mice showed ChR-2 expression efficiently in the IHCs plasma membrane, without any apparent intracellular aggregations (Fig. 3.23C, Lina María Jaime Tobón).

3.4.3 Ultrastructural preservation in *Ai32VC* transgenic mice after Opto-HPF/FS showed good structural preservation

Ultrathin sections obtained after Opto-HPF showed good structural preservation of the IHCs (Fig. 3.23A) and ribbon synapses (Fig. 3.23D-E) and were comparable to the structural preservation described above in section 3.2.1 for wild-type IHCs. SVs surrounded the ribbons and all analyzed tomograms showed intact presynaptic densities anchoring the ribbon and continuous AZ membranes in apposition to the PSD (Fig. 3.24B-C).

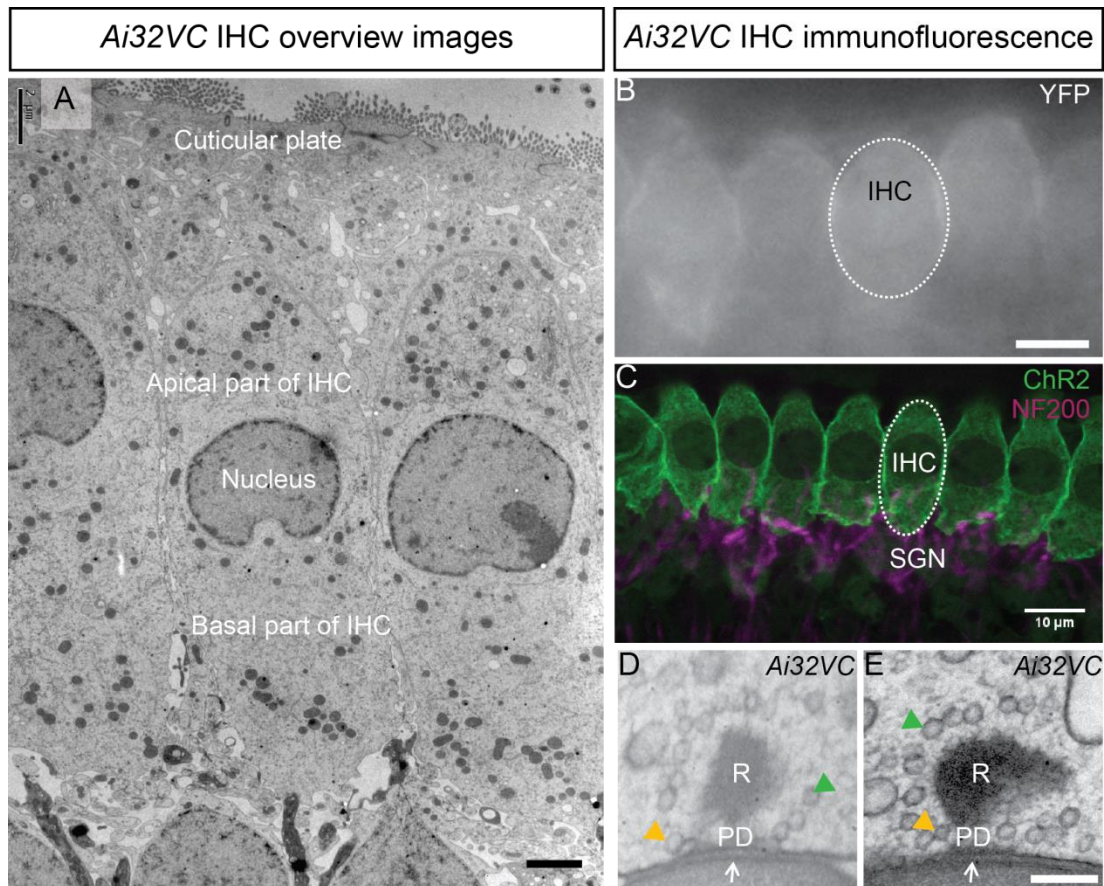


Figure 3.23: Intact structural preservation of *Ai32VC* IHC and with plasma membrane expression of ChR-2-H134R in IHCs

(A) EM samples prepared by Opto-HPF exhibit excellent structural preservation of the IHCs. Shown is a representative overview of a row of IHCs in an *Ai32VC* organ of Corti. Scale bar, 2 μm ; magnification 800x.

(B) Depicted is a representative image of IHCs expressing ChR-2H134R (ChR-2) under the control of the chicken beta-actin-promoter, YFP fluorescence during excitation with 490 nm wavelength. Scale bar, 10 μm .

(C) Immunolocalization of ChR-2 in the IHCs. Maximum projections of confocal stacks from whole-mount preparations of the apical turn of a P14 mouse organ of Corti, immunolabeled for YFP (labeling ChR-2, in green) and NF200 (labeling spiral ganglion neurons (SGN), in magenta). Scale bar, 10 μm . Images B and C, kindly provided by Lina María Jaime Tobón (AG Moser, Institute for Auditory Neuroscience, Göttingen).

(D-E) Shown are representative electron micrographs of ribbon synapses in *Ai32VC* mice. Ribbons (R) are anchored with presynaptic density (PD) to the AZ membrane (white arrow). They are surrounded by a typical halo of SVs, RA (green arrowheads) and MP (yellow arrowheads). Scale bar, 100 nm; magnification, 12,000x.

3.4.4 LED stimulation in the HPM-100

This thesis describes the very first experiments to carry out Opto-HPF at IHC ribbon synapses. However, the results here are very preliminary and further modifications regarding the temporal coupling of stimulation and freezing are still ongoing, as well as for the optimal extracellular buffer conditions for the light stimulation. Within the scope of this thesis, I have so far not reached the very early exocytosis events at IHC ribbon synapses,

although the temporal coupling of a precise stimulus and freezing greatly improved compared to the high K^+ stimulation (section 3.2). For the experiments described here 10 ms optical stimulation was used (also see methods section Fig. 2.4). In the experiments, the coupling between the 10 ms stimulation and freezing was on average 15 ms (described in method section 2.3.3.2). The light intensity at the sample was measured to be 34.6 mW with a mean intensity of 1.2 mW/mm² and a peak intensity of 6 mW/mm².

3.4.5 Analysis of RA pool in *Ai32VC* mice after optical stimulation

3.4.5.1 Reduced number of RA SVs but a normal fraction of SVs with filaments after 10 ms optical stimulation

First, I concentrated on the RA SV pool (see 2.5.3.2 point i for definition). The organs of Corti (P14-16) were incubated in an extracellular solution containing 2.8 mM K^+ , 2 mM Ca^{2+} , 5 mM 4-AP and 35 mM TEA-Cl (solution details in materials and methods section 2.8.3, same was used for electrophysiological recordings' described in section 3.4.1). 10 ms blue LED light pulse was used to stimulate the IHCs of *Ai32VC* mice. As controls, *C57BL/6* (wild-type) and littermate *Ai32VC* mice, both non-stimulated (without light) were used (an experimental work flow for this section is provided in Appendix III). No significant difference in terms of ribbon synapse vesicle dynamics was observed between non-stimulated *Ai32VC* and *C57BL/6* ribbon synapses (data not shown). Therefore, for tomogram analysis, these two groups were pooled together for further comparisons during the first set of experiments (will be referred to as Control hereafter).

First, the size of the RA pool was determined similarly to my previous experiments (section 3.2.8). I observed that the average SV count/tomogram was significantly reduced within 80 nm around the ribbon (Fig. 3.24D, Control = 46.1 ± 4.8 , $n = 8$ tomograms; *Ai32VC*-10 ms = 31 ± 3.5 , $n = 9$ tomograms). The reduced number of RA SVs could be a result of the mobilization of SVs closer to the membrane during active release.

Next, I was interested to see if the complexity of filaments was altered after 10 ms light stimulation. Therefore, the fraction of SVs with filaments/tomogram was calculated (as described above in section 3.2.6 and 3.3.2). I observed that, after optical stimulation, the fraction of SVs with filaments remained comparable to the control tomograms (Fig. 3.24E, Table 3.13A), in contrast to 15 min K^+ stimulation where it increased. Moreover, the fractions of SVs with single and multiple-filaments/tomogram were as well comparable between Control and *Ai32VC*-10 ms samples (Table 3.13B-D). My previous experiments proposed that filament connectivity at the RA pool is required for organization and resupply to sustain replenishment of SVs (described in section 3.2.6) during the sustained component of release as shown with electrophysiological experiments (20 ms or more

continuous depolarization, Moser and Beutner, 2000; Pangrsic et al., 2010). Therefore, an unaltered fraction of single and multiple-filaments/tomogram after 10 ms stimulation indicates that here a different release phase was captured, as also indicated by the proposed time between stimulation and freezing (~ 15 ms, see materials and method section 2.3.3.2). Still, also here further experiments and refinements of the correlation stimulus to freezing are required. The statistical tests and the number of ribbons analyzed are mentioned in the legend of Fig. 3.24 and Table 3.13.

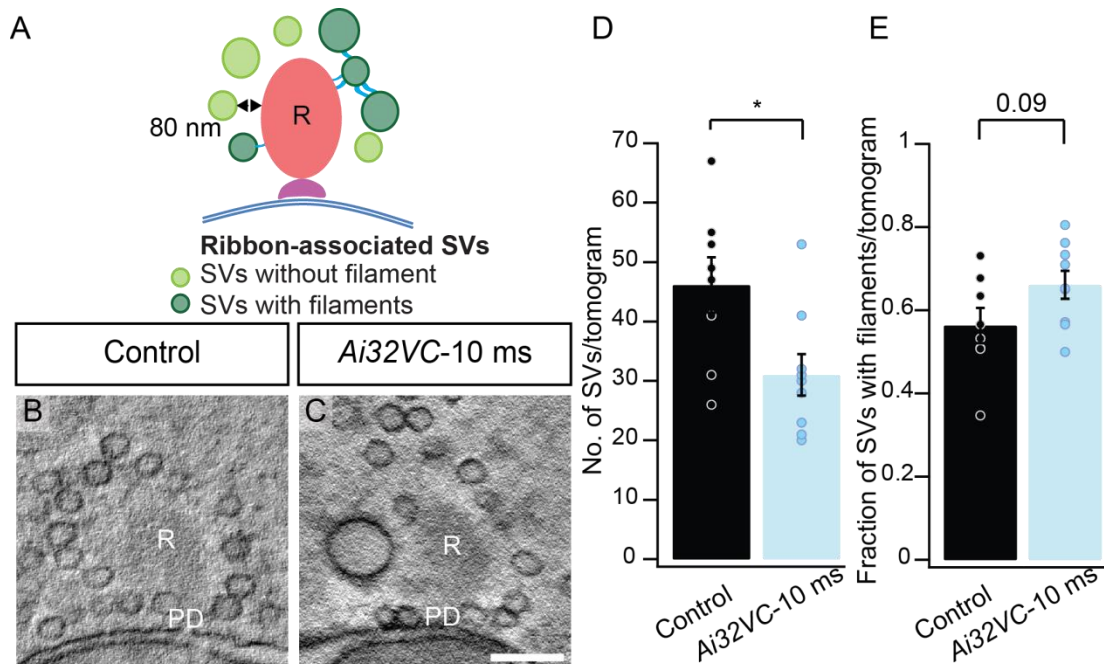


Figure 3.24: The number of RA SVs is reduced, but the fraction of SVs with filaments is unaltered after 10 ms optical stimulation and ~ 15 ms stimulus-freezing temporal coupling

(A) Illustration summarizing the tomogram analysis of RA pool, not drawn to scale. Refer to Fig. 2.7 panel B for details.

(B-C) Representative tomographic virtual sections of Control (without light) (B) and *Ai32VC* after 10 ms light stimulation (C). Scale bar, 100 nm; magnification, 12,000x.

(D) The average RA SV count/tomogram reduces but (E) the fraction of SVs with filaments/tomogram is unaltered in *Ai32VC* after 10 ms light stimulation. Data are represented as mean \pm SEM. P-values are calculated with Student's unpaired two-tailed t-test, Control (without light), $n = 8$ tomograms and *Ai32VC* after 10 ms light stimulation, $n = 9$ tomograms; * $p < 0.05$, exact p-value is written in case of a trend.

	Parameter	Control	<i>Ai32VC-10ms</i>	p-values
A	Fraction of SVs without filament	0.43 ± 0.04	0.34 ± 0.03	0.09 \$
B	Fraction of SVs with filaments	0.60 ± 0.04	0.70 ± 0.03	0.09 \$
C	Fraction of SVs with single filaments	0.30 ± 0.03	0.33 ± 0.04	0.8 \$
D	Fraction of SVs with multiple-filaments	0.30 ± 0.02	0.32 ± 0.04	0.9 \$

Table 3.13: Fraction of RA SVs with filaments in Control and *Ai32VC* after 10 ms optical stimulation

Data are presented as mean ± SEM to show differences between Control (without light) and *Ai32VC* after 10 ms light stimulation. In (A, B) the p-values are calculated by the Student's unpaired two-tailed t-test (\$). In (C, D) the p-values are calculated by one way ANOVA followed by Tukey's test (§). Data are acquired from one *C57/BL6* wild-type and one *Ai32VC* mouse (pooled together as Control without light, two mice) and one *Ai32VC* mouse after 10 ms light stimulation. Eight tomograms from the Control (without light) (four tomograms from *C57/BL6* control and four tomograms from *Ai32VC* control) and nine tomograms from *Ai32VC* mice after 10 ms light stimulation are analyzed.

3.4.5.2 Filament length was moderately increased in the RA pool after 10 ms optical stimulation

Next, the average filament length in RA pool/tomogram was analyzed for both Control and *Ai32VC-10 ms* (as described in section 2.5.3.3) IHCs. Comparable to my previous observation in section 3.2.8, RA SVs had longer ribbon-attached tethers than ribbon-associated inter-connectors for both Control and *Ai32VC-10 ms* (Fig. 3.25D, Table 3.14D, E). Moreover, the average filament length/tomogram (combining both: ribbon-attached tethers and –associated inter-connectors) revealed that filaments were slightly, but not significantly longer at *Ai32VC-10 ms* ribbon synapses (Fig. 3.26C, Control = 16.0 ± 1.5 nm, n = 8 tomograms; *Ai32VC-10ms* = 18.1 ± 0.9 nm, n = 9 tomograms). Additionally, the lengths of single filaments and individual filament from the multiple-filaments categories remained comparable between Control and *Ai32VC-10 ms* ribbon synapses (Table 3.14B, C). The statistical tests and the number of ribbons analyzed are mentioned in the legend of Fig. 3.25 and Table 3.14.

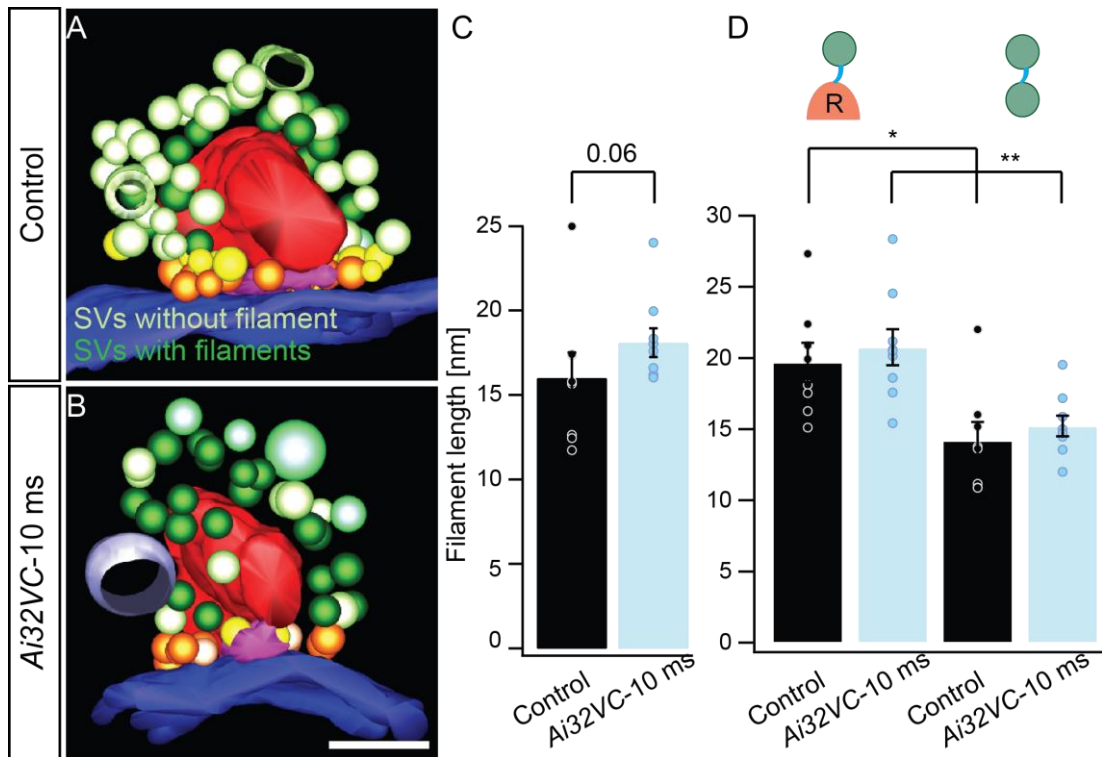


Figure 3.25: Average filament length is moderately increase in *Ai32VC* after 10 ms light stimulation with a ~ 15 ms stimulus-freezing temporal coupling

(A-B) Depicted are the 3-D reconstructions of the RA SVs from tomograms (front view) of Control (without light) **(A)** and *Ai32VC* after 10 ms light stimulated **(B)** ribbon synapses. Classified and color-coded as stated in Fig. 2.7 panel B. For clarity these filaments are not depicted. Scale bar, 100 nm.

(C) The graph is representing the average RA filament length. The average length modestly increased in *Ai32VC* after 10 ms light stimulation. Data are represented as mean \pm SEM. P-value is calculated with two-tailed Wilcoxon-Rank-Sum test, Control (without light), $n = 8$ tomograms and *Ai32VC* after 10 ms light stimulation, $n = 9$ tomograms. The exact p-value is written in case of a trend.

(D) In both Control and *Ai32VC* after 10 ms light stimulation ribbon-attached tethers are longer than ribbon-associated inter-connectors. Data are represented as mean \pm SEM. P-values are calculated by one way ANOVA followed by Tukey's test, Control (without light), $n = 8$ tomograms and *Ai32VC* after 10 ms light stimulation, $n = 9$ tomograms; * $p < 0.05$ and ** $p < 0.01$.

	Parameter	Control	<i>Ai32VC</i> -10 ms	p-values
A	Filament length [nm]	16.0 ± 1.5	18.1 ± 0.9	0.06 Δ
B	Single filament length [nm]	18.5 ± 2.0	20.1 ± 1.2	0.9 §
C	Multiple-filament length [nm]	15.1 ± 1.5	17.6 ± 1.0	0.6 §
D	Ribbon-attached tether length [nm]	19.7 ± 1.4	20.8 ± 1.3	0.9 §
E	Ribbon-associated inter-connector [nm]	14.2 ± 1.3	15.2 ± 0.7	0.9 §

Table 3.14: Length of filaments in the RA pool of Control and *Ai32VC* after 10 ms optical stimulation

Data are presented as mean ± SEM to show differences between Control (without light) and *Ai32VC* after 10 ms light stimulation. In (A) the p-value is calculated by two-tailed Wilcoxon-Rank-Sum test (Δ). In (B-E) p-values are calculated by one way ANOVA followed by Tukey's test (§). Data are acquired from one *C57/BL6* wild-type and one *Ai32VC* mouse (pooled together as Control without light stimulation, two mice) and one *Ai32VC* mouse after 10 ms light stimulation. Eight tomograms from Control (without light) (four tomograms from *C57/BL6* control and four tomograms from *Ai32VC* control) and nine tomograms from *Ai32VC* after 10 ms light stimulation are analyzed.

3.4.6 Analysis of MP SV pool in *Ai32VC* mice after optical stimulation

3.4.6.1 MP SV count remained unaltered, but the fraction of tethered SVs increased significantly after 10 ms stimulation

The MP pool was proposed earlier to represent the RRP of SVs closer to the Ca²⁺ channels (Lenzi and von Gersdorff, 2001; Lenzi et al., 1999). Therefore, in my previous experiments using a high K⁺ stimulation (described in section 3.2.9), the MP pool of SVs was studied thoroughly. Further, I could show that different sub-pools of SVs exist based on the number of tethers and localization close to the AZ membrane, probably representing different release states. To test this working hypothesis the size of the MP pool was investigated at IHC ribbon synapses (P14-16) after 10 ms optical stimulation (see methods Fig. 2.4). Tomogram analysis revealed that the average SV count/tomogram remained unaltered in *Ai32VC*-10 ms (Fig. 3.26F, Control = 15.6 ± 2.0, n = 8 tomograms; *Ai32VC*-10 ms = 12.6 ± 1.2, n = 9 tomograms). Additionally, similar to my earlier observations, both, non-tethered and tethered SVs were observed in the MP pool (Fig. 3.26B-E), whereby mostly single membrane-attached tethers were found (Table 3.15D, E). Furthermore, the fraction of tethered SVs increased significantly after optical 10 ms stimulation (Fig. 3.26G, Control = 0.48 ± 0.03, n = 8 tomograms; *Ai32VC*-10ms = 0.68 ± 0.05, n = 9 tomograms). These observations strengthen my earlier hypothesis (section 3.2.10) that tethered SVs might

represent the recruitment of SVs at the AZ membrane before they docked at the IHC ribbon synapses. The statistical tests and the number of ribbons analyzed are mentioned in the legend of Fig.3.26 and Table 3.15.

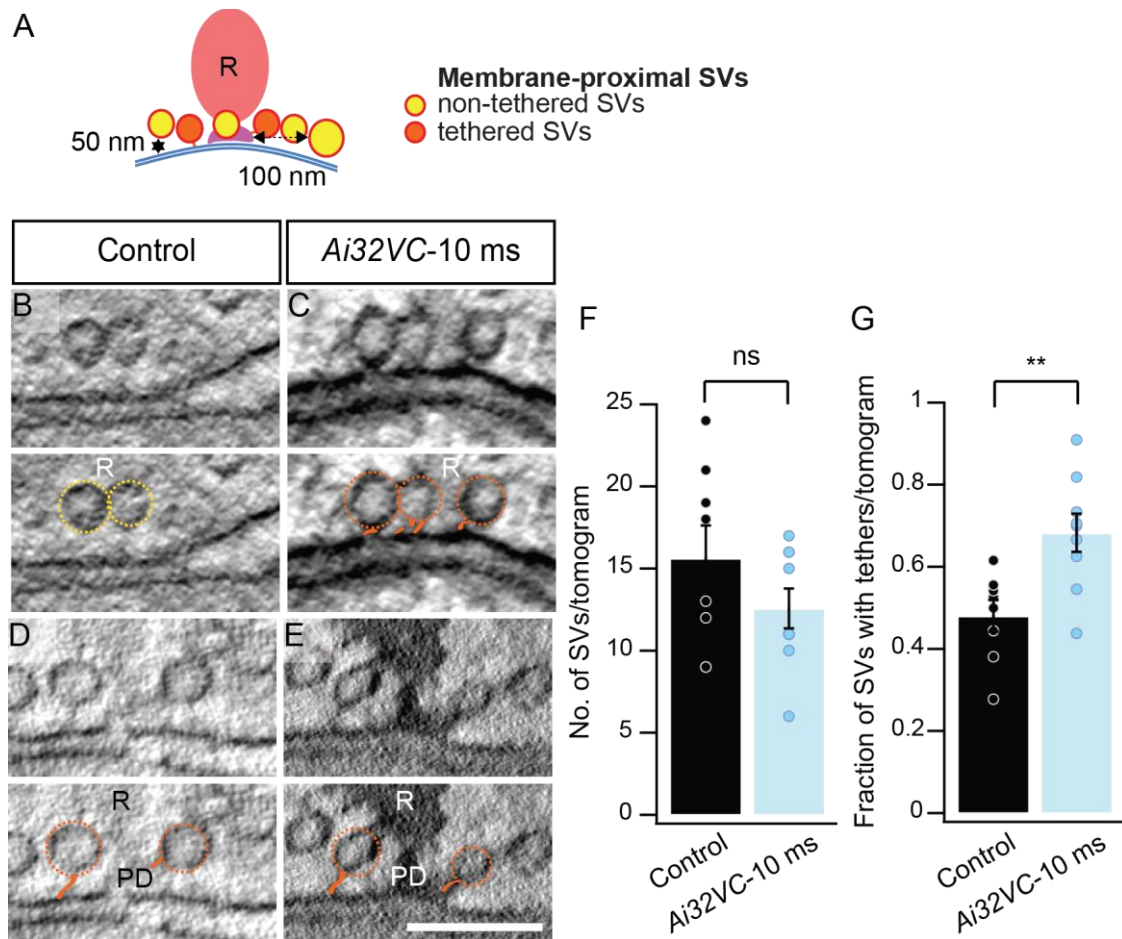


Figure 3.26: MP SV count is unaltered, but the fraction of tethered SVs increases after 10 ms optical stimulation with ~ 15 ms stimulus-freezing temporal coupling

(A) The depicted illustration is summarizing the tomogram analysis, not drawn to scale. Color-coded according to the inset legend.

(B-E) Representative tomographic virtual sections from control (without light) (**B, D**) and *Ai32VC* after 10 ms light stimulation (**C, E**). MP tethered SVs are encircled orange, orange solid lines highlight tether(s) and non-tethered SVs are encircled yellow. Scale bar, 100 nm; magnification, 12,000x.

(F) The average MP SV count/tomogram is unaltered in *Ai32VC* after 10 ms light stimulation. Data are represented as mean \pm SEM. The p-value is calculated with Student's unpaired two-tailed t-test, Control (without light), $n = 8$ tomograms and *Ai32VC* after 10 ms light stimulation, $n = 9$ tomograms; ns $p > 0.05$.

(G) The fraction of tethered SVs/tomogram increases in *Ai32VC* after 10 ms light stimulation. The p-value is calculated with two-tailed Wilcoxon-rank-sum test, Control (without light), $n = 8$ tomograms and *Ai32VC* after 10 ms light stimulation, $n = 9$ tomograms.

3.4.6.2 Fraction of multiple-tethered and docked SVs increased after 10 ms optical stimulation

Upon continuous high K^+ stimulation at wild-type ribbon synapses rarely multiple-tethered and docked SVs were observed, whereas in *Otof*^{Pga/Pga} showing deficits in vesicle replenishment (Pangrsic et al., 2010) these events increased significantly upon stimulation. Therefore, I postulated that these events were transient and fast at IHC ribbon synapses but became visible in the mutants due to impaired sustained exocytosis (section 3.2.11 and 3.2.12). To verify this hypothesis the fractions of multiple-tethered and docked SVs were evaluated after short 10 ms optical stimulation with a stimulus-freezing temporal coupling of ~ 15 ms. In the tomograms analyzed, 50 % of the Control and 100 % *Ai32VC-10* ms had multiple-tethered SVs (Fig. 3.27B, E). Therefore, the fraction of multiple-tethered SVs increased in *Ai32VC-10* ms compared to Control ribbon synapses (Fig. 3.27G). Further, in the Control, no docked vesicles could be captured, but 50 % of the *Ai32VC-10* ms tomograms exhibited docked SVs at the AZ (Fig. 3.27C, F and Table 3.15F). In one *Ai32VC-10* ms tomogram, even five docked SVs were found out of 16 MP SVs and an average of 1.00 ± 0.04 docked SVs/tomogram was observed in *Ai32VC-10* ms mice (Fig. 3.27H and Table 3.15G). In conclusion, these findings supported the hypothesis that multiple-tethered and docked SVs are in particular visible at activated IHC ribbon synapses due to its capability to replenish RRP almost immediately. However, during prolonged stimulation docked and multiple-tethered SVs were rather rare because they were likely to be released

In the end, the tether length/tomogram was measured as described previously (Jung et al., 2015a; Vogl et al., 2015), which remained unaltered in both Control and *Ai32VC-10* ms mice (Fig. 3.27I and Table 3.15H). Neither for the tether categories based on localization (membrane-attached tether Table 3.15J and presynaptic density-attached tether Table 3.15K) nor based on the number of tethers (single tether Table 3.15I and multiple-tethers Table 3.15L) was altered in length. The statistical tests and the number of ribbons analyzed are mentioned in the legend for Fig. 3.27 and Table 3.15.

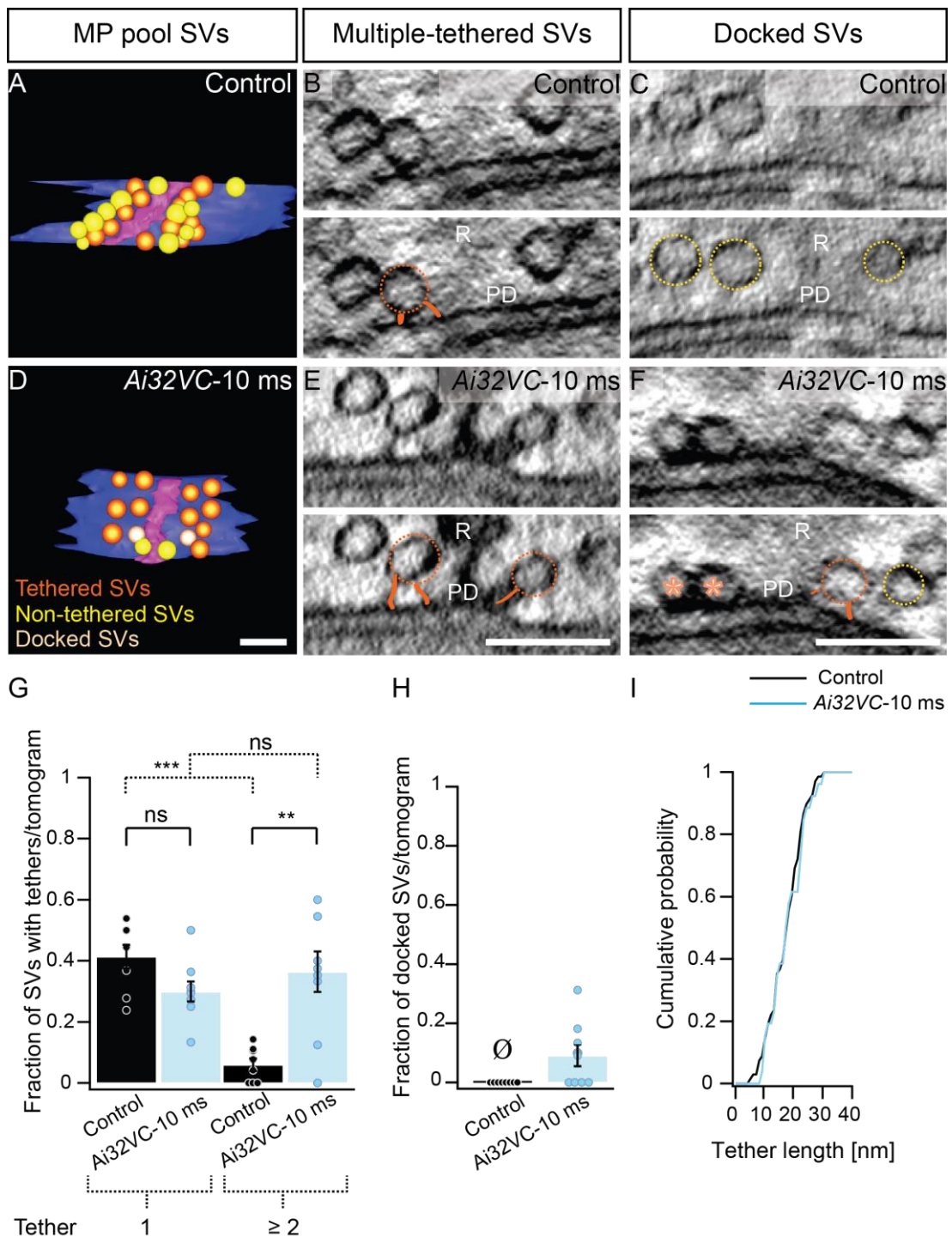


Figure 3.27: The fractions of multiple-tethered and docked SVs increase in the MP pool of *Ai32VC* IHCs after 10 ms light stimulation

(A, D) Shown are 3-D reconstructions of the MP SVs (top view) at Control (without light) and **(A)** *Ai32VC* after 10 ms light stimulated **(D)** ribbon synapses. MP SVs are classified and analyzed as described in Fig. 2.7 panel B. Scale bar, 100 nm.

(B, E) Representative tomographic virtual sections from Control (without light) **(B)** and *Ai32VC* IHCs after 10 ms light stimulation **(E)**. MP, multiple-tethered SVs are encircled with orange dotted lines and orange solid lines as tethers. Scale bar, 100 nm; magnification, 12,000x.

(C, F) Representative tomographic virtual sections from Control (without light) **(C)** and *Ai32VC* IHCs after 10 ms light stimulation **(F)**. MP, non-tethered SVs are encircled with yellow dotted lines and docked SVs with light orange and orange asterisks. Scale bar, 100 nm; magnification, 12,000x.

(G) The fraction of MP SVs with single tether/tomogram is comparable between Control and *Ai32VC* after 10 ms light stimulation. The fraction of SVs with multiple-tethers increases at *Ai32VC* ribbon synapses after 10 ms light stimulation. Data are represented as mean \pm SEM. P-values are calculated by one way ANOVA followed by Tukey's test, Control (without light), n = 8 tomograms and *Ai32VC* after 10 ms light stimulation, n = 9 tomograms; ** p < 0.01, *** p < 0.001 and ns p > 0.05.

(H) More docked SVs are observed at *Ai32VC* ribbon synapses after 10 ms light stimulation (50 % of the analyzed tomograms). None of the Control tomograms exhibit docked SVs. Therefore, statistics could not be performed. Data are represented as mean \pm SEM. Control (without light), n = 8 tomograms and *Ai32VC* after 10 ms light stimulation, n = 9 tomograms.

(I) The cumulative probability distribution of the MP tether length. The tether length is overlapping between Control (without light) and *Ai32VC* after 10 ms light stimulation. Control n = 68 tethered SVs and *Ai32VC* after 10 ms light stimulation = 118 tethered SVs.

	Parameters	Control	<i>Ai32VC-10ms</i>	p-values
A	Fraction of non-tethered SVs	0.52 \pm 0.04	0.23 \pm 0.04	0.0001 \$
B	Fraction of tethered SVs	0.50 \pm 0.03	0.70 \pm 0.05	0.004 \$
C	Fraction of SVs with single tethers	0.41 \pm 0.04	0.30 \pm 0.03	0.3 \$
D	Fraction of SVs with single membrane-attached tethers	0.31 \pm 0.04	0.30 \pm 0.07	0.7 \$
E	Fraction of SVs with single presynaptic density-attached tethers	0.10 \pm 0.03	0.06 \pm 0.03	0.7 \$
F	Fraction of SVs with multiple-tethers	0.06 \pm 0.02	0.40 \pm 0.07	0.002 \$
G	Fraction of docked SVs	0	1.00 \pm 0.04	---
H	Tether length [nm]	17.7 \pm 0.8	16.8 \pm 0.9	0.4 Δ
I	Single tether length [nm]	18.6 \pm 0.9	15.2 \pm 1.2	0.4 \$
J	Single membrane-attached tether length [nm]	19.6 \pm 1.1	15.8 \pm 1.3	p > 0.05 #
K	Single presynaptic attached tether length [nm]	15.4 \pm 1.2	10.2 \pm 1.8	p > 0.05 #
L	Multiple-tether length [nm]	15.3 \pm 2.17	18.5 \pm 2.1	0.6 \$

← **Table 3.15: Fraction of SVs and length of tethers in the MP pool of Control and *Ai32VC* after 10 ms optical stimulation**

Data are presented as mean \pm SEM to show differences between Control (without light) and *Ai32VC* after 10 ms light stimulation. In (A, B) p-values are calculated by Student's unpaired two-tailed t-test (§); in (C-F) and (I, L) by one way ANOVA followed by Tukey's test (§); in (H) by two-tailed Wilcoxon-Rank-Sum test (Δ); In (J, K) by Kruskal-Wallis test followed by NPMC test (#). Data are acquired from one *C57/BL6* wild-type and one *Ai32VC* mouse (pooled together as Control without light stimulation, two mice) and one *Ai32VC* mouse after 10 ms light stimulation. Eight tomograms from control (without light) (Four tomograms from *C57/BL6* control and four tomograms from *Ai32VC* control) and nine tomograms from *Ai32VC* after 10 ms light stimulation are analyzed.

3.4.7 SV diameter for RA SVs was larger than for MP SVs after 10 ms stimulus

Earlier results could not encounter any homotypic fusion event at the IHC ribbon synapses (described in section 3.1 and 3.2, published in Chapochnikov et al., 2014; Strenzke et al., 2016), one possible reason could be the fast release of these structures. To evaluate this after shorter stimulation, vesicle diameter/tomogram was quantified in RA and MP vesicles after 10 ms optical stimulation. Most of the SVs showed a diameter between be 35-45 nm at Control and *Ai32VC*-10 ms ribbon synapses (Chapochnikov et al., 2014; Neef et al., 2014; Strenzke et al., 2016, also described above in section 3.1.3, 3.2.2). I did not encounter any fused vesicular structures around the ribbon or close to the AZ membrane. However, in *Ai32VC*-10 ms, several large vesicles and tubular structures were found in proximity of the ribbon synapse similar to previous observations (Chapochnikov et al., 2014; Lenzi et al., 1999, 2002; Neef et al., 2014). In *Ai32VC*-10 ms, SVs were significantly bigger in the RA pool compared to the MP vesicles, whereas for the Control no difference could be detected (Table 3.16).

	SV diameter [nm]	Control	<i>Ai32VC</i>-10ms	p-values
A	Ribbon-associated pool [nm]	50.9 \pm 0.06	52 \pm 1.60	0.9 §
B	Membrane-proximal pool [nm]	48.6 \pm 0.64	46.8 \pm 0.90	0.6 §

Table 3.16: Average SV diameter in the RA and MP pool of Control and *Ai32VC* after 10 ms light stimulation

Data are presented as mean \pm SEM to show differences between Control (without light) and *Ai32VC* after 10 ms light stimulation. P-values are calculated by one way ANOVA followed by Tukey's test (§). Data are acquired from one *C57/BL6* wild-type and one *Ai32VC* mouse (pooled together as Control without light stimulation, two mice) and one *Ai32VC* mouse after 10 ms light stimulation. Eight tomograms from control (without light) (Four tomograms from *C57/BL6* control and four tomograms from *Ai32VC* control) and nine tomograms from *Ai32VC* after 10 ms light stimulation are analyzed.

3.4.8 Summary

In section 3.4, I incorporated for the first time Opto-HPF at IHC ribbon synapses. This allowed the analysis of early exocytosis events in *Ai32VC* mice after 10 ms optical stimulation. Upon optical stimulation, the RA SV count was reduced compared to the non-stimulated Control. However, the complexity associated with filament formation remained comparable between Control and 10 ms stimulated *Ai32VC* IHCs. Together these observations indicate that the resupply of SVs to the ribbon, likely mediated by these tethers, might not start immediately after 10 ms optical stimulation with a ~ 15 ms stimulus-freezing temporal coupling, as shown with 20 ms or more continuous depolarization in cell physiology experiments (Moser and Beutner, 2000). On the contrary the MP SV count remained comparable to the non-stimulated control animals, possibly because RA SVs are mobilized to the AZ membrane to replenish the vesicles released upon optical stimulation. However, the fraction of tethered SVs in the MP pool increased significantly upon stimulation as SV are recruited at the AZ as proposed for conventional synapses (Fernández-Busnadiego et al., 2010; Siksou et al., 2007; Stigloher et al., 2011). In line with this, significantly more multiple-tethered and docked SVs were observed upon 10 ms optical stimulation, which were rarely observed when using 15 min high K^+ stimulation (described above in section 3.2.10 and 3.2.11). Therefore, the findings from Opto-HPF support the initial hypothesis that these steps are transient in wild-type during prolonged stimulation. Finally, fused SVs could not be captured after 10 ms stimulation. The comparative analysis of other time points remains to be investigated in future.

4. Discussion

Sensory synapses, involved in vision, hearing and balance are specialized structural and functional units, characterized by synaptic ribbons at the active zone (AZ). The synapses of the cochlear inner hair cells (IHCs) transmit acoustic information at rates of hundreds of Hz with sub-millisecond precision over long periods of time. They achieve this by employing a highly synchronous mode of exocytosis (Moser and Beutner, 2000). Possibly, different synaptic vesicle (SV) pools at ribbon synapses mediate different kinetic phases of exocytosis (Lenzi and von Gersdorff, 2001). A smaller population of membrane-proximal SVs contribute to the rapid phase of exocytosis (fusion of the readily releasable pool, RRP), whereas fusion of ribbon tethered SVs is likely to be underlying the slower component of exocytosis (sustained exocytosis) (Lenzi et al., 1999). Disruption of this delicate synaptic structure can lead to impaired vesicle release (Akil et al., 2012; Frank et al., 2010; Maxeiner et al., 2016) and auditory synaptopathy (Jing et al., 2013; Moser and Starr, 2016; Roux et al., 2006; Seal et al., 2008). In this thesis, I highlighted mechanism(s) and key regulators of the IHC presynaptic compartment, crucial for fast and temporally precise sustained exocytosis and SV replenishment. A systematic ultrastructural characterization of vesicle pools associated to the synaptic ribbon was performed to apprehend different functional release states at IHC ribbon synapses. The crucial findings are discussed in depth here.

4.1 New role of otoferlin in vesicle reformation

Otoferlin (*Otof*) mutations in human patients cause severe to profound deafness (Yasunaga et al., 1999). Interestingly, several missense mutations of *Otof* result in deafness only at elevated temperatures (Marlin et al., 2010; Starr et al., 1998). Therefore, in this thesis, I specifically concentrated on the Ile515Thr (I515T) mutation, which was earlier identified in human patients suffering from hearing loss with the onset of fever or rise in body temperature due to physical activities (Varga et al., 2006). In my experiments I induced an increased temperature condition in a mouse model carrying the same mutation (*Otof*^{I515T/I515T}) and compared the vesicle pools at physiological (36 °C) and elevated temperatures (39 °C) in wild-type littermate control (*Otof*^{+/+}) and *Otof*^{I515T/I515T} mutant ribbon synapses, first with random ultrathin sections and then by electron tomography (Strenzke et al., 2016).

Moreover, significant efforts have been made to understand different functionality of otoferlin using different vertebrate (mice and zebrafish) models (Chatterjee et al., 2015; Pangrsic et al., 2010; Pangršič et al., 2012; Roux et al., 2006; Strenzke et al., 2016; Vogl et al., 2015). So far, otoferlin has been implicated in SV tethering and priming (Pangrsic et al., 2010; Vogl et al., 2015) in addition to AZ clearance (Jung et al., 2015b; Pangrsic et al.,

2010). However, severe hearing impairments in otoferlin mouse mutants studied till date, was either accompanied by a severe reduction in otoferlin level (in *Otof*^{Pga/Pga}, 70 % reduction, Pangrsic et al., 2010) or complete abolishment of the protein (in *Otof* knockouts (KOs), Roux et al., 2006), probably masking other potential role of otoferlin in neurotransmission. However, in *Otof*^{d515T/I515T} mutants, the otoferlin protein level was reduced by 65 %. Also, *Otof*^{d515T/I515T} has a mild hearing impairment but enhanced adaptation rates of spiral ganglion neurons to continuous sound stimulus (Strenzke et al., 2016). Therefore, the *Otof*^{d515T/I515T} mutant mouse line with an intermediate hearing defect and substantial reduction in protein levels, but not complete absence served as an excellent mouse model to bring forth other unidentified roles of otoferlin in maintaining the dynamic vesicle pools at IHC ribbon synapses (Strenzke et al., 2016). Here the results imply towards the involvement of otoferlin in proper size vesicle reformation.

4.1.1 Sustained component of exocytosis at IHC ribbon synapse requires otoferlin

As stated above otoferlin is an important protein governing the presynaptic functionality at IHC ribbon synapses. Disruption or perturbation of otoferlin in the murine system heavily interferes with the presynaptic function of IHCs (Jung et al., 2015b; Pangrsic et al., 2010; Pangršič et al., 2012; Reisinger et al., 2011; Roux et al., 2006; Strenzke et al., 2016; Vogl et al., 2015). Therefore, in Strenzke et al., 2016, the involvement of otoferlin in presynaptic function was tested by perforated patch clamp recordings at different temperatures. The capacitance measurements at room temperature (RT) highlighted that in *Otof*^{d515T/I515T} mutants the RRP was unaffected upon depolarization of 2-20 ms. However, upon longer depolarization (50 ms or more), the rate of the sustained component of exocytosis was reduced (~ 340 SVs/s/AZ, compared to *Otof*^{+/+} where ~ 700 SVs/s/AZ are released) (Strenzke et al., 2016). Earlier studies have proposed that the sustained phase of exocytosis is pivotal for preparing release-competent SVs and replenishment of the RRP, for the next round of depolarization (Pangrsic et al., 2010). Therefore, it is conceivable that in *Otof*^{d515T/I515T} mutants the replenishment of the RRP was affected, but less severe than in *Otof* pachanga (*Otof*^{Pga/Pga}) mutants (~ 200 SVs/s/AZ were released during the sustained phase of exocytosis, Pangrsic et al., 2010, this mutant will be discussed thoroughly in section 4.2). Furthermore, this phenotype scaled well with the reduction in membrane-bound otoferlin levels, in *Otof*^{Pga/Pga} ~ 3 % membrane-bound otoferlin was detected whereas in *Otof*^{d515T/I515T} ~ 34 % otoferlin remained in the IHCs.

4.1.2 Large vesicles appear at 39 °C at *Otof*^{d515T/I515T} IHC ribbon synapses

In this study, the structural details of IHC ribbon synapses were resolved using conventional embedding of EM. The samples were incubated at two different temperatures: 36 and 39 °C, in either an inhibitory (Chapochnikov et al., 2014; Pangrsic et al., 2010; Strenzke et al.,

2016) and a mild-stimulatory (Neef et al., 2014; Strenzke et al., 2016) solution, to investigate the vesicle dynamics at physiological and elevated temperatures in activity altered IHCs (Strenzke et al., 2016). At first random ultrathin sections (70 nm) were analyzed. Most of the SVs were in the size range of 35 - 45 nm, comparable to previous reports (Chapochnikov et al., 2014; Neef et al., 2007, 2014). At physiological temperature i.e. 36 °C large vesicles > 45 nm were absent in the ribbon-associated (RA) and the membrane-proximal (MP) vesicle pool of *Otof*^{+/+} and *Otof*^{d515T/1515T}. On elevating the temperature to 39 °C, apart from the normal sized vesicles (35 - 45 nm), > 45 nm vesicles were observed in the RA and MP pool at *Otof*^{+/+} and *Otof*^{d515T/1515T} ribbon synapses. Interestingly, the accumulation of large vesicles was more pronounced upon stimulation in the *Otof*^{d515T/1515T} mutants (Strenzke et al., 2016). This suggest that the origin of these large vesicles could be either due to improper SV reformation from endocytosed compartments or represent large quanta release by homotypic fusion of vesicles that became visible only in the *Otof*^{d515T/1515T} mutant due to impaired replenishment. However, random ultrathin section analysis did not allow me to answer this question by singular effort as the spatial organization of the synapse and the associated vesicles was not resolved in 70 nm sections. To pinpoint the large vesicle spatial organization and size in 3-D, I refined my analysis further using electron tomography after mild-stimulation at 36 and 39 °C, which is in detail discussed below (in section 4.1.3 and 4.1.4).

4.1.3 EM study argues against homotypic fusion of vesicles

The mechanism of release at the IHC ribbon synapse is a topic of intense debate and still remains vague. The excitatory postsynaptic currents (EPSC) appear heterogeneous in amplitudes and shapes, which could be due to synchronized multi-vesicular release as proposed in rat IHC (Glowatzki and Fuchs, 2002) or frog saccular hair cell (Graydon et al., 2011) ribbon synapses. Alternatively, the heterogeneity of EPSC could be resultant of uni-vesicular release, through dynamic fusion pore flickering, as suggested for mice IHC ribbon synapses (Chapochnikov et al., 2014). In this thesis, one of the important findings was that the wild-type SV diameters at physiological temperature (both in the RA and MP pool) was comparable to those at room temperature (RT), as described previously (Chapochnikov et al., 2014). Further, in the *Otof*^{d515T/1515T} mutant the vesicle size increase was not a perfect squaring or cubic function, as it would be expected in the case of homotypic fusion of two or more SVs. Although large vesicles were observed far away from the ribbon (excluding the RA SVs, in a 350 nm radius), their occurrence remained unaltered irrespective of the temperature/genotype/activity state. Similar observations have been made earlier as well, where after high K⁺ stimulation for 15 min large vesicles or tubular structures (associated with homotypic fusion events) could not be detected in the proximity of AZ membrane. Instead, larger vesicles were observed at the distal part of ribbons after high K⁺ stimulation

(Chapochnikov et al., 2014). In addition STED and EM together indicated the presence of tubular compartments emerging distant from the ribbon, most likely representing bulk endocytosis (Lenzi et al., 2002; Neef et al., 2014; Revelo et al., 2014). These observations, pose arguments against homotypic fusion of SVs at *Otof*^{+/+} as well as at *Otof*^{d515T/I515T} ribbon synapses. Further, such events could not be detected after K⁺ stimulation of 1 min 45 sec (Neef et al., 2014) or 15 min (Chapochnikov et al., 2014) as well, which makes homotypic vesicle fusion very unlikely scenario at IHC ribbon synapses.

4.1.4 Vesicle reformation is affected in *Otof*^{d515T/I515T}

Using tomography, I observed apart from normal round vesicles, several flattened vesicles in the RA and the MP pool in *Otof*^{+/+} and *Otof*^{d515T/I515T} animals (Strenzke et al., 2016). These flattened vesicles were quite variable in size and on average larger than the SVs. This phenomenon was similar to previous observations after chemical fixation of empty vesicles in mutants for the glutamate transporters vGlut1 and vGlut3 (Siksou et al., 2013; Akil et al., 2012) or the acetylcholine transporter (vAcht) (Rodrigues et al., 2013). However, the variability between the mutant and wild-type was not statistically significant for the flattened vesicles, irrespective of the temperature (Strenzke et al., 2016). Therefore, in *Otof*^{d515T/I515T} glutamate refilling of SVs seems to be intact at IHC ribbon synapses. However, the round vesicles of the RA and the MP were significantly bigger at *Otof*^{d515T/I515T} synapses at both investigated temperatures (36 and 39 °C) (Strenzke et al., 2016). Previously, EM and STED microscopy highlighted that endosomal structures occupy the basal part of IHCs close to synaptic ribbons (Jung et al., 2015b; Lenzi et al., 2002; Neef et al., 2007; Revelo et al., 2014). STED microscopy elaborated our understanding further by showing that otoferlin labels such endosomal structures (Jung et al., 2015b; Revelo et al., 2014). Similarly, immunogold EM revealed that gold clusters labeling otoferlin were found on large cellular compartments, exceeding the size of SVs (35 - 45 nm) at the ribbon synapses (Strenzke et al., 2016). In *Otof*^{d515T/I515T} mutant IHCs these compartments were significantly larger than those observed in *Otof*^{+/+} (Strenzke et al., 2016). Therefore, appearance of large vesicles in the RA and MP pool and bigger endosomal structures found in ribbon vicinity cumulatively indicates a possible defect in reformation of normal sized SVs in *Otof*^{d515T/I515T} mice: Considering the high vesicle turnover rates at IHC ribbon synapses (~ 700 SVs/s/AZ published in Pangrsic et al., 2010), it would require an ultrafast SV reformation to cope up with this demand. The point mutation I515T in the C₂C domain of otoferlin obviously slows down the rate of SV turnover (~ 340 SVs/s/AZ published in Strenzke et al., 2016), therefore allowing the observation of large vesicles more frequently at the synaptic ribbon (Strenzke et al., 2016).

Finally, the analysis of tomograms allowed a better Z-resolution (Chen et al., 2008) to investigate approximately half of the synaptic ribbon (Frank et al., 2010; Jung et al., 2015a), unlike in ultrathin random sections. In the tomogram analysis, the number of vesicles in the RA and MP pool at either temperature remained comparable between *Otof*^{+/+} and *Otof*^{J515T/J515T} (Strenzke et al., 2016). The higher number of MP vesicles found in the random ultrathin sections at both temperatures upon stimulation might be due to transverse cuts of elongated vesicular structures.

At IHCs the adaptor protein-2 μ (AP-2 μ) which acts as an adapter molecule for clathrin-mediated endocytosis and an interaction partner of otoferlin (Duncker et al., 2013; Jung et al., 2015b), was proposed to mediate reformation of SVs from bulk-endocytic compartments upon 15 min high K⁺ stimulation at IHC ribbon synapses (Jung et al., 2015b). Disruption of AP-2 μ causes depletion of RA SVs at the distal ribbon part and a reduction of clathrin-coated structures close to ribbon synapses (Jung et al., 2015b). This is not the case in *Otof*^{J515T/J515T} mutants (Strenzke et al., 2016) or when otoferlin was completely abolished (Vogl et al., 2015). Therefore, this suggests that otoferlin and AP-2 μ act on different steps of the vesicle reformation process at IHC ribbon synapses (Strenzke et al., 2016).

4.1.5 Conclusion

The *Otof*^{J515T/J515T} mutant mice have enhanced adaptation to repetitive sound stimulation. Further, the sustained component of exocytosis was reduced (Strenzke et al., 2016). A similar but aggravated phenotype was demonstrated before in *Otof*^{Pga/Pga} mice supports an impairment of RRP replenishment (Pangrsic et al., 2010) or defective in AZ clearance (Jung et al., 2015b). The improper sized vesicle formation confirms the replenishment defect in *Otof*^{J515T/J515T} mutants (Strenzke et al., 2016). However, the defective reformation of SVs seem to be unaffected by a temperature rise (Strenzke et al., 2016). Therefore, we propose a new role for otoferlin in formation of proper sized SVs during the sustained phase of exocytosis (Strenzke et al., 2016). Fig. 4.1 summarizes the key findings of this section.

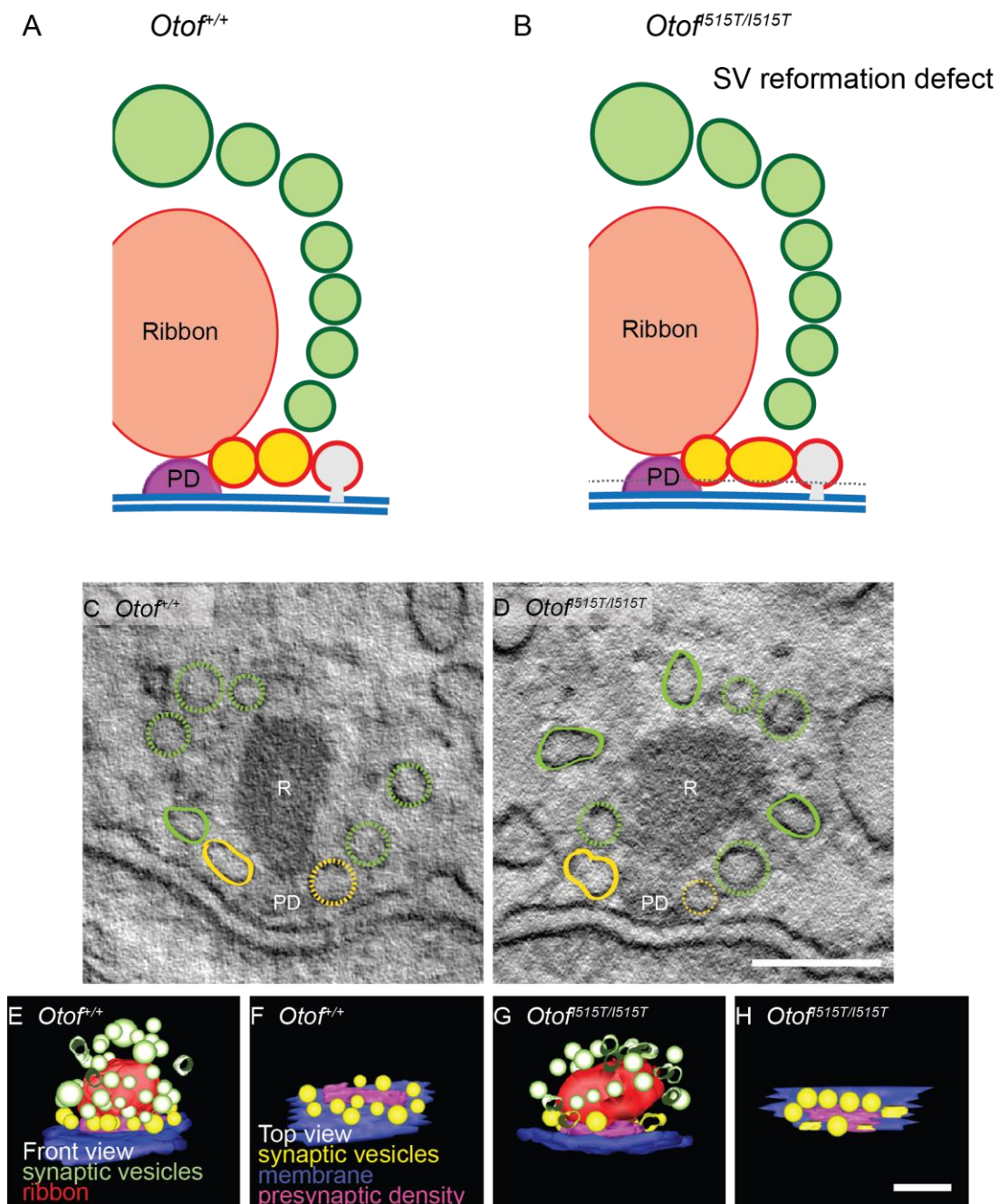


Figure 4.1 Enlarged vesicles indicate a SV reformation defect in *Otof*^{Δ515T/Δ515T} IHC ribbon synapses
 Upon stimulation large vesicles appear in the RA and MP pool of *Otof*^{Δ515T/Δ515T} IHC ribbon synapses.
(A-B) Schematic representation of *Otof*^{+/+} **(A)** and *Otof*^{Δ515T/Δ515T} **(B)** IHC ribbon synapses. Not drawn to scale.
(C-D) Exemplary tomographic virtual sections from the stimulatory condition of *Otof*^{+/+} **(C)** and *Otof*^{Δ515T/Δ515T} **(D)**. The round vesicles are highlighted with dotted lines (round vesicles: RA green and MP yellow). Flattened vesicle boundaries are drawn with solid lines (flattened vesicles: RA green and MP yellow). Scale bar, 100 nm; magnification, 12,000x.
(E-H) 3-D reconstruction of the RA (front view; **E, G**) and MP (top view; **F, H**) pools of SVs for *Otof*^{+/+} **(E-F)** and *Otof*^{Δ515T/Δ515T} **(G-H)** from the stimulatory condition. Scale bar, 100 nm. Panels E-H published in Strenzke et al., 2016.

4.2 Stimulation alters the vesicle tethering at IHC ribbon synapses

Sound encoding relies on precise and tonic neurotransmitter release at IHC ribbon synapses upon sustained Ca^{2+} influx (von Gersdorff, 2001). This part of the thesis concentrated on the structural basis for precise neurotransmission on the level of single IHC ribbon synapses. In order to do so, ribbon synapses were studied in an activity dependent manner to correlate structure and function. Exocytosis was either triggered by depolarizations using high K^+ solutions (Chapochnikov et al., 2014; Jung et al., 2015b; Pangrsic et al., 2010; Vogl et al., 2015) or inhibited by preventing Ca^{2+} influx (Chapochnikov et al., 2014; Pangrsic et al., 2010; Strenzke et al., 2016) for 15 min coupled to high-pressure freezing (HPF) (Moor, 1987).

Moreover, vesicle morphology and vesicular filaments' (tethers and inter-connectors) distribution at the ribbon and the AZ membrane were compared methodologically between wild-type and *Otof*^{Pga/Pga} mutant (earlier shown to have impaired replenishment defect in IHC ribbon synapses, Pangrsic et al., 2010). These mutants previously showed an intermediate reduction in overall expression of otoferlin (~ 70 %, Pangrsic et al., 2010), quite comparable to *Otof*^{d515T/515T} mutant described in the previous section (~ 65 %, Strenzke et al., 2016, section 4.1). However, *Otof*^{Pga/Pga} mouse line was completely deaf (Pangrsic et al., 2010; Schwander et al., 2007) like *Otof* KOs (Roux et al., 2006) due to reduced levels of membrane-bound otoferlin fraction (Pangrsic et al., 2010). Therefore, by revisiting *Otof*^{Pga/Pga} mutants, I probed the structural correlate for the reported replenishment deficit in *Otof*^{Pga/Pga} mouse line. Additionally, the effect of partial loss of otoferlin in tether formation was tested in *Otof*^{Pga/Pga} IHCs, providing a correlation to the absence of otoferlin in *Otof* KOs (previously shown to have reduced number of the short tether in the MP pool, Vogl et al., 2015). In the end, I speculate about a release sequence of SV at IHC ribbon synapses.

4.2.1 Ribbon morphology was unaltered in the *Otof*^{Pga/Pga} mutant

Organization of AZ is crucial for neurotransmission release. So far the absence of presynaptic scaffolding proteins such as ribeye, the main component of presynaptic ribbons (Schmitz et al., 2000b) and the cytomatrix of the AZ (CAZ)-associated structural protein (CAST) were shown to maintain either the presence (Maxeiner et al., 2016) or the size of the ribbon (tom Dieck et al., 2012) in the photoreceptor terminal. However, a mutation in the "probable Ca^{2+} sensing" protein otoferlin (Johnson and Chapman, 2010; Roux et al., 2006) did not indicate any gross morphological changes of synaptic ribbon at the IHCs (Pangrsic et al., 2010; Strenzke et al., 2016; Vogl et al., 2015, in this study). However, *Otof* KOs showed a small fraction of floating ribbons which were shaped accordingly to the age (P15, flat and plate likes, Roux et al., 2006) indicating that the

maturation and development of IHCs were intact (Roux et al., 2006; Sobkowicz et al., 1986). This observation was in contrast to the bassoon deficient (Dick et al., 2003; Frank et al., 2010; Khimich et al., 2005) or *ribeye* *KOs* (Maxeiner et al., 2016) where ribbon synapses lacking the major components fail to develop.

4.2.2 *Otof*^{*Pga/Pga*} mutation does not alter the size of vesicles

Similar to conventional embedding, in HPF samples, a broad range of vesicle sizes (~ 25 – 230 nm) was found at the synaptic ribbon. Moreover, the SV diameter of RA and MP pool in wild-type and *Otof*^{*Pga/Pga*} remained unaltered in inhibitory/stimulatory conditions of IHCs in contrast to already published work on *Otof*^{*d515T/1515T*} mice mutant (Strenzke et al., 2016, described above in section 4.1). This discrepancy could be due to distinct immobilization methods employed (conventional embedding Strenzke et al., 2016 vs. HPF for EM here), but since the maximum peak of the SV diameter distribution was comparable between both analysis, this appears rather unlikely. Over the past years, a variety of EM studies on IHCs synaptic vesicle diameters (Chapochnikov et al., 2014; Neef et al., 2007, 2014; Strenzke et al., 2016) proposed a diameter of ~ 40 nm, which is in-line with my work on vesicles of *Otof*^{*Pga/Pga*} mutants. However, the significantly bigger vesicles in the RA pool compared to MP vesicles upon stimulation of wild-type IHCs was previously reported and suggested to represent bulk endosomal compartments distal to the AZ membrane (Chapochnikov et al., 2014). A striking difference between both experimental series was that the experiments for *Otof*^{*Pga/Pga*}, were carried out at RT, whereas in Strenzke et al., 2016 the experiments were performed at physiological temperature. The higher temperature might have resulted in larger vesicles in *Otof*^{*d515T/1515T*} mutants. In line with this, it has been shown that exocytosis recorded by whole-cell capacitance increments upon depolarizations was increased 3 fold at physiological temperature compared to RT at IHCs (Nouvian, 2007; Strenzke et al., 2016). Therefore, experiments at higher temperature are required in parallel with *Otof*^{*d515T/1515T*} mutants to confirm this hypothesis in future.

4.2.3 In the *Otof*^{*Pga/Pga*} mutants clusters of synaptic and pleomorphic vesicles are observed

The exact role of the synaptic ribbon as specialized machinery for neurotransmitter release remains enigmatic. Several roles of synaptic ribbons were proposed: (i) promotion of a large RRP of vesicles via clustering of Ca²⁺ channels at vesicular release sites (Frank et al., 2010; Khimich et al., 2005, Maxeiner et al., 2016) (ii) facilitating vesicle replenishment at the AZ ('conveyor belt' and 'crowd surfing' models, Bunt, 1971; Gray and Pease, 1971; Graydon et al., 2014; Lenzi and von Gersdorff, 2001; Snellman et al., 2011; Vollrath and Spiwoks-Becker, 1996) (iii) facilitating multi-vesicular release by synchronization of the vesicle fusion (Edmonds, 2004; Fuchs, 2005) and (iv) functioning as a diffusion barrier to

keep high local Ca^{2+} concentrations (Graydon et al., 2011). In this thesis, comparison of *Otof*^{Pga/Pga} and wild-type mice aimed to identify the structural correlates for processes at the synaptic ribbon by analyzing RA pool in depth.

In my experiments, the total RA SV count was unaltered between inhibitory and stimulatory conditions, for wild-type. However, at *Otof*^{Pga/Pga} the SVs were densely packed around the ribbon, which became even more apparent in the absence of extracellular Ca^{2+} (inhibition). As a consequence, under the inhibitory condition of *Otof*^{Pga/Pga}, more SVs accumulated at the distal and the proximal part of the ribbon. My data confirm a contribution of Ca^{2+} in SV replenishment, as shown for cone photoreceptor ribbon synapses (Babai et al., 2010) in addition to this otoferlin is crucial for sustaining SV replenishment at IHC ribbon synapses (Pangrsic et al., 2010; Strenzke et al., 2016). Consequently, under reduced otoferlin levels in addition to the absence of Ca^{2+} , RA SVs accumulated at the synaptic ribbon of *Otof*^{Pga/Pga}. Upon continuous Ca^{2+} influx during prolonged stimulation, RA SV count reverts to wild-type level in *Otof*^{Pga/Pga}, despite that the vesicles were closely packed around the ribbon. I propose that the RA vesicles might take a back seat and accumulate at the synaptic ribbon due to a downstream block after SV docking (will be discussed later in section 4.2.7) accounting for reduced sustained exocytosis in *Otof*^{Pga/Pga} (Pangrsic et al., 2010), Ca^{2+} can only partly rescue this block. This hypothesis is strengthened by the previous report, suggesting that Ca^{2+} dependent vesicle resupply was unaltered in *Otof*^{Pga/Pga} and the replenishment deficiency can partly be rescued by increasing extracellular Ca^{2+} (Pangrsic et al., 2010). Even though the SVs were densely packed around the ribbon; I did not observe homotypic fusion between adjacent SVs, similar to previous observations (Chapochnikov et al., 2014; Graydon et al., 2011; Strenzke et al., 2016).

Strikingly, pleomorphic vesicles of unknown origin accumulated in the cytoplasm of the *Otof*^{Pga/Pga} IHCs. In *Otof*^{Pga/Pga} inhibitory condition, these clusters were found in the proximity of the ribbon and were often overlapping with the RA vesicles. These pleomorphic vesicles closer to the ribbon were significantly bigger than normal SVs in *Otof*^{Pga/Pga} under inhibitory condition. Upon stimulation, these clusters appeared only further away from the ribbons and the pleomorphic vesicles in each cytosolic cluster were even bigger compared to those found in the ribbon proximity. Similar compartments were also observed in the cytoplasm of the deaf *Otof* *KOs*, but less frequent and never in wild-types. This might indicate a correlation of otoferlin protein levels and the presence of such clusters in IHCs. Comparable (in appearance) pleomorphic compartments were earlier observed using conventional embedding upon mutation of tryptophan-rich basic (Wrb) protein in the receptor of transmembrane recognition complex (TRC40) pathway (Vogl et

al., 2016). The authors proposed that TRC40 pathway mediate membrane insertion of tail anchor protein otoferlin into the endoplasmic reticulum crucial for exocytosis at hair cells of zebrafish and mice. The IHC specific conditional *Wrb KO* showed a reduction in otoferlin level (~ 40 % reduction) caused due to impaired biogenesis of otoferlin. This was supported by the observation that lysosomal marker (Lamp1) staining was increased in the *Wrb KO* (Vogl et al., 2016). *Otof^{Pga/Pga}* and *Otof KO*s mice exhibit reduced or no otoferlin in the IHCs (Pangrsic et al., 2010; Roux et al., 2006), possibly explaining such pleomorphic structures appear in deaf mutants of otoferlin. Moreover, both *Otof^{Pga/Pga}* and *Wrb KO* show replenishment deficits, also more pronounced in *Otof^{Pga/Pga}* mutants (Pangrsic et al., 2010; Vogl et al., 2016). Therefore, these structures could be lysosomal, but vesicle reformation defect due to impaired replenishment cannot be completely ruled out for *Otof^{Pga/Pga}*. Notably, such structures did not resemble bulk endocytic events observed in the AZ of wild-type ribbon synapse (Chapochnikov et al., 2014; Lenzi and von Gersdorff, 2001; Neef et al., 2014, and here).

4.2.4 Distinct vesicle pools determine different stages of release at IHC ribbon synapses

At IHC ribbon synapses two functional vesicle pools have been described, based on capacitance measurements. (i) The initial exponential phase of capacitance increase upon 10 - 20 ms depolarization of IHCs represents the exocytosis of the RRP (Moser and Beutner, 2000; Rutherford and Roberts, 2006) and (ii) the linear phase upon > 20 ms depolarization accounts for the SVs to be released upon depletion of the RRP (Moser and Beutner, 2000). Ultrastructurally, the RRP was proposed to be constituted by the MP SVs (Lenzi and von Gersdorff, 2001; Lenzi et al., 1999) and the RA SVs represented the slower release component (Lenzi et al., 1999). Therefore, in this study these two morphological vesicle pools were systematically investigated at wild-type and *Otof^{Pga/Pga}* IHC ribbon synapses.

My data after HPF/FS showed elaborate filament connectivity (tethers and inter-connectors), organizing SVs in the RA and MP pools. Such filaments were earlier reported using conventional aldehyde fixation for EM (Frank et al., 2010, in AZ membrane proximity ; and Sobkowicz et al., 1982, in synaptic ribbon proximity) and by using HPF/FS and freeze-etched/FS samples (Jung et al., 2015b and Vogl et al., 2015, at AZ membrane; Usukura and Yamada, 1987, at synaptic ribbons). Most likely different proteins orchestrate SV tethering at IHC ribbon synapses, governing the release competence of each vesicle pool. I observed in this thesis that these tethers can be categorized according to the number of filament connections and their localization (depending on where the SV was connected: synaptic ribbon/adjacent SVs/presynaptic densities/AZ membrane). A similar organization of proteinaceous tethers and inter-connectors is observed in the presynaptic terminals of murine excitatory synapses between parallel fibers and Purkinje cells (Landis et al., 1988),

in the rat and mice hippocampus (Siksou et al., 2007), rat cerebrocortical synaptosomes (Fernández-Busnadiego et al., 2010) and at the neuromuscular junctions (NMJs) of *C. elegans* (Stigloher et al., 2011) and zebrafish (Helmprobst et al., 2015). The structure of such filaments has been associated with three major functions at the synapses: (i) organization of SVs in the presynaptic compartment (Cole et al., 2016; Fernández-Busnadiego et al., 2010; Hirokawa et al., 1989; Landis et al., 1988; Siksou et al., 2007; Stigloher et al., 2011), (ii) mobilization of SVs to the AZ membrane (Fernández-Busnadiego et al., 2010; Landis et al., 1988; Siksou et al., 2007; Stigloher et al., 2011), and (iii) linking (possible recruitment) and spatial coupling of SVs to the AZ membrane prior to docking (Cole et al., 2016; Fernández-Busnadiego et al., 2010, 2013; Helmprobst et al., 2015; Siksou et al., 2007; Stigloher et al., 2011).

4.2.5 The *Otof*^{Pga/Pga} mutation hinders multiple-filament formation at the distal part of the ribbon which is present in wild-type upon stimulation

In the current study, upon stimulation, the number of filaments per SV increased in the RA pool of wild-type and also *Otof*^{Pga/Pga} IHCs. However, the fraction of SVs with filaments was reduced in *Otof*^{Pga/Pga}. Could an increased presence of filaments at SVs help with the demanding task of SV replenishment at IHC ribbon synapses? Speculatively, at least two mutually not exclusive scenarios could explain the role of these filaments in the SV turnover: (i) this could represent a scaffold around the synaptic ribbon to keep SVs in proximity to ensure vesicle resupply during the sustained phase of exocytosis, as proposed in conventional synapses (Hallermann and Silver, 2013) and (ii) filaments could provide a mechanism for SV transport along the ribbon to the AZ membrane, as it was proposed earlier for photoreceptor ribbon synapses (Bunt, 1971; Gray and Pease, 1971).

In my experiments, the RA filaments were either ribbon-attached tethers (tethering SV with the ribbon) or ribbon-associated-inter-connectors (interconnecting adjacent SVs). Similar filaments were proposed to serve as a scaffold to organize SVs before release at the synapse with larger electron dense projections (Fouquet et al., 2009; Hallermann and Silver, 2013; Helmprobst et al., 2015; Kittelmann et al., 2013; Stigloher et al., 2011). At wild-type IHC ribbon synapses the average RA filament length was ~ 20 nm. The ribbon-attached tethers were ~ 25 nm and ribbon-associated inter-connectors were ~ 15 nm long. In contrast, at NMJs, the inter-connectors were ~ 30 nm long and the filaments emanating from the electron dense projection could reach up to 100 nm (Helmprobst et al., 2015; Stigloher et al., 2011). Therefore, it is tempting to speculate that the synaptic ribbon, in association with ribbon-attached tethers and ribbon-associated inter-connectors, provides a closer spatial scaffold for the SVs compared to synapses with structural homologous electron dense projections. Otoferlin does not seem to affect the length of the filaments in

the RA pool, as the filament length remained comparable between wild-type and *Otof*^{Pga/Pga}, indicating other proteins might be involved in the spatial organization of SVs in the RA pool. However, it will be interesting to see if complete deletion of otoferlin results in a reduction of a subset of short filaments in the ribbon-associated pool as shown previously in case of the membrane-proximal tethers (Vogl et al., 2015). Moreover, the presence of in general shorter inter-connector lengths at the IHC ribbon synapses compared to conventional synapses (Fernández-Busnadiego et al., 2010; Landis et al., 1988; Siksou et al., 2007) might also reflect divergent molecular players between conventional and ribbon synapses. At conventional synapses, such inter-connectors were associated with synapsin, which is suggested to act as SV 'binder' in the 'reserve' pool restricting the mobility of SVs (Fernández-Busnadiego et al., 2010; Landis et al., 1988; Pieribone et al., 1995). However, in *synapsin* triple-KO mice the inter-connectors were not completely abolished (reduced by 63 %) (Siksou et al., 2007), suggesting, that the function of synapsin can be partially compensated by other inter-connector components. Since IHCs are lacking synapsin (Safieddine and Wenthold, 1999), they might exhibit higher vesicle mobility than observed in conventional synapses (Holt et al., 2004). Moreover, at IHC ribbon synapses, I observed that the complexity of RA filaments (in terms of number of filaments/SVs) increases during stimulation at both wild-type and *Otof*^{Pga/Pga} mutants. However, upon stimulation at wild-type ribbon synapses significantly more SVs with multiple-filaments were observed compared to *Otof*^{Pga/Pga} stimulated IHCs, only at the distal part of the ribbon. This observation could suggest that at the distal end of the ribbon SVs are spatially organized around the synaptic ribbon with help of multiple-filaments in wild-type than *Otof*^{Pga/Pga} mutants. This could be a mechanism for efficient vesicle resupply at the synaptic ribbon for the next round of release.

The second possibility is that these multiple-filaments assist SVs' mobility along the ribbon. A previous study using live epifluorescence microscopy showed that SVs loaded with FM1-43 moved to the presynaptic AZ in goldfish retinal bipolar cells (Zenisek et al., 2000). However, until today it is not clear if these SVs require filaments around the ribbon for mobility. Two proposed models for ribbon synapses could explain the mobility of SVs along the ribbon synapses. The "crowd surfing" model suggests that SVs are passively diffusing, where-in transient binding and unbinding of multiple-tethers provides directed guidance to the SVs to move along the ribbon, at retinal bipolar cell ribbon synapses (Graydon et al., 2014). In contrast, the conveyor belt model proposed that SVs are transported in an ATP dependent manner in association with motor proteins (Bunt, 1971; von Gersdorff et al., 1996; Gray and Pease, 1971). The active vesicle transport theory (ATP dependent) by motor proteins was prompted by the identification of a kinesin polypeptide (Kif3a) at the murine photoreceptor ribbon synapses by post-embedding immunogold EM (tom Dieck et al.,

2005; Muresan et al., 1999), while microtubules (the pathway for kinesin motors) were missing (Muresan et al., 1999). Moreover, freeze-etching/FS of frog retina photoreceptors showed that the ribbon surface was decorated with proteinaceous knobs, which were proposed to function as 'stepping stones' on which the motorized filaments might still walk (Usukura and Yamada, 1987). Another potential candidate protein that could mediate active SV transport along the ribbon to the AZ membrane could be the actin-based motor protein myosin VI (Myo6). Post-embedding immunogold EM showed Myo6 presence at IHC AZs. The labeling was found at the AZ membrane, similar to otoferlin (Roux et al., 2006, 2009; Strenzke et al., 2016), but also around the synaptic ribbon itself (Roux et al., 2009). Moreover, using capacitance measurements Roux et al., 2009 could show that exocytosis was significantly reduced in *Myo6* *KOs* despite normal Ca^{2+} currents. Further, biochemical evidences suggest that otoferlin and Myo6 physically interact with each other (Heidrych et al., 2009; Roux et al., 2009). Additionally, actin filaments (the pathway for myosin to move) were proposed to regulate exocytosis at IHC ribbon synapses (Guillet et al., 2016; Vincent et al., 2015). Actin was proposed to limit the access of SVs to the release sites (Vincent et al., 2015). Thus it can be suggested that the ribbon in combination with F-actin control the flow of SVs during exocytosis by limiting excessive and asynchronous glutamate release (Vincent et al., 2015), as it was previously proposed for central synapses (Cingolani and Goda, 2008). However, the immunohistochemistry data of these two studies are quite contradictory. Vincent et al., 2015 proposed an F-actin 'cage' directly around the synaptic ribbon, but in Guillet et al., 2016, F-actin localization was detected at the basolateral part of the IHCs, they did not detect enrichment near the synaptic ribbons. Similarly, using HPF, I did not identify the proposed 'cage' like structure around the ribbon, however in future experiments after disrupting the actin filaments by latrunculin A and cytochalasin D need to be performed at the ultrastructural level. Moreover, it is essential to keep in mind another finding at retinal bipolar cells that argues against the ATP-dependent conveyor belt hypothesis. It was shown that neither the fast nor the slow component of SV exocytosis were affected when ATP- γ S was dialyzed into isolated goldfish retinal bipolar cell terminals (Heidelberger et al., 2002).

My data could not unanimously agree to either one of these hypotheses. In the future, experiments with correlative light and electron microscopy should be performed to understand the true molecular nature of these filaments at the RA pool.

4.2.6 Single membrane-attached tethers recruit vesicles to the membrane at both wild-type and *Otof*^{Pgα/Pgα} IHC ribbon synapses

In the MP SV pool, I observed SVs without tethers, with single membrane-attached and presynaptic density-attached tethers. Additionally, multiple-tethered and docked SVs were

encountered in rare cases possibly representing different stages of vesicles before being released. At conventional synapses tethering of vesicles to the AZ membrane has been suggested to recruit SVs before docking and priming (Fernández-Busnadiego et al., 2010, 2013; Verhage and Sørensen, 2008). At IHC ribbon synapses, proper demarcation of these steps remains unclear. That might be due to the peculiar protein composition at the IHC AZ. Neuronal soluble NSF attachment receptor proteins (SNAREs) (Nouvian et al., 2011) or the mammalian homologue of Unc-13 (Munc13) (Vogl et al., 2015) appear to be dispensable for IHC ribbon synapse functionality, which further strengthens the pursuit of other unknown molecular players involved in tethering. Recently, rab-3 interacting molecule 2 α (RIM2 α) was shown to participate in tether formation at the AZ membrane of IHCs (Jung et al., 2015a, will be described later in detail in section 4.3). A further possible candidate seems to be otoferlin since the *Otof* KO mice lack the fraction of short tethers at the AZ membrane (Vogl et al., 2015). In the current study in-depth analysis of the MP pool upon stimulation revealed that significantly more SVs get tethered to the AZ membrane of wild-type synapses via a single tether. A comparable fraction of SVs gets tethered at *Otof*^{Pga/Pga} synapses as well. As stated above, tether formation was not restricted to the membrane, but also takes place at the presynaptic density. Probably scaffold proteins like bassoon as part of the presynaptic density at IHC ribbon synapses (Frank et al., 2010; Jing et al., 2013; Khimich et al., 2005) could play a role in vesicle binding or recruitment. However this is yet to be verified for IHC ribbon synapses, as the isolated role of the presynaptic density in vesicle replenishment/release is hard to approach because the loss of bassoon is accompanied by the loss of the synaptic ribbon as well (Frank et al., 2010; Khimich et al., 2005). In the current experiments, presynaptic density-attached tethers remained comparable irrespective of the activity state or genotype, possibly due to the intact anchoring of the synaptic ribbons. In the end, I propose that most likely SVs are recruited closer to the membrane via single tethers upon stimulation, which was unaffected in the *Otof*^{Pga/Pga} synapses.

4.2.7 Further steps after recruitment of vesicles at the AZ membrane

At conventional synapses, the recruitment of SVs to the AZ is followed by a tight coupling of SVs to the membrane, first by multiple short-tethers (Fernández-Busnadiego et al., 2010, 2013) and finally SVs are docked at release sites (Imig et al., 2014; Siksou et al., 2009). This phenomenon is still elusive for IHC ribbon synapses. I observed that SVs with multiple-tethers were extremely rare at wild-type IHCs; in line with this observation, morphologically docked SVs were not frequent as well and if captured, mostly upon stimulation. These results indicate that either one of the two scenarios might take place: (i) the involvement of a faster release machinery at IHCs compared to conventional synapses or (ii) the steps of multiple-tether formation and SV docking does not occur at IHCs because

of the peculiar molecular machinery as stated before (Nouvian et al., 2011; Vogl et al., 2015) compared to conventional synapses (Fernández-Busnadiego et al., 2013; Imig et al., 2014; Siksou et al., 2009). I propose the former scenario. At IHCs the exocytosis occurs in two stages the exponential phase deplete the RRP pool constituted by the docked SVs close to the Ca^{2+} channels within 20 ms depolarization (Moser and Beutner, 2000). As a consequence the multiple-tethered and docked SVs, which earlier shown to represents the active state of release at conventional synapses (Fernández-Busnadiego et al., 2013; Imig et al., 2014; Siksou et al., 2009; Stigloher et al., 2011) were already released at the wild-type ribbon synapses. Thus could not be captured frequently with 15 min stimulation in my experiments. Additionally, IHCs are distinct from conventional synapses because of its capability to continue a tonic release upon continuous depolarization (von Gersdorff, 2001). The continuous depolarization of 20 ms or more, excites a slower component of exocytosis (Moser and Beutner, 2000), that is sustained by the striking replenishment of SVs for the next round of release (Pangrsic et al., 2010). Therefore, the docked SVs in my wild-type samples if at all observed were always under the stimulatory condition, due to the capability of IHC ribbon synapse to sustain the replenishment of the RRP (Pangrsic et al., 2010) even after 15 min high K^+ stimulation. Interestingly, both multiple-tethered and docked SVs in the MP pool seem to accumulate at *Otof*^{*Pga/Pga*} AZs in close proximity to the ribbon upon stimulation. This either direct towards improper Ca^{2+} sensing (Roux et al., 2006) or obstruction downstream of SV docking in *Otof*^{*Pga/Pga*} IHC ribbon synapses, like fusion of docked SVs (Roux et al., 2006; Vincent et al., 2014) or release site clearance (Jung et al., 2015b). As stated in the former study Ca^{2+} sensing and Ca^{2+} dependent fusion was intact in *Otof*^{*Pga/Pga*}, as the depletion of RRP within 20 ms depolarization was unaffected (Pangrsic et al., 2010). Therefore improper release site clearance upon prolonged stimulation is the most probable candidate mechanism. In agreement, normal recruitment of SVs at the membrane and a roadblock downstream of docking creates a 'bottleneck' situation consequently the RA SVs were piled-up. Thereafter, these SVs start to accumulate at release sites upon strong stimulation in *Otof*^{*Pga/Pga*} AZs. Interestingly, most of the docked SVs were located close to the presynaptic density (< 100 nm), where the Ca^{2+} channels cluster at mature IHC ribbon synapses (Frank et al., 2010; Jung et al., 2015a; Rutherford, 2015; Wong et al., 2014). Therefore, in conclusion, I hypothesize that multiple-tethered and docked SVs at ribbon synapses represent the distinct steps of exocytosis ultimately preceding to SV fusion, as observed at conventional synapses (Fernández-Busnadiego et al., 2010; Siksou et al., 2009; Stigloher et al., 2011; Szule et al., 2012).

Additionally, in my experiments, variable tether lengths were observed spanning a range of 4.4 to 48.7 nm. Remarkably, at stimulated *Otof*^{*Pga/Pga*} IHC ribbon synapses, the average tether length was reduced compared to wild-type stimulatory condition, regardless

whether they were single tethers to the presynaptic density or to the membrane. However, the length of multiple-tethers was comparable between wild-type and *Otof*^{Pga/Pga}. This was in contrast to previous estimates in *Otof KO* mice. Multiple-tethered vesicles were not reported, as well as the fraction of short tethers was significantly reduced, thus on average longer tethers were present in the *Otof KO* (Vogl et al., 2015). Both, *Otof*^{Pga/Pga} and *Otof KO* mice are profoundly deaf (Pangrsic et al., 2010; Roux et al., 2006), but residual otoferlin expression in *Otof*^{Pga/Pga} IHCs (~ 30 % left) seems to allow vesicle fusion of the RRP upon short depolarization (< 20 ms) (Pangrsic et al., 2010). What makes the *Otof*^{Pga/Pga} mutant distinct from *Otof KO*s is the impaired vesicle replenishment, possibly due to impaired release site clearance with normal fusion kinetics (Pangrsic et al., 2010; Roux et al., 2006; Vogl et al., 2015).

Moreover, using conventional embedding for EM, it was further shown that the number of MP SVs was reduced upon stimulation in both wild-type and *Otof*^{Pga/Pga} mutant, although the number remained comparable between genotypes (Pangrsic et al., 2010). In the present study, a reduction of MP SV count was not observed, neither by comparing inhibition and stimulation nor between genotypes. HPF/FS allowed a close-to-native state preservation (Imig et al., 2014; Moor, 1987; Siksou et al., 2007; Stigloher et al., 2011) in contrast to conventional aldehyde fixation, as was used in the former study (Pangrsic et al., 2010). A further advantage was the incorporation of 3-D analysis using electron tomography in this study, which allowed analysis of the SV distribution in Z-axis with better resolution compared to ultrathin sections (Chen et al., 2008).

In the end, the temporal resolution to capture the ultrafast RRP fusion was not achieved with prolonged K⁺ stimulation. Therefore, in future experiments combining optogenetic stimulation with HPF (Opto-HPF) are required (Kittelman et al., 2013; Watanabe et al., 2013a, 2013b). This way, a very short and tissue-specific stimulus can be applied immediately prior to freezing arresting the dynamic exocytosis events. Furthermore, by using different stimulus durations, the sequential events can be observed at IHC ribbon synapses. My first experiments with Opto-HPF will be described in section 4.4.

4.2.8 Conclusion

In summary, the present study focused on the localization of SVs and associated phenomena of tethering. Incorporation of HPF/FS in combination with electron tomography at IHC ribbon synapses allowed faithful correlation of presynaptic anatomy and functionality at the IHC ribbon synapses of wild-type. Further, *Otof*^{Pga/Pga} mice (Pangrsic et al., 2010; Schwander et al., 2007) served as a model to study the vesicle pool dynamics and role of filaments during SV replenishment (earlier shown to have a replenishment

impairment, Pangrsic et al., 2010). Two morphological pools were defined and analyzed: the RA and MP SV pool as described previously (Jung et al., 2015a; Strenzke et al., 2016).

At the RA pool, the filament connectivity of the RA SVs appeared more complex upon stimulation, especially at the distal part of the ribbon in wild-type. This filament connectivity most likely is required for a close spatial organization of SVs with synaptic ribbon and this way promotes sustained vesicle resupply in wild-type ribbon synapses. The filament connectivity was significantly reduced in the *Otof*^{Pga/Pga} mice, indicating that filaments in association with properly anchored ribbon could play a role in vesicle replenishment. Moreover, in *Otof*^{Pga/Pga} IHCs large vesicle clusters of unknown origin and variable diameters were observed in the vicinity of the synaptic ribbons upon inhibition.

At the MP pool, most of the vesicles were tethered at wild-type IHC ribbon synapses upon stimulation, with a more substantial fraction of single membrane-attached tethers. Morphologically docked vesicles were rarely found at wild-type AZs but appeared more often at *Otof*^{Pga/Pga} ribbon synapses especially upon stimulation. Most of the docked SVs were observed close to the ribbon, where the Ca²⁺ channels are clustered ensuring a tight Ca²⁺ influx-vesicle coupling. Additionally, at *Otof*^{Pga/Pga} ribbon synapses multiple-tethered vesicles were distinctively frequent at the AZ membrane. Based on these observations I contemplate following takes place at *Otof*^{Pga/Pga} IHC ribbon synapses: at the beginning of the stimulus, vesicles are available as a consequence the RRP pool size is comparable between wild-type and *Otof*^{Pga/Pga} (Pangrsic et al., 2010). Upon continuous and long stimulation the release sites close to the Ca²⁺ channels get occupied and further not cleared. Consequently, multiple-tethered (as defined in, Fernández-Busnadiego et al., 2013) and docked SVs (as defined in, Imig et al., 2014) starts to accumulate at the membrane leading to further accumulation of RA SVs upstream. However, which release phase is affected in *Otof*^{Pga/Pga} cannot be fully solved, but our data confirm previous findings, suggesting a defect in release site clearance.

Here I propose the following release sequence is taking place at wild-type IHC ribbon synapses: Upon stimulation, different modes of endocytosis contributes to the efficient reuptake of membrane at IHC ribbon synapses, such as clathrin-dependent retrieval and clathrin-independent bulk endocytosis (Neef et al., 2014). The proper sized SVs are then reformed from these endocytic compartments (Jung et al., 2015b; Lenzi et al., 2002; Strenzke et al., 2016) and translocate to the proximity of the distal part of the ribbon. Most likely, multiple-filaments ensure close spatial coupling of SVs with synaptic ribbon to ensure resupply of vesicles. However, how the SVs mobilize to the release site remains to be answered. Two contingent mechanisms are ATP-dependent (Bunt, 1971; von Gersdorff

et al., 1996; Gray and Pease, 1971) and -independent transport (Graydon et al., 2014; Heidelberger et al., 2002; Zenisek et al., 2000). Later, SVs are tethered to the membrane by a single tether, followed by multiple-tether formation, docking and finally vesicle fusion. Fig. 4.2 summarizes the key findings of this section.

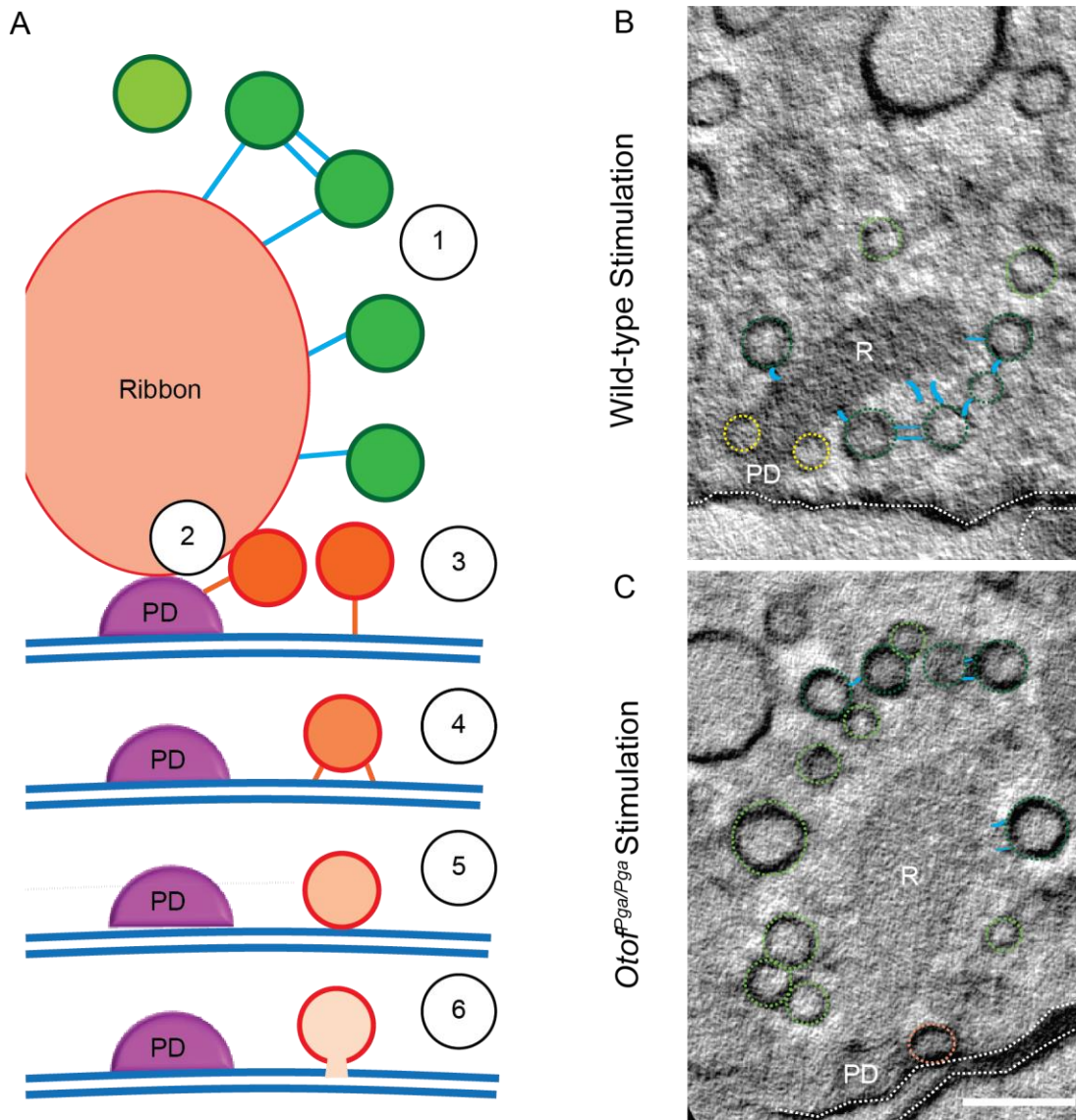


Figure 4.2 Proposed release sequence of SVs at IHC ribbon synapses

(A) Abridged representation of the release sequence at IHC ribbon synapses. Following steps occur at the ribbon synapses. (1) Multiple-filaments are formed upon stimulation at the ribbon. Vesicles are then transported towards the membrane possibly via the (2) presynaptic density. (3) Single tethers form at the membrane, followed by (4) multiple tethers that prepare the vesicles for fusion. (5) After docking, (6) fusion occurs

(B-C) Exemplary virtual sections through EM tomograms for the stimulatory condition of wild-type **(B)** and *Otof*^{Pga/Pga} **(C)**. Scale bar, 100 nm; magnification, 12,000x. RA SV with filaments (dark green, blue filaments), without filament (light green); MP non-tethered (yellow) and docked (light orange). Upon stimulation complexity of filaments (in blue) increases at the distal end of the wild-type ribbon but multiple-tethered and docked vesicles at the membrane are rare. On the other hand, *Otof*^{Pga/Pga} mice exhibit reduced filament connectivity at the ribbon, compact vesicle packing accompanied by the presence of multiple-tethered and docked vesicles (in orange) at the membrane.

4.3 Rab-3 interacting molecules (RIM) 2 α promotes vesicle tethering to the AZ

At IHCs the molecular identity of vesicle tethering/docking factors associated with the vesicular release machinery remains elusive. As stated already, previous studies showed that ribbon synapses operate in the absence of synapsin (Safieddine and Wenthold, 1999), neural SNAREs (Nouvian et al., 2011) and the conventional priming factors Munc13 and CAPS (Vogl et al., 2015). Jung et al., 2015a investigated the role of RIM2 α and RIM2 β in synaptic transmission at mice IHC ribbon synapses. In this study it was shown by using single cell RT-PCR and immunohistochemistry that Rim2 α and 2 β but not RIM1 and 4 were expressed in IHCs. IHC electrophysiological recordings of *RIM1/2 double-KO* (lacking Rim2 α and 2 β) animals presented a substantial decrease in Ca²⁺-currents due to a reduced number of Ca²⁺ channels at the AZ (Jung et al., 2015a). Moreover both the RRP release (in response to 20 ms depolarization) and the sustained exocytosis (20 ms or more depolarization) was reduced in *RIM2 α KO*, while Ca²⁺-influx exocytosis coupling was not affected indicating that RIM2 is actively involved in vesicle release (Jung et al., 2015a). In my thesis, I supported the above-mentioned findings by investigating whether RIM2 α is required for the ultrastructural organization of ribbon synapses and whether it is involved in tethering vesicles to the AZ (Jung et al., 2015a) and at the ribbon.

4.3.1 Unaltered gross morphology of IHCs in *RIM2 α KO*

I studied the ultrastructure of IHC using HPF/FS in combination to electron tomography, to investigate ribbon synapse AZ with greater z-resolution (Chen et al., 2008; Helmprobst et al., 2015; Imig et al., 2014; Vogl et al., 2015). I could show, at the nanostructural level, that every AZ in *RIM2 α KO* IHCs harbor an anchored synaptic ribbon, whereas KO of localization homolog bassoon at IHCs showed floating ribbons and ribbon-less synapses (Frank et al., 2010; Jing et al., 2013; Khimich et al., 2005).

4.3.2 Disruption of RIM2 α hinders vesicle tethering to the proximal ribbon part and AZ membrane

The mechanism underlying the spatial organization of Ca²⁺ channels with respect to tethered SVs at the ribbon synapse AZ is mostly unknown. RIM was proposed to link SVs to Ca²⁺ channels at the conventional synapses (Kaesler, 2011; Stanley, 1993). Moreover, in

cultured hippocampal neurons RIM1 was shown to directly activate Munc13 and promotes vesicle priming (Deng et al., 2011), vesicle docking in the calyx of Held (RIM2; Han et al., 2011) and vesicle tethering to the AZ in synaptosomes (RIM1; Fernández-Busnadiego et al., 2013). Using cryo-EM tomography it could be demonstrated that in *RIM1 α KO*s the number of tethers per vesicle were reduced and the tether length was significantly increased placing SVs further away from the AZ membrane (Fernández-Busnadiego et al., 2013). As stated above, RIM1 is absent in IHCs but RIM2 α seems to be the only α -RIM in IHCs (Jung et al., 2015a). Therefore I investigated the SV tethering in *RIM2 α KO*s.

In all the tomograms analyzed, quite a variable filament and tether lengths were observed at IHC ribbon synapses reaching up to 50 nm. At wild-type ribbon synapses, the filament length in RA pool was longer than the tether length at the MP pool. This diversity in filament length might indicate the involvement of different proteins and/or protein-interactions. However, the average length of filaments in RA pool and tether connecting SV to the AZ membrane/presynaptic density in MP pool were comparable between littermate control and *RIM2 α KO*s (only MP pool published in Jung et al., 2015a).

Moreover, the number of SVs in the RA (without and with filaments) and MP pool (without and with tethers) were comparable between *RIM2 α KO* and littermate control IHC ribbon synapses. Interestingly, the fraction of tethered SVs in the MP pool (Jung et al., 2015a) and the fraction of SVs with the filament in the proximal part of the ribbon (closer to the AZ membrane) were significantly reduced in *RIM2 α KO* ribbon synapses. These findings show the involvement of RIM2 α in linking SVs closer to the AZ membrane of IHCs, supporting the role of RIM protein in mediating tethering of vesicles before release as shown in cerebocortical synaptosomes (Fernández-Busnadiego et al., 2013). Additionally, it has been demonstrated that the deletion of all RIM isoforms resulted in a reduced number of docked SVs in the calyx of Held and in cultured hippocampal neurons (Kaeser, 2011). Partially distinctive molecular composition of IHC ribbon type in terms of SVs docking and priming machinery (Pangrsic et al., 2010; Vogl et al., 2015), release states at the ultrastructural level could potentially be different from conventional synapses (Imig et al., 2014; Siksou et al., 2009). The previous experiments (described in section 4.2), suggested that IHCs are equipped with highly efficient vesicle replenishment mechanism(s), preventing a working synapse from a lack of vesicles, even upon strong stimulation. Thus, docked vesicles were observed only in wild-type stimulated conditions or when the replenishment was impaired. In agreement with this hypothesis, I did not see morphologically docked SVs in both *RIM2 α KO*s and littermate controls, as the experiments were conducted under resting conditions. However, future experiments are required to decipher whether RIMs are the sole vesicle tethering factors at IHC ribbon synapses by

investigating mice lacking all IHC specific RIM isoforms (*RIM1/2 double-KOs* (lacking both 2α , 2β) and *RIM3 γ KOs*).

4.3.3 Conclusion

The morphological data did not reveal major deficits in *RIM2 α KOs*. Proper ribbon anchorage to the presynaptic AZ membrane and a normal number of RA and MP SVs were observed. Further, 2-color STED microscopy revealed stripe-like RIM2 localization between the synaptic ribbon and AZ membrane (Jung et al., 2015a). A weaker signal of RIM2 was observed in *RIM2 α KOs* and was completely absent in *RIM1/2 double-KOs* which lacked all RIM2 isoforms (Jung et al., 2015a). Furthermore, my observation of reduced fraction of SV with filaments in the proximal part of the ribbon and tethered SVs in the MP pool of *RIM2 α KOs* supported the previous observation that RIMs regulate vesicle tethering (Fernández-Busnadiego et al., 2013; Jung et al., 2015a), although RIM2 α seems not to be the only protein governing this process at the IHC ribbon synapses. Fig. 4.3 summarizes the key findings of this section.

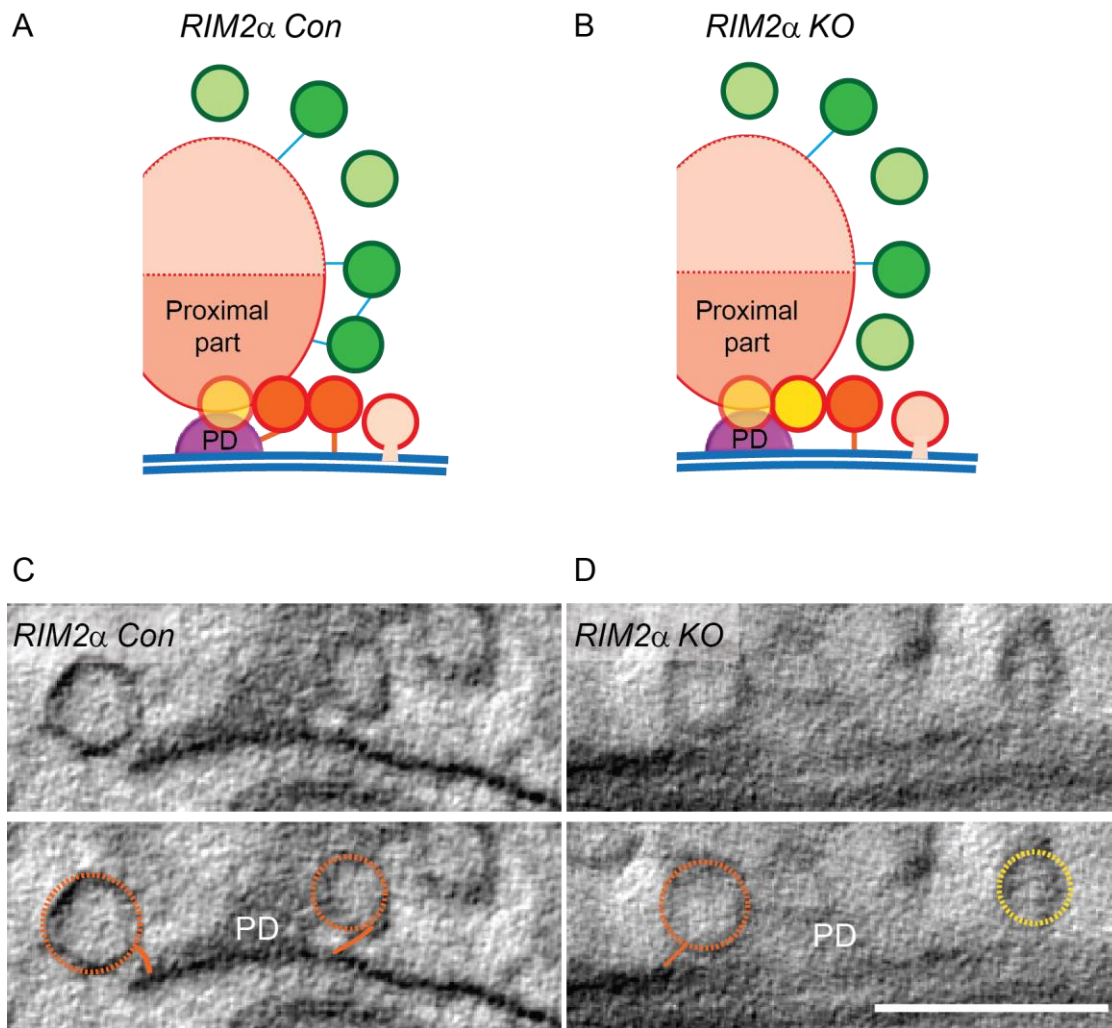


Figure 4.3: RIM2 α regulates vesicle tethering to the membrane

More MP tethered SVs are found at the MP pool (Jung et al., 2015a) and in the proximal part of the ribbon in *RIM2 α Con* compared to *RIM2 α KO*.

(A-B) Schematic representation of *RIM2 α Con* (A) and *RIM2 α KO* (B) IHC ribbon synapses highlighting the proximal ribbon part and the MP pool.

(C-D) Exemplary virtual sections of EM tomograms (only the MP pool depicted) of *RIM2 α Con* (C) and *RIM2 α KO* (D). In the lower panel tethered MP SVs are highlighted with orange dotted line and tethers with the solid orange line; non-tethered SVs are highlighted with the yellow dotted line. Scale bar, 100 nm; magnification, 12,000x.

4.4 First glimpse at the early exocytosis in IHC ribbon synapses

The release at IHC is tonic (von Gersdorff, 2001) with a high rate of SV replenishment (Pangrsic et al., 2010). Furthermore, capacitance measurements of the IHCs suggested that SV fusion is taking place in a coordinated manner at the ribbon synapses (Neef et al., 2007). From postsynaptic recordings of the spiral ganglion neurons, a high variability in the amplitude and size of excitatory postsynaptic currents (EPSCs) was reported, possibly indicating that multiple SVs are released in a synchronized fashion (Glowatzki and Fuchs, 2002). This could be a result of different possible scenarios of multi-quantal release (Neef et al., 2007) like the synchronized release of multiple SVs (Edmonds, 2004; Fuchs, 2005) or homotypic fusion of SVs prior to release (Matthews and Sterling, 2008). However, a recent study argued for a uni-quantal release mode (Chapochnikov et al., 2014), where a single SV release through a complete collapse or a transient pore flickering. The high-density clustering of postsynaptic α -amino-3-hydroxy-5-methyl-4-isoxazolepropionic acid (AMPA) receptors allows one SV to elicit large EPSCs (Chapochnikov et al., 2014). However, the exact mechanism(s) of exocytosis and SV pool dynamics at the IHC ribbon synapses remained perplexing and was further analyzed in this thesis.

Significant efforts have been made to address these scenarios by studying different morphological SV pools at the hair cells ribbon synapses using EM. These studies proposed that the SVs situated close to the AZ membrane represent the “ultrafast release pool” (Lenzi and von Gersdorff, 2001; Lenzi et al., 1999) and SVs further away around the ribbon are accessible for slower release (Lenzi et al., 1999). However, conventional embedding for EM limited these studies to a greater extent regarding temporal resolution resulting from slow chemical fixation (Rosenmund and Stevens, 1997; Smith and Reese, 1980). Still, the excellent Z-resolution due to the use of EM-tomography (Chen et al., 2008) allowed them to study the spatial organization of SVs at the ribbon synapse in greater detail. This thesis moved the understanding a step forward (described above in 4.2). The methodology incorporated here (HPF) allowed the SV immobilization within milliseconds close to native state (Moor, 1987). I could show that not all SVs in the MP pool are morphologically similar, most likely associated with different functional release states. However, in section 4.2, I could not capture the ultrafast events that are likely multiple-tethered and docked SVs at the AZ membrane (as discussed in section 4.2.7) and the very moment of SV fusion in wild-type ribbon synapses. 15 min high K^+ stimulation (Chapochnikov et al., 2014; Jung et al., 2015b; Pangrsic et al., 2010, also described in section 4.2) used so far could not offer the temporal resolution to study short-term dynamic changes. To have a better understanding of the underlying morphology exocytosis at IHC ribbon synapses (millisecond time scale), it is an absolute need to gain both, a temporal and a spatial resolution of release events.

Heuser and Reese classical experiments on isolated frog NMJ incorporated the freeze-slammer to overcome the challenge of temporal resolution. The isolated neurons were electrically stimulated at various time points before the samples were frozen by slamming rapidly against the metal block cooled at 4 K (-269.15° C) liquid helium temperature (Heuser et al., 1979). Unfortunately, the biggest disadvantage is that this methodology is capable of freezing only the surface of the specimen perfect for thin tissues slices, without ice crystal formation. For tissues like the organ of Corti, this methodology does not serve the purpose because of the tissue thickness. However, recently, with the incorporation of optogenetic stimulation with HPF (Opto-HPF) opened a gateway to study the synaptic ultrastructure before and during neurotransmission (Kittelmann et al., 2013; Watanabe et al., 2013a, 2013b) for thicker tissues as well. Using Opto-HPF provides three major advantages: (i) optogenetic allows specific targeted short stimulation of cells/neurons in a noninvasive manner (Yizhar et al., 2011). (ii) The user can have a precise control of the stimulation-freezing onset time coupling. (iii) HPF allows freezing of thick tissue (~ 200 μm) with reduced ice crystal formation (Moor, 1987). The objective of this thesis was to explore the potential of this method to address the release mechanism at IHC ribbon synapses.

4.4.1 Exocytosis in IHCs can be evoked by optogenetic stimulation

In order to evoke optical depolarization of the IHCs, a variant of channelrhodopsin-2 (ChR2-H134R) was expressed under the control of the vGlut3 promoter, which ensured successful expression of ChR-2 specific to IHC plasma membrane in *Ai32VC* mice without any cellular aggregates. During her master's thesis, Lina María Jaime Tobón performed perforated patch-clamp experiments in the presence of the K^+ channel blockers tetraethyl ammonium-Cl (TEA-Cl) and 4-aminopyridine (4-AP) and optically stimulated the IHCs. Low laser intensities of 0.2 - 0.4 mW/mm^2 were enough to activate ChR-2 and trigger photocurrents leading to a change in membrane potential (Jaime Tobón, 2015). This threshold was significantly lower than what was demonstrated to be required to evoke spikes in ChR2-transfected neurons (here ranging from as low as 1 mW/mm^2 to as high as 12 mW/mm^2) (Boyden et al., 2005; Nikolic et al., 2009). Her experiments with a short light pulse (application of 473 nm laser light for 5 ms), could show a photodepolarization of the IHCs that escalated with increasing light intensity (4 mW/mm^2 laser intensity evoked a photodepolarization of 11 mV to -73 mV and 1822 mW/mm^2 evoked a photodepolarization of 84 mV to 0 mV membrane potential). With high-intensity blue light, a strong exocytosis was elicited (as measured by membrane capacitance increments), exceeding the size of the RRP (Jaime Tobón, 2015). I intended to reproduce the typical light stimulation protocol applied during these electrophysiological recordings, but in the preliminary Opto-HPF experiments I could not reach such high light intensity stimulation. However, my results suggest that a peak intensity of 6 mW/mm^2 , as achieved using LED stimulation, was

sufficient to activate ChR-2 and to evoke exocytosis also at lower receptor potentials than reached in the patch-clamp experiments. This is in line with previous publications showing that IHCs (*in vivo*) can respond to moderate and low-frequency sound intensities with quite low receptor potentials (Russell and Sellick, 1983). Thus, the stimulation used in the Opto-HPF experiments while most likely reaching levels that are comparable to *in vivo* depolarizations is not as strong as that used in patch-clamp experiments. In the future, a higher intensity light source needs to be incorporated into the stimulation paradigm to obtain results that are more comparable to the electrophysiological recordings and allow clearer statements on whether the state in which the IHC has been frozen is during release of the RRP or during sustained release.

4.4.2 Considering the time points of the optical stimulation

This thesis aimed at establishing Opto-HPF for the first time at the IHC ribbon synapses and complements it with EM tomography, to achieve both the temporal and spatial resolution required to visualize the dynamics of SV pools upon brief optical stimulation. However, certain pitfalls were encountered in the current experiments. Stimulation here was determined by back-calculating from the time point when the pressure drops in the HPM-100. This was done based on the correlation of the external accelerometer data (absolute time scale) with the pressure/temperature data (relative time scale) obtained from high-pressure freezing machine (described in materials and method section 2.3.3.2). The initial idea was to have a tight temporal coupling of stimulation with the freezing (see materials and method section Fig. 2.4) which should have allowed the samples to be frozen immediately after stimulation. During my experiments based on the accelerometer data obtained, I encountered fluctuations for the time took for the initial valves opening, pressure build-up and in the end pressure drop ($T_{\text{mechanics}}$), for every freezing round (described in methods section 2.3.3.2), resulting in a time lag between light stimuli and freezing in my first experiments. Here, the light stimulus was set according to the time point of 472 ms provided by Leica Microsystems; accounting for the time liquid N_2 takes to enter the freezing chamber ($T_{N_2 \text{ entry}}$) plus the $T_{\text{mechanics}}$. However, during our calibrations using the accelerometer to sense the last strong signal upon application of the pressure on to the sample (noted by the pressure drop at the end of the freezing) we now encounter a total delay of 485 ms. In addition we consider the time it takes for the sample to be frozen (~ 9.11 ms), as estimated earlier (Watanabe et al., 2013b) (described in methods section 2.3.3.2). However, further optimizations and correlation of the signals with the accelerometer still need to be performed in the future.

In the current experiments, a 10 ms optical pulse was used to stimulate, which ended ~ 15 ms before the freezing onset (because of the time lag described above), similar to what has

also been described previously in both the reports on this methodology (Watanabe et al., 2013a, 2013b). Consequently, I could not capture the very moment of RRP release at IHC ribbon synapses, which occurs during the first 20 ms of stimulation as proposed earlier by capacitance measurements (Moser and Beutner, 2000). However, the vesicle pools studied here likely represent the vesicles available immediately after the fusion of the RRP SVs (in the range of 10-25 ms), as IHCs are capable of immediate recruitment of SVs at the release site for the next round of release (Moser and Beutner, 2000; Neef et al., 2007; Pangrsic et al., 2010) and the SVs observed here were not captured during the sustained component of exocytosis as the samples were frozen within ~ 15 ms of the stimulation and sustained component of exocytosis is elicited upon continuous depolarization of IHCs (Moser and Beutner, 2000). The details of the findings are discussed in the coming section.

4.4.3 Filament connectivity was unaltered in the RA pool

I started with the analysis of the RA pool of SVs, as stated earlier contribute to the slower component of exocytosis at frog saccular hair cell ribbon synapses (Lenzi et al., 1999). In my previous experiments (section 4.2.5) I proposed that synaptic ribbon in association with multiple-filaments could assist in the close spatial organization of SVs to ensure the demanding task of vesicle resupply at the ribbon to sustain the exocytosis over a long period. However, after 10 ms optical stimulation (and freezing within ~ 15 ms) no difference in the fraction of SVs with filaments or the number of filaments/SV was observed. Therefore, I propose that in the short time window between optical stimulation and freezing, the resupply of SVs to the ribbon did not start as of yet. If that is the case, there will be a time lag between RRP release at the membrane and arrival of new SVs at the ribbon. Consequently, this will result in a temporary decrease in exocytosis after the release of RRP. However, that is not the case with ribbon synapses, as synaptic ribbons are accepted as a “storehouse” of SVs to support continuous neurotransmission in response to graded depolarization (Lenzi et al., 1999; Matthews and Fuchs, 2010). In this experimental condition synaptic ribbons most likely compensate for the time lag encountered due to resupply of SVs at the ribbon.

4.4.4 Synaptic vesicles at the ribbon redistribute to the membrane upon optical stimulation

Tomogram analysis further revealed that following 10 ms optical stimulation the SV counts in the RA pool decreased significantly compared to unstimulated controls (reduced by 32 %). Two scenarios could contribute to this together: (i) the resupply of the RA SVs did not start immediately after the stimulus (as described above) and (ii) RA SVs redistribute to the MP pool. Most likely, the RA SVs are not disappearing per se on account of the release, but are rather redistributed or moved down to the MP pool of SVs as described previously

(Bunt, 1971; Gray and Pease, 1971; Graydon et al., 2014; Zenisek et al., 2000) by a still unknown mechanism as describe above in section 4.2.5. This should have caused an accumulation at the MP vesicles in case of no release. Instead the SV count in the MP pool remained unaltered post 10 ms stimulation, indicating that indeed some SVs were already released. However, I could not discern any omega shaped structures at the membrane, the morphological correlate of SV fusion (Heuser and Reese, 1981; Heuser et al., 1979). This was probably because release already ceased at the time of freezing. So far, a true estimate for the duration of fusion pore opening is not available for IHC ribbon synapses or any other ribbon type synapses, but a montage of freeze fracture replicas obtained by Heuser and Reese, 1981 at the NMJ showed minute pores appeared 3 - 4 ms after a single electrical stimulation with a peak opening at ~ 5 ms and within 20 ms SVs coalescence with the plasma membrane. This shows the time scale we are challenged with. Given the divergent fusion machinery employed at the IHCs when compared to conventional synapses, the opening of the fusion pore can expect to be extremely fast at IHC ribbon synapses to facilitate the initial high rates of exocytosis defined via capacitance measurements (Moser and Beutner, 2000). My current experiments could not achieve such tight stimulus-freezing coupling as Heuser and Reese, 1981 (in a few experiments they accounted for < 3 ms stimulus-freezing coupling). Therefore, it needs further optimizations by incorporating shorter duration of the light stimulus and by improving the temporal coupling between freezing and stimulus encountered here.

4.4.5 Recruitment of vesicles mediated by tethers at the MP pool

In section 4.2.6, I showed that not all MP SVs are in the same release state, rather a small fraction of SVs in membrane proximity might be the “release ready” SVs, in contrast to the previous interpretation (Lenzi et al., 1999). With short optical stimulation, I reconfirmed my previous hypothesis. Upon 10 ms optical stimulation, a fraction of tethered SVs increased significantly in the MP pool (\sim by 40 %). Interestingly, the increase was comparable irrespective of the stimulation paradigm, i.e., 10 ms optical stimulation or 15 min high K^+ stimulation. Given the proposed role of similar tethers, this could suggest that SVs are constantly recruited, allowing the ribbon synapses to carry out a tonic release (von Gersdorff, 2001). Furthermore, the initial recruitment was proposed to happen over a single tether linking the SVs at conventional synapses (Fernández-Busnadiego et al., 2010; Stigloher et al., 2011). Comparable configuration was observed in the current and my earlier experiments (described in section 4.2.6). Additionally, the 10 ms optical stimulation (with ~ 15 ms stimulus-freezing temporal coupling) and 15 min high K^+ stimulation both showed that these single tethers on average spanned over a distance of half a SV diameter (≤ 20 nm). However, small tethers (≤ 5 nm) as shown with cryo-EM (Fernández-Busnadiego et al., 2010) were missing at the IHC ribbon synapses.

4.4.6 Multiple-tethered and docked vesicles increase after 10 ms optical stimulation

What happens to these vesicles which are recruited? At the conventional synapses short-multiple-tethers at the membrane was proposed to tightly bind SVs closer to the membrane (Fernández-Busnadiego et al., 2010, 2013), as a preparatory step before docking and priming (Fernández-Busnadiego et al., 2013; Gerber et al., 2008; Siksou et al., 2009; Verhage and Sørensen, 2008). My earlier observation showed that the multiple-tethered SVs rarely occur at wild-type ribbon synapses (described above in section 4.2.7). However, the current experiments could capture these multiple-tethered SVs in Controls (unstimulated) MP pool as well, which were missed in my previous experiments possibly due to use of different extracellular solutions. For optical stimulation paradigm, the samples were frozen in 5 mM 4-aminopyridine (4-AP); a K⁺ channel blocker, to assure that the depolarization of the IHC was strictly due to opening of ChR-2, additionally this was shown to increase the quantal of release at NMJ (Heuser and Reese, 1981). Nonetheless, upon 10 ms optical stimulation, the fraction of SVs with multiple-tethers increased significantly, indicating that a later release phase was captured earlier during 15 min high K⁺ stimulation (discussed in 4.2.7). Yet again the length of individual tethers from the multiple-tether category did not change and was comparable to single tether, supporting the hypothesis that different proteins could assist in tether formation at IHCs on account of unconventional priming and docking (Jung et al., 2015a; Nouvian et al., 2011; Vogl et al., 2015). However, we should keep in mind that the true protein constituting these tethers are not yet clear at conventional synapses as well, but neuronal SNAREs, Munc13 and RIM1 are potential candidates for tethers (Fernández-Busnadiego et al., 2013, 2013; Siksou et al., 2009; Stigloher et al., 2011). In line with the multiple-tethered SVs, upon stimulation the probability to capture docked SVs was significantly higher as 50 % of the tomograms analyzed showed the presence of docked SVs. Statistical tests could not be carried out because none of the control synapses had docked SVs in the MP pool. Interestingly, at one of the optically stimulated tomograms we could capture five docked out of 16 MP SVs. On an average, one docked SV was observed per IHC AZ and most of the analyzed docked SVs reside within 100 nm of the presynaptic density. This supports my previous hypothesis that the release ready SVs are predominantly docked in vicinity of the Ca²⁺ channels (Issa and Hudspeth, 1996; Moser and Beutner, 2000). However, results of the peripheral docked SVs analysis are still awaited. Both, the increased occurrence of multiple-tethered and docked SVs strengthen the initial working hypothesis that these vesicles represent the active release states at IHC ribbon synapses, quite similar to conventional synapses. Upon strong and prolonged stimulation the release goes down with time (Moser and Beutner, 2000; Pangrsic et al., 2010) since the docked and multiple-tethered SVs get released. Only few docked vesicles were observed earlier upon 15 min K⁺ stimulation indicates that the ribbon

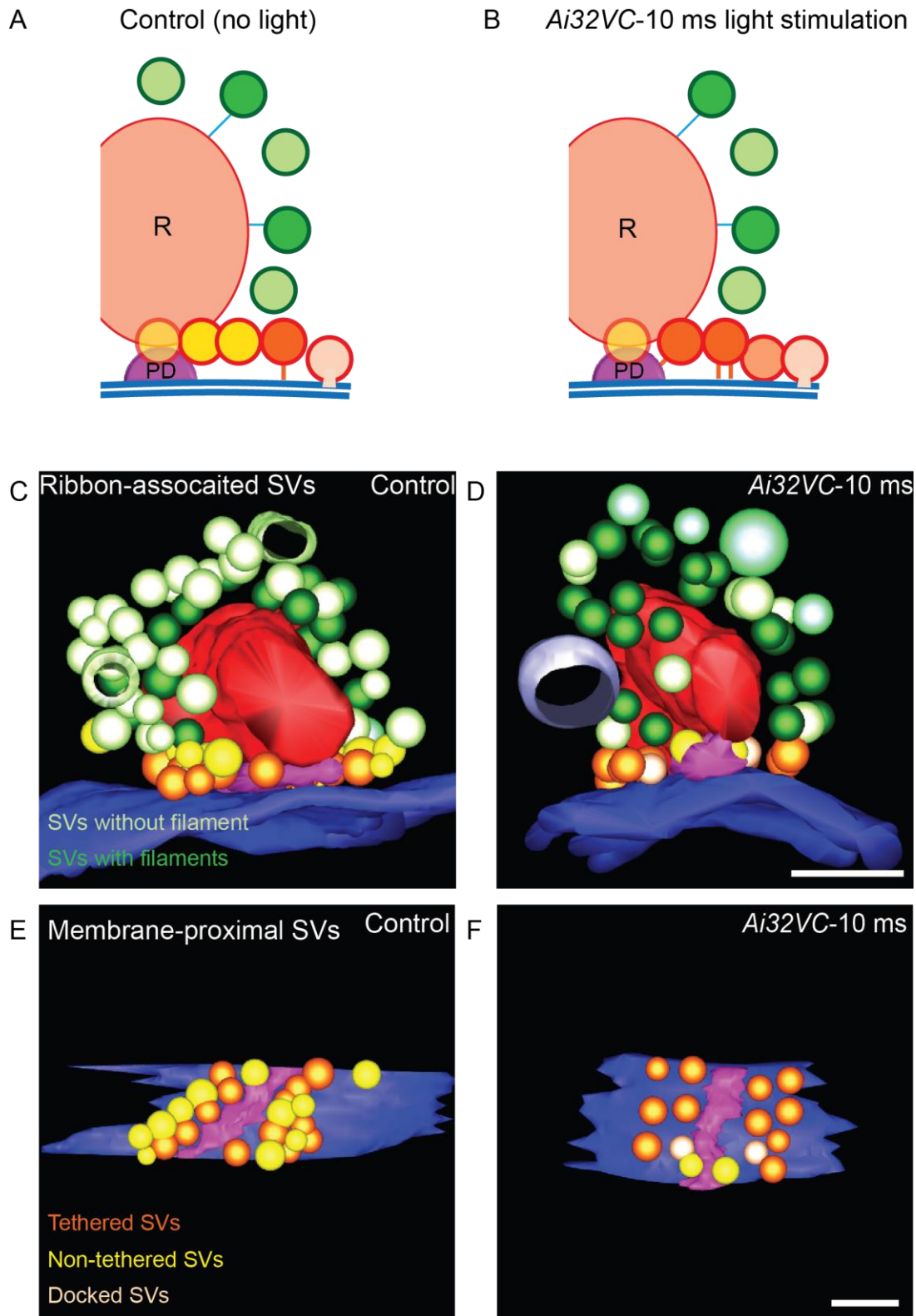
synapses are capable of sustaining release over a long period (described above in section 4.2.7) (von Gersdorff, 2001; Pangrsic et al., 2010).

In future, to get the holistic picture of the release at IHC ribbon synapses, (i) different duration of stimulations need to be tested sequentially. (ii) The temporal coupling of stimulus and freezing should be improved. (iii) Different recovery durations after stimulus should be tested. This way different exocytosis stages can be investigated.

4.2.7 Conclusion

Opto-HPF in combination with electron tomography is an appropriate tool to understand the vesicle pool dynamics at IHC ribbon synapses. With 10 ms stimulation the RA SVs redistributes to the membrane as proposed earlier (Bunt, 1971; Gray and Pease, 1971; Graydon et al., 2014; Zenisek et al., 2000). Since the samples were frozen within 15 ms after the optical stimulus, I could not encounter immediate resupply of the SVs to the ribbon. These observations together resulted in partial depletion of RA SVs after 10 ms stimulation.

The MP SVs count, however, remains comparable to the unstimulated controls due to the innate capability of IHC ribbon synapses to recruit SVs for the next round of release (Moser and Beutner, 2000; Pangrsic et al., 2010). In line with this, the fraction of tethered SVs in the MP pool increases upon optical stimulation, which might represent the recruitment of SVs in the membrane proximity as shown in conventional synapses (Fernández-Busnadiego et al., 2010; Stigloher et al., 2011). Furthermore, short and precise stimulation allowed observation of transient exocytosis steps (multiple-tether formation and SV docking) before fusion at the AZ membrane. However, the very moment of SV fusion with membrane could not be observed after 10 ms stimulation with ~ 15 ms stimulus-freezing temporal coupling. Therefore, optimization of this method is needed for future experiments. Fig. 4.4 summarizes the key findings of this section.



←

Figure 4.4: Active release states of IHC ribbon synapse

Upon 10 ms optical stimulation and ~ 15 ms coupling with freezing results in partial depletion of RA SVs with no change in the multiple-filament organization. The MP SVs count remains comparable to the unstimulated controls. However, more docked and multiple-tethered SVs are observed after 10 ms optical stimulation.

(A-B) A Schematic representation of control **(A)** and *Ai32VC-10 ms* **(B)** IHC ribbon synapses.

(C-F) The 3-D reconstructions of the RA (front view, **C-D**) and MP (top view, **E-F**) pools of SVs for control **(C, E)** and *Ai32VC-10 ms* **(D, F)**. Scale bar, 100 nm.

Bibliography

1. Achanzar, W.E., and Ward, S. (1997). A nematode gene required for sperm vesicle fusion. *J. Cell Sci.* *110*, 1073–1081.
2. Acuna, C., Liu, X., Gonzalez, A., and Südhof, T.C. (2015). RIM-BPs Mediate Tight Coupling of Action Potentials to Ca²⁺-Triggered Neurotransmitter Release. *Neuron* *87*, 1234–1247.
3. Akil, O., Seal, R.P., Burke, K., Wang, C., Alemi, A., During, M., Edwards, R.H., and Lustig, L.R. (2012). Restoration of Hearing in the VGLUT3 Knockout Mouse Using Virally Mediated Gene Therapy. *Neuron* *75*, 283–293.
4. Ashmore, J. (2008). Cochlear Outer Hair Cell Motility. *Physiol. Rev.* *88*, 173–210.
5. Babai, N., Bartoletti, T.M., and Thoreson, W.B. (2010). Calcium Regulates Vesicle Replenishment at the Cone Ribbon Synapse. *J. Neurosci.* *30*, 15866–15877.
6. Bernatchez, P.N., Sharma, A., Kodaman, P., and Sessa, W.C. (2009). Myoferlin is critical for endocytosis in endothelial cells. *Am. J. Physiol. - Cell Physiol.* *297*, C484–C492.
7. Betz, W.J., and Henkel, A.W. (1994). Okadaic acid disrupts clusters of synaptic vesicles in frog motor nerve terminals. *J. Cell Biol.* *124*, 843–854.
8. Beurg, M., Michalski, N., Safieddine, S., Bouleau, Y., Schneggenburger, R., Chapman, E.R., Petit, C., and Dulon, D. (2010). Control of exocytosis by synaptotagmins and otoferlin in auditory hair cells. *J. Neurosci. Off. J. Soc. Neurosci.* *30*, 13281–13290.
9. Borisovska, M., Zhao, Y., Tsytsyura, Y., Glyvuk, N., Takamori, S., Matti, U., Rettig, J., Südhof, T., and Bruns, D. (2005). v-SNAREs control exocytosis of vesicles from priming to fusion. *EMBO J.* *24*, 2114–2126.
10. Boyden, E.S., Zhang, F., Bamberg, E., Nagel, G., and Deisseroth, K. (2005). Millisecond-timescale, genetically targeted optical control of neural activity. *Nat Neurosci* *8*, 1263–1268.
11. Bunt, A.H. (1971). Enzymatic digestion of synaptic ribbons in amphibian retinal photoreceptors. *Brain Res.* *25*, 571–577.
12. Chapochnikov, N.M., Takago, H., Huang, C.-H., Pangršič, T., Khimich, D., Neef, J., Auge, E., Göttfert, F., Hell, S.W., Wichmann, C., et al. (2014). Uniquantal Release through a Dynamic Fusion Pore Is a Candidate Mechanism of Hair Cell Exocytosis. *Neuron* *17*, 1389–1403.
13. Chatterjee, P., Padmanarayana, M., Abdullah, N., Holman, C.L., LaDu, J., Tanguay, R.L., and Johnson, C.P. (2015). Otoferlin Deficiency in Zebrafish Results in Defects in Balance and Hearing: Rescue of the Balance and Hearing Phenotype with Full-Length and Truncated Forms of Mouse Otoferlin. *Mol. Cell. Biol.* *35*, 1043–1054.
14. Chen, X., Winters, C.A., and Reese, T.S. (2008). Life Inside a Thin Section (Tomography). *J. Neurosci. Off. J. Soc. Neurosci.* *28*, 9321–9327.

15. Cingolani, L.A., and Goda, Y. (2008). Actin in action: the interplay between the actin cytoskeleton and synaptic efficacy. *Nat. Rev. Neurosci.* *9*, 344–356.
16. Cole, A.A., Chen, X., and Reese, T.S. (2016). A Network of Three Types of Filaments Organizes Synaptic Vesicles for Storage, Mobilization, and Docking. *J. Neurosci.* *36*, 3222–3230.
17. Coppola, T., Magnin-Lüthi, S., Perret-Menoud, V., Gattesco, S., Schiavo, G., and Regazzi, R. (2001). Direct Interaction of the Rab3 Effector RIM with Ca²⁺Channels, SNAP-25, and Synaptotagmin. *J. Biol. Chem.* *276*, 32756–32762.
18. Corey, D.P., and Hudspeth, A.J. (1979). Ionic basis of the receptor potential in a vertebrate hair cell. *Nature* *281*, 675–677.
19. Covian-Nares, J.F., Koushik, S.V., Puhl, H.L., and Vogel, S.S. (2010). Membrane wounding triggers ATP release and dysferlin-mediated intercellular calcium signaling. *J. Cell Sci.* *123*, 1884–1893.
20. Dallos, P. (1996). *The Cochlea* (Springer Verlag, New York, Inc).
21. Dallos, P., and Fakler, B. (2002). PRESTIN, A NEW TYPE OF MOTOR PROTEIN. *Nat. Rev. Mol. Cell Biol.* *3*, 104–111.
22. Deng, L., Kaeser, P.S., Xu, W., and Südhof, T.C. (2011). RIM Proteins Activate Vesicle Priming by Reversing Autoinhibitory Homodimerization of Munc13. *Neuron* *69*, 317–331.
23. Denker, A., and Rizzoli, S.O. (2010). Synaptic Vesicle Pools: An Update. *Front. Synaptic Neurosci.* *2*.
24. Dick, O., Hack, I., Altmann, W.D., Garner, C.C., Gundelfinger, E.D., and Brandstätter, J.H. (2001). Localization of the presynaptic cytomatrix protein Piccolo at ribbon and conventional synapses in the rat retina: Comparison with Bassoon. *J. Comp. Neurol.* *439*, 224–234.
25. Dick, O., tom Dieck, S., Altmann, W.D., Ammermüller, J., Weiler, R., Garner, C.C., Gundelfinger, E.D., and Brandstätter, J.H. (2003). The Presynaptic Active Zone Protein Bassoon Is Essential for Photoreceptor Ribbon Synapse Formation in the Retina. *Neuron* *37*, 775–786.
26. tom Dieck, S., Altmann, W.D., Kessels, M.M., Qualmann, B., Regus, H., Brauner, D., Fejtová, A., Bracko, O., Gundelfinger, E.D., and Brandstätter, J.H. (2005). Molecular dissection of the photoreceptor ribbon synapse: physical interaction of Bassoon and RIBEYE is essential for the assembly of the ribbon complex. *J. Cell Biol.* *168*, 825–836.
27. tom Dieck, S., Specht, D., Strenzke, N., Hida, Y., Krishnamoorthy, V., Schmidt, K.-F., Inoue, E., Ishizaki, H., Tanaka-Okamoto, M., Miyoshi, J., et al. (2012). Deletion of the presynaptic scaffold CAST reduces active zone size in rod photoreceptors and impairs visual processing. *J. Neurosci.* *32*, 12192–12203.
28. Dulon, D., Safieddine, S., Jones, S.M., and Petit, C. (2009). Otoferlin Is Critical for a Highly Sensitive and Linear Calcium-Dependent Exocytosis at Vestibular Hair Cell Ribbon Synapses. *J. Neurosci.* *29*, 10474–10487.
29. Duncker, S.V., Franz, C., Kuhn, S., Schulte, U., Campanelli, D., Brandt, N., Hirt, B., Fakler, B., Blin, N., Ruth, P., et al. (2013). Otoferlin Couples to Clathrin-Mediated Endocytosis in Mature Cochlear Inner Hair Cells. *J. Neurosci.* *33*, 9508–9519.

30. Eatock, R.A., and Songer, J.E. (2011). Vestibular Hair Cells and Afferents: Two Channels for Head Motion Signals. *Annu. Rev. Neurosci.* *34*, 501–534.
31. Edmonds, B.W. (2004). Evidence that fast exocytosis can be predominantly mediated by vesicles not docked at active zones in frog saccular hair cells. *J. Physiol.* *560*, 439–450.
32. Elliott, S.J., and Shera, C.A. (2012). The cochlea as a smart structure. *Smart Mater. Struct.* *21*, 064001.
33. Fernández-Busnadiego, R., Zuber, B., Maurer, U.E., Cyrklaff, M., Baumeister, W., and Lučić, V. (2010). Quantitative analysis of the native presynaptic cytomatrix by cryoelectron tomography. *J. Cell Biol.* *188*, 145–156.
34. Fernández-Busnadiego, R., Asano, S., Oprisoreanu, A.-M., Sakata, E., Doengi, M., Kochovski, Z., Zürner, M., Stein, V., Schoch, S., Baumeister, W., et al. (2013). Cryo-electron tomography reveals a critical role of RIM1 α in synaptic vesicle tethering. *J. Cell Biol.* *201*, 725–740.
35. Fouquet, W., Oswald, D., Wichmann, C., Mertel, S., Depner, H., Dyba, M., Hallermann, S., Kittel, R.J., Eimer, S., and Sigrist, S.J. (2009). Maturation of active zone assembly by *Drosophila* Bruchpilot. *J. Cell Biol.* *186*, 129–145.
36. Frank, T., Rutherford, M.A., Strenzke, N., Neef, A., Pangršič, T., Khimich, D., Fejtova, A., Gundelfinger, E.D., Liberman, M.C., Harke, B., et al. (2010). Bassoon and the synaptic ribbon organize Ca²⁺ channels and vesicles to add release sites and promote refilling. *Neuron* *68*, 724–738.
37. Fuchs, P.A. (2005). Time and intensity coding at the hair cell's ribbon synapse. *J. Physiol.* *566*, 7–12.
38. Fuchs, P.A., Glowatzki, E., and Moser, T. (2003). The afferent synapse of cochlear hair cells. *Curr. Opin. Neurobiol.* *13*, 452–458.
39. Gebhart, M., Juhasz-Vedres, G., Zuccotti, A., Brandt, N., Engel, J., Trockenbacher, A., Kaur, G., Obermair, G.J., Knipper, M., Koschak, A., et al. (2010). Modulation of Cav1.3 Ca²⁺ channel gating by Rab3 interacting molecule. *Mol. Cell. Neurosci.* *44*, 246–259.
40. Geisler, C.D. (1998). *From Sound to Synapse* (New York: Oxford University Press).
41. Gerber, S.H., Rah, J.-C., Min, S.-W., Liu, X., de Wit, H., Dulubova, I., Meyer, A.C., Rizo, J., Arancillo, M., Hammer, R.E., et al. (2008). Conformational switch of syntaxin-1 controls synaptic vesicle fusion. *Science* *321*, 1507–1510.
42. von Gersdorff, H. (2001). Synaptic ribbons: versatile signal transducers. *Neuron* *29*, 7–10.
43. von Gersdorff, H., Vardi, E., Matthews, G., and Sterling, P. (1996). Evidence that vesicles on the synaptic ribbon of retinal bipolar neurons can be rapidly released. *Neuron* *16*, 1221–1227.
44. Glowatzki, E., and Fuchs, P.A. (2002). Transmitter release at the hair cell ribbon synapse. *Nat. Neurosci.* *5*, 147–154.
45. Gray, E.G., and Pease, H.L. (1971). On understanding the organisation of the retinal receptor synapses. *Brain Res.* *35*, 1–15.

46. Graydon, C.W., Cho, S., Li, G.-L., Kachar, B., and Gersdorff, H. von (2011). Sharp Ca²⁺ Nanodomains beneath the Ribbon Promote Highly Synchronous Multivesicular Release at Hair Cell Synapses. *J. Neurosci.* *31*, 16637–16650.
47. Graydon, C.W., Zhang, J., Oesch, N.W., Sousa, A.A., Leapman, R.D., and Diamond, J.S. (2014). Passive Diffusion as a Mechanism Underlying Ribbon Synapse Vesicle Release and Resupply. *J. Neurosci.* *34*, 8948–8962.
48. Guillet, M., Sendin, G., Bourien, J., Puel, J.-L., and Nouvian, R. (2016). Actin Filaments Regulate Exocytosis at the Hair Cell Ribbon Synapse. *J. Neurosci.* *36*, 649–654.
49. Hallermann, S., and Silver, R.A. (2013). Sustaining rapid vesicular release at active zones: potential roles for vesicle tethering. *Trends Neurosci.* *36*, 185–194.
50. Hammarlund, M., Jorgensen, E.M., and Bastiani, M.J. (2007). Axons break in animals lacking β -spectrin. *J. Cell Biol.* *176*, 269–275.
51. Han, Y., Kaeser, P.S., Südhof, T.C., and Schneggenburger, R. (2011). RIM Determines Ca²⁺ Channel Density and Vesicle Docking at the Presynaptic Active Zone. *Neuron* *69*, 304–316.
52. Heidelberger, R., Sterling, P., and Matthews, G. (2002). Roles of ATP in depletion and replenishment of the releasable pool of synaptic vesicles. *J. Neurophysiol.* *88*, 98.
53. Heidrych, P., Zimmermann, U., Kuhn, S., Franz, C., Engel, J., Duncker, S.V., Hirt, B., Pusch, C.M., Ruth, P., Pfister, M., et al. (2009). Otoferlin interacts with myosin VI: implications for maintenance of the basolateral synaptic structure of the inner hair cell. *Hum. Mol. Genet.* *18*, 2779–2790.
54. Helmprobst, F., Frank, M., and Stigloher, C. (2015). Presynaptic architecture of the larval zebrafish neuromuscular junction. *J. Comp. Neurol.* *523*, 1984–1997.
55. Heuser, J.E., and Reese, T.S. (1981). Structural changes after transmitter release at the frog neuromuscular junction. *J. Cell Biol.* *88*, 564–580.
56. Heuser, J.E., Reese, T.S., Dennis, M.J., Jan, Y., Jan, L., and Evans, L. (1979). Synaptic vesicle exocytosis captured by quick freezing and correlated with quantal transmitter release. *J. Cell Biol.* *81*, 275–300.
57. Hibino, H., Pironkova, R., Onwumere, O., Vologodskaja, M., Hudspeth, A.J., and Lesage, F. (2002). RIM - binding proteins (RBPs) couple Rab3 - interacting molecules (RIMs) to voltage - gated Ca²⁺ channels. *Neuron* *34*, 411–423.
58. Hida, Y., and Ohtsuka, T. (2010). CAST and ELKS proteins: structural and functional determinants of the presynaptic active zone. *J. Biochem. (Tokyo)* *148*, 131–137.
59. Hirokawa, N., Sobue, K., Kanda, K., Harada, A., and Yorifuji, H. (1989). The cytoskeletal architecture of the presynaptic terminal and molecular structure of synapsin 1. *J. Cell Biol.* *108*, 111–126.
60. Holt, M., Cooke, A., Neef, A., and Lagnado, L. (2004). High Mobility of Vesicles Supports Continuous Exocytosis at a Ribbon Synapse. *Curr. Biol.* *14*, 173–183.
61. Hudspeth, A.J. (2014). Integrating the active process of hair cells with cochlear function. *Nat. Rev. Neurosci.* *15*, 600–614.

62. Imig, C., Min, S.-W., Krinner, S., Arancillo, M., Rosenmund, C., Südhof, T.C., Rhee, J., Brose, N., and Cooper, B.H. (2014). The morphological and molecular nature of synaptic vesicle priming at presynaptic active zones. *Neuron* *84*, 416–431.
63. Issa, N.P., and Hudspeth, A.J. (1996). The entry and clearance of Ca²⁺ at individual presynaptic active zones of hair cells from the bullfrog's sacculus. *Proc. Natl. Acad. Sci. U. S. A.* *93*, 9527.
64. Jaime Tobón, L.M. (2015). Role of Endophilin in Exocytosis and Endocytosis in Inner Hair Cell (IHC) Ribbon Synapses. University of Göttingen.
65. Jing, Z., Rutherford, M.A., Takago, H., Frank, T., Fejtova, A., Khimich, D., Moser, T., and Strenzke, N. (2013). Disruption of the presynaptic cytomatrix protein bassoon degrades ribbon anchorage, multiquantal release, and sound encoding at the hair cell afferent synapse. *J. Neurosci.* *33*, 4456–4467.
66. Johnson, C.P., and Chapman, E.R. (2010). Otoferlin is a calcium sensor that directly regulates SNARE-mediated membrane fusion. *J. Cell Biol.* *191*, 187–197.
67. Jovanovic, J.N., Sihra, T.S., Nairn, A.C., Hemmings, H.C., Greengard, P., and Czernik, A.J. (2001). Opposing changes in phosphorylation of specific sites in synapsin I during Ca²⁺-dependent glutamate release in isolated nerve terminals. *J. Neurosci. Off. J. Soc. Neurosci.* *21*, 7944–7953.
68. Jung, S., Oshima-Takago, T., Chakrabarti, R., Wong, A.B., Jing, Z., Yamanbaeva, G., Picher, M.M., Wojcik, S.M., Göttfert, F., Predoehl, F., et al. (2015a). Rab3-interacting molecules 2 α and 2 β promote the abundance of voltage-gated Ca_v1.3 Ca²⁺ channels at hair cell active zones. *Proc. Natl. Acad. Sci.* *112*, E3141–E3149.
69. Jung, S., Maritzen, T., Wichmann, C., Jing, Z., Neef, A., Revelo, N.H., Al-Moyed, H., Meese, S., Wojcik, S.M., Panou, I., et al. (2015b). Disruption of adaptor protein 2 μ (AP-2 μ) in cochlear hair cells impairs vesicle reloading of synaptic release sites and hearing. *EMBO J.* *34*, 2686–2702.
70. Kaeser, P.S. (2011). Pushing synaptic vesicles over the RIM. *Cell. Logist.* *1*, 106–110.
71. Kandel, E.R. (2012). Principles of neural science (New York: McGraw-Hill Medical).
72. Khimich, D., Nouvian, R., Pujol, R., tom Dieck, S., Egnér, A., Gundelfinger, E.D., and Moser, T. (2005). Hair cell synaptic ribbons are essential for synchronous auditory signalling. *Nature* *434*, 889–894.
73. Kittelmann, M., Liewald, J.F., Hegermann, J., Schultheis, C., Brauner, M., Steuer Costa, W., Wabnig, S., Eimer, S., and Gottschalk, A. (2013). In vivo synaptic recovery following optogenetic hyperstimulation. *Proc. Natl. Acad. Sci. U. S. A.* *110*, E3007-3016.
74. Kiyonaka, S., Wakamori, M., Miki, T., Uriu, Y., Nonaka, M., Bito, H., Beedle, A.M., Mori, E., Hara, Y., De Waard, M., et al. (2007). RIM1 confers sustained activity and neurotransmitter vesicle anchoring to presynaptic Ca²⁺ channels. *Nat. Neurosci.* *10*, 691–701.
75. Kremer, J.R., Mastrorarde, D.N., and McIntosh, J.R. (1996). Computer visualization of three-dimensional image data using IMOD. *J. Struct. Biol.* *116*, 71–76.
76. Landis, D.M., Hall, A.K., Weinstein, L.A., and Reese, T.S. (1988). The organization of cytoplasm at the presynaptic active zone of a central nervous system synapse. *Neuron* *1*, 201–209.

77. Lek, A., Evesson, F.J., Sutton, R.B., North, K.N., and Cooper, S.T. (2012). Ferlins: Regulators of Vesicle Fusion for Auditory Neurotransmission, Receptor Trafficking and Membrane Repair. *Traffic* *13*, 185–194.
78. Lenzi, D., and von Gersdorff, H. (2001). Structure suggests function: the case for synaptic ribbons as exocytotic nanomachines. *Bioessays* *23*, 831–840.
79. Lenzi, D., Runyeon, J.W., Crum, J., Ellisman, M.H., and Roberts, W.M. (1999). Synaptic Vesicle Populations in Saccular Hair Cells Reconstructed by Electron Tomography. *J. Neurosci.* *19*, 119–132.
80. Lenzi, D., Crum, J., Ellisman, M.H., and Roberts, W.M. (2002). Depolarization redistributes synaptic membrane and creates a gradient of vesicles on the synaptic body at a ribbon synapse. *Neuron* *36*, 649–659.
81. Liberman, M.C., Dodds, L.W., and Pierce, S. (1990). Afferent and efferent innervation of the cat cochlea: quantitative analysis with light and electron microscopy. *J. Comp. Neurol.* *301*, 443–460.
82. Liberman, M.C., Gao, J., He, D.Z.Z., Wu, X., Jia, S., and Zuo, J. (2002). Prestin is required for electromotility of the outer hair cell and for the cochlear amplifier. *Nature* *419*, 300–304.
83. Madisen, L., Mao, T., Koch, H., Zhuo, J., Berenyi, A., Fujisawa, S., Hsu, Y.-W.A., Iii, A.J.G., Gu, X., Zanella, S., et al. (2012). A toolbox of Cre-dependent optogenetic transgenic mice for light-induced activation and silencing. *Nat. Neurosci.* *15*, 793–802.
84. Magupalli, V.G., Schwarz, K., Alpadi, K., Natarajan, S., Seigel, G.M., and Schmitz, F. (2008). Multiple RIBEYE-RIBEYE interactions create a dynamic scaffold for the formation of synaptic ribbons. *J. Neurosci. Off. J. Soc. Neurosci.* *28*, 7954–7967.
85. Marlin, S., Feldmann, D., Nguyen, Y., Rouillon, I., Loundon, N., Jonard, L., Bonnet, C., Couderc, R., Garabedian, E.N., Petit, C., et al. (2010). Temperature-sensitive auditory neuropathy associated with an otoferlin mutation: Deafening fever! *Biochem. Biophys. Res. Commun.* *394*, 737–742.
86. Mastronarde, D.N. (2005). Automated electron microscope tomography using robust prediction of specimen movements. *J. Struct. Biol.* *152*, 36–51.
87. Matthews, G., and Fuchs, P. (2010). The diverse roles of ribbon synapses in sensory neurotransmission. *Nat. Rev. Neurosci.* *11*, 812–822.
88. Matthews, G., and Sterling, P. (2008). Evidence that vesicles undergo compound fusion on the synaptic ribbon. *J. Neurosci.* *28*, 5403.
89. Maxeiner, S., Luo, F., Tan, A., Schmitz, F., and Südhof, T.C. (2016). How to make a synaptic ribbon: RIBEYE deletion abolishes ribbons in retinal synapses and disrupts neurotransmitter release. *EMBO J.* *35*, 1098–1114.
90. Mittelstaedt, T., Alvaréz-Baron, E., and Schoch, S. (2010). RIM proteins and their role in synapse function. *Biol. Chem.* *391*, 599–606.
91. Moor, H. (1987). Theory and Practice of High Pressure Freezing. In *Cryotechniques in Biological Electron Microscopy*, P.D.R.A. Steinbrecht, and D.K. Zierold, eds. (Springer Berlin Heidelberg), pp. 175–191.

92. Moser, T., and Beutner, D. (2000). Kinetics of exocytosis and endocytosis at the cochlear inner hair cell afferent synapse of the mouse. *Proc. Natl. Acad. Sci. U. S. A.* *97*, 883–888.
93. Moser, T., and Starr, A. (2016). Auditory neuropathy — neural and synaptic mechanisms. *Nat. Rev. Neurol.* *12*, 135–149.
94. Moser, T., Brandt, A., and Lysakowski, A. (2006). Hair cell ribbon synapses. *Cell Tissue Res.* *326*, 347–359.
95. Müller, U. (2008). Cadherins and mechanotransduction by hair cells. *Curr. Opin. Cell Biol.* *20*, 557–566.
96. Muresan, V., Lyass, A., and Schnapp, B.J. (1999). The Kinesin Motor KIF3A Is a Component of the Presynaptic Ribbon in Vertebrate Photoreceptors. *J. Neurosci.* *19*, 1027–1037.
97. Nagel, G., Szellas, T., Huhn, W., Kateriya, S., Adeishvili, N., Berthold, P., Ollig, D., Hegemann, P., and Bamberg, E. (2003). Channelrhodopsin-2, a directly light-gated cation-selective membrane channel. *Proc. Natl. Acad. Sci.* *100*, 13940–13945.
98. Nagel, G., Szellas, T., Kateriya, S., Adeishvili, N., Hegemann, P., and Bamberg, E. (2005). Channelrhodopsins: directly light-gated cation channels. *Biochem. Soc. Trans.* *33*, 863–866.
99. Neef, A., Khimich, D., Pirih, P., Riedel, D., Wolf, F., and Moser, T. (2007). Probing the mechanism of exocytosis at the hair cell ribbon synapse. *J. Neurosci.* *27*, 12933–12944.
100. Neef, J., Jung, S., Wong, A.B., Reuter, K., Pangrsic, T., Chakrabarti, R., Kugler, S., Lenz, C., Nouvian, R., Boumil, R.M., et al. (2014). Modes and Regulation of Endocytic Membrane Retrieval in Mouse Auditory Hair Cells. *J. Neurosci.* *34*, 705–716.
101. Nicholls, D.G., and Sihra, T.S. (1986). Synaptosomes possess an exocytotic pool of glutamate. *Nature* *321*, 772–773.
102. Nicolson, T. (2015). Ribbon synapses in zebrafish hair cells. *Hear. Res.*
103. Nikolic, K., Grossman, N., Grubb, M.S., Burrone, J., Toumazou, C., and Degenaar, P. (2009). Photocycles of Channelrhodopsin-2. *Photochem. Photobiol.* *85*, 400–411.
104. Nouvian, R. (2007). Temperature enhances exocytosis efficiency at the mouse inner hair cell ribbon synapse. *J. Physiol.* *584*, 535–542.
105. Nouvian, R., Beutner, D., Parsons, T.D., and Moser, T. (2006). Structure and function of the hair cell ribbon synapse. *J. Membr. Biol.* *209*, 153–165.
106. Nouvian, R., Neef, J., Bulankina, A.V., Reisinger, E., Pangršič, T., Frank, T., Sikorra, S., Brose, N., Binz, T., and Moser, T. (2011). Exocytosis at the hair cell ribbon synapse apparently operates without neuronal SNARE proteins. *Nat. Neurosci.* *14*, 411–413.
107. Ohara-Imaizumi, M., Ohtsuka, T., Matsushima, S., Akimoto, Y., Nishiwaki, C., Nakamichi, Y., Kikuta, T., Nagai, S., Kawakami, H., Watanabe, T., et al. (2005). ELKS, a Protein Structurally Related to the Active Zone-associated Protein CAST, Is Expressed in Pancreatic β Cells and Functions in Insulin Exocytosis: Interaction of ELKS with Exocytotic Machinery Analyzed by Total Internal Reflection Fluorescence Microscopy. *Mol. Biol. Cell* *16*, 3289–3300.

108. Pangrsic, T., Lasarow, L., Reuter, K., Takago, H., Schwander, M., Riedel, D., Frank, T., Tarantino, L.M., Bailey, J.S., Strenzke, N., et al. (2010). Hearing requires otoferlin-dependent efficient replenishment of synaptic vesicles in hair cells. *Nat. Neurosci.* *13*, 869–876.
109. Pangršič, T., Reisinger, E., and Moser, T. (2012). Otoferlin: a multi-C2 domain protein essential for hearing. *Trends Neurosci.* *35*, 671–680.
110. Parsons, T.D., and Sterling, P. (2003). Synaptic Ribbon. *Neuron* *37*, 379–382.
111. Pickles, J.O., Comis, S.D., and Osborne, M.P. (1984). Cross-links between stereocilia in the guinea pig organ of Corti, and their possible relation to sensory transduction. *Hear. Res.* *15*, 103–112.
112. Pieribone, V.A., Shupliakov, O., Brodin, L., Hilfiker-Rothenfluh, S., Czernik, A.J., and Greengard, P. (1995). Distinct pools of synaptic vesicles in neurotransmitter release. *Nature* *375*, 493–497.
113. Raphael, Y., and Altschuler, R.A. (2003). Structure and innervation of the cochlea. *Brain Res. Bull.* *60*, 397–422.
114. Regus-Leidig, H., Ott, C., Löhner, M., Atorf, J., Fuchs, M., Sedmak, T., Kremers, J., Fejtová, A., Gundelfinger, E.D., and Brandstätter, J.H. (2013). Identification and Immunocytochemical Characterization of Piccolino, a Novel Piccolo Splice Variant Selectively Expressed at Sensory Ribbon Synapses of the Eye and Ear. *PLoS ONE* *8*, e70373.
115. Regus-Leidig, H., Fuchs, M., Löhner, M., Leist, S.R., Leal-Ortiz, S., Chiodo, V.A., Hauswirth, W.W., Garner, C.C., and Brandstätter, J.H. (2014). In vivo knockdown of Piccolino disrupts presynaptic ribbon morphology in mouse photoreceptor synapses. *Front. Cell. Neurosci.* *8*, 259.
116. Reisinger, E., Bresee, C., Neef, J., Nair, R., Reuter, K., Bulankina, A., Nouvian, R., Koch, M., Bückers, J., Kastrup, L., et al. (2011). Probing the functional equivalence of otoferlin and synaptotagmin 1 in exocytosis. *J. Neurosci. Off. J. Soc. Neurosci.* *31*, 4886–4895.
117. Revelo, N.H., Kamin, D., Truckenbrodt, S., Wong, A.B., Reuter-Jessen, K., Reisinger, E., Moser, T., and Rizzoli, S.O. (2014). A new probe for super-resolution imaging of membranes elucidates trafficking pathways. *J. Cell Biol.* *205*, 591–606.
118. Rizo, J., and Südhof, T.C. (1998). C2-domains, Structure and Function of a Universal Ca²⁺-binding Domain. *J. Biol. Chem.* *273*, 15879–15882.
119. Rizo, J., Chen, X., and Araç, D. (2006). Unraveling the mechanisms of synaptotagmin and SNARE function in neurotransmitter release. *Trends Cell Biol.* *16*, 339–350.
120. Rizzoli, S.O., and Betz, W.J. (2005). Synaptic vesicle pools. *Nat. Rev. Neurosci.* *6*, 57–69.
121. Rodrigues, H.A., Fonseca, M. de C., Camargo, W.L., Lima, P.M.A., Martinelli, P.M., Naves, L.A., Prado, V.F., Prado, M.A.M., and Guatimosim, C. (2013). Reduced expression of the vesicular acetylcholine transporter and neurotransmitter content affects synaptic vesicle distribution and shape in mouse neuromuscular junction. *PLoS One* *8*, e78342.
122. Rodríguez-Ballesteros, M., del Castillo, F.J., Martín, Y., Moreno-Pelayo, M.A., Morera, C., Prieto, F., Marco, J., Morant, A., Gallo-Terán, J., Morales-Angulo, C., et al. (2003). Auditory neuropathy in patients carrying mutations in the otoferlin gene (OTOF). *Hum. Mutat.* *22*, 451–456.

123. Rodríguez-Ballesteros, M., Reynoso, R., Olarte, M., Villamar, M., Morera, C., Santarelli, R., Arslan, E., Medá, C., Curet, C., Völter, C., et al. (2008). A multicenter study on the prevalence and spectrum of mutations in the otoferlin gene (OTOF) in subjects with nonsyndromic hearing impairment and auditory neuropathy. *Hum. Mutat.* *29*, 823–831.
124. Rosenmund, C., and Stevens, C.F. (1997). The rate of aldehyde fixation of the exocytotic machinery in cultured hippocampal synapses. *J. Neurosci. Methods* *76*, 1–5.
125. Rostaing, P., Real, E., Siksou, L., Lechaire, J.-P., Boudier, T., Boeckers, T.M., Gertler, F., Gundelfinger, E.D., Triller, A., and Marty, S. (2006). Analysis of synaptic ultrastructure without fixative using high-pressure freezing and tomography. *Eur. J. Neurosci.* *24*, 3463–3474.
126. Roux, I., Safieddine, S., Nouvian, R., Grati, M. 'hamed, Simmler, M.-C., Bahloul, A., Perfettini, I., Le Gall, M., Rostaing, P., Hamard, G., et al. (2006). Otoferlin, defective in a human deafness form, is essential for exocytosis at the auditory ribbon synapse. *Cell* *127*, 277–289.
127. Roux, I., Hosie, S., Johnson, S.L., Bahloul, A., Cayet, N., Nouaille, S., Kros, C.J., Petit, C., and Safieddine, S. (2009). Myosin VI is required for the proper maturation and function of inner hair cell ribbon synapses. *Hum. Mol. Genet.* *18*, 4615–4628.
128. Russell, I., and Sellick, P. (1983). Low-frequency characteristics of intracellularly recorded receptor potentials in guinea-pig cochlear hair cells. *J. Physiol.* *338*, 179–206.
129. Russell, I.J., Kossl, M., and Richardson, G.P. (1992). Nonlinear Mechanical Responses of Mouse Cochlear Hair Bundles. *Proc. R. Soc. Lond. B Biol. Sci.* *250*, 217–227.
130. Rutherford, M.A. (2015). Resolving the structure of inner ear ribbon synapses with STED microscopy. *Synapse* *69*, 242–255.
131. Rutherford, M.A., and Roberts, W.M. (2006). Frequency selectivity of synaptic exocytosis in frog saccular hair cells. *Proc. Natl. Acad. Sci. U. S. A.* *103*, 2898.
132. Safieddine, S., and Wenthold, R.J. (1999). SNARE complex at the ribbon synapses of cochlear hair cells: analysis of synaptic vesicle- and synaptic membrane-associated proteins. *Eur. J. Neurosci.* *11*, 803–812.
133. Saito, K. (1990). Freeze-fracture organization of hair cell synapses in the sensory epithelium of guinea pig organ of Corti. *J. Electron Microsc. Tech.* *15*, 173–186.
134. Schmitz, F., Königstorfer, A., and Südhof, T.C. (2000a). RIBEYE, a component of synaptic ribbons: a protein's journey through evolution provides insight into synaptic ribbon function. *Neuron* *28*, 857–872.
135. Schmitz, F., Königstorfer, A., and Südhof, T.C. (2000b). RIBEYE, a Component of Synaptic Ribbons. *Neuron* *28*, 857–872.
136. Schoch, S., Mittelstaedt, T., Kaeser, P.S., Padgett, D., Feldmann, N., Chevaleyre, V., Castillo, P.E., Hammer, R.E., Han, W., Schmitz, F., et al. (2006). Redundant functions of RIM1[alpha] and RIM2[alpha] in Ca²⁺-triggered neurotransmitter release. *EMBO J* *25*, 5852–5863.
137. Schwander, M., Sczaniecka, A., Grillet, N., Bailey, J.S., Avenarius, M., Najmabadi, H., Steffy, B.M., Federe, G.C., Lagler, E.A., Banan, R., et al. (2007). A Forward Genetics Screen in Mice Identifies

- Recessive Deafness Traits and Reveals That Pejvakin Is Essential for Outer Hair Cell Function. *J. Neurosci.* *27*, 2163–2175.
138. Seal, R.P., Akil, O., Yi, E., Weber, C.M., Grant, L., Yoo, J., Clause, A., Kandler, K., Noebels, J.L., Glowatzki, E., et al. (2008). Sensorineural Deafness and Seizures in Mice Lacking Vesicular Glutamate Transporter 3. *Neuron* *57*, 263–275.
139. Sheets, L., Trapani, J.G., Mo, W., Obholzer, N., and Nicolson, T. (2011). Ribeye is required for presynaptic CaV1.3a channel localization and afferent innervation of sensory hair cells. *Development* *138*, 1309–1319.
140. Siksou, L., Rostaing, P., Lechaire, J.-P., Boudier, T., Ohtsuka, T., Fejtová, A., Kao, H.-T., Greengard, P., Gundelfinger, E.D., Triller, A., et al. (2007). Three-dimensional architecture of presynaptic terminal cytomatrix. *J. Neurosci.* *27*, 6868–6877.
141. Siksou, L., Varoqueaux, F., Pascual, O., Triller, A., Brose, N., and Marty, S. (2009). A common molecular basis for membrane docking and functional priming of synaptic vesicles. *Eur. J. Neurosci.* *30*, 49–56.
142. Siksou, L., Triller, A., and Marty, S. (2011). Ultrastructural organization of presynaptic terminals. *Curr. Opin. Neurobiol.* *21*, 261–268.
143. Siksou, L., Silm, K., Biesemann, C., Nehring, R.B., Wojcik, S.M., Triller, A., El Mestikawy, S., Marty, S., and Herzog, E. (2013). A role for vesicular glutamate transporter 1 in synaptic vesicle clustering and mobility. *Eur. J. Neurosci.* *37*, 1631–1642.
144. Smith, C.A., and Sjöstrand, F.S. (1961). A synaptic structure in the hair cells of the guinea pig cochlea. *J. Ultrastruct. Res.* *5*, 184–192.
145. Smith, J.E., and Reese, T.S. (1980). Use of aldehyde fixatives to determine the rate of synaptic transmitter release. *J. Exp. Biol.* *89*, 19–28.
146. Snellman, J., Mehta, B., Babai, N., Bartoletti, T.M., Akmentin, W., Francis, A., Matthews, G., Thoreson, W., and Zenisek, D. (2011). Acute destruction of the synaptic ribbon reveals a role for the ribbon in vesicle priming. *Nat. Neurosci.* *14*, 1135–1141.
147. Sobkowicz, H.M., Rose, J.E., Scott, G.E., and Slapnick, S.M. (1982). Ribbon synapses in the developing intact and cultured organ of Corti in the mouse. *J. Neurosci.* *2*, 942–957.
148. Sobkowicz, H.M., Rose, J.E., Scott, G.L., and Levenick, C.V. (1986). Distribution of synaptic ribbons in the developing organ of Corti. *J. Neurocytol.* *15*, 693–714.
149. Spassova, M.A., Avissar, M., Furman, A.C., Crumling, M.A., Saunders, J.C., and Parsons, T.D. (2004). Evidence that rapid vesicle replenishment of the synaptic ribbon mediates recovery from short-term adaptation at the hair cell afferent synapse. *J. Assoc. Res. Otolaryngol. JARO* *5*, 376–390.
150. Spiwoks-Becker, I., Maus, C., tom Dieck, S., Fejtová, A., Engel, L., Wolloscheck, T., Wolfrum, U., Vollrath, L., and Spessert, R. (2008). Active zone proteins are dynamically associated with synaptic ribbons in rat pinealocytes. *Cell Tissue Res.* *333*, 185–195.
151. Stanley, E.F. (1993). Single calcium channels and acetylcholine release at a presynaptic nerve terminal. *Neuron* *11*, 1007–1011.

152. Starr, A., Sininger, Y., Winter, M., Derebery, M.J., Oba, S., and Michalewski, H.J. (1998). Transient deafness due to temperature-sensitive auditory neuropathy. *Ear Hear.* *19*, 169–179.
153. Sterling, P., and Matthews, G. (2005). Structure and function of ribbon synapses. *Trends Neurosci.* *28*, 20–29.
154. Stigloher, C., Zhan, H., Zhen, M., Richmond, J., and Bessereau, J.-L. (2011). The presynaptic dense projection of the *Caenorhabditis elegans* cholinergic neuromuscular junction localizes synaptic vesicles at the active zone through SYD-2/liprin and UNC-10/RIM-dependent interactions. *J. Neurosci. Off. J. Soc. Neurosci.* *31*, 4388–4396.
155. Strenzke, N., Chanda, S., Kopp-Scheinflug, C., Khimich, D., Reim, K., Bulankina, A.V., Neef, A., Wolf, F., Brose, N., Xu-Friedman, M.A., et al. (2009). Complexin-I Is Required for High-Fidelity Transmission at the Endbulb of Held Auditory Synapse. *J. Neurosci.* *29*, 7991–8004.
156. Strenzke, N., Chakrabarti, R., Al-Moyed, H., Müller, A., Hoch, G., Pangrsic, T., Yamanbaeva, G., Lenz, C., Pan, K.-T., Auge, E., et al. (2016). Hair cell synaptic dysfunction, auditory fatigue and thermal sensitivity in otoferlin Ile515Thr mutants. *EMBO J.* e201694564.
157. Südhof, T.C. (2012). The presynaptic active zone. *Neuron* *75*, 11–25.
158. Südhof, T.C. (2013). Neurotransmitter release: the last millisecond in the life of a synaptic vesicle. *Neuron* *80*, 675–690.
159. Szule, J.A., Harlow, M.L., Jung, J.H., De-Miguel, F.F., Marshall, R.M., and McMahan, U.J. (2012). Regulation of synaptic vesicle docking by different classes of macromolecules in active zone material. *PLoS One* *7*, e33333.
160. Takei, Y., Harada, A., Takeda, S., Kobayashi, K., Terada, S., Noda, T., Takahashi, T., and Hirokawa, N. (1995). Synapsin I deficiency results in the structural change in the presynaptic terminals in the murine nervous system. *J. Cell Biol.* *131*, 1789–1800.
161. Usukura, J., and Yamada, E. (1987). Ultrastructure of the synaptic ribbons in photoreceptor cells of *Rana catesbeiana* revealed by freeze-etching and freeze-substitution. *Cell Tissue Res.* *247*, 483–488.
162. Uthiaiah, R.C., and Hudspeth, A.J. (2010). Molecular Anatomy of the Hair Cell's Ribbon Synapse. *J. Neurosci.* *30*, 12387–12399.
163. Varga, R., Kelley, P.M., Keats, B.J., Starr, A., Leal, S.M., Cohn, E., and Kimberling, W.J. (2003). Non-syndromic recessive auditory neuropathy is the result of mutations in the otoferlin (OTOF) gene. *J. Med. Genet.* *40*, 45–50.
164. Varga, R., Avenarius, M.R., Kelley, P.M., Keats, B.J., Berlin, C.I., Hood, L.J., Morlet, T.G., Brashears, S.M., Starr, A., Cohn, E.S., et al. (2006). OTOF mutations revealed by genetic analysis of hearing loss families including a potential temperature sensitive auditory neuropathy allele. *J. Med. Genet.* *43*, 576–581.
165. Verhage, M., and Sørensen, J.B. (2008). Vesicle Docking in Regulated Exocytosis. *Traffic* *9*, 1414–1424.
166. Vincent, P.F., Bouleau, Y., Petit, C., and Dulon, D. (2015). A synaptic F-actin network controls otoferlin-dependent exocytosis in auditory inner hair cells. *eLife* *4*.

167. Vincent, P.F.Y., Bouleau, Y., Safieddine, S., Petit, C., and Dulon, D. (2014). Exocytotic machineries of vestibular type I and cochlear ribbon synapses display similar intrinsic otoferlin-dependent Ca²⁺ sensitivity but a different coupling to Ca²⁺ channels. *J. Neurosci. Off. J. Soc. Neurosci.* *34*, 10853–10869.
168. Vogl, C., Cooper, B.H., Neef, J., Wojcik, S.M., Reim, K., Reisinger, E., Brose, N., Rhee, J.-S., Moser, T., and Wichmann, C. (2015). Unconventional molecular regulation of synaptic vesicle replenishment in cochlear inner hair cells. *J. Cell Sci.* *128*, 638–644.
169. Vogl, C., Panou, I., Yamanbaeva, G., Wichmann, C., Mangosing, S.J., Vilardi, F., Indzhukulian, A.A., Pangršič, T., Santarelli, R., Rodriguez-Ballesteros, M., et al. (2016). Tryptophan-rich basic protein (WRB) mediates insertion of the tail-anchored protein otoferlin and is required for hair cell exocytosis and hearing. *EMBO J.* e201593565.
170. Vollrath, L., and Spiwoks-Becker, I. (1996). Plasticity of retinal ribbon synapses. *Microsc. Res. Tech.* *35*, 472–487.
171. Wang, Y., and Südhof, T.C. (2003). Genomic definition of RIM proteins: evolutionary amplification of a family of synaptic regulatory proteins. *Genomics* *81*, 126–137.
172. Wang, D.-Y., Wang, Y.-C., Weil, D., Zhao, Y.-L., Rao, S.-Q., Zong, L., Ji, Y.-B., Liu, Q., Li, J.-Q., Yang, H.-M., et al. (2010). Screening mutations of OTOF gene in Chinese patients with auditory neuropathy, including a familial case of temperature-sensitive auditory neuropathy. *BMC Med. Genet.* *11*, 79.
173. Washbourne, P., Thompson, P.M., Carta, M., Costa, E.T., Mathews, J.R., Lopez-Bendito, G., Molnár, Z., Becher, M.W., Valenzuela, C.F., Partridge, L.D., et al. (2002). Genetic ablation of the t-SNARE SNAP-25 distinguishes mechanisms of neuroexocytosis. *Nat. Neurosci.* *5*, 19–26.
174. Watanabe, S., Liu, Q., Davis, M.W., Hollopeter, G., Thomas, N., Jorgensen, N.B., and Jorgensen, E.M. (2013a). Ultrafast endocytosis at *Caenorhabditis elegans* neuromuscular junctions. *eLife* *2*, e00723.
175. Watanabe, S., Rost, B.R., Camacho-Pérez, M., Davis, M.W., Söhl-Kielczynski, B., Rosenmund, C., and Jorgensen, E.M. (2013b). Ultrafast endocytosis at mouse hippocampal synapses. *Nature* *504*, 242–247.
176. Wichmann, C., and Moser, T. (2015). Relating structure and function of inner hair cell ribbon synapses. *Cell Tissue Res.*
177. Wong, A.B., Rutherford, M.A., Gabrielaitis, M., Pangršič, T., Göttfert, F., Frank, T., Michanski, S., Hell, S., Wolf, F., Wichmann, C., et al. (2014). Developmental refinement of hair cell synapses tightens the coupling of Ca²⁺ influx to exocytosis. *EMBO J.* *33*, 247–264.
178. Yasunaga, S., Grati, M., Cohen-Salmon, M., El-Amraoui, A., Mustapha, M., Salem, N., El-Zir, E., Loiselet, J., and Petit, C. (1999). A mutation in OTOF, encoding otoferlin, a FER-1-like protein, causes DFNB9, a nonsyndromic form of deafness. *Nat. Genet.* *21*, 363–369.
179. Yasunaga, S., 'ichiro, Grati, M., 'hamed, Chardenoux, S., Smith, T.N., Friedman, T.B., Lalwani, A.K., Wilcox, E.R., and Petit, C. (2000). OTOF Encodes Multiple Long and Short Isoforms: Genetic Evidence That the Long Ones Underlie Recessive Deafness DFNB9. *Am. J. Hum. Genet.* *67*, 591–600.
180. Yizhar, O., Fenno, L.E., Davidson, T.J., Mogri, M., and Deisseroth, K. (2011). Optogenetics in neural systems. *Neuron* *71*, 9–34.

181. Zenisek, D., Steyer, J.A., and Almers, W. (2000). Transport, capture and exocytosis of single synaptic vesicles at active zones. *Nature* *406*, 849–854.
182. Zhai, R.G., and Bellen, H.J. (2004). The Architecture of the Active Zone in the Presynaptic Nerve Terminal. *Physiology* *19*, 262–270.
183. Zheng, J., Shen, W., He, D.Z., Long, K.B., Madison, L.D., and Dallos, P. (2000). Prestin is the motor protein of cochlear outer hair cells. *Nature* *405*, 149–155.

Acknowledgments

First and foremost, I would like to express my most profound appreciation and gratitude to Professor Dr. Carolin Wichmann, for accepting me in her group, for providing me a scientific niche and always encouraging me even when I was wrecked by the complexity of the project(s). In the initial stages of my Ph.D. she introduced me to the methods of electron microscopy with utmost care and precision. She highly encouraged my independence, however without her attention to details and constant supervision the task would have been cumbersome. I extend my thanks to the thesis committee advisors, Dr. Camin Dean and Professor Dr. Thomas Dresbach for their timely advice and critical evaluation of my progress in last four years. The TAC meetings always helped me to look at the question from different perspectives and streamline the further investigations based on that. Also, I highly appreciate Dr. Manuela Schmidt, Professor Dr. Silvio. O. Rizzoli and Professor Dr. Jochen Staiger for taking out time to be my extended TAC members.

Further, I would like to acknowledge the funding body Deutsche Forschungsgemeinschaft, DFG for assuring continuous funding through the SFB 889-A7 project (AG Wichmann) and the graduate program of Sensory and Motor Neuroscience (SMN) at the Göttingen Graduate School for Neurosciences, Biophysics, and Molecular Biosciences (GGNB) for organizing several productive method/skill courses and for providing a platform to interact with fellow graduate students, alumni and people from diverse professional backgrounds. Two years, as a student representative of SMN, made me realize how challenging it must be to keep things running in such a multi-disciplinary and international program.

This thesis would not be complete without close collaborations with the groups of Professor Dr. Tobias Moser, Dr. Ellen Reisinger, Dr. Nicola Strenzke and Dr. Tina Pangršič Vilfan, who played a crucial role in developing my analytical and critical questioning. These collaborations lead to two successful publications from this thesis (Jung et al., 2015a; and Strenzke et al., 2016). I especially thank Dr. SangYong Jung (former AG Moser), Hanan Al-Moyed (AG Reisinger), Gerhard Hoch (AG Moser), Lina Maria Jaime Tobón (AG Moser) Dr. Jakob Neef (AG Moser) and Dr. Kai Bodensiek (AG Moser) for open discussions, free data sharing and countless late night pizzas.

I would like to thank every colleague (with whom I overlapped during my tenure) at the Institute for Auditory Neuroscience and InnerEarLab for providing a relaxed environment and ensuring a creative workspace. My special thanks go to Dr. Jakob Neef for being the most generous person I have ever met! He became the “to go guy” on various occasions.

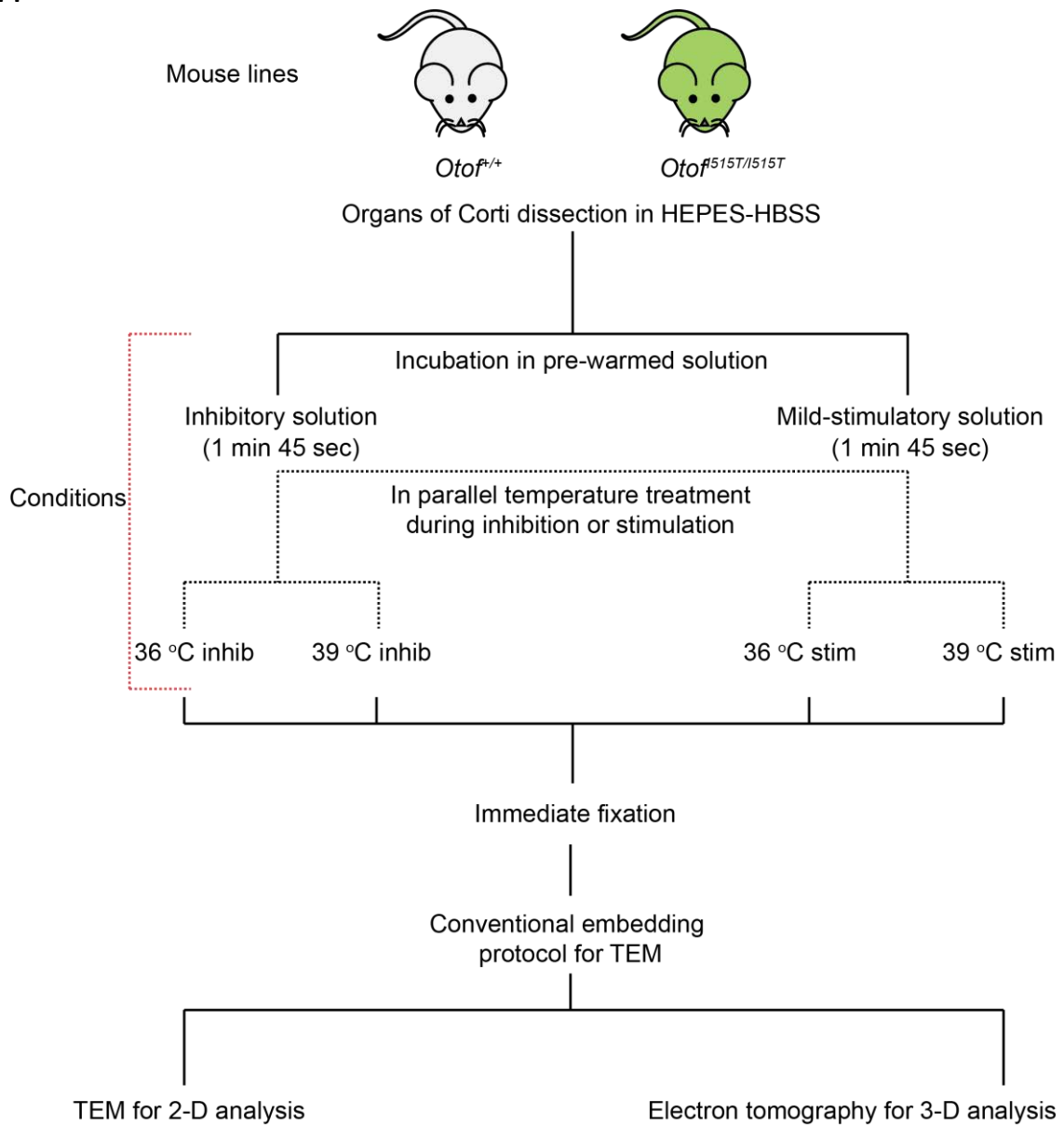
He helped me a lot with this thesis and always offered a positive feedback. I would further like to thank Susann Michanski first and foremost for always having the channel of communication open and helping me especially when my sensory and motor reflexes refused to coordinate for that "one last experiment" or for that "one last figure legend". I extend my gratitude to Dr. Maria Magdalena Picher, Dr. Christian Vogl, Dr. Chao-Hua Huang, and Tanvi Butola for being critical of my projects from the very start, yet relentlessly supportive. I thank Dr. Mehmet Gültas and Dr. Evgenia Kalogeraki, to sit with me till the very last moment to proofread this thesis. I am thankful to Tobias Goldak, Christiane Senger-Freitag and Sandra Gerke for excellent technical support and to Patricia Räke-Kügler and Susann Müller for making German bureaucracy "a bit" easier for me.

These four years would not have been possible without the love and moral support from friends beyond the borders. Thank you! Iliana, Evgenia, Leni, Norma, Susi, Tanvi, Chao-Hua, Vandana, Chaitali, Steffi, Chitkala, Vartika, Siddhartha, Samudra, Prakrith, Florian, Daniel, David, Jakob and Christian for turning my nomadic settlements into a home away from home.

Last but not the least I owe my sincere thanks to my parents and my sister for continually loving and blessing me. No words can ever be enough to express my gratitude for them. I dedicate this thesis to the two strong women who shaped me and my principles, your love for science and strong support for women in science inspired me deeply quite early on; Thank you! Maa and Dr. Kavitha Thirumurgan.

Appendix information

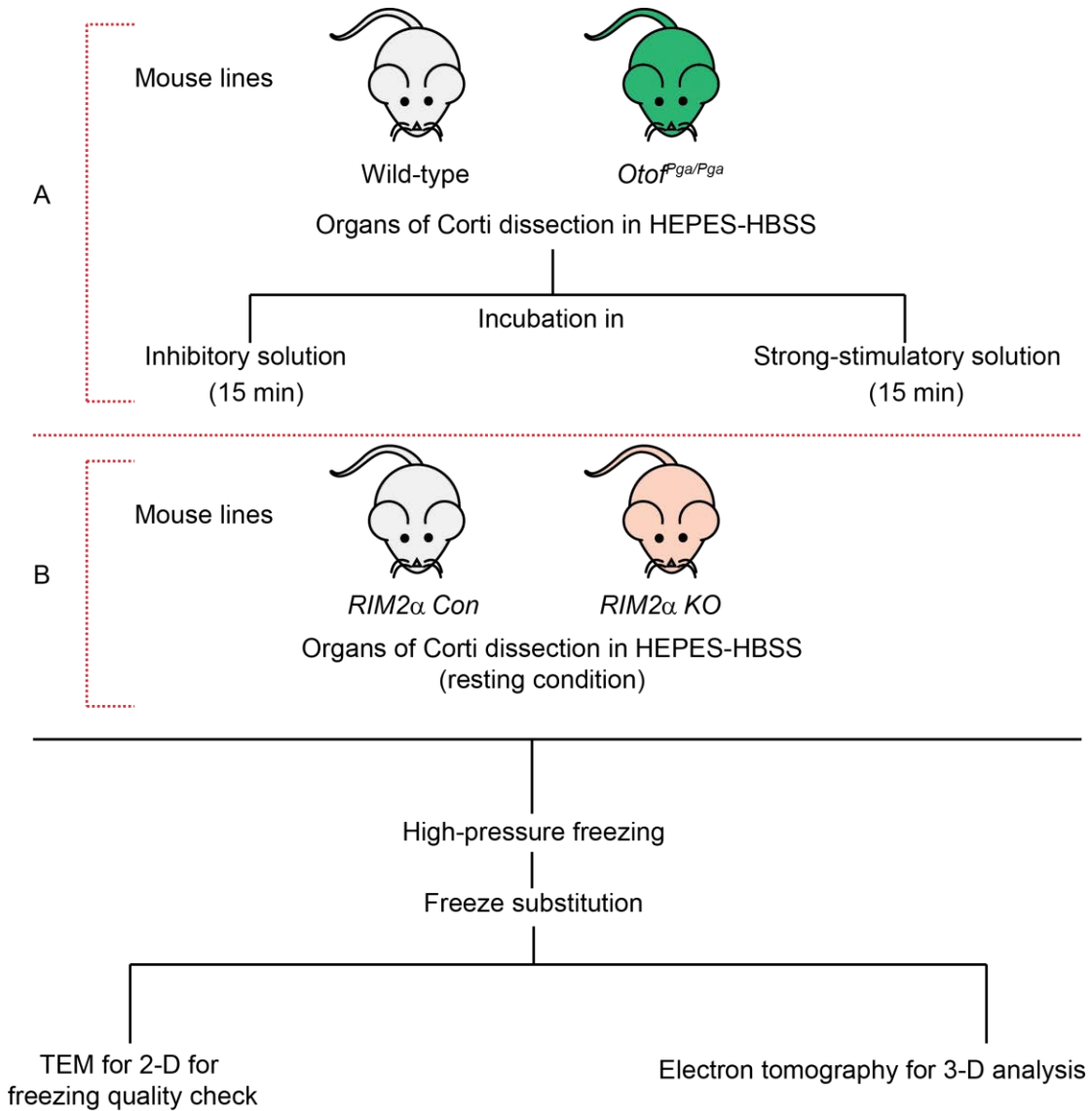
Appendix I: Work flow for the results section 3.1



Experimental work flow incorporated for the section 3.1

In depth methodology explained in materials and methods (chapter-2)

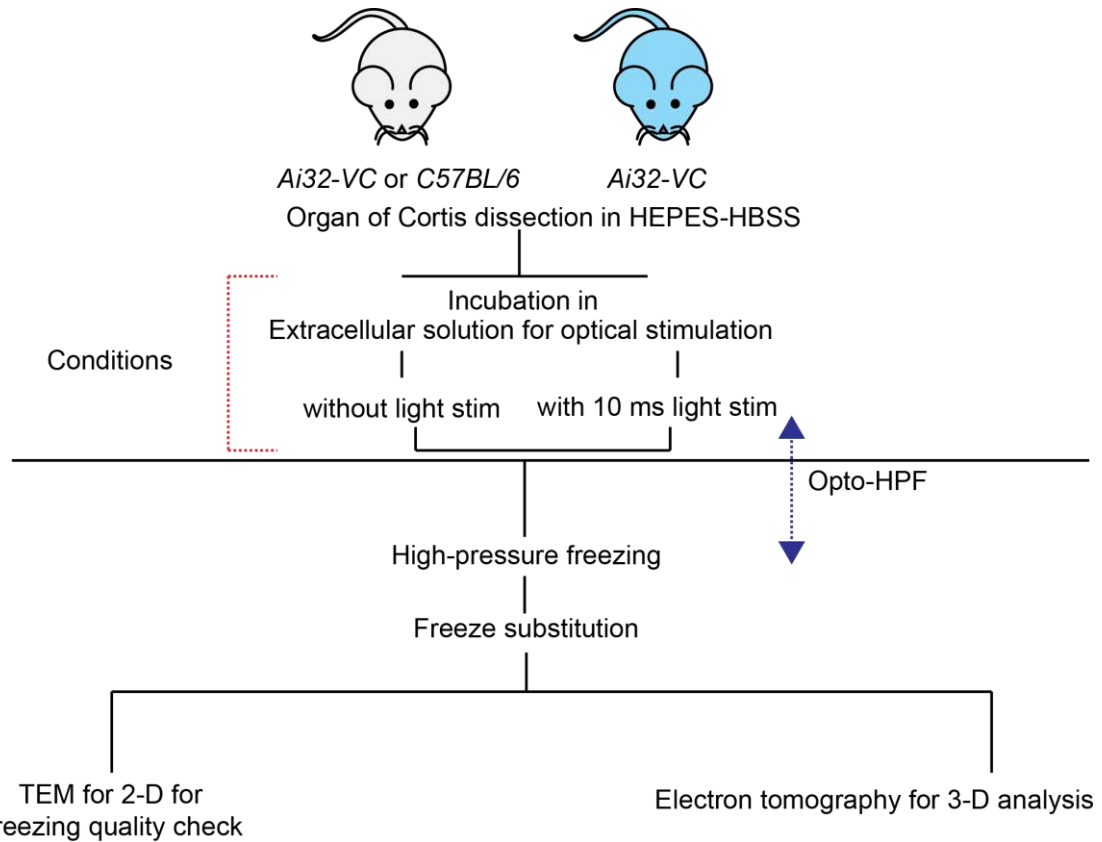
Appendix II: Work flow for the results section 3.2 and 3.3



Experimental work flow incorporated for the section 3.2 (A) and 3.3 (B)

In depth methodology explained in materials and methods (chapter-2)

Appendix III: Work flow for the results section 3.4



Experimental work flow incorporated for the section 3.4

In depth methodology explained in materials and methods (chapter-2)

Curriculum vitae

Personal Information

Name: Rituparna Chakrabarti

Address: Grüner Weg-8, Göttingen, Germany 37075

Email: rituparna.chakrabarti@gmail.com

Date/Place of birth: 5th August, 1989/Kolkata, West Bengal, India

Nationality: Indian



Education

2012 - 2016 PhD Neuroscience

- PhD scholar at Göttingen Graduate School for Neurosciences, Biophysics, and Molecular Biosciences, focused on Sensory and Motorneuroscience/ University of Göttingen/ Germany
- *Thesis title: Investigation of vesicle pool dynamics at activity modulated inner hair cell ribbon synapses*
- Supervisor: Prof. Dr. Carolin Wichmann

2011 - 2012 Junior research fellow (JRF)

- Tata Institute of Fundamental Research, Mumbai, India
- Supervisor: Prof. Dr. Krishanu Ray

2010 - 2012 M.Sc. Biotechnology

- VIT University, Vellore, India.
- Cumulative grade point (CGP): 9.31/10 (10 being the highest)
- *Thesis title: Investigating the role of kinesin-2 mutations on synaptic ultra-structure in the ventral ganglion of Drosophila third instar larvae*
- Supervisor: Prof. Dr. Krishanu Ray
- Co-Supervisor: Prof. Dr. Kavitha Thirumorgan

2007 - 2010 B.Sc. Biotechnology

- VIT University, Vellore, India.
- CGP: 9.13/10 (10 being the highest)

Honors and awards

2015	Best speaker award (2 nd place), SMN/SFB-889 Retreat, Goslar, Germany
2015	Best scientific presentation award (1 st place), Ribbon Synapse Symposium 2015, Göttingen, Germany
2013	Faculty of 1000 Best scientific presentation award (3 rd place), Ribbon Synapse Symposium 2013, Göttingen, Germany
2011	UGC-CSIR/NET- Junior Research Fellowship, the Council for Scientific and Industrial Research, Government of India
2012	Gold medalist, M.Sc. Biotechnology, VIT University, Vellore, India
2010	Third rank, B.Sc. Biotechnology, VIT University, Vellore, India

Teaching experiences

September, 2014 - March, 2015	Subhashree Nayak, Fulbright Scholarship Exchange student
April, 2014 – May, 2014	Sarah Grant, Master's laboratory rotation student
2013-2015	Bi-annual GGNB method course: Basic methods of TEM-from tissue preparation to 3-D reconstruction

Conferences and symposiums

- **Poster presentations**

Bilateral meeting SFB889/SFB890

Activity dependent nanostructure of Inner hair cell ribbon synapses, Chakrabarti R, Michanski S and Wichmann C/Munich, Germany/Oct 2016

Association with Research in Otolaryngology-39th Annual Mid-Winter Meeting

1. Activity-induced ultrastructural changes at wild-type and mutant inner hair cell ribbon synapses, Chakrabarti R, Michanski S, Jung S, Moser M and Wichmann C/San-Diego, USA/Feb 2016
2. Optical stimulation and readout of inner hair cell vesicle release, Krinner S, Jaime L, Chakrabarti R, Neef J, Jung S, Hoch G, Wichmann C, Moser T/San-Diego, USA/Feb 2016

Ribbon Synapse Symposium

Activity dependent nanostructure of inner hair cell ribbon synapses, Chakrabarti R, Michanski S, Jung S, Moser T and Wichmann C/Göttingen, Germany/Sep 2015

9th FENS Forum for Neuroscience

Role of otoferlin in vesicle dynamics at the inner hair cell ribbon synapses, Chakrabarti R, Al-Moyed H, Moser T, Reisinger E and Wichmann C/Milan, Italy/July 2014

Ribbon Synapse Symposium

Role of otoferlin in vesicle dynamics at the inner hair cell ribbon synapses, Chakrabarti R, Reisinger E, Strenzke N, Moser T, and Wichmann C/Göttingen, Germany/Sep2013

- **Oral presentations**

Mechanism of Synaptic Transmission Symposium

Activity dependent nanostructure of inner hair cell ribbon synapses/Paris, France/Sep 2015

11th Göttingen Meeting of the German Neuroscience Society

Tethering and vesicle dynamics at the active zone of Inner hair cell ribbon synapses under different activity state/Göttingen, Germany/ March 2015

Publications

1. Strenzke N. #, **Chakrabarti R** #, Al-Moyed H #, Müller A, Hoch G, Pangrsic T, Yamanbaeva G, Lenz C, Pan K-T, Auge E, et al. (2016). Hair cell synaptic dysfunction, auditory fatigue and thermal sensitivity in otoferlin Ile515Thr mutants. EMBO J. e201694564. **# first co-author**
2. Jung S #, Oshima-Takago T #, **Chakrabarti R** §, Wong A.B §, Jing Z, Yamanbaeva G, Picher M.M, Wojcik S.M, Göttfert F, Predoehl F, et al. (2015). Rab3-interacting molecules 2 α and 2 β promote the abundance of voltage-gated CaV1.3 Ca²⁺ channels at hair cell active zones. Proc. Natl. Acad. Sci. 112, E3141–E3149. **# first co-author and § equal contributing author**
3. Neef J, Jung S, Wong A.B, Reuter K, Pangrsic T, **Chakrabarti R**, Kugler S, Lenz C, Nouvian R, Boumil R.M, et al. (2014). Modes and Regulation of Endocytic Membrane Retrieval in Mouse Auditory Hair Cells. J. Neurosci. 34, 705–716.
4. **Chakrabarti R**, Singh B, Narendra P, Vanchhawng L, and Thirumurugan K (2014). Screening of nice herbal plants for alpha-amylase inhibition. Asian J. Pharm. Clin. Res. 0, 84–89.
5. **Chakrabarti R**, Bhavtaran S, Narendra P, Varghese N, Vanchhawng L, Mohamed Sham Shihabudeen H, and Thirumurgan K (2011). Dipeptidyl peptidase-IV inhibitory activity of Berberis aristata. J Nat Prod 4, 158–63.